SCUOLA DOTTORALE IN

GEOLOGIA DELL'AMBIENTE E DELLE RISORSE

(SDIGAR)

Sezione Geodinamica

Ciclo XXIV

The evolution of fracturing process in fault damage-zones and its influence on the rock permeability: case study of the shallow marine and ramp carbonates of Central Apennines (Italy)

Irene Mannino

A. A. 2011/2012

Tutor
Prof. Francesco Salvini

Direttore SDIGAR
Prof. Domenico Cosentino

Revisori
Prof. Jan Tveranger
Centre for Integrated Petroleum Research

Dr. Claudio Coelho de Lima
Consultor Senior
Petrobras

Irene Mannino

XXVI ciclo dottorale-2008-2011

Email: imannino@uniroma3.it
irenemannino@virgilio.it

Università degli Studi "Roma Tre"
Dipartimento di Scienze Geologiche
L. go S. Leonardo Murialdo 1
00146 Roma, Italia

Acknowledgments

Firstly, I would like to thank my supervisor, Prof. Francesco Salvini for encouraging to undertake this project and for the confidence he always put in me. Thanks to his versatile mind he introduced me to the beauty and difficulty of the "fracturing world". His scientific support, both on the field and during the processing of the data, has been fundamental to plan and improve my research. With him I'm also thankful to Dott. Paola Cianfarra for the suggestions and support she gave me during these three years.

I would like to address my heartfelt thanks to all the students and person who passed for the GeoQute Laboratory. In particular, my special recognitions go to Alini, Matteo, Santosh and Chiara, who warmly supported me during the most difficult times.

I'm grateful to all the member of the research group of CIPR (Centre for Integrated Petroleum Research) for the constructive discussions, collaborations and for the excellent time spent together during my staying in Bergen. In particular, I'm extremely indebted to Jan Tveranger for his teaching about fault modelling approach and for the stimulating geological discussions.

I want to express my warmest gratitude to Eivind Bastesen and Atle Rotevatn, for the constructive geology and non-geology discussions and for the pleasant moments during breaks and lunches time. Their suggestions have been very useful during the data analysis and the drafting of the manuscript. I would also like to thank Dmitry Kolyukhin for the mathematical and the statistical suggestions.

Thanks are also due to Dr. Claudio Coelho de Lima who provided stimulating and helpful reviews of my Thesis.

I dedicate this Thesis to all my beautiful family, Mammapapà, Zio Gigi, Carla and Mauro, Marianna and Viola, and to my sisters Betta and Stella. My dedication is also addressed to my dearest journey friends Fabietto and Peppe, Francesca, Monia, Vale, Isa, Andrea, Lea and Anna who helped me to "open that door".

Last but not the least this work is dedicated to my Sognefjord Fabio, my serenity.

"The evolution of fracturing process in fault damage-zones and its influence on the rock permeability: the case study of shallow marine and ramp carbonates of Central Apennines (Italy)"

ABSTRACT

More than 60% of the world's oil and 40% of the world's gas reserves are held in carbonates. For this reason there are significant challenges in term of recovery due to the highly complex internal structure and specificity of carbonate reservoirs. The presence of faults, both seismic and subseismic, compartmentalized the reservoirs and therefore ruled the pathway of deep fluid. This is particularly true in carbonate rocks, where fault-core and the damage-zones show different hydraulic behaviours from the pristine rock as well as between them.

This study, by means of an original methodology, proposes a conceptual model of brittle deformation evolution and a predictive computer model of deformation distribution in carbonate damage-zones, starting from the statistical analysis of field data. In particular, this work faces the following main challenges: the field characterization of fault zones and the quantification of the brittle deformation; the analytical study of the field data by means of a Monte Carlo approach; the numerical modelling of fault zones. Since the fracture patterns of petroleum reservoirs *in situ* are difficult to study in detail, field analogues represent a good opportunity for understanding their fracture-related permeability.

The field work was performed in Central Apennine on the Meso-Cenozoic units of carbonate platform and ramp, which represent a very good analogue of rock reservoirs. A total amount of 22 faults have been analysed on the field for this study. The fault database consists mostly on sub-seismic scale faults (scale below the resolution of seismic observation, 10 m); the database was completed with the study of 6 seismic scale faults (scale over the resolution of seismic observation). The results from these study show that the fault-related deformation intensity (H/S) is always significantly higher than the regional one, ranging 9.5-2.7 and 5-2 respectively, so that we can determine the lower threshold of H/S as 2.7 for faults and 2 for regional deformation. The fault kinematic rules the development of the fault deformation patterns. This is true mostly for the faults that showed double dip-slip and strike-slip kinematics, which are more deformed. The evolution of fault-related fracture sets is controlled by the rock anisotropy and the intensity of deformation of the main fracture cleavage is always higher than their suborded. The development of the stratabound and the non stratabound fractures in layered rocks depends on the stress intensity and the fault scale, and is controlled by the mechanical layering. A new methodology was improved to define the boundary between the damage zone and the pristine rock. A good relation exists between the damage-zone width and the intensity of deformation (H/S) for the subseismic scale faults. A power low trend was found between the damage-zone widths and the fault throws, suggesting that the fault damage-zones fracturing process is more intense in the early stage of fault development. The fault-related deformation intensity shows a clear variation through the distance from the master fault plane and three main trends have been detected: a) Exponential decrease; b) Semi-Gaussian decrease; c) Gaussian decrease. The Monte Carlo converging method provides a statistical tool to study the geological factors affecting the fracturing evolution in the fault damage-zone and the results show that the throw affects the deformation distribution mainly in the early stage of fault evolution.

A general equation was found to define quantitatively the distribution of the intensity of deformation in fault damage-zones, whose parameters have a geological meaning and are related

to the stress intensity. This equation provides a deformation intensity prediction with an error of + 2 H/S, which is the RMS resulting from simulation. The equation was implemented in the fracturing predictive software. The comparison between the models and the field data proves that the resulting models provide a reliable prediction of fracturing distribution in fault damage-zones.
Several methodologies and approaches have been proposed to predict the role of faults on brittle deformation distribution and their impact on permeability distribution, for instance indirect method as borehole and seismic imaging technologies, analogical and numerical simulations, micro tectonic studies, or direct method as field studies. The current study starting from real field data is fundamental to fill the gap of information between seismic data and well data, and hence necessary to allow including this information in 3-D reservoir models, simulating fluid flow.

1 – INTRODUCTION

More than 60% of the world's oil and 40% of the world's gas reserves are held in carbonates (Schlumberger Market Analysis, 2007; BP, 2011) (Fig. 1.1). From statistics it is clear that the relative importance of carbonate reservoirs compared with other types of reserves will increase dramatically during the first half of 21st century. For this reason there are significant challenges in term of recovery due to the highly complex internal structure and specificity of carbonate reservoirs.

Carbonate rocks, typically, have a complex texture and pore network resulting from their depositional history and later diagenesis. The porosity of carbonate rocks can be grouped into three types: a) connected porosity, existing between the carbonate grains; b) vugs, which are unconnected pores resulting from the dissolution of calcite by water during diagenesis; and c) fracture porosity, named secondary permeability, which is caused by stresses following deposition. Together, these three forms of porosity create a very complex path for fluids and directly affect well productivity. This heterogeneity also has an impact on the response of logging measurements and therefore on the determination of oil in place.

One of the most important questions that drive basin research on carbonate rocks is how deformation is accommodated, because it is very heterogeneous over time and space, and over a wide range of scales (e.g. Y; Pickering et al., 1996; Bonnet et al., 2001).

Techniques that were initially developed to characterize sandstone reservoirs are being applied to carbonate reservoirs, yet we know that these types of reservoirs have different requirements. In particular, carbonate reservoirs present a number of specific characteristics (diagenesis, porosity, secondary permeability, etc…) posing complex challenges in reservoir characterization, production and management. Most carbonate reservoirs are naturally fractured (Mimran, 1976, 1977; Nelson, 2001; Ameen et al., 1995; Long et al., 1996; Jones et al. 1998, Aydin et al., 2000; Yielding et al., 2010). The fractures exist at all scales, from microscopic fissures to kilometres sized structures, creating complex flow networks. As a consequence, the movement of hydrocarbons and other fluids is often not as expected or predicted. Therefore, knowing the fractures exact position is critical for planning new wells and for simulating and forecasting reservoir production.

The presence of faults, both seismic and subseismic, compartmentalized the reservoirs and therefore ruled the pathway of deep fluid (Yielding et al., 1997, 2010, Knipe, 1997; Moretti 1998; Manzocchi et al., 1999; Fisher 2001). This is particularly true in carbonate rocks, where fault-core and the damage-zones (Caine et al., 1996) show different hydraulic behaviours from the pristine rock as well as between them (Engelder, 1974; Sibson, 1977; Sammis et al., 1989; Blenkinsop, 1991; Chester et al., 1986, 1993; Antonellini et al., 1994; Evans et al., 1997; Rawling 2001; Storti et al., 2003; Cello et al. 2003; Micarelli et al. 2006; Billi et al., 2003, 2007; Wibberley et al., 2008).

The key to understanding the distribution and interaction of small and medium-scale fractures lies in the evolution and kinematics of large-scale structures, because the dominant strain component is commonly accommodated by large-scale faults with offsets of several tens or hundreds of meters (e.g. Scholz et al., 1990; Pickering et al., 1996; Ackermann et al., 1997; Bonnet et al., 2001).

These faults are typically identified by the interpretation of 2-D or 3-D seismic data, (Yielding et al., 1996). Around these major faults, smaller faults develop (for normal or inverted faults predominantly in the hangingwall, which accommodate minor strain with respect to the major fault. On the contrary, a partly isolated 1-D well data are hardly identified by spatially (e.g. McLeod et al., 2000), but their implementation within 3-D geo-models is a major goal of reservoir modeling. Nonetheless, the total amount of this subseismic brittle deformation can locally reach up to 50 % (Gauthier et al., 1993; Endres, 2008; Lohr et al. 2008) but the precise position, orientation, or density variation of sub-seismic faults and fractures is difficult to estimate. Hence, to approach this issue, it is fundamental to perform a multiscalar study of faults, which is what is being proposed in this Thesis.
This study is focussed on fault damage-zones and the main aim of my work has been to propose a conceptual and analytical model of damage-zone brittle evolution by means of field analogues study and a statistical approach. Since the fracture patterns of petroleum reservoirs in situ are difficult to study in detail, field analogues represent a good opportunity for understanding their fracture-related permeability. In particular, the following main goals have been reached:

1) The quantification of the brittle deformation intensity with particular attention to *a)* the quantitative study of the deformation patterns through the distance from the fault-core; *b)* the relation between the regional-related deformation and the fault-related deformation, in order to define a new methodology to estimate the limits between the damage-zone and the pristine rock; *c)* the study of the footwall fault deformation and the hangingwall one.
2) The study of the geological factors affecting the development and the evolution of fault-related fracturing and the statistical model of deformation intensity, via Monte Carlo approach.
3) The impact of fault-related fracturing evolution on permeability distribution around faults.

The field work was performed in Central Apennine on the Meso-Cenozoic units of carbonate platform and ramp, which represent a very good analogue of rock reservoirs. A total amount of 22 faults have been analysed on the field for this study. The fault database consists mostly on sub-seismic scale faults (Gauthier et al., 1993) (Fig. 2.2 b), characterized by a scale below the resolution of seismic observation (10 m); the database was completed with the study of 6 seismic scale faults, which have a scale over the resolution of seismic observation (Fig. 2.2 a). The predictive model of fracturing distribution in damage-zones was performed using a pseudo-statistical approach by means of the Monte Carlo method (Mosegaard *et a*l. 1995, Tarantola 2005). This approach was largely used in science to solve and to understand phenomena related to a huge number of variables. For this reason, in this work, this approach has been proposed to study and parameterize the fracturing process, which is related to a huge number of factors, as described by Caine et al. 1996.

Eventually, the implementation of the proposed model in a software fault environment (Frap-3) allows us to perform predictive models of fracturing distribution in fault zones at several distances from the master faults plane. This software is a true 4-D tool that can predict stress conditions and the brittle deformation patterns associated to a single fault or a given set of faults during single or multiple tectonic events, as well as under different stress conditions during time.

Several methodologies and approaches have been proposed to study the role of faults on the permeability distribution in rocks, for instance indirect method as borehole and seismic imaging technologies, analogical and numerical simulations, micro tectonic studies, or direct method as field studies. The current study starting from real field data is fundamental to fill the gap of information between seismic data and well data, and hence necessary to allow including this information in 3-D reservoir models, simulating fluid flow.

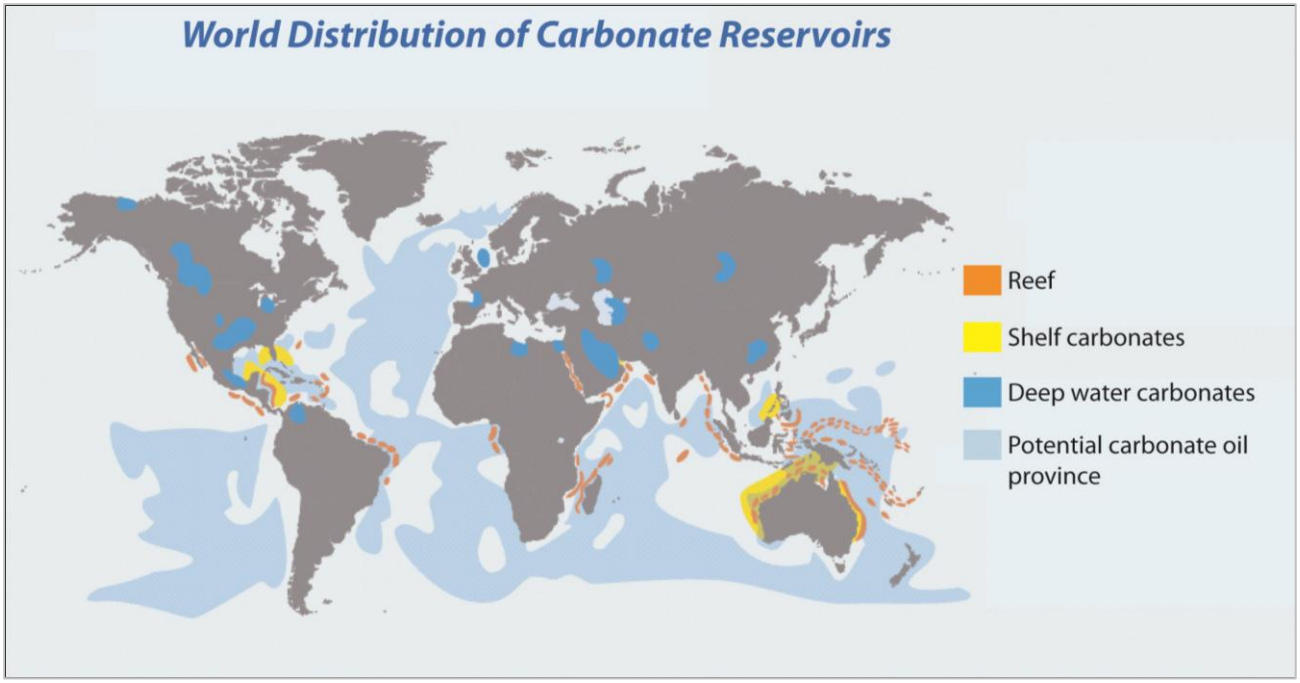

Fig. 1.1 – Word distribution of carbonate reservoirs (Modified from Schlumberger Market Analysis, 2007)

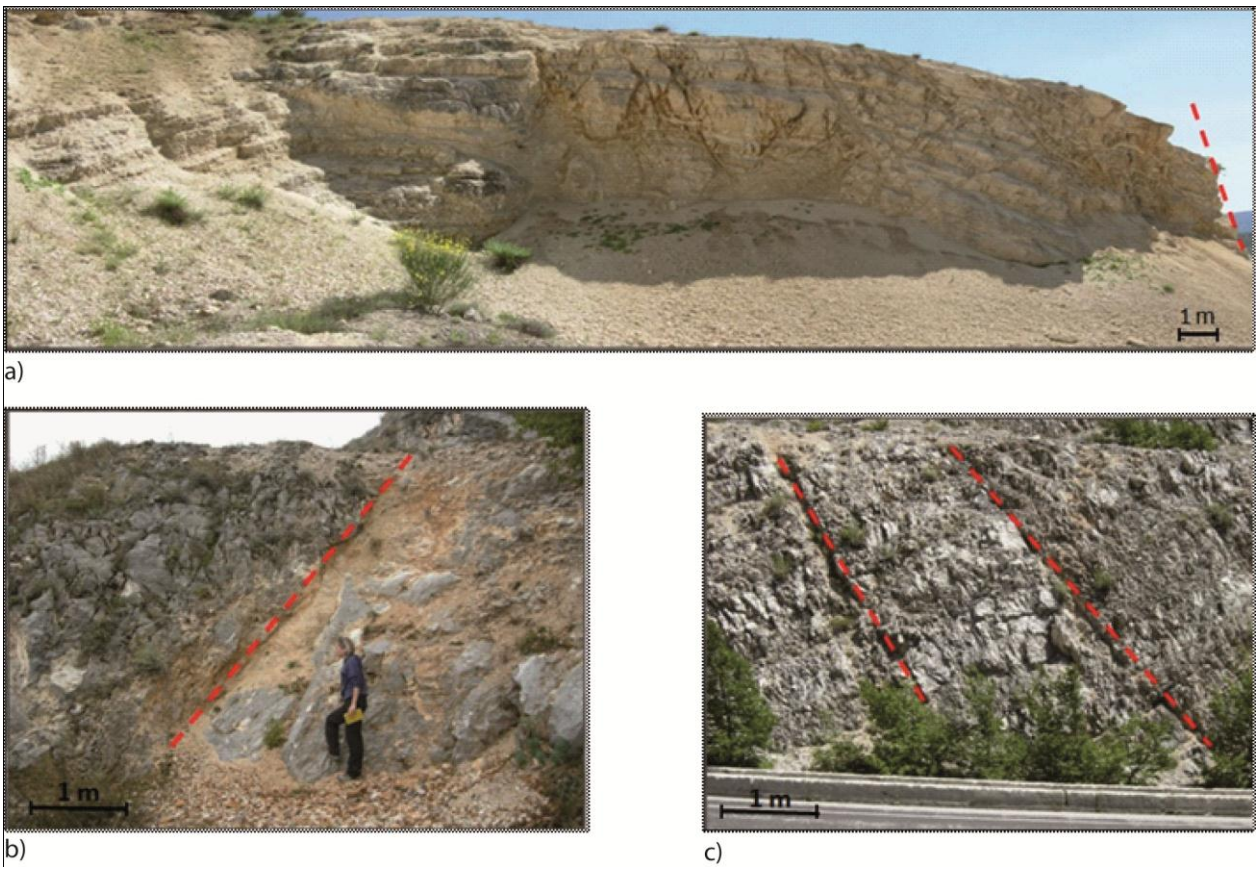

Fig. 4 –*a)* Example of a seismic-scale fault (throw > 10 m); *b)* and *c)* Examples of subseismic-scale faults (throw < 10 m)

2 – BACKGROUND

2.1 The fault architecture

One of the most important issues for the characterization of reservoirs and the assessment of the fluid flow behavior is the role of faults and fractures in rocks. As just introduced in the foregoing chapter, at different scales these features have a strong impact on the reservoir drainage and in the overall productivity of an oil or gas field. For this reason, it is very important to define the fault architecture and the deformation mechanism which rules the development of fracturing.

Brittle fault zones are highly heterogeneous, leading to large uncertainties in understanding and predicting the resulting mechanical and fluid flow behaviour of fault. The temporal and the spatial evolution of permeability in fault zones are strongly influenced by the host rock type, stress and strain rate, deformation mechanisms, fault architecture, and the presence of brittle deformation patterns, related to faults, i.e. pressure-solution surfaces, extensional fractures, and shear fractures. The compartmentalization of the reservoirs is governed by the density and connectivity of fractures (micro and meso-fractures), that can act as a path for fluid flows (Sibson 2000) or otherwise can become a seal if they are cemented or closed (Putnis et al. 2001; Ferrill et al., 2003; Parnell et al., 2004). The reservoir models should take into account all these features in order to reproduce the real internal reservoir architecture and provide a reliable input for the numerical simulation of the fluid flows.

In recent years, a considerable number of geological works have been performed in order to define and describe the internal structure of fault zones (Sibson 1977; Bruhn et al., 1994; Caine et al., 1996; Sibson 1996; Evans et al., 1997; Sibson, 2003; Gudmunsson, 2004; Berg et al., 2005; Agosta et al., 2006; Micarelli et al., 2006; Faulkner et al., 2006).

The fault architecture is divided in three different domains: fault-core, damage-zone and protolith (Caine et al. 1996) (Fig. 2.1). Fault-core is the inner part near the fault plane, where the most displacement is accommodated. It is characterized by clay-rich gouge-zones with a grain-size reduction, and a possible highly indurate cataclasite zones (Hadizadeh, 1994; Bruhn et al., 1994; Sibson, 2003). Damage-zones are the network of fractures that bound the fault-core and may enhance fault zone permeability (McGrath et al., 1995, Odling et al., 2005; Kim et al., 2004). The fault-core and the damage-zone are surrounded by the protolith, characterized by the background regional deformation.

As outlined Caine et al. (1996) and many other authors afterwards, a huge number of factors influence the evolution of permeability in fault rocks, such as the lithology, the fault scale, the fault type, the deformation style, the fluid chemistry, or the fault displacement. This last one, for example, along faults can change the juxtaposition between layers, which can lead to clay smearing and lenses on fault surfaces and, therefore, to a reduction in fluid flow (e.g. Stewart 1991, Bastesen 2009). Several studies in the last years were performed in order to investigate the other factors controlling the evolution of the deformation and to understand the relation between the faults rocks and the permeability. One of the most important factors affecting connectivity in fault zones and, hence, the permeability zonation is the fracturing process.

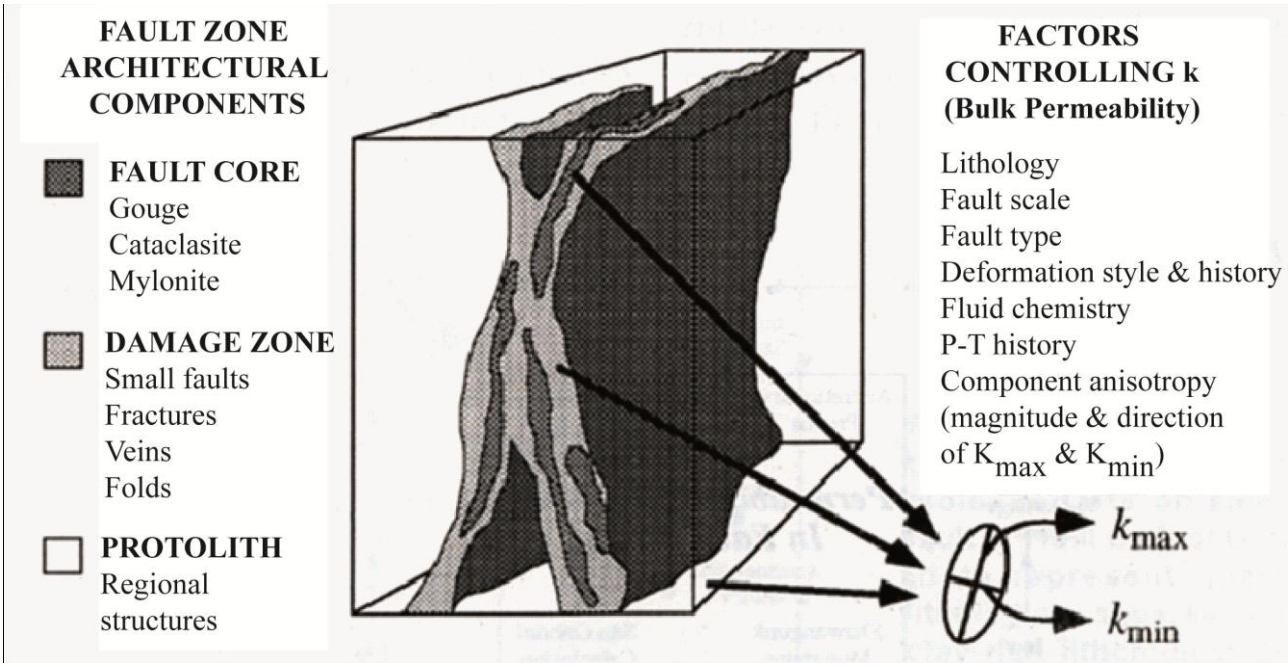

Fig. 2.1 – Conceptual model of fault zone with protolith removed; the ellipse represents the relative magnitude and orientation of 2-D bulk permeability (k) tensor (modified from Caine, 1996)

2.2 The evolution of fracturing in fault zone and the relation with permeability

The evolution of the fracturing process in stratified brittle rocks, such as carbonate, is related to the fault propagation in time and space (Salvini et al. 1999). Furthermore, the propagation and arrest of fractures was strongly influenced by the "mechanical layer" (Gudmundson et al. 2004; Gudmundson 2006; Larsen 2009).

Salvini et al., 1999 proposed that cleavage nucleate as solution planes at the front of advancing fault as the results of stress concentration in this region. Two distinct, time-sequential processes are shown to operate during the fault propagation: 1) typical millimeter to centimeter spaced solution surfaces in the distal tip zone of the advancing fault plane; 2) as the tip advances, the fault plane breaks through the cleavage as minor shear displacements reactivate some of these nascent surfaces.

Several studies have been performed on natural carbonate fault-cores combining field analysis, laboratory experiments and micromechanical modeling (Blenkinsop, 1991; Storti et al., 2003, 2007; Billi et al. 2004, 2005, 2007, 2009; Bastesen 2009). These works outlined the influence of the particle size distribution of cataclastic rocks on the mechanical and fluid flow behavior of fault zones. Storti et al. 2007 proposed that the fragmentation mechanism progressively changes with the intensity of comminution and this process in the narrow shear zones produces the preferential formation of smaller diameter particles resulting in particle size distributions characterized by D (fractal dimension) values approaching or exceeding 3. Billi 2007 suggests that for increasing D-values, also the largest particles tend to decrease in number and he proposed a preliminary definition of scaling rules for fault rocks particles that may serve as a tool for predictive a large

scale of fault rock particles. Also others studies focused on particle shapes show that particle angularity decreases with size and, for a given size class, it decreases with increasing fractal dimension of particle size distribution (Storti et al., 2007). These results offer support to the temporally and variable nature of rock comminution and permeability. These networks, when transporting fluids, give the core a granular-media structure at the millimeter or centimeter scale, thereby supporting its being modeled as a porous medium.

Less attention has been dedicated to carbonate damage-zones, the broader volume of distributed deformation between fault-core and pristine rock. A first studied on this topic has made by McGrath et al. 1995. It regarded a description of damage-zones around small-scale normal, strike-slip, and reverse faults cutting horizontally-bedded carbonate, shale and siltstone. Two different types of brittle damage zones have been recognize by this work, namely: a) fracture branching directly from the fault tips; b) fractures forming an *en echelon* array, which are disconnected from the fault tip. In addition, strike-slip and thrust faults were observed to produce more variable damage-zone geometry compared to those at normal fault tips. In Kim et al. (2004, 2009) a classification of damage-zones based on their location within and around the fault zone has been proposed. 3 types of damage-zones were recognized (Fig. 2.2): a) Tip Damage-Zones, which develop in response to a stress concentration at a fault tip; b) Wall Damage-Zones, that may represent mode II and mode III tip Damage-Zones abandoned in the wall rocks as faults propagate through the rock, they may also represent wall-rock deformation associated with the build-up of slip on faults; c) Linking Damage-Zones, which are caused by the interaction and linkage of fault segments in a relatively small region. In this work the term “Damage-zone” will be referred to the Kim’s “Wall Damage-Zone”.

Billi et al. (2003) studied the nucleation and growth of cataclastic fault-core from fractured damage-zones in carbonate rocks. This work underlines that at damage-zone fault-core transition orthorhombic lithons reduces in size and adopt an isometric shape (Fig. 2.3). These results suggest that fault-core development initiates from rock masses in damage-zones, where the shape anisotropy of orthorhombic lithons favours additional fracturing of orthorhombic lithons. In summary, damage-zone of faults in carbonates are characterized by the great abundance of fractures that are consistently oriented with respect to the major slip surface, i.e. to the total stress field governing deformation. Approaching the transition to the fault-core, fracture intensity increases and fracture-bounded lithons have an average aspect ratio of 1.4 +/- 0.5 (Billi et al. 2003).

Field analysis performed by Bastesen et al. (2009, 2010) support a model in which fluids entered the core by damage-zone fractures that linked to the principal slip surface. Flow along the fault core was controlled by the fracture system of lenses, and thereby lens connectivity, but may have been hampered by flow-retarding fault rocks. The flow potential is especially well developed in fault bends and breached relay due to frequent lenses and well-developed fracture networks.

Storti et al. 2003 describes the development of faults in carbonate rocks as a two-step process (Fig. 2.4). The initial fracturing processes are responsible for the development of a damage zone characterized generally by increase in permeability. As brittle deformation intensity (i.e. number and dimensions surface of fracture per cubic meter) increases either in time and space, the second

step begins with the concentration of relative movements in the inner fracture zone. This induces further fragmentation by the grinding of the clasts produced by the fracturing and the development of the fault core. In carbonates this process may repeat several times due to cementation processes in the fault core. The result is a dramatic reduction in permeability across the fault that becomes a seal. This contrasts with higher permeability values preserved along the sides of the faults, due to the presence of the fractured damage zones.

Micarelli et al. 2006 supports the models proposed by Storti et al. (2003), outlining the importance of the throw in fault-related fractures evolution. In particular, the structural evolution of cataclastic fault cores from nucleation to growth was studied for the case of normal fault zones affecting high-porosity carbonates. A comparison was made between faults with increasing displacements affecting a similar lithology at shallow depth conditions. In the first few millimeters to centimeters adjacent to the fault surface, porosity is significantly reduced by a sequence of pore collapse, grain crushing, rotation-enhanced abrasion and calcite precipitation, which is a function of increasing displacement. Consequently, fault planes have strongly reduced permeability even for very small displacements. Adjacent damage zones are characterized by fracture density and connectivity increasing towards the fault plane. Cataclastic rock production and consequent fault-core development initiate as the fault displacement reaches values of 1–5 m. This displacement threshold coincides with a decrease in the widening of the damage zone per unit increase of fault displacement, which relates to a change in the mechanism of deformation accumulation in the fault zone. The change is interpreted as a result from strain-softening in the fault zone due to the onset of cataclasis. In that study, permeability data indicates that normal faults in high-porosity carbonates are effective transversal seals even at very small offsets and their combined conduit-barrier hydraulic behavior are accentuated as displacement increases. These results show some similarities but key differences with respect to fault zone development for the analogous cases of sandstones and low-porosity limestones.

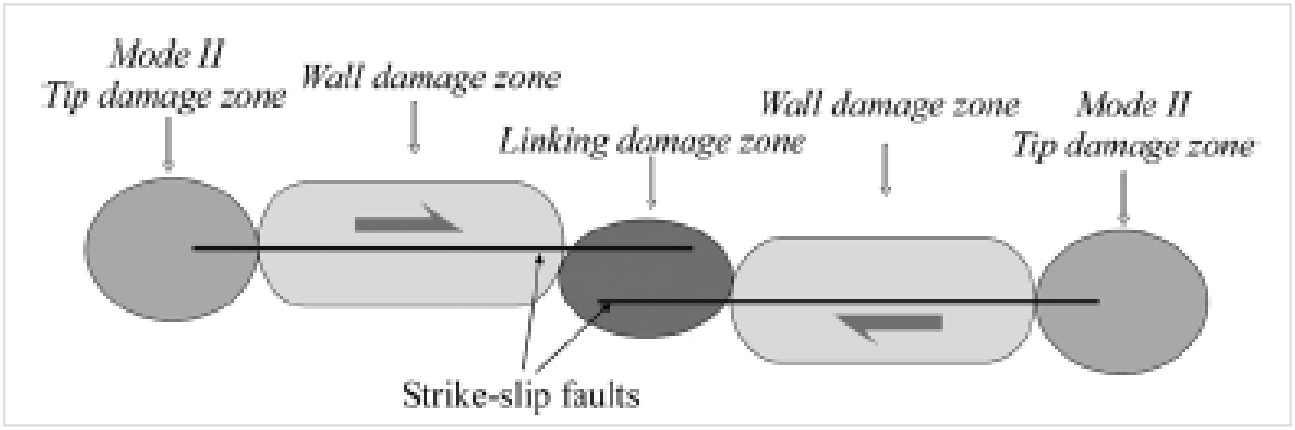

Fig. 2.2 – Classification of fault damage-zones (From Kim et al. 2004)

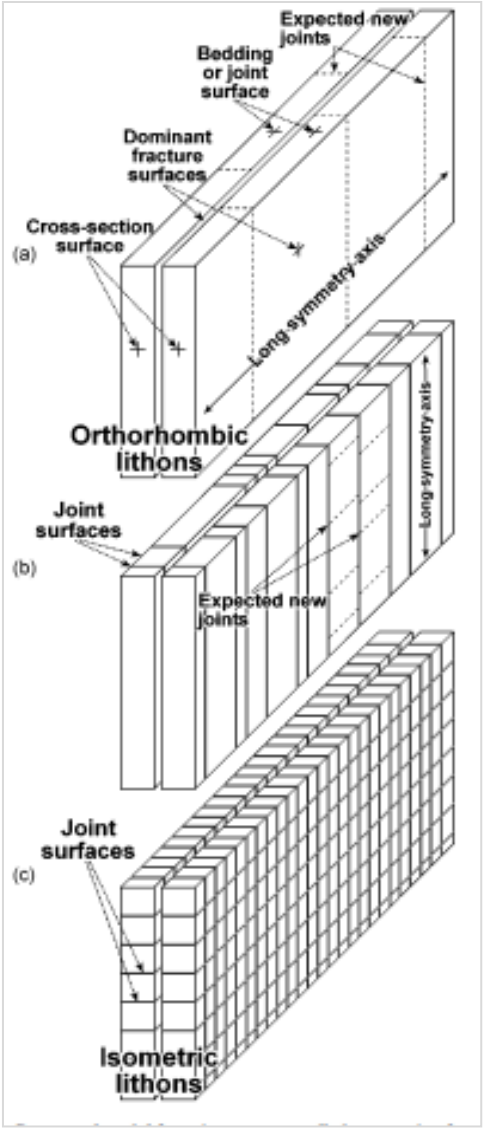

Fig. 2.3 – Evolution of fractures in fault damage zones (From Billi et al.2003)

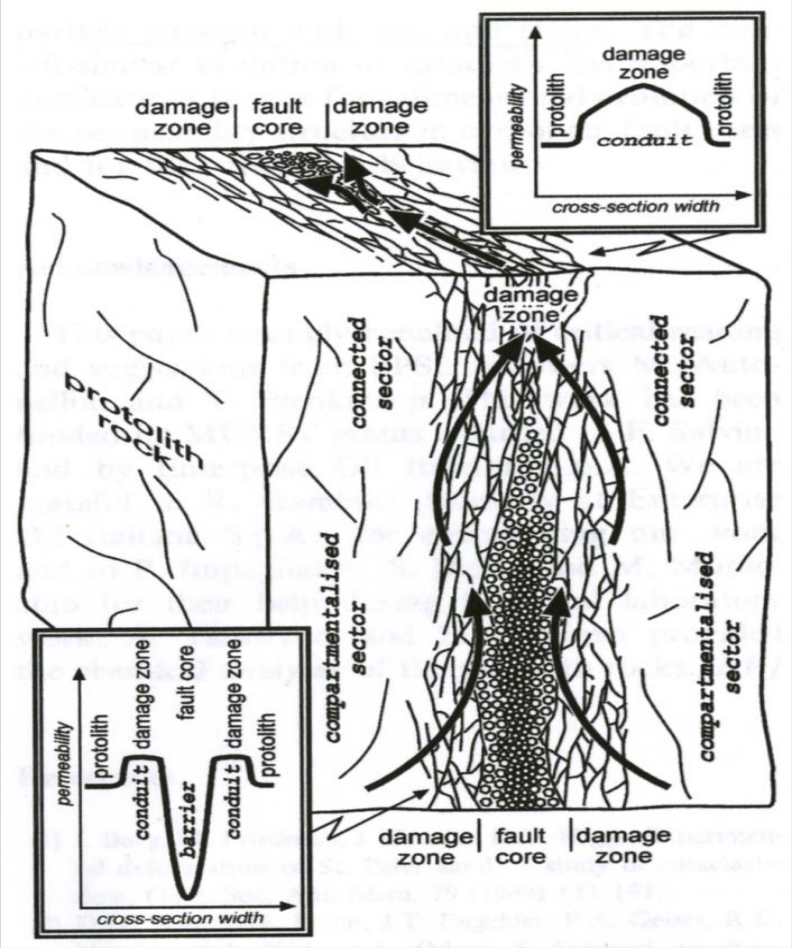

Fig. 2.4 - Fault architecture and evolutionary models of fault deformation (from Storti et al. 2003)

3 – GEOLOGICAL FRAMEWORK

The studied area is located in the Central Apennines that is part of a peri-cratonic region which has undergone several tectonic events, in response to Neogene tectonic interaction between the European and the African plate, leading to the peri-Mediterranean orogenesis (Dinaric and Apenninic) (Fig. 3.1).

A thrust and fold belt with NE vergence built up during the late Tortonian and Pliocene deforming different domains of sediments: the shallow water limestones (carbonate platform and ramp domains) (Middle Miocene-Upper Triassic), and the deep water carbonates (slope and pelagic basin domains) (Middle Miocene-Lower Triassic) (Parotto and Praturlon, 1975). The geometry of the chain, the diachronism of the eastward migrating fore-deep basins, and the age of the thrusts, are consistent with a regional foreland propagating model for the Central Apennines, from SE sector to NW (Bally et al., 1988; Endignoux et al., 1989; Sage et al., 1991; Cipollari and Cosentino, 1992b; Cavinato et al., 1994; Cipollari and Cosentino, 1995). During the Early Miocene, extensional processes took place disrupting and fragmenting the continuity of the pre-existing Alpine Late Cretaceous-Paleogene mountain belt. The gravity collapse of the chain related to the extension is proved by the presence of several normal faulting with an associated high seismicity, bounding the intra mountain basins (Galadini et al., 2003; Centamore and Nisio, 2003).

Eventually, the present day geological architecture of the Mediterranean area is characterized by extensional domains surrounded by arcuate mountain belts. Some authors propose that the occurrence of both contractional and extensional tectonics, and the east- ward propagating orogenic system are caused by the oceanization processes affecting the Tyrrhenian area due to the subduction and under-thrusting of oceanic and continental litosfere (Malinverno and Ryan, 1986; Patacca and Scandone, 1989; Sartori, 1989; Patacca et al. 1990; Patacca et al., 1992a; Doglioni, 1995; Faccenna et al. 1996; Faccenna et al. 2003).

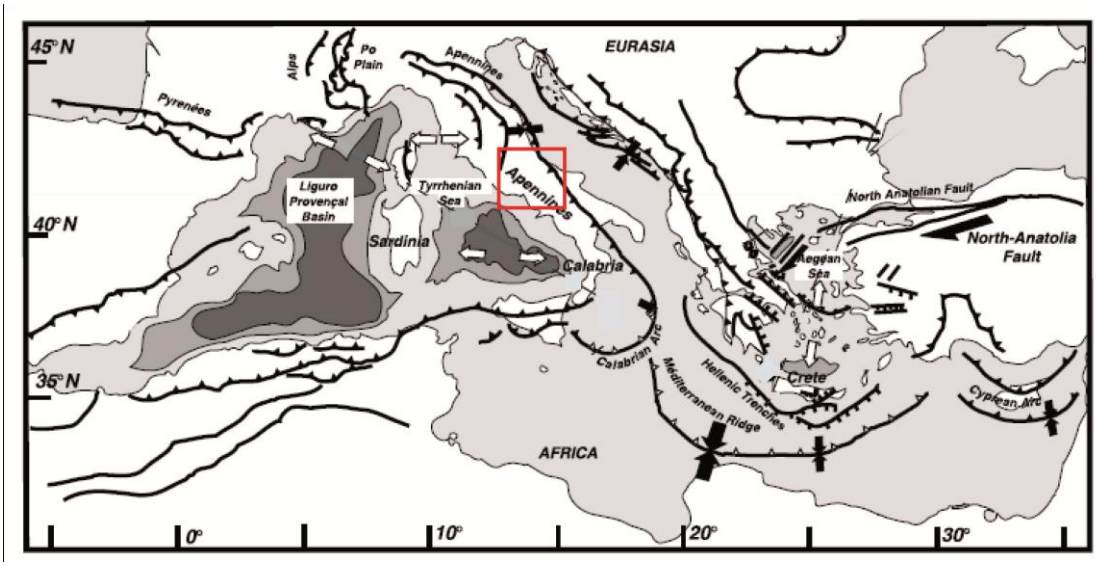

Fig. 3.1 – Geological setting of Mediterranean Area; the red square corresponds to the interested area of the current work (Modified from Faccenna et al. 2003)

3.1 Location and tectonic description of studied sites

In this work a total number of 22 faults, including seismic to subseismic scale faults, have been studied from 7 sites located in different tectonic environments (compressive, extensional, and transpressive) (Fig. 3.2). The studied faults are developed at different ages and depths during the evolution of the chain. The database includes normal and strike-slip faults. In the area of work, the Meso-Cenozoic carbonate-platform units and carbonate-ramp deposits (Middle Miocene-Upper Triassic) crop out. The lithologies have been described and classified by the Dunham classification of carbonate rocks (Dunham R. J., 1962). They are characterized by mudstones, wackestones, packstones, and grainstones, which represent good analogues of carbonate reservoirs.

Site 1: Prenestini Mountains

The Prenestini Mountains are located on the south-western portion of Olevano-Antrodoco thrust system (Salvini and Vittori, 1982; Bigi et al., 1990) (Fig. 3.2). This thrust front characterizes the Central Apennine with N-S trend for a length of more than 80 km. It consists of the eastward over-thrust, with a strike-slip component, of pelagic and transitional shelf-to-basin deposits (Middle Miocene- Lower Triassic) over the coeval carbonate platform sequences and carbonate–ramp deposits (Latium-Abruzzi carbonate platform).

Site 2 and Site 3: Simbruini-Ernici Mountains and Velino-Sirente Mountains

The Simbruini-Ernici Mountains and the Velino-Sirente Mountains (Fig. 3.2) represent a thrust and fold belt oriented NW-SE of carbonates platform sequence and ramp deposits on the fore-deep deposits. The structures are located on the South-Eastern portion of Olevano-Antrodoco thrust system and are disrupted by normal faults, related to the extension of the chain.

Site 4: Fucino Plain

The Fucino Plain (Fig. 3.2) is a half-graben structure that was formed by the movement of a set of normal faults oriented NW-SE bounding the eastern margin of the basin. The fault juxtaposes basin fluvio-lacustrine filling sediments (Late Pliocene-Late Pleistocene) against the Upper Jurassic-Lower Cretaceous, platform carbonate of Lazio-Abruzzi units (Vezzani and Ghisetti, 1998). This region has been uplifted at rates of 1.4–2.5 mm/yr since 3.5 and 1.6 Ma (Ghisetti et al., 1999 and references therein).

Site 5: Sagittario Gully

The Sagittario Gully (Fig. 3.2) is located in the hanging wall of a north-eastern verging Pliocene thrust system (Miccadei, 1993). The thrust system is dissected by a NNW–SSE left-lateral, strike-slip to transpressional fault zone paralleling the thrust ramp zone.

Site 6: Subequana Plain

The Subequana Plain (Fig. 3.2) is a quaternary intra-Apennines extensional plain, bounded by a NW-SE system of normal faults along the western side. The fault juxtaposes basin fluvio-lacustrine

quaternary filling sediments against the Eocene carbonate units. The quaternary fault activity was documented by the dislocation of Pleistocenic continental deposits (Miccadei et al., 1998).

Site 7: Maiella Mountain

The Maiella Mountain (Fig. 3.2) is a thrust-related, box-shaped anticline characterized by an active normal fault on the West side (Ghisetti et al., 1997). The main units of the area are comprised of a carbonate sequence (Lower Cretaceous to Miocene age), which is topped by silicoclastic sediments (Messinian-Lower Pleistocene age). The Cretaceous sequence in this area consists of platform tight micritic carbonate mudstone, in the south and in the centre of the mountain, and slope-basin carbonates grainstone, in the north (Eberli et al., 1993; Mutti, 2008).

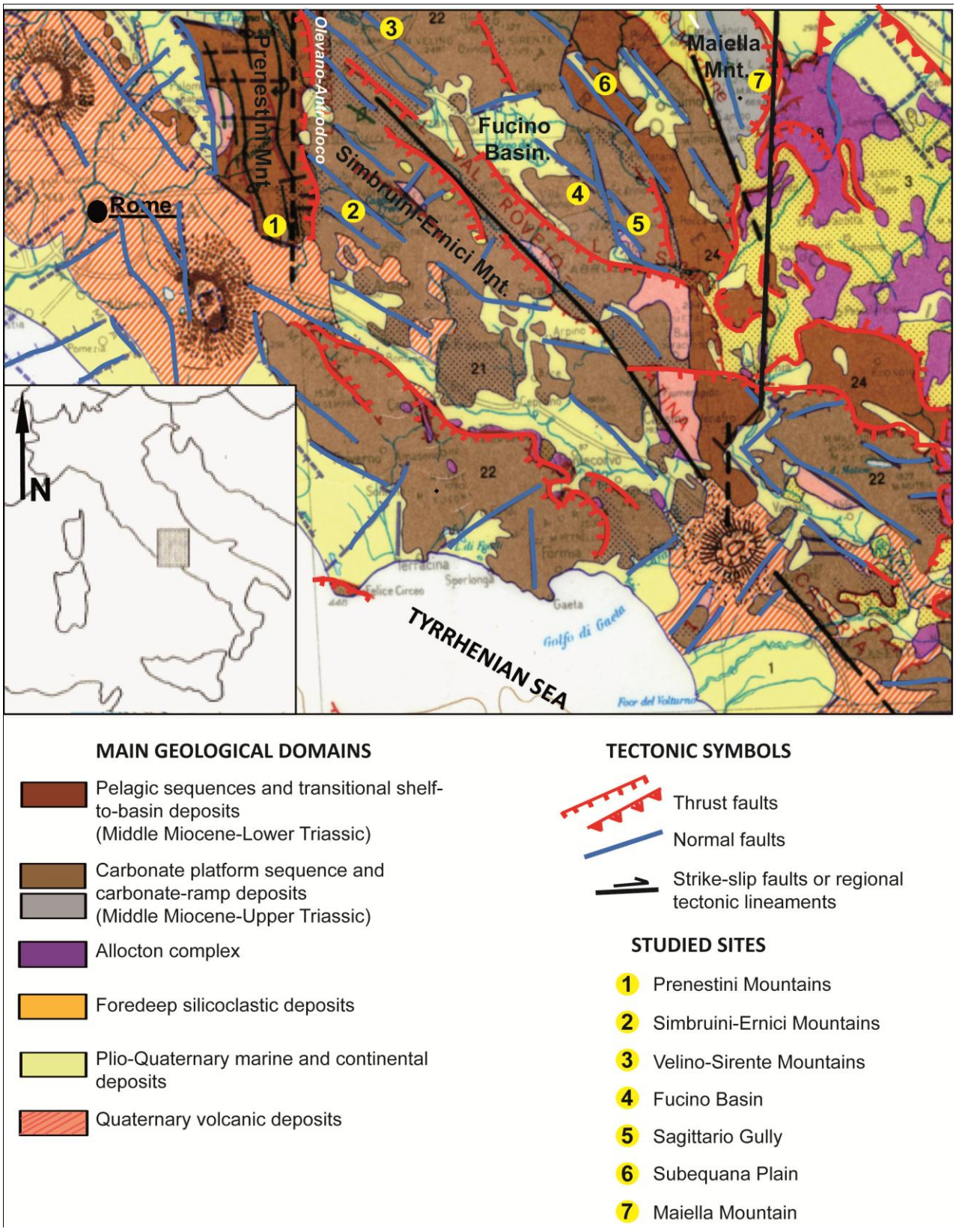

Fig. 3.2 – Schematic tectonic maps of the studied area (Modified from "*Carta tettonica d'Italia 1: 500000*)

4 - METHODOLOGIES

In the current work, an *in situ* systematic study of fault zone has been performed in order to constrain the fault kinematic, quantify the spatial distribution of fault-related and regional-related fractures, and define the rock types and the fault characteristics.
An original field methodology has been used to measure and quantify the intensity of deformation (H/S method, see paragraph 4.1.2). This methodology was successfully used in other field works to study the rock brittle deformations (Tavani et al. 2006).
Three original non-commercial software packages: Smooth Software; Monte Carlo based Software, and Frap-3 Software have been used as methodological tools and they were tuned *ad hoc* for the Thesis. The code of these software packages were written by Prof. Francesco Salvini and are available at the GeoQute Laboratory of Roma Tre University. It is necessary to point out that the objective of this Thesis in not specifically the software development since the software has only been useful as a methodological tool to better understand and quantify the fracturing distribution in fault damage-zones.
Specifically, Smooth Software allows preparing the row field data to be analysed. Monte Carlo based Software allows the analysis of field data to produce the predictive modelling of fractures distribution in carbonate fault zones. This final model has been implemented in Frap-3, a fault environment modelling software package. It is a true 4-D tool that can predict stress conditions and the brittle deformation patterns associated to a given set of faults during single or multiple tectonic events, as well as under different stress conditions during the stress condition evolution. Frap-3 have been used in the past for fault modelling exclusively in the silicoclastic environment and thanks to the current work, it was adapted to work also in a carbonate environment.
Eventually, the models of 6 faults, which represent a good sample of fault scale variability, have been performed, and they have been compared with the field data (H/S mean value through distance from the fault plane), in order to test the reliability of the predictive model and to assess its limits.
The methodology presented in this work represents an original tool to quantify and predict the intensity and the distribution of fractures related to fault, starting from field data, through an analytical analysis, up to a final prediction model.

4.1 Fieldwork and data analyses

4.1.1 Structural field measurements and sampling

For each fault a 1-D scan-line has been performed (Fig. 4.1), for both hangingwall and footwall, when it was allowed by the fault exposure. This methodology is generally employed in fault zone characterization by orienting scan lines perpendicular to the faults (Caine et al., 1996; Yielding et al., 1996; Cello et al., 2003; Marchegiani et al., 2006). In particular, the measurements include: the main fault attitudes, using the right hand rule; secondary faults and shear plane attitudes; fracture types (pressure solution, extensional fracture), attitudes, dimensions (H), spacing (S), and spatial locations (d) respect to the fault plane. In addition, in order to better constrain the fault setting

and characterize the fault zones, other measurements have been collected, namely: the bedding attitude and thickness, the fault-core thickness, and the fault throw.

For each fault a handle-sampling has been made collecting samples at several distances from the fault plane (Fig. 4.1). The superficial part has been removed to erase the alteration due to the exposure.

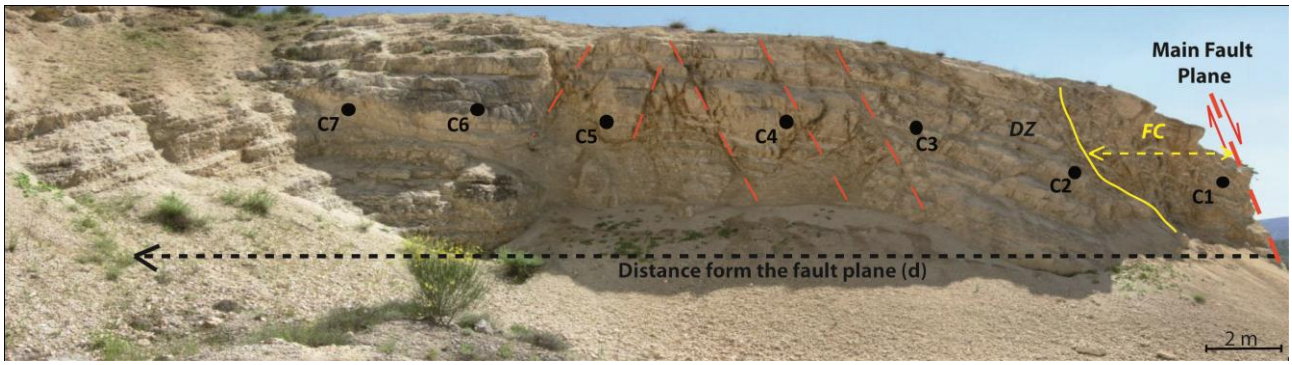

Fig. 4.1 – Example of 1-D fault scan-line; the thick red dashed line corresponds to the master fault plane; the thin red dashed lines correspond to the secondary fault planes; the yellow line represents the limit between the fault-core and the damage-zone; the points C_1, C_1, C_n, correspond to the sampling sites.

4.1.2 Quantitative field measure of the fault-related deformation intensity: H-S ratio

Out of the four main types of fracture cleavages, most of the fractures that were found in the fault damage zones can be grouped in two types, the synthetic shear fractures (i.e. the Riedel R Planes or minor synthetic faulting) and pressure-solution surfaces, depending on the resulting stress conditions. Less frequently we observe the formation of extensional fractures (i.e. joints) related to negative minimum stress conditions as in the presence of high fluid pressures

Detailed field analyses of fault-related fractures (FRF) have been performed. In the current work we define as fracture all the extensional joints and the pressure-solution surfaces related to the stress accumulation due to the fault development.

Several studies have been performed in the last years regarding the quantification of the faults brittle deformation intensity. The more frequent field tools used to quantify the deformation intensity and to define the limits between the fault-core, the damage-zone, and the pristine rock are the spatial distribution of the fractures frequency (Micarelli et al. 2003, 2006); the length, the spacing or the aperture of fractures (Ortega 2006; Agosta 2010).

In the present work, a new quantitative method was proposed. It is based on the H/S ratio (Tavani et al. 2006), that is the ratio between H, the length of the fracture, and S, the spacing between two adjacent and ”homologue” fractures of the same set (Fig. 4.2). H corresponds to the bed thickness if the fractures are perpendicular to the bed thickness; on the contrary it corresponds to the length of the fracture if it forms an angle with the bed thickness. “Homologue” means two fractures which have almost a similar length or in which the second one has a smaller dimension than the first one. For each fracture the distance from the fault plane was measured.

The H/S ratio is numerically equivalent to the C/B fissility proposed by Durney and Kisch (1994) and it is widely used as bedding normaliser both for joints and veins (Narr et al., 1991; Gross,

1995, Balsamo 2011), and pressure solutions (Tavani et al. 2010). These authors used H/S ratio as a direct comparison of deformation intensities in beds of different thickness, because there exists a real relationship between cleavage spacing and bed thickness. These results support the validity of the H/S ratio for a quantification of deformation intensity in layering rocks, instead of S, as commonly used in the past.
Furthermore, the original concept of H/S allows quantifying the intensity of the brittle deformation because it is a function of the tectonic stress acting on the rock (τ), the strength (Σ) and the time of the stress application (t):

$$H/S = f(\tau, \Sigma, t) \qquad \text{(eq. 4.1)}$$

The physical demonstration of this concept is shown in Fig. 4.4. In a layered media, at the equilibrium the force from the tectonic stress (P_T) acting on the surface HW (that is the tectonic pressure) is equal to that produced by the pressure (τ) transmitted through the rock layer SW (the shear stress or flexural-slip):

$$- P_T * H * W = \tau * SW \qquad \text{(eq. 4.2)}$$

On failure condition the tectonic pressure is equal to the strength of the rock (Σ_e):

$$- P_T = \Sigma \qquad \text{(eq. 4.3)}$$

Replacing:

$$\Sigma * H * W = \tau * SW \qquad \text{(eq. 4.4)}$$

And simplified, H/S becomes a function of stress and of the rock strength:

$$H/S = \tau/\Sigma \qquad \text{(eq. 4.5)}$$

Integrating through the time of the stress application, we obtain the Time Stress Integral (TSI):

$$(H/S)_t = \int (\tau/\Sigma)\, dt = TSI \qquad \text{(eq. 4.6)}$$

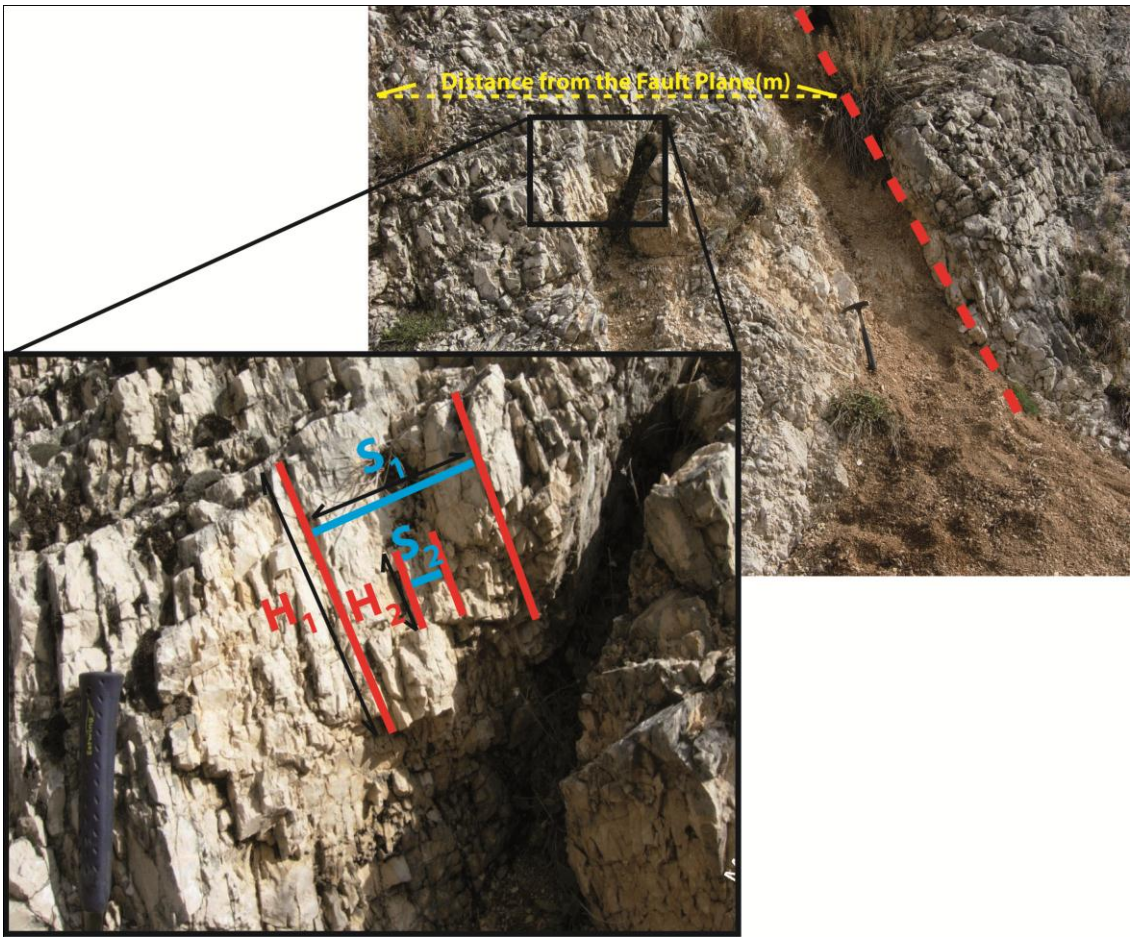

Fig. 4.3 – The H/S field theory. The red dashed line corresponds to the fault plane; the yellow dashed line corresponds to the distance from the fault plane; the red lines are the measurements of the fracture height (H) and the blue lines are the fracture spacing measurements (S)

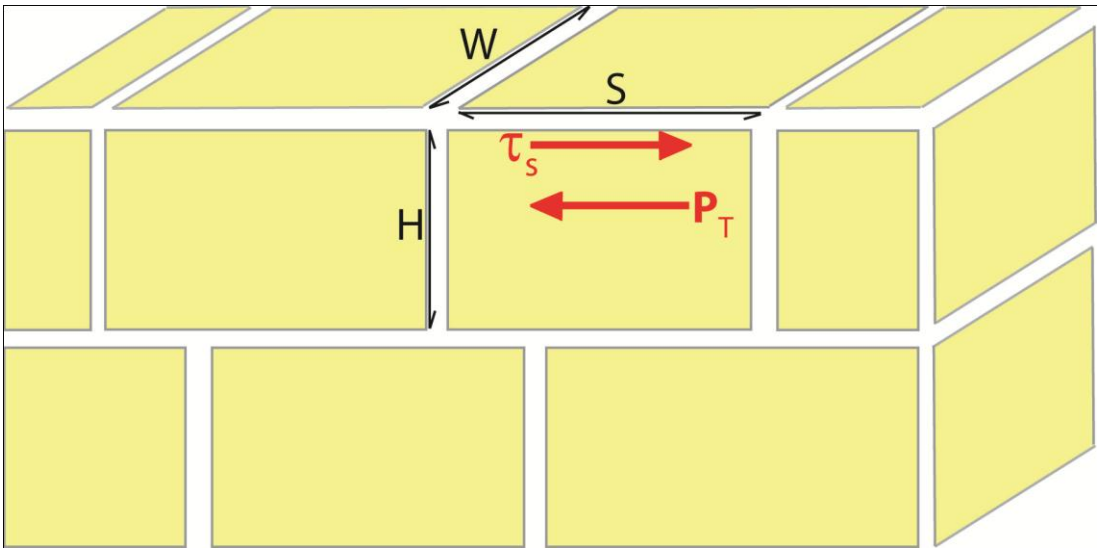

Fig. 4.4 – Physical demonstration of the H/S ratio; P_T is the tectonic stress, τ_S is the shear stress

4.1.3 Spatial analysis of deformation: transect technique

The spatial distribution of the deformation measurements have been analysed by the transect technique (Salvini et al., 1999) included as a tool in an open source structural data analysis software package (Daisy). Briefly, H/S data are projected onto the transect trace, orthogonally to the fault direction. The transect length is divided into N cells of a given width, and for each a frequency histogram of the analysed parameter is produced. The along-transect smoothing of the results improves their interpretation and a Uni-Polimodal Gaussian best fit is applied to each cell histogram. The smoothing procedure consists of a selected number of moving weighted averages (Wise et al., 1985). For the mathematical explanation see Storti et al., 2006. The final Gaussian fit analysis allows analysing the polymodal distribution of variable values. Polynomial Gaussian distribution statistics is by far the most used probability distribution in statistical analysis and is based on the reasonable assumption that the data derived from various sets have a normal distribution around their mean value (Swan et al. 1995).

For a graph of transect results (Fig. 4.5 a), the X-axis represents the position along the transect trace (Distance from the fault plane), the Y-axis represents the parameter value (H/S), and the chromatic scale represents the frequency associated with each Y value, normalized to 100. The Mean Value analysis (Fig. 4.5 b) is useful to study the general trend of the variable. In the Mean Value analysis (lower graph) the y-axis corresponds to the mean value of the analysed variable and the chromatic scale to the error +/- the standard deviation.

In this work this technique has been used to investigate three main issues:

1) The fracture spatial variability in the fault-damage-zones
2) The relation between the regional related deformation and the fault one
3) The relation between the footwall and the hangingwall deformation intensity

4.1.4 Quantitative analysis of the regional deformation

In the current work the term “regional deformation” is referred to the background deformation depending on the tectonic contest in which each fault is developed. The resulting fault deformation pattern is due to the overlapping of the regional stress to kinematic stress produced by the fault movement. For this reason it is very important to define the temporary relation between the fault development and the regional deformation in order to discriminate one from another. The regional deformation, namely the regional related fracture (RRF) was studied measuring and analysing the attitude and the intensity of deformation (H/S) away from the fault plane at multiple distances from the fault plane, in order to have a number of measurements statistically significant (Fig. 4.6). By means of the histogram analysis included as a tool in Daisy Software package (Salvini 1999), the data was analysed and the H/S mean value was computed. Comparing the fault values and the regional one, the two deformations have been discriminated and the limits between the damage-zone and the pristine rock have been defined. Generally, the damage zone is distinguished from the pristine rock on the basis of a change in the density of subsidiary faults and fractures, although the boundary between them is often gradational

(Micarelli et al., 2003). In the present study, we added the H/S measurement. In particular, the boundaries between the damage-zone and the pristine rocks are defined on the basis of change in H/S values with the increase of distance from the fault plane.

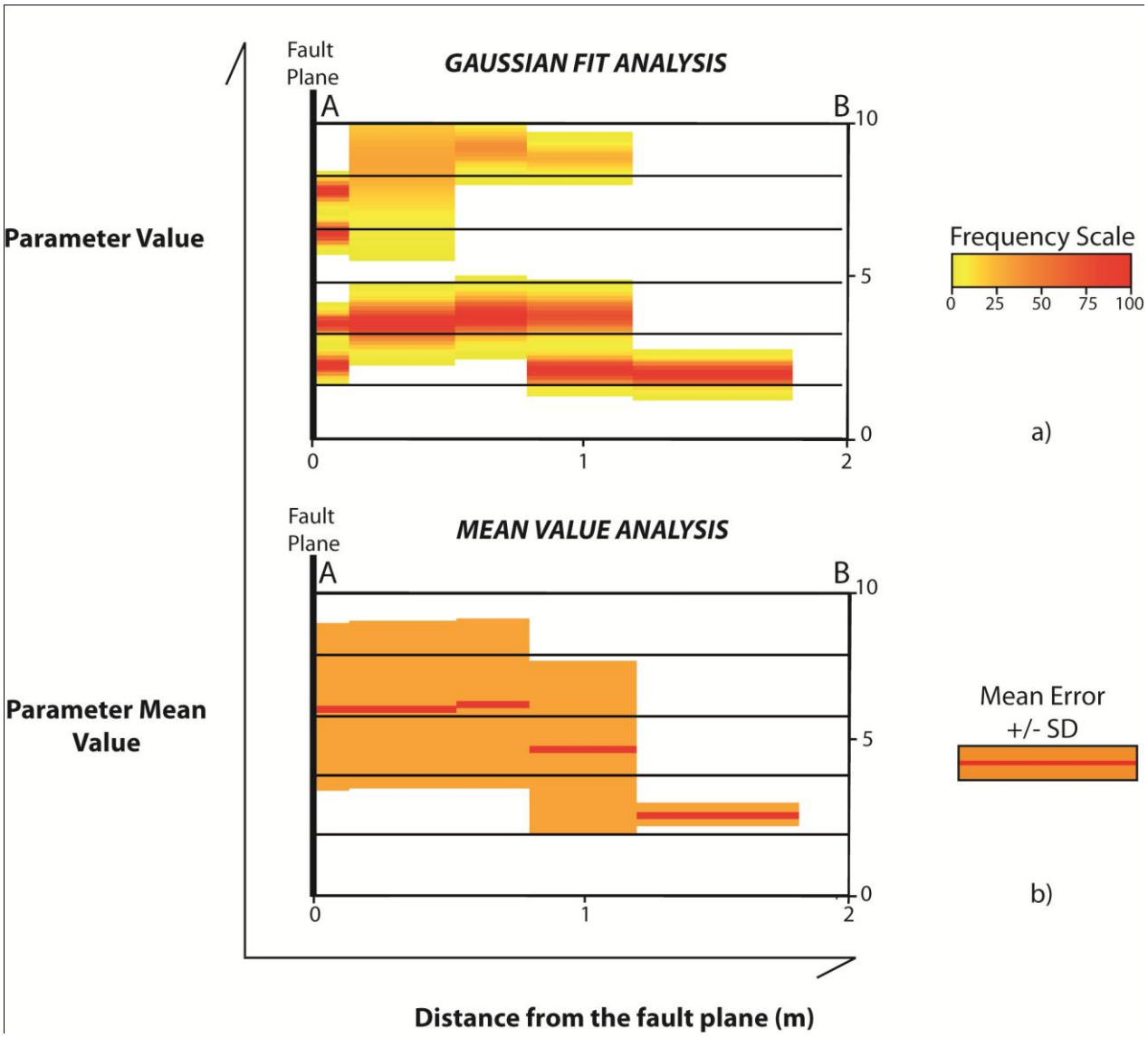

Fig. 4.5 – Example of transect analyses; a) Gaussian Fit analysis; b) Mean Value analysis

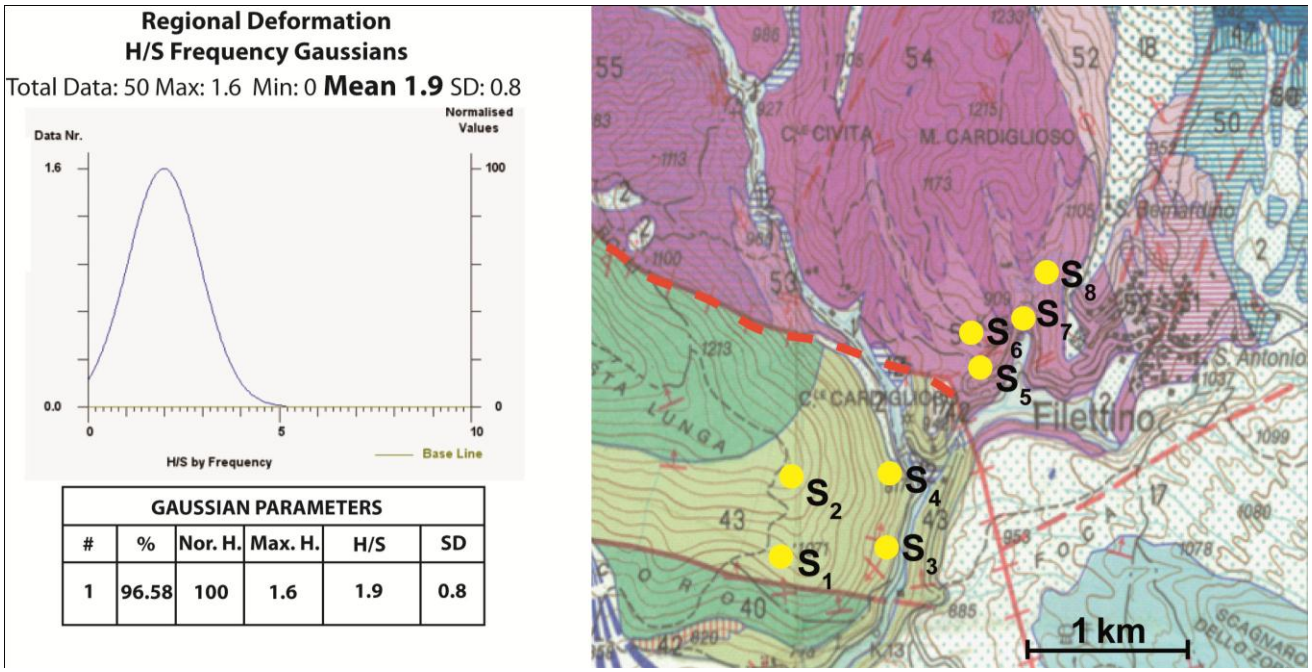

Fig. 4.5 – Computation of regional-related deformation

4.1.5 Fault and rock characterization

Two major features have been chosen in order to characterize the fault zones and the related brittle deformation: the throw and the deformation depth which are deeply related to the applied stress intensity. The rock characterization has been performed *in situ* by using Dunham classification for carbonate (Dunham, 1962). In addition, in order to have a measure of the rock rheology, insoluble content analyse have been performed both on deformed fault rock and horst rock. These analyses have been performed in the Geochemical Laboratory of Roma Tre University, by the supervising of Prof. Paola Tuccimei.

These features, together with the H/S measurements, have been used as input data to perform the analytical model (via Monte Carlo method), in order to study if any relation exists between them and the deformation trends around the fault.

4.1.5.1 The fault kinematics and the total throw computation

The fault throw was measured *in situ* when it does not exceed the height of the outcrop and typically, it occurs for the subseismic scale faults. On the other hand, the stratigraphic technique was used to compute the fault throws for the seismic-scale faults. The accuracy of this method depends on the accuracy of the maps information.

A correction was applied to the throw measurement. It takes into account the strike component affecting the fault. As show in Fig. 4.6, the Total Throw (T_{tot}) can be divided in two components: the Dip Throw (T_D) and the Lateral Throw (T_L). The dip component was measured on *in situ* or by stratigraphic technique, as explained before. The Total Throw can be computed by the following relation:

Total Throw = **Dip Throw**/ [sin (90°- **R****0.01745923*)] (eq. 4.7)

With:

0.01745923 is the Conversion Factor from degrees to radiant
R is the Fault Rotax

The Fault Rotax (Fig. 4.7) corresponds to the vector on the fault plane normal to the slip and it coincides with the intersection between the fault plane and synthetic or antithetic cleavages (Serva and Salvini 1979).

4.1.5.2 The deformation age and depth

The deformation depth is an index of fault exhumation that strongly influence the development and the evolution of the fracturing process in rocks. It has been computed using the following relation:

Deformation Depth = **Age of Deformation*****Erosion Rate** (eq. 4.8)

The age of deformation of the faults related to the thrust-belt system can be considered as the age of thrust development which corresponds to the deposition age of the fore-deep sediments. On the contrary, for the faults bounding the intra-mountains Apennines plain the age of fault deformation was considered as the age of the extensional collapse of the chain (Quaternary).
The erosion rate used for the computation is 0.0016 mm/a how suggest Scrocca et al. 2006, that correspond to the typical uplift rate in active chain as the Central Apennine.

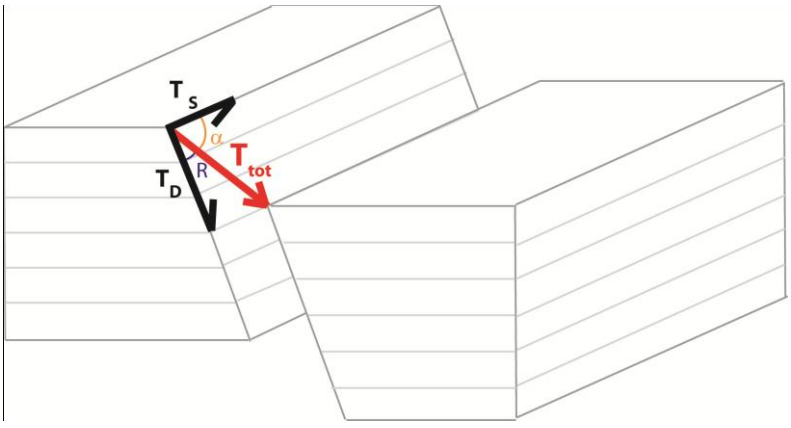

Fig. 4.6 – The Total Throw (T_{tot}) computation; T_D is the Dip Throw; T_S is the Strike Throw; R is the Rotax

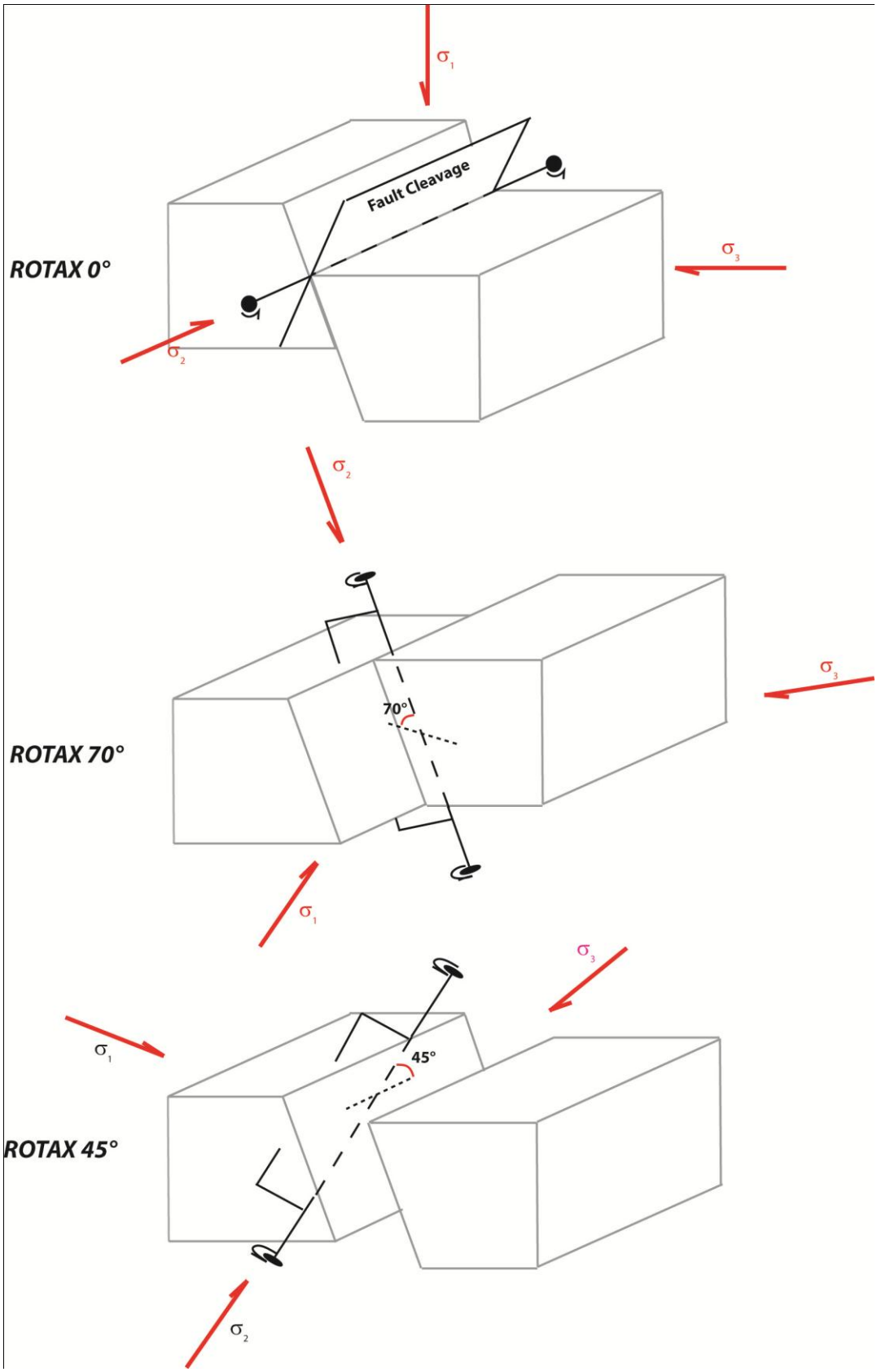

Fig. 4.7 – The rotax computation (R). σ1, σ2, and σ3 corresponds to the stress tensors; the black axis is the rotax axis and the arrows shows the sense of rotation

4.1.5.3 Insoluble content analysis

In order to have a measure of the rock rheology, insoluble content analysis has been performed both on deformed fault rock and horst rock. For each fault two samples have been chosen: one nearby the fault plane and the other one on the protolith, at a certain distance from the fault plane, depending on the damage-zone width.

The analysis was performed by means of the Calcimeter Dietrich-Fruling (Fig. 4.8). This instrument is formed by a glass container and connected glass-holders.

This kind of laboratory analysis is based on the reaction between the **$CaCO_3$** of the rock and the hydrochloric acid (**HCl**) by the following equation:

$$\mathbf{CaCO_3} + 2\mathbf{HCl} = CaCl_2 + \mathbf{CO_2} + H_2O \qquad \text{(eq. 4.9)}$$

Knowing the **CO_2** amount it is possible to compute the $CaCO_3$ amount (1 Mol of $CaCO_3$ = 1 Mol of CO_2) and therefore the Insoluble Content (see step 13 of the analysis procedure)

ANALYSIS PROCEDURE:

It consists in the following steps:

1) Pulverize a part of the sample and weight the quantity for the analysis using an analytic balance (for the same sample at least two analyses)
2) Introduce the pulverized sample in the flask
3) Fill the glass test-tube with 5 cm^3 of HCl
4) Close the tap cap and introduce the test-tube in the flask
5) Reset the instrument equalling the internal pressure to the external one
6) Tilt the flask to fall down the acid and do the reaction
7) The development of CO_2 reduces the level of the coloured liquid in the cylinder
8) Shake softly the flak since the reaction stops (2-3 min) and the level of the gas contained in the cylinder does not fall down anymore
9) Read the value in the burette
10) Open the tap cap to leak the CO_2 in order to get started for the next analysis
11) The environment correction must be applied. It means a standardization of the CO_2 volume to a standard temperature (0 °C) and pressure (760 mmHg), using the following equation:

$$\mathbf{V_0} = \mathbf{V_t}\,(\mathbf{P_t}\text{-}\mathbf{j})\ 273 / 760*(273 + \mathbf{t}) \qquad \text{(eq. 4.10)}$$

With:

V_0, the volume of CO_2 rectified at 0 °C and 760 Hg.

V_t, the volume of CO_2 at external temperature and pressure (ml).

P_t, the atmospheric pressure of the analysis
t, the atmospheric temperature of the analysis.
j, the vapour tension of water at t (mm Hg)

12) Finally, the carbonate content (%) of the sample has been computed by the following equation:

$C = V_0 * 0.0044655 * 100 / M$ (eq. 4.11)

With:
0.0044655 is the equivalent volumetric gas
M that is the mass of the sampling (g)

13) The results Insoluble Content (%) was computed subtracting a 100 the measured carbonatic content

Fig. 4.8 - Calcimeter Dietrich-Fruling

4.2 The analytical modelling

The quantitative modelling of the fracturing in the fault damage zones starts from the physical approach. Fracturing around a fault is produced by the resulting stress conditions and strength of the rock nearby. The resulting stress in the damage zone of a fault during its activity is the combination of four main components, namely the overburden conditions, the regional (i.e. tectonic-related) stress, the elastic stress accumulated around the fault, and the pore fluid pressure. The model was prepared to find a predictive equation of the expected H/S value in the fault damage zones from the geological characteristics of a fault. The geological characteristics of a fault in carbonates that have been considered in the physical model were: the fault displacement, the fault deformation depth, the regional deformation and the rock mechanical characteristics including insoluble content during the fault activity.

The model fit was done in two steps (Fig. 4.9). In the first step the empirical equation that could replicates the H/S distribution was fitted to the H/S by distance data for each single studied fault. In the second step, the found parameters of the empirical equation for each fault were compared to the abovementioned geological characteristics of the faults to find existing relations. In this way, the final equation would link the geological factors of a fault in carbonates with the relative fracture intensity as H/S values.

The fit of the equations with the collected data was done by using a Monte Carlo approach slightly different from classical methods (Mosegaard *et a*l. 1995, Tarantola 2005), the Monte Carlo Converging Method (MCM). This method proved useful tool to quantify complex relations with a high number of variables. It creates a large sequence of possible solution parameters and results are compared with field data. For each item an error mean value is computed (RMS), representing the effectiveness of the fit and the validity of the analysis. Eventually, the method selects the set of parameters that produced the least values.

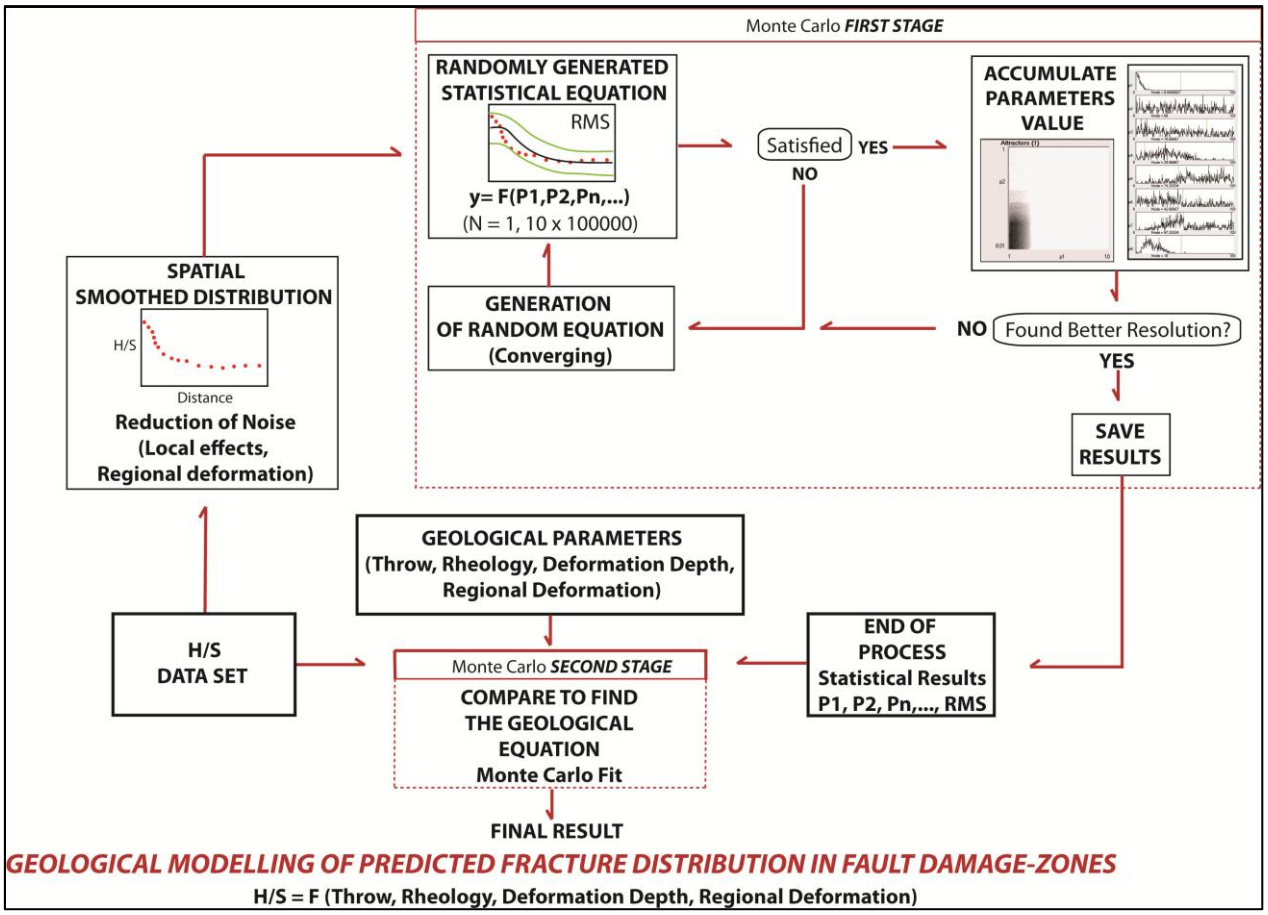

Fig. 4.9 - Workflow of the analytical approach

4.2.1 Monte Carlo converging method

The method was implemented into an in house developed software, MONTECARLO_MCM (Fig. 10), which starting from field data (*Data Fit Range*), uses an *algorithm* (Fig. 4.10) to create a set of very large numbers of uncorrelated solutions that have the distribution of probability of the phenomena. The solutions were created by a generator of prime numbers. The effectiveness of the analysis depends on the number of random variables created by the software. Setting the *Monte Carlo Analysis Parameters* (Fig. 4.10) it is possible to improve the effectiveness of the analysis: *a)* Number of iterations, the number of times that the software makes a cycle; *b)* Number of cycles, the number of combination of parameters that the software creates; *c)* Converging, the range width of the searching solution. It implies the possibility of the reduction of the parameter search interval around the temporary best result. The effectiveness of the founding results increase with the decreasing of the convergence; *d)* Number of Solution for Attractor Analysis; *e)* Minimum acceptable RMS, is the minimum error (Root Mean Square) accepted for the analysis. A further parameter in the Monte Carlo MCM software allows to set the threshold RMS value (**Trms)** to identify and save results with an RMS < **Trms**. This allows obtaining the required statistics for the evaluation of the attractors in the probability/solution space. This parameter was set to **Trms** = 0.1 for the first step. Eventually, the method selects the set of parameters with the least error.

Specific attractor analysis ensures the uniqueness of the solution. A huge number of analyses were performed changing *the Parameter Search Range* (P_1, P_2, P_3, etc...) (Fig. 4.10) in order to find the best equation parameters (*Resulting Parameters*) and link the equation to specific physical features (*i.e.* insoluble content, throw, depth of the fault, age of the fault, regional H/S). An example of a resulting analysis is showed in Fig. 4.11. The *Data Space* (Fig. 4.11 *a*), represents a 2-D projection of the data (grey dots in Fig. 11 *a*). The *Parameters Section Attractor*, represents the statistic distribution of the solutions for each parameter (Fig. 4.11 *b*), and the *Parameter Space*, is a 2-D analysis of the solution space (Fig. 4.11 *c*).

In this way the software provides graphical windows during the inversion to describe the distribution of preliminary solutions in given sections/surfaces of the multidimensional probabilistic/solution space. It is possible to have a visual check on the convergence of the solution (i.e. the consistency of the solution attractors, if any (Fig. 11 *b*). This allowed controlling the parameters that rules the Monte Carlo MCM inversion to the final values used.

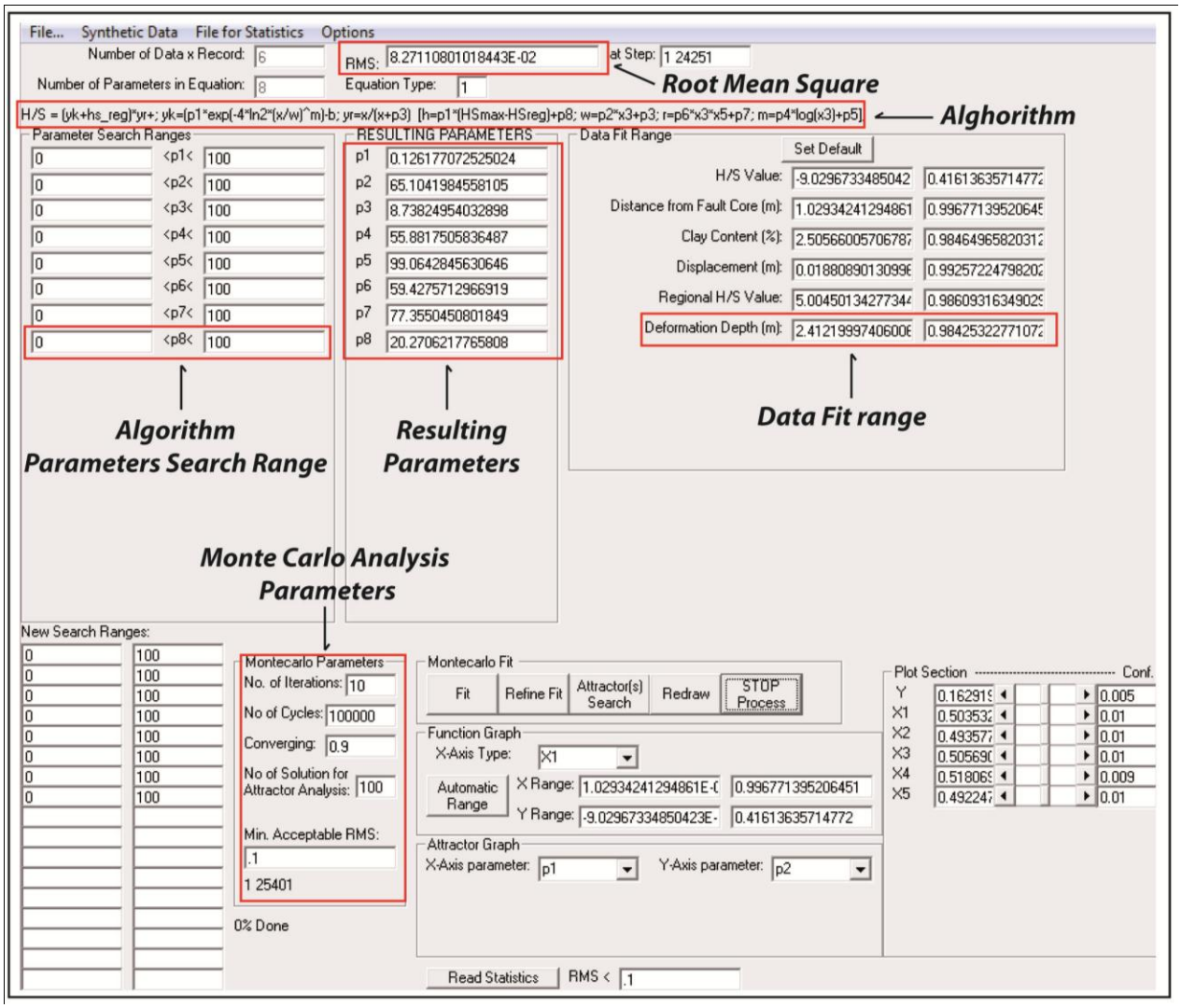

Fig. 4.10 – Monte Carlo based software (Main window)

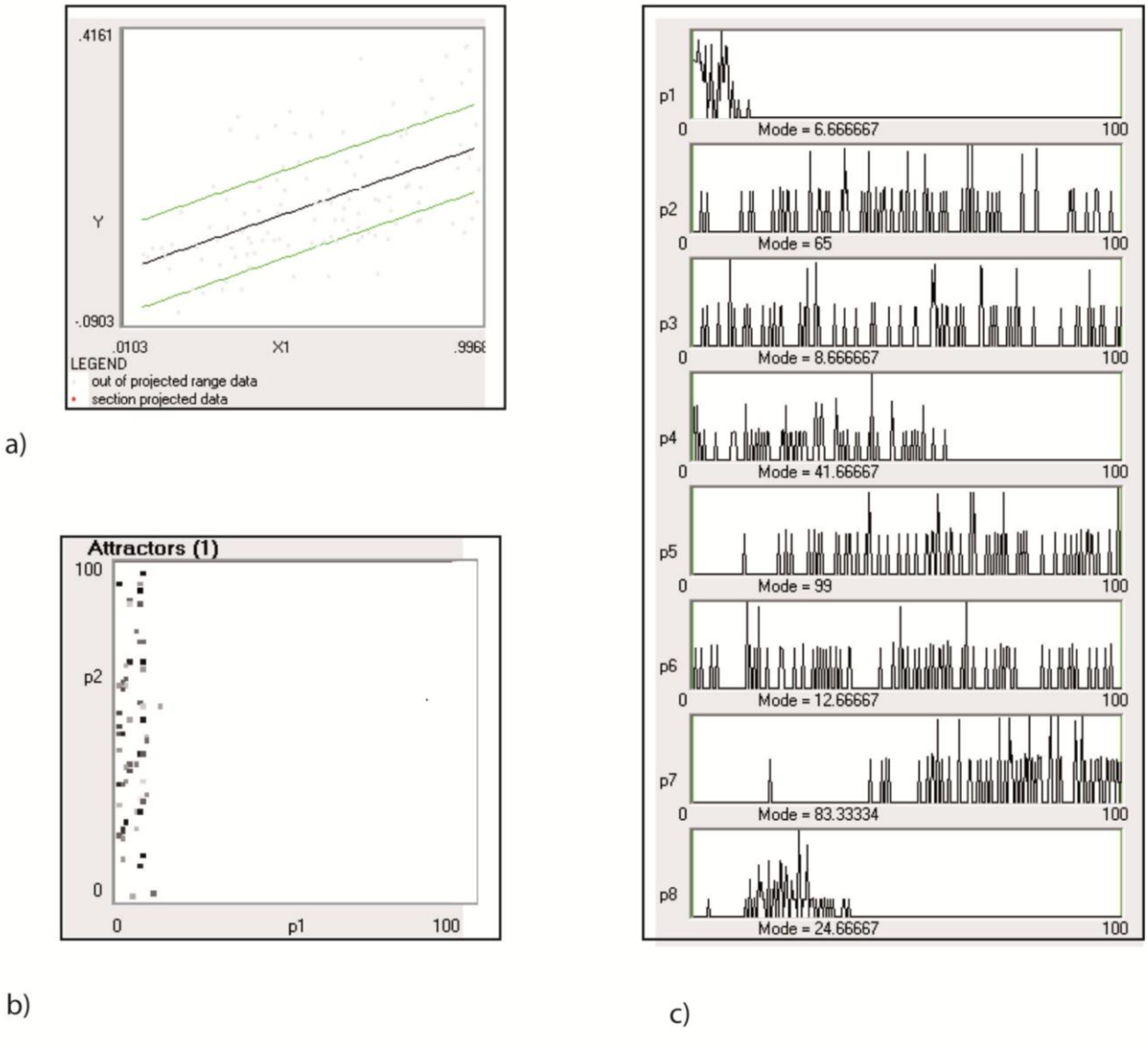

Fig. 4.11 – Monte Carlo software results windows; *a)* Data Space; *b)* Parameters Section attractor; *c)* Parameter Space

4.3 The fracturing predictive modelling

The final model has been implemented in Frap-3, a fault environment modelling software package. It is a true 4-D tool that can predict stress conditions and the brittle deformation patterns associated to a given set of fault surfaces, during single or multiple tectonic events, as well as under different stress conditions during the stress condition evolution. Results provided by Frap 3 include: rheological properties of the faulted rocks; stress condition during faulting; deformation structure type (joints, pressure-solution cleavages…), their attitude, and their probability of occurrence; predictions of the occurrence and location of fault gouge layers. Frap 3 can input data in various formats and results can be exported into reservoir models in standard formats, including Eclipse ™ and GOCAD™ grids. Frap 3 already computed specific predictions for the Fault-Core, and now with this new implementation can predict the Damage-Zone characteristics as well. The total

stress conditions computed by Frap 3 results from the sum of the static components of stress: a) Overburden; b) Fluid Pressure; c) Regional deformation (Fig. 4.12). The dynamic components are: d) Kinematic, which includes either the elastic stress accumulation in the fault zone and the friction during the movement of the fault in the fault deformation zone; e) Stress Drop, that occurs during the sudden stress release that follows the failure along a fault surface, it has an orientation opposite to the stress tensor immediately before failure takes place. The total stress field was computed in the following 4 conditions: a) Static component, in static conditions the fault does not move and the computed deformation is produced by the regional (external) stress field alone; b) Pure kinematic component, in pure kinematic conditions the fault moves and only the kinematic stress field component induced by the fault movement is computed; c) kinematic component, in kinematic conditions the fault moves and the resulting stress field is given by the sum of the static and kinematic stress components; d) Stress Drop, in stress drop conditions the difference between the stress field across a fault surface before and after the slip (i.e. an earthquake) is computed.
The attitude of 4 main deformation structures, namely the joints, the pressure-solution surfaces, the synthetic small scale faults (e.g. R_1 shears), and the antithetic small scale faults (e.g. R_2 shears), is computed from the total stress field in each cell of the damage zone and the probability of each deformation structure to develop is computed, based on field-derived empiric relationships. Several factors influence fracture azimuth, frequency and, hence, permeability properties. Their interaction (computed in Frap 3), can produce a complex fracture network. The most critical factors are: a) fault attitude, changing the geometry (azimuth or dip) of the fault causes a consistent change of fracture attitude; b) tectonic stress, changing the tectonic stress field produces significant variation in fracture attitude; c) rock rehology, the pore fluid pressure and rock type produce variations in fracture attitude.
The tendency of the rocks to deform along the fault zone is computed by the deformation function (**DF**) (Storti et al., 1997) (Fig. 4.13), which is the difference between the effective stress ($\boldsymbol{\tau}$) necessary to failure and the strength of the rock ($\boldsymbol{\Sigma}$) at any point on a plane:

$$\mathbf{DF} = \boldsymbol{\tau} - \boldsymbol{\Sigma} \qquad \text{(eq. 4.12)}$$

Since fracturing results from stress conditions in fault zones, the fracturing evolution of a fault zone can be numerically simulated at each discrete portion of a fault plane by integrating the failure capability (i.e. the DF, eq. 1) through time (eq. 2):

$$\int^{t} \mathrm{DF}\, dx \qquad \text{(eq. 4.13)}$$

We obtain the Time Stress Integral (**TSI**):

$$\mathbf{TSI} = f(\boldsymbol{\phi}, \boldsymbol{\tau}, \boldsymbol{\Sigma})\, dt \approx \mathbf{H/S} \qquad \text{(eq. 4.14)}$$

Where, $\boldsymbol{\phi}$ is the frictional coefficient, $\boldsymbol{\tau}$ is the stress, and $\boldsymbol{\Sigma}$ is the strength of the rock.

The TSI value represents the time-cumulative deformation function that acts as the given part of the structure and is measured in Pa for Time (years). The TSI is related to the H/S ratio (see section 4.1.2) and it allows comparing computer based models with field data.
The DF is also related to the fault displacements (**d**) but it is possible that the same DF results in different total brittle deformation if the effective displacements are not the same and in the same way different deformation paths can result into the same total deformation (Fig. 4.14).
Eventually, the software allows producing H/S distribution and intensity grid surfaces at multiple distances from the fault plane as showed in Fig. 4.15.

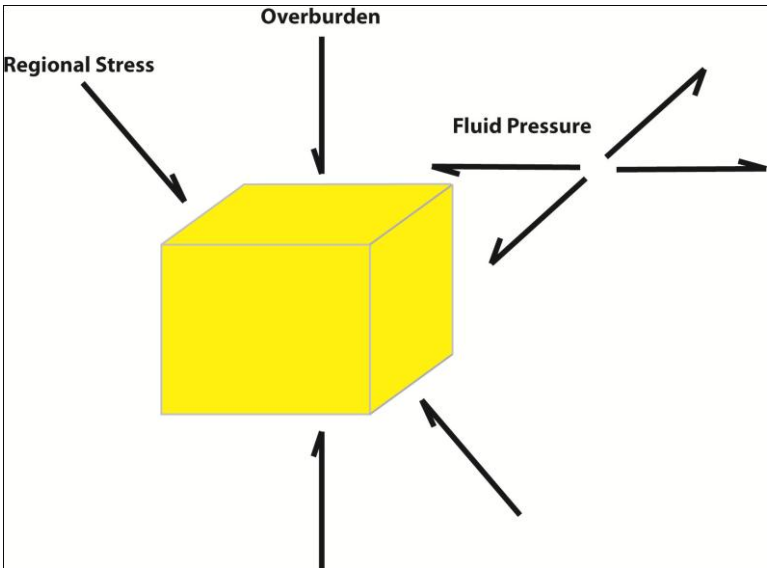

Fig. 4.12 - The static components of stress

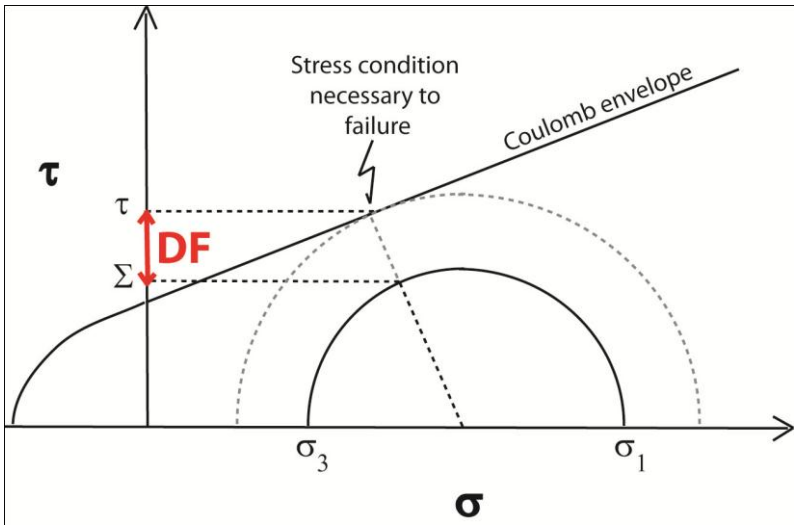

Fig. 4.13 – The Deformation Function (DF) on the Mohr-Coulomb diagram; σ is the normal stress and τ is the shear stress; Σ is the cohesion; ϕ the friction angle

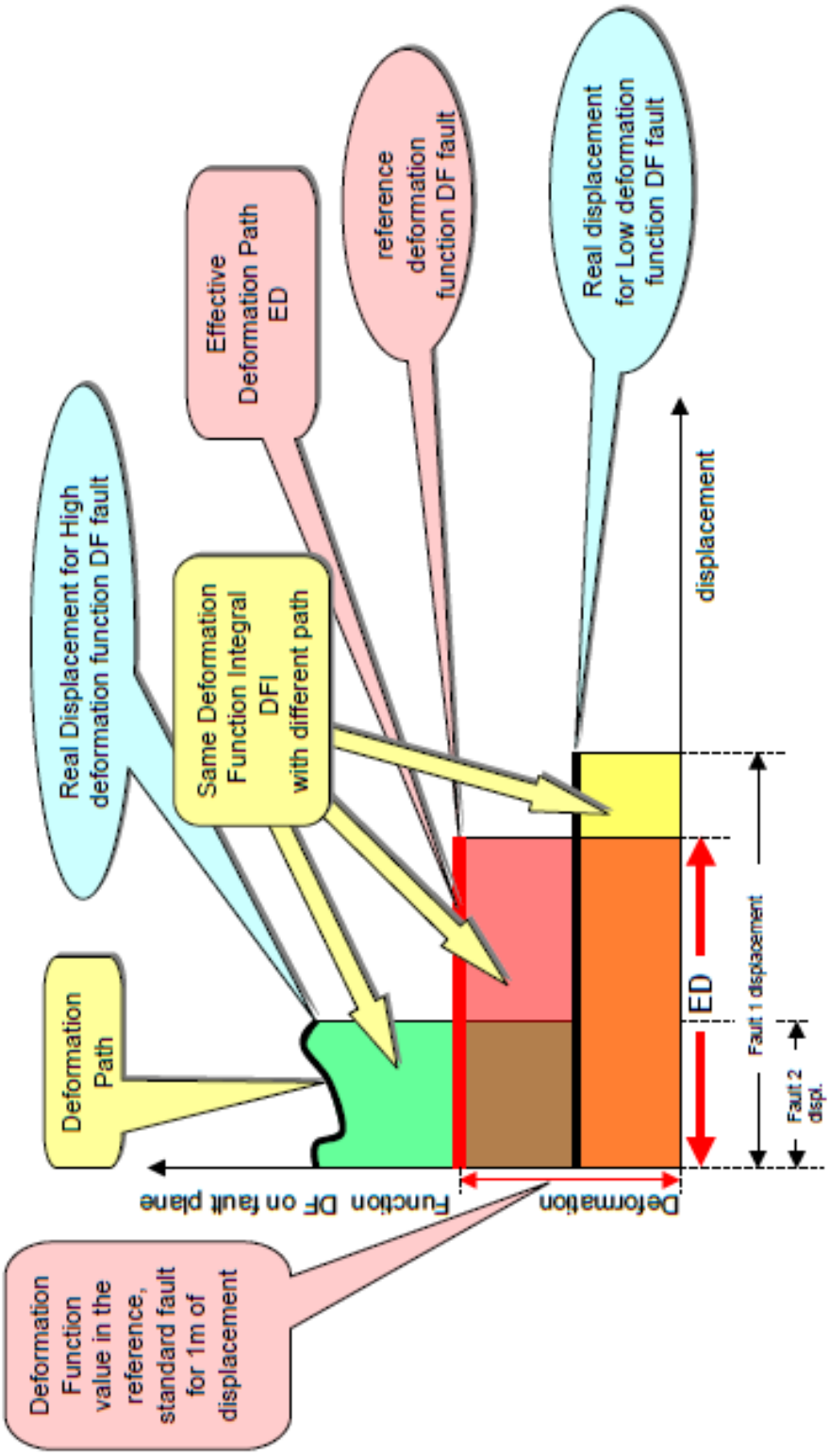

Fig. 4.14 – The relation between the Deformation Function, the throw and the deformation path

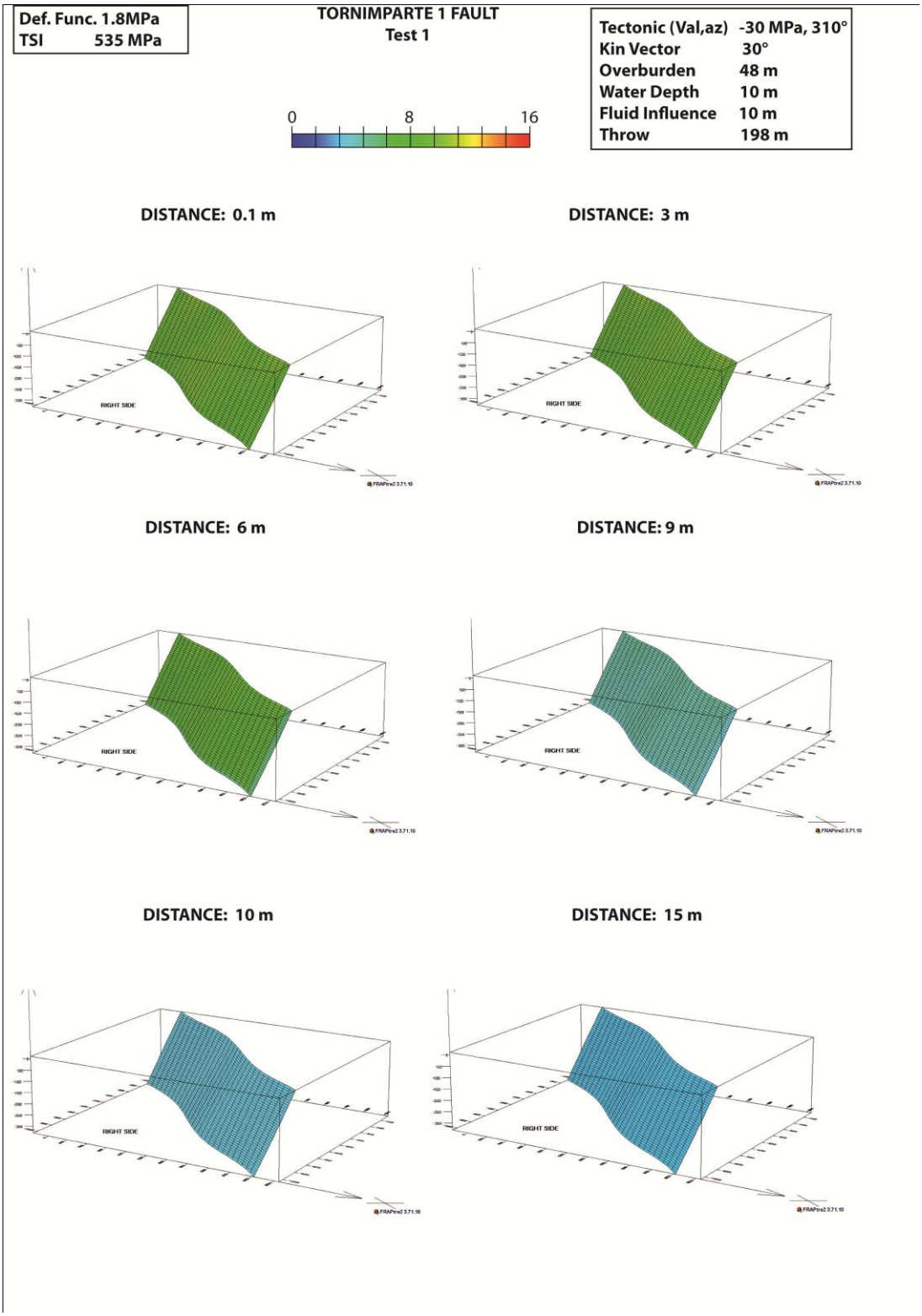

Fig. 4.15 – Example of predictive model results for the Tornimparte 1 fault

5 - RESULTS

5.1 Geological and structural characterization of the studied faults

In this section it will present the main results of the geological and the structural analyses performed *in situ* in order to characterize the fault kinematics, to discriminate and quantify the fault-related (FRD) and the regional-related deformation (RRD), and to characterized the rock rheology. To allow an easy reading the fault data set will be presented separately for each site (Tab. 5.1).

5.1.1 Prenestini Mountains

In this area a total number of 3 faults have been studied: **Rocca di Cave 1**; **Rocca di Cave 2**, and **Rocca di Cave 3** (Fig. 5.1 and Tab. 5.1).

The Rocca di Cave 1 fault (Fig. 5.2) is a subseismic scale fault located along a regional tectonic lineament striking N-S (Fig. 5.1). The fault is located on the grainstone carbonate of platform-ramp depositional environment, Paleocene-Eocene in age. The rocks are well stratified and the average bed thickness is 0.2 m. The strata strikes N 332°, 29° while the master fault plane N 41°, 42° (Fig. 5.4 a). The fault is characterized by a non-continuous fault-core (Fig. 5.2), made by smear lenses. Their thickness ranges from 0.10 to 0.15 m. The RRD is characterized by the "losanga" fracture network, which typically characterized the rocks in that area. The RRD azimuths have been statistically analysed using the rose diagram (Fig. 5.4 d) which petals correspond to the main fracture systems, and the petal lengths indicate the fracture frequency. The main regional fracture system strikes N 30°. The FRD is characterized by the presence of three main fracture systems (Fig. 5.4 c). The N 30° set has the same orientation of the RRD. The other two systems, the N-S and the N 60° form an angle of 20° with the fault attitude suggesting the occurrence of some lateral movement. The rotax (theoretical explanation in the section 4.1.5.1 of the current work) contour analysis of FRD confirms this hypothesis dipping 38° (Fig. 5.4 b). The field observation of FRD, suggests that the dip component of movement is prevalently normal.

The *in situ* observation of the fault deformation shows an asymmetric deformation pattern for the fault hangingwall and footwall, due to different stress condition. In particular, the hangingwall is more deformed than the footwall. This is consistent with the prevalent normal movement for this fault. The fault deformation pattern is characterized mostly by pressure-solution fractures enhanced the high value of clay content (quantified in this work by the insoluble content) of the protolith and by the fluid circulation. The fault throw hasn't been measured on the field. It has been computed using the Schliche et al. 1996 relation (Tab. 5.4). The age of the fault is 52 Ma. It is the age of the fore-deep deposits (see Tab. 5.3). Afterwards this first deformation stage, the fault has been affected by secondary movement related to the strike-slip tectonic and the tectonic collapse of the area. The tectonic contest seems to be intensely deformed.

The Rocca di Cave 2 and Rocca di Cave 3 (Fig. 5.3) are two subseismic scale faults located on the back-limb of a thrust and fold structure, affected by the post-orogenic extensional regime. The faults strikes N 347°, 82° and N 353°, 52° respectively (Fig. 5.5 a and 5.6 a) and are located on

carbonate platform limestone, Paleocene-Eocene in age (Fig. 5.1). The rocks are well stratified with an average bed thickness of 0.33 m. The bedding strikes N 71°, 11° (Fig. 5.5 a and Fig. 5.6 a). The fault deformation is characterized by a prevalence of extensional joints on the pressure-solutions. For both the faults the main fracturing system strikes N 64°, 41°. The rotax contour of FRF is N 50° and 36° respectively, suggesting prevalent lateral movements.

The area is intensely fractured and the main RRF system strikes NE-SW. It represents the longitudinal cleavage of the regional fold (Fig. 5.6 d). There are not any differences between the hangingwall and the footwall deformation patterns for those faults.

The throw values ranges between 0.20 and 0.25 m for both the faults. The fault does not show any core due to the low values of throws. The age of deformation for both the faults is 52 Ma (Tab. 5.3).

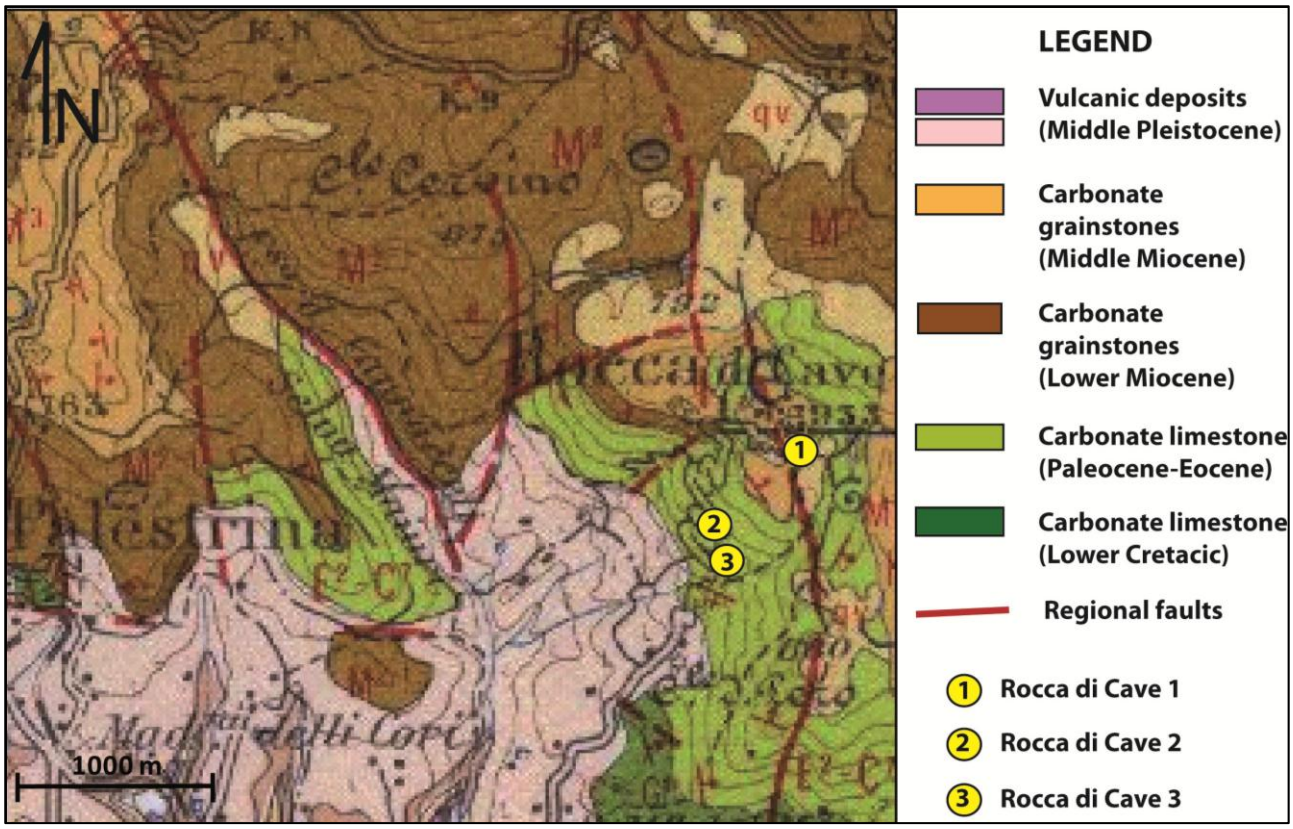

Fig. 5.1 – Geological map of Prenestini Mountains and location of the studied faults (Modified from "Carta geologica d'Italia 1:100000, Foglio ROMA -150)

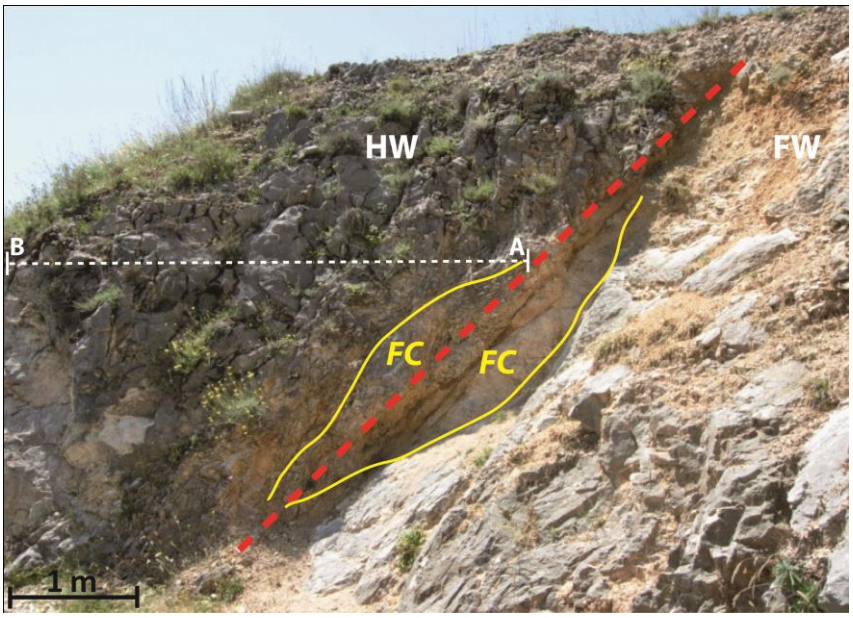

Fig. 5.2 – Rocca di Cave 1 fault; the red dashed line corresponds to the master fault plane; the yellow lines correspond to the fault-core (FC) damage-zone boundaries; HW and FW are the fault hangingwall and the footwall respectively; the white dashed line corresponds to the trace of the scan line (A-B)

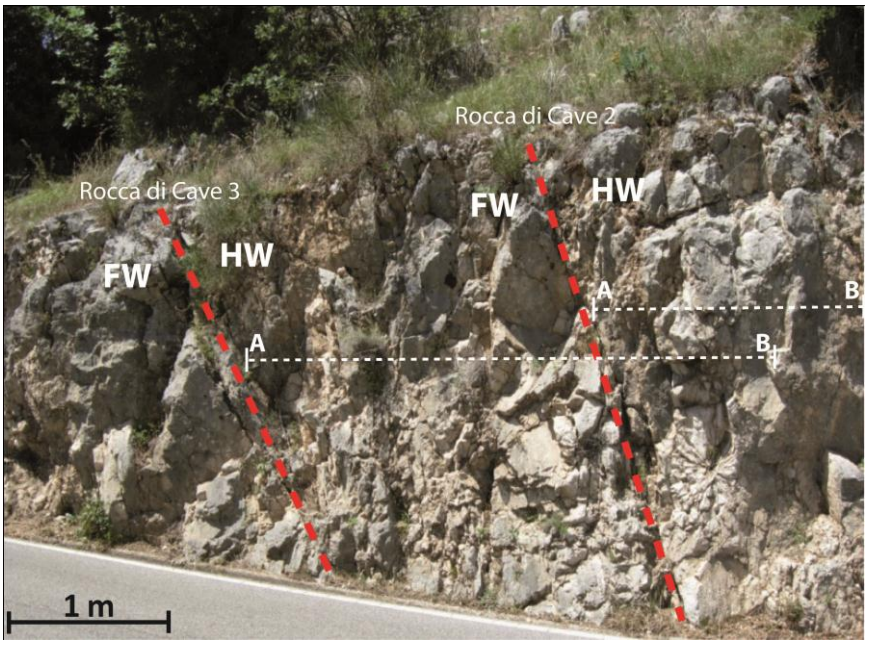

Fig. 5.3 – Rocca di Cave 2 and Rocca di Cave 3 faults; the red dashed lines corresponds to the master fault planes; HW and FW are the fault hangingwall and the footwall respectively; the white dashed lines correspond to the trace of the scan lines (A-B)

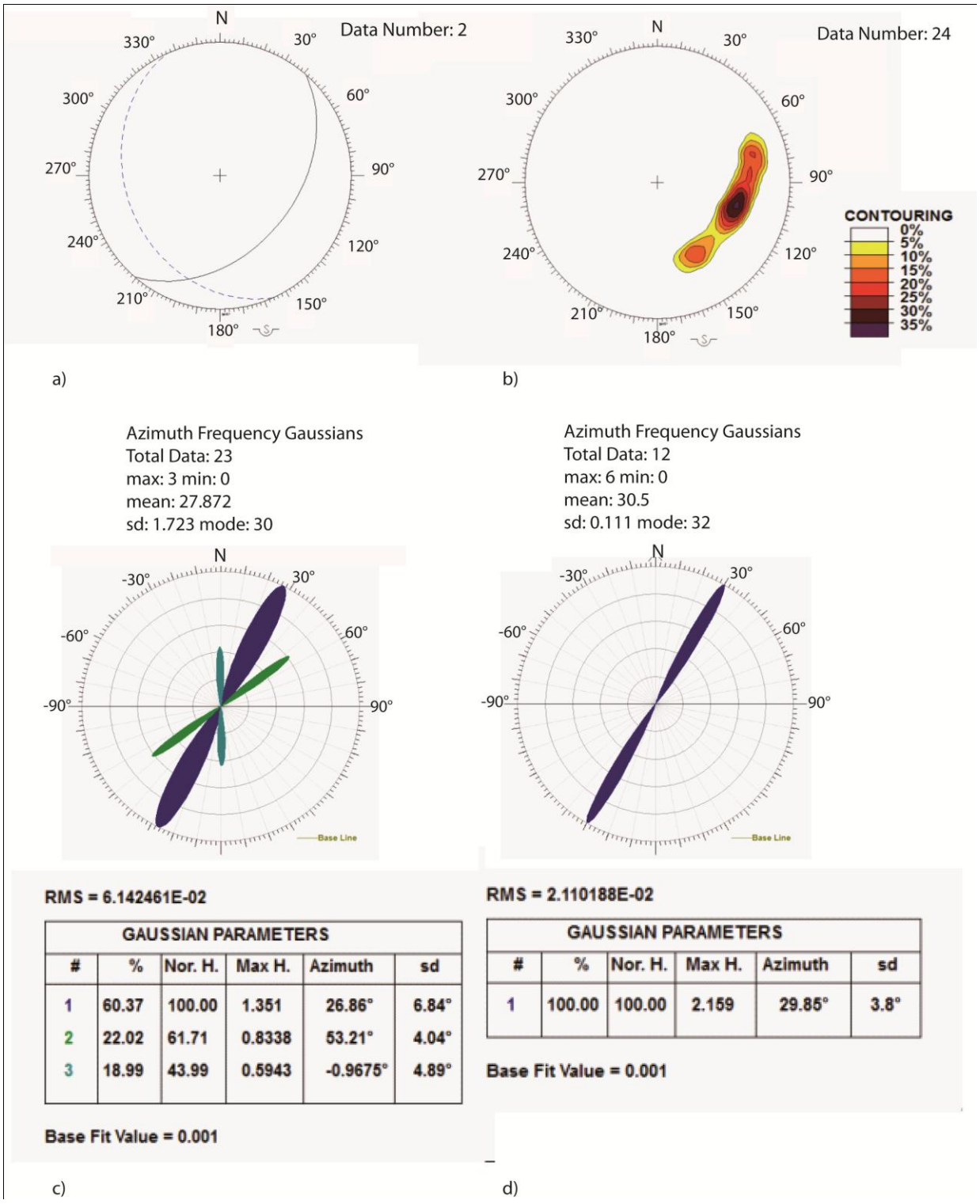

Fig. 5.4 – Structural data analysis of the Rocca di Cave 1 fault. a) Fault and bedding stereoplot; b) FRD rotax contour; c) FRD azimuth rose diagram; d) RRD azimuth rose diagram

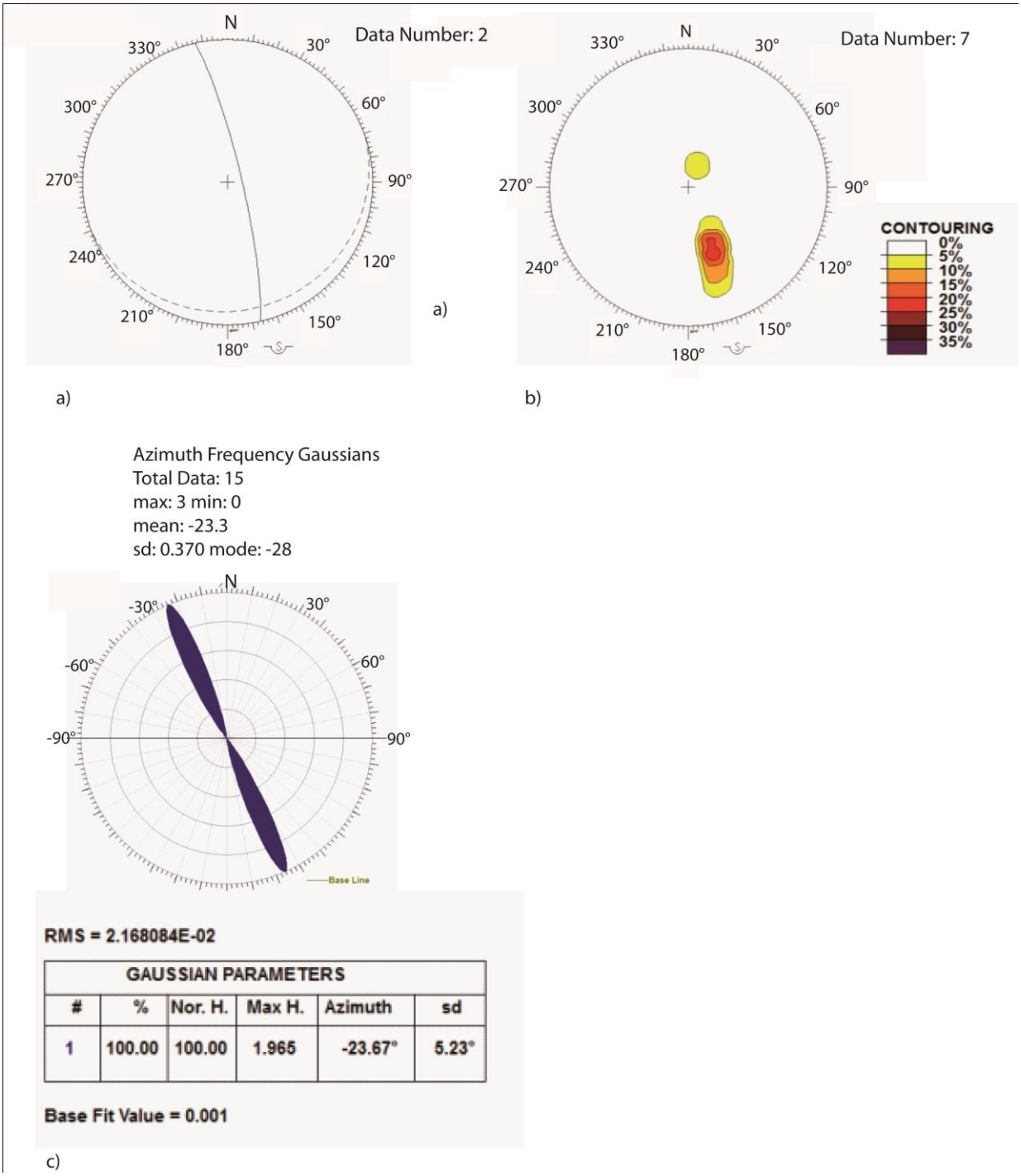

Fig. 5.5 – Structural data analysis of the Rocca di Cave 2 fault. a) Fault and bedding stereoplot; b) FRD rotax contour; c) FRD azimuth rose diagram

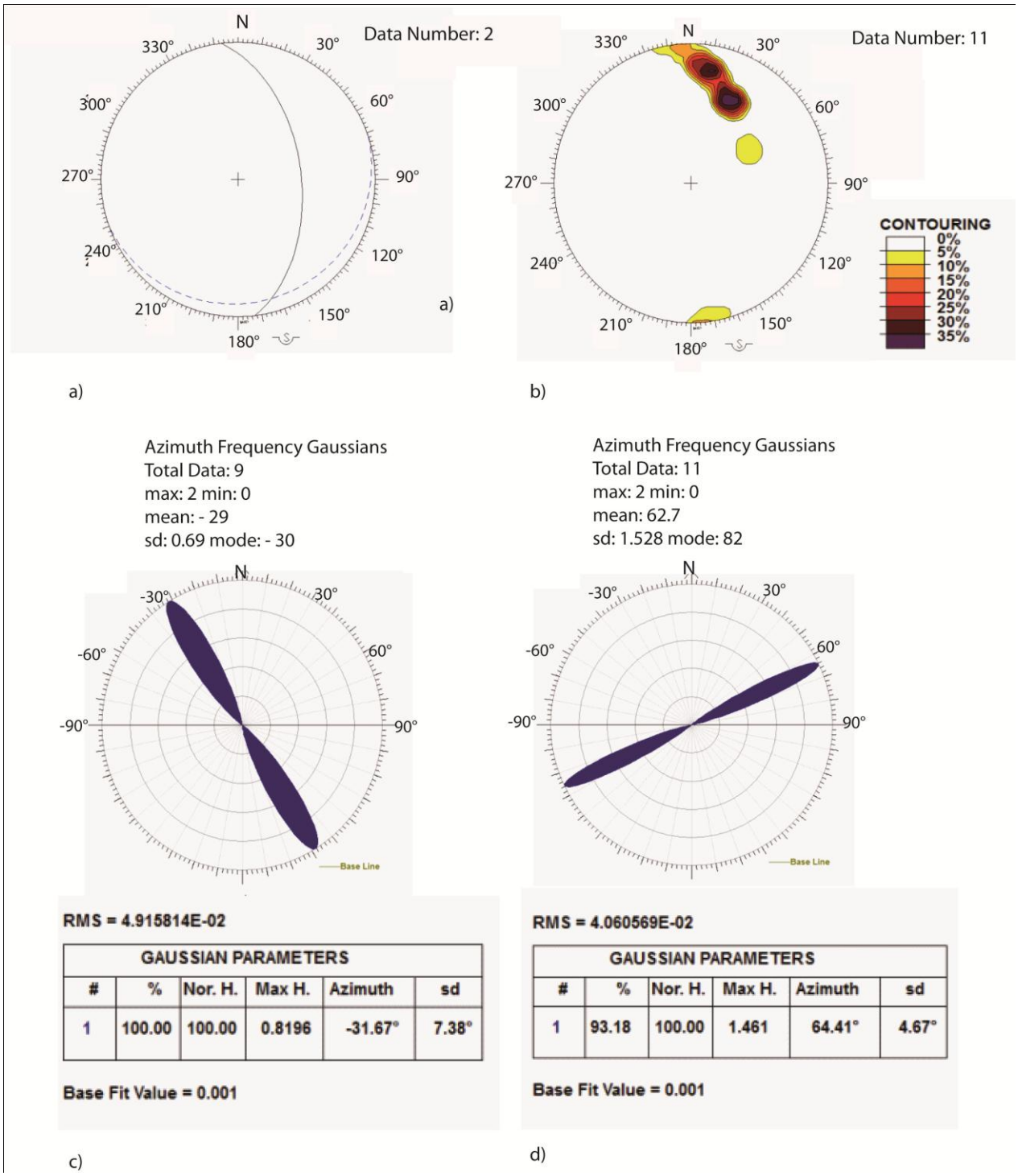

Fig. 5.6 Structural data analysis of the Rocca di Cave 3 fault. a) Fault and bedding stereoplot; b) FRD rotax contour; c) FRD azimuth rose diagram; d) RRD azimuth rose diagram

5.1.2 Simbruini-Ernici Mountains

A total number of 3 faults have been studied in this area: **Filettino fault**, **Ienne fault**, and **Pietrasecca fault** (Fig. 5.7, 5.8, 5.9, and Tab. 5.1).

The Filettino fault strikes N 104°, 35° (Fig. 5.13 a) and is located on the forelimb of a younger-on-older out of–sequence thrusting (i.e. Lower Cretaceous units over-thrusting the Upper Triassic ones). The fault plane plunge, that is lower than the expected normal fault plunging (45°-75°), suggests that fault development occurs earlier than the out of-sequence thrust, probably during the evolution of the major thrust. Subsequently, the fault was leaded and rotated during the evolution of the out of-sequence. The expected first deformation age has been fixed at 67 Ma (Tab. 5.3). The fault juxtaposes two different rocks. At the footwall the oldest portion of the Latium-Abruzzi platform succession crops out. It is a dolostone rock, Lower Triassic in age, characterized by a lagoonal-type facies with high organic content that can be considered a typical productive source rock. At the fault hangingwall an alternation of dolostone and mudstone Lower Cretacic in age crops out. Both lithologies are well stratified and their average bed thickness is 0.6 m. The field observations highlight that the fault hangingwall is more deformed than the footwall. The fracturing pattern is characterized by an abundance of pressure-solutions fractures perpendicular to the fault plane which frequency increases nearby the fault plane. Several systems of extensional fractures have been detected. The rose diagram of Fig. 5.13 c shows two main fracture systems, both related to fault kinematic. The main RRF system strikes N 80°, and it represents the longitudinal cleavage of the regional fold (Fig. 5.13 d).The rotax contour analysis (Fig. 5.13 b) shows two main values both almost horizontal (N 113°, 8° and N 284°, 2°), suggesting a prevalent dip movement for this fault. The fault shows a developed and continuous fault-core (Fig. 5.10). Its average thickness is 7 m. The fault throw was computed by the stratigraphic method (20 m).

The Ienne fault is located on the back-limb of the main regional thrust and fold striking NW-SE. The main fault attitude is N 309°, 45° (Fig. 5.14 a). As the case of the previous fault, the dip is lower than the expected for normal fault. This is probably due to a leading and a rotation occurred during the formation of the regional thrust and fold. This fact suggests that the fault was formed before or during the thrust development, and the expected age of deformation is 67 Ma. The fault juxtaposes two different lithologies which show different deformation behaviours (Fig. 5.11). At the fault hangingwall crops out an alternation of carbonatic packstone and mudstone with abundant rudists, typically of platform depositional environment, Upper Cretacic in age. These rocks are well stratified with an average bed thickness of 0.2 m. At the fault footwall, micritic dolostones with stromatolitic laminations, Lower Cretacic in age, crop out

The fault footwall is intensely deformed showing a predominant pressure-solution parallel to the bedding. Vertical extensional fractures are the most prevalent deformation features in the hangingwall. The rotax analysis shows a value of 2° suggesting a prevalent dip movement (Fig. 5.14 b). The angles between the riddle planes and the fault show a prevalent normal movement for this fault. The rose diagram shows the presence of 4 main fracture systems (Fig. 5.14 c). The two systems striking NW-SE are related to fault; otherwise the NE-SW systems have the same orientation of the regional deformation (Fig. 5.14 d). Their frequency is lower nearby the fault

plane and became higher away from the fault plane. There is a continuous and recemented fault-core, thickening 1.9 m (Fig. 5.11). The fault throw was computed using the stratigraphic method (100 m).

Pietrasecca fault is a subseismic scale fault that strikes N 74°, 84° (Fig 5.15 a). It is located on the fore-limb of a regional fault-bend folding, which involves the upper part of the Latium-Abruzzi succession and has the expected NW-SE axis and north eastern vergence. The fault is bounded by two tear faults that play an important role in fractured permeability and the development in karst system in the area. The expected fault age was fixed at 67 Ma, which corresponds to the age of the over-thrusting fore-deep deposits. Pietrasecca fault is located on the carbonatic grainstones of the ramp deposits. The rocks are well stratified with an average bed thickness of 0.4 m. The rose diagram of Fig 5.15 c highlights two main fracture systems. They have almost the same orientation of the longitudinal and transversal regional deformation sets (Fig. 15 d). The deformation pattern of the normal fault is influenced by the presence of the near strike-slip fault. The contour analysis shows two main rotax values (Fig. 15 b). The horizontal rotax value is related to the movement of the normal fault, otherwise the vertical rotax is related to the lateral movement of the near tear fault. The fault hangingwall is characterized by a prevalence of extensional fractures. The fault footwall is affected by the tear fault deformation and shows an intense pressure-solution deformation parallel to the fault plane. The fault-core is continuous and its average thickness is 3.46 m. The stratigraphic method can't be applied to measure the throw, so that it was used the Schlishe et al. 1996 relation (see chapter 5.1.2).

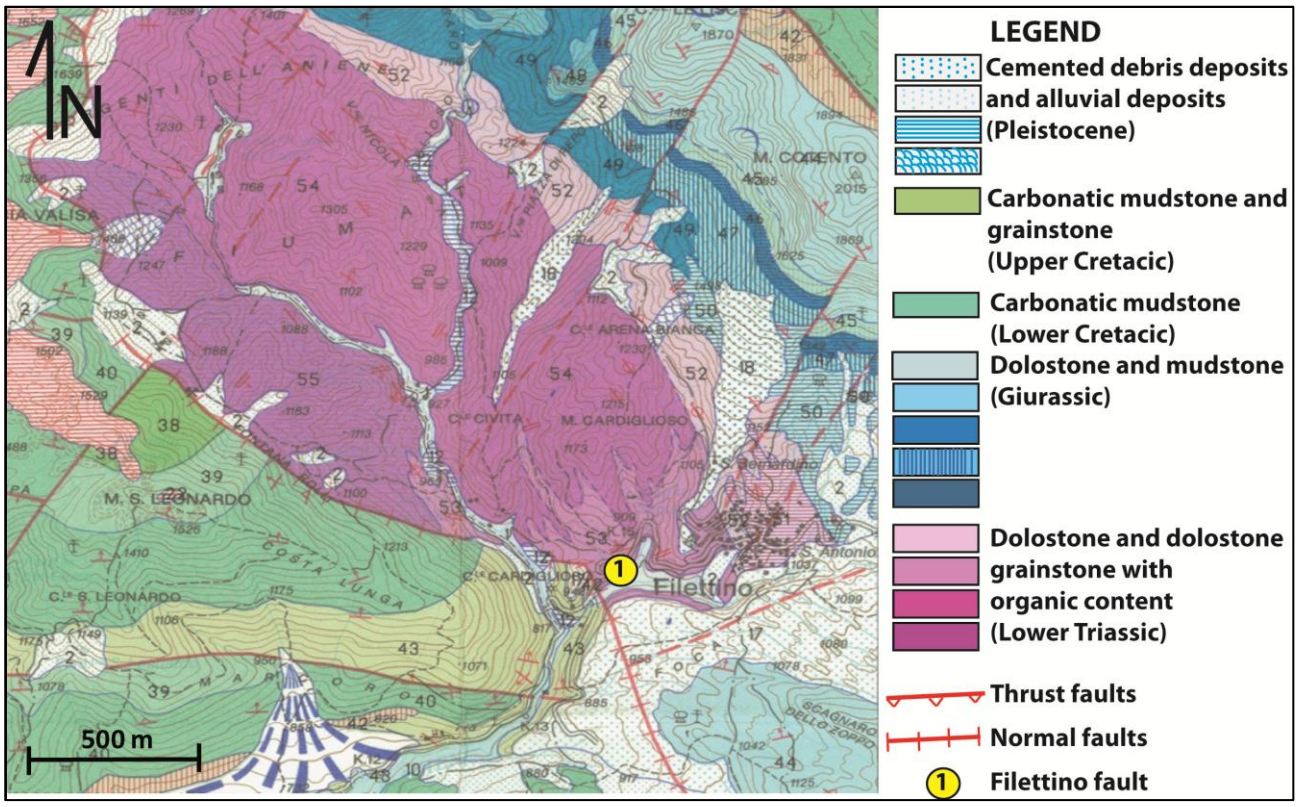

Fig. 5.7 – Geological map of Filettino area and location of Filettino fault. (Modified from "Carta geologica d'Italia 1:50000, Foglio SUBIACO - 376)

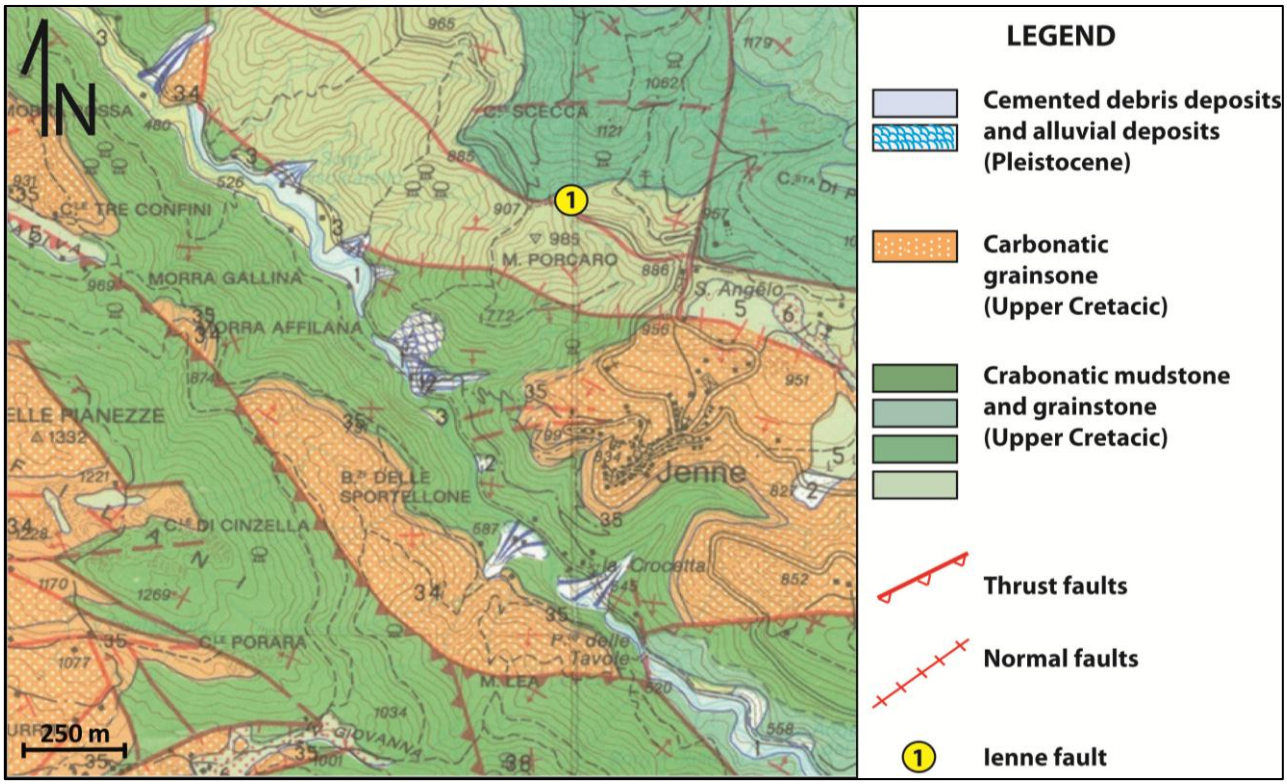

Fig. 5.8 – Geological map of Ienne area and location of Ienne fault (Modified from "Carta geologica d'Italia 1:50000, Foglio SUBIACO - 376

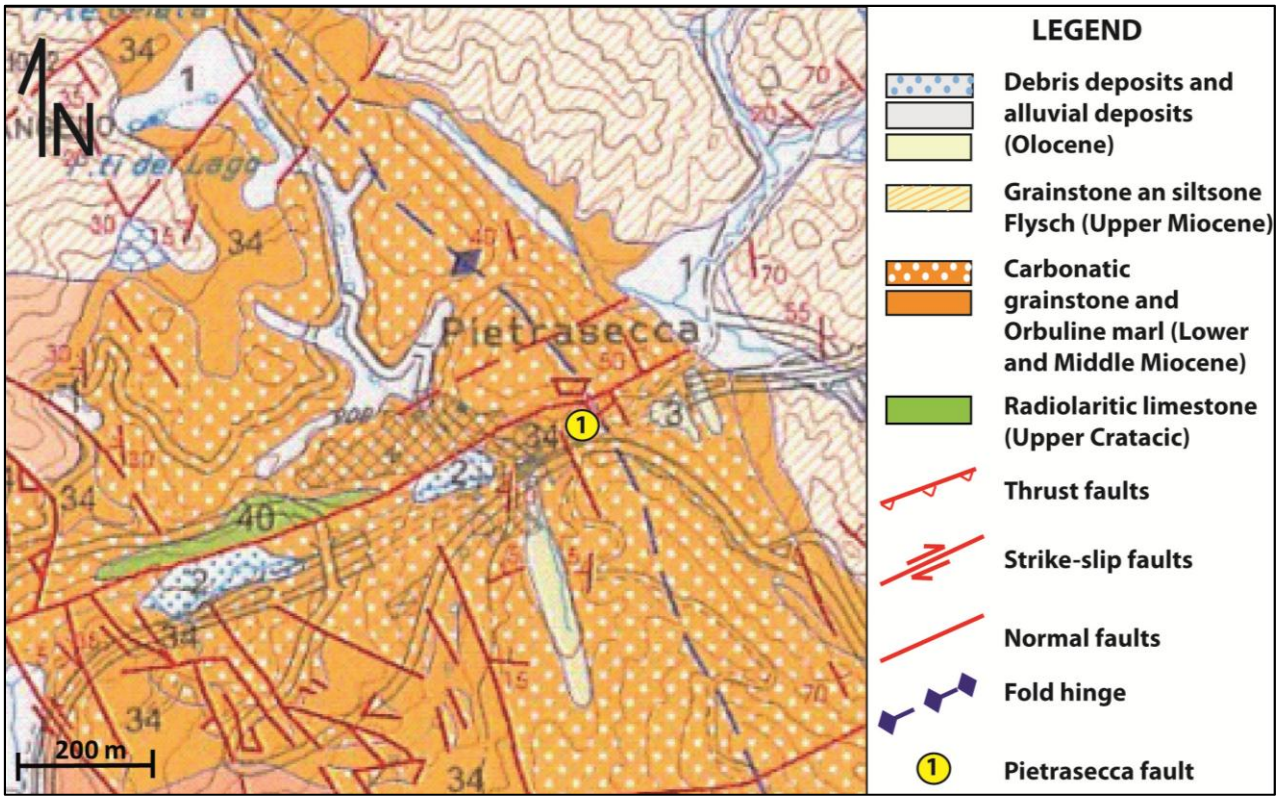

Fig. 5.9 – Geological map of Pietrasecca area and location of Pietrasecca fault (Modified from "Carta geologica d'Italia 1:50000, Foglio SUBIACO - 376)

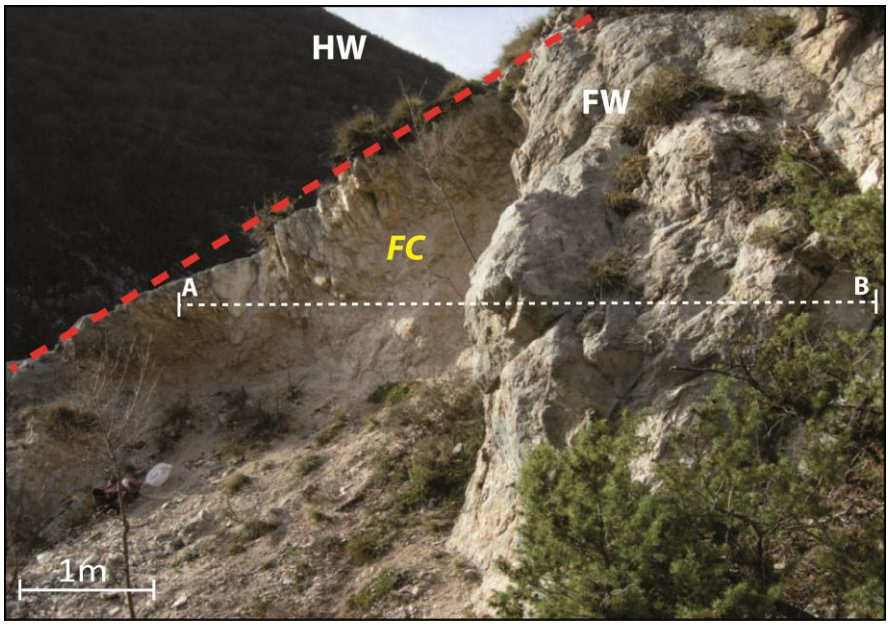

Fig. 5.10 – Filettino fault; the red dashed line corresponds to the master fault planes; HW and FW are the fault hangingwall and the footwall respectively; the white dashed line corresponds to the trace of the scan line (A-B)

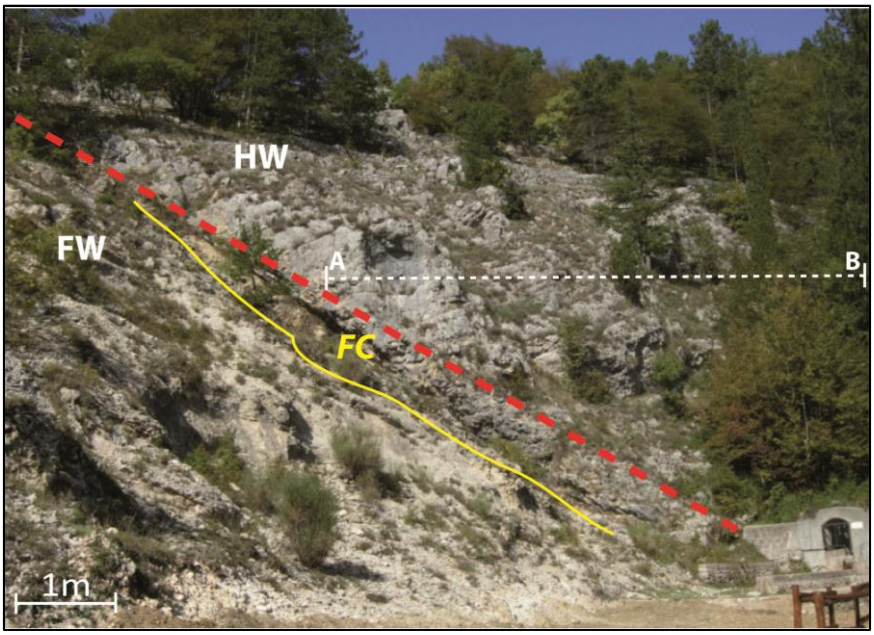

Fig. 5.11 – Ienne fault; the red dashed line corresponds to the master fault plane; HW and FW are the fault hangingwall and the footwall respectively; the white dashed line corresponds to the trace of the scan line (A-B)

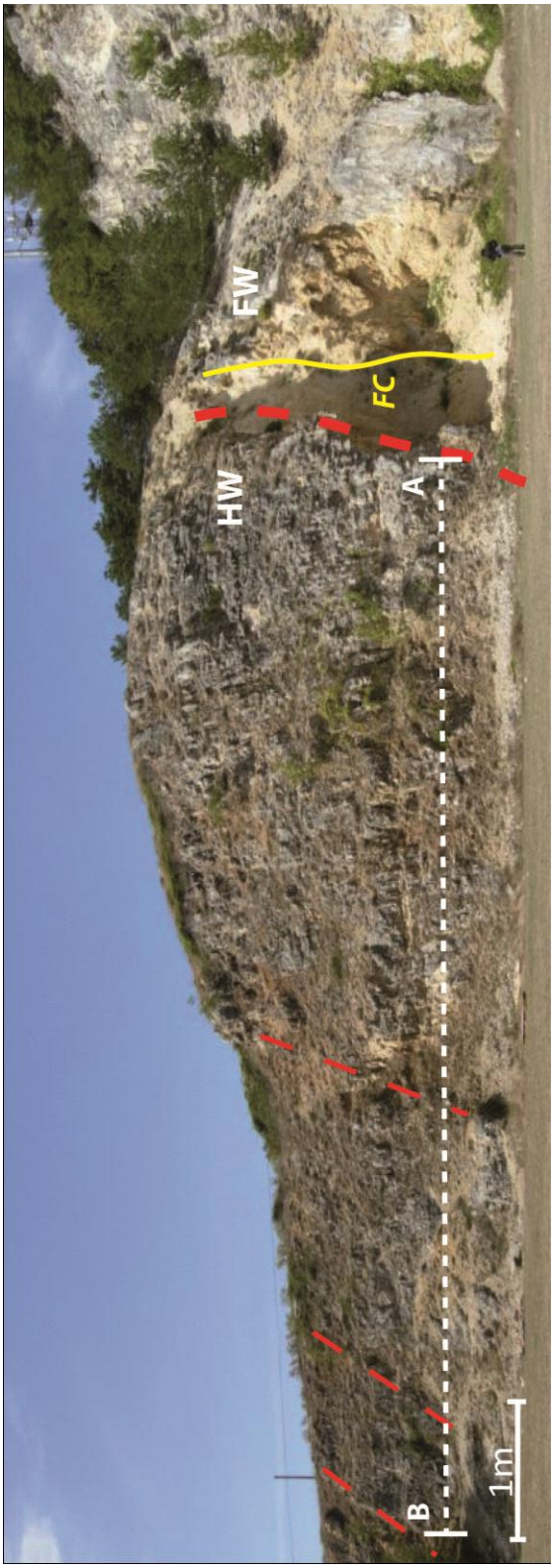

Fig. 5. 12 – Pietrasecca fault; the thicker red dashed line corresponds to the master fault plane; the thinner red dashed lines correspond to the secondary fault planes; HW and FW are the fault hangingwall and the footwall respectively; the white dashed line corresponds to the trace of the scan line (A-B)

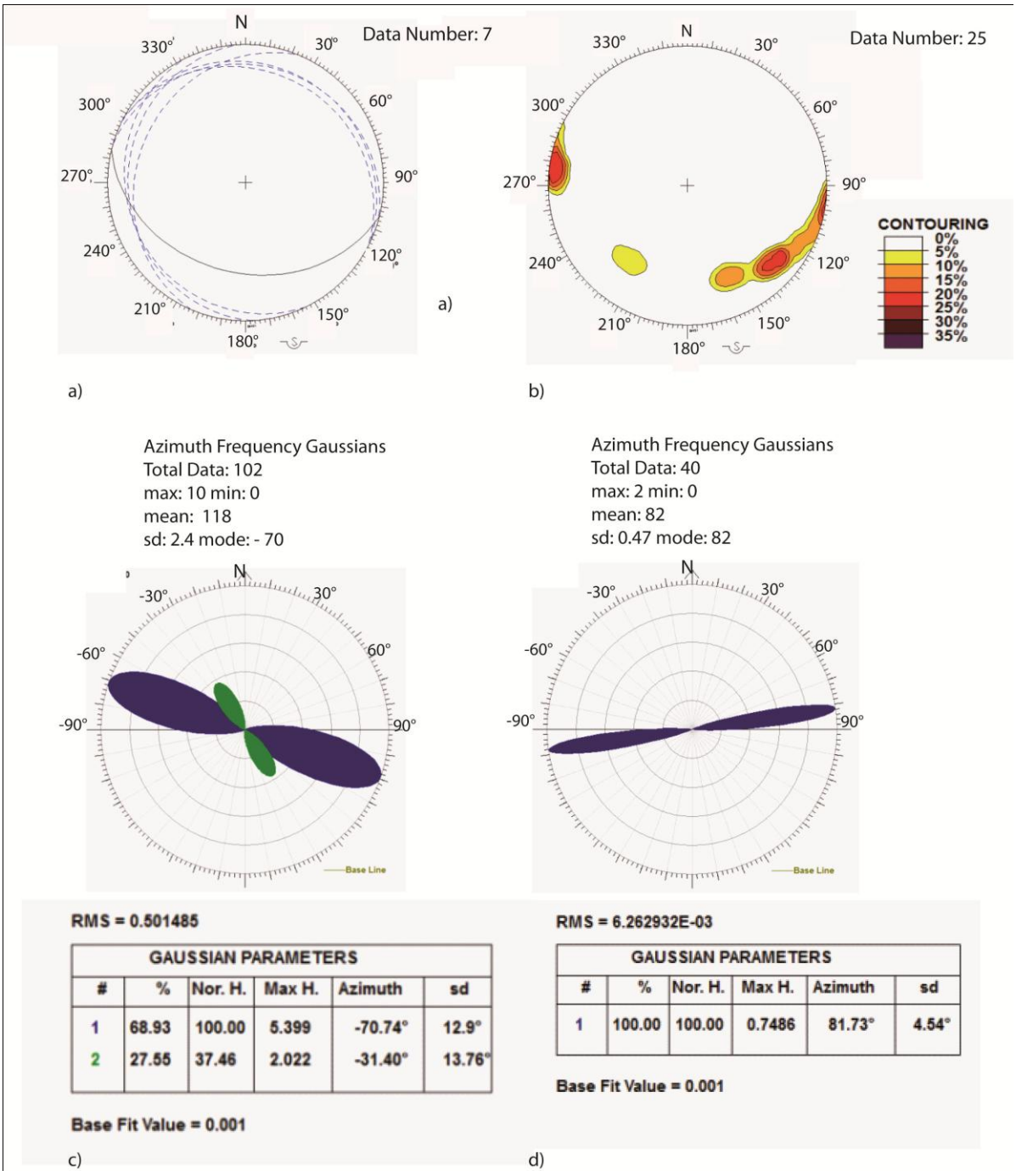

Fig. 5.13 – Structural data analysis of the Filettino fault. a) Fault and bedding stereoplot; b) FRD rotax contour; c) FRD azimuth rose diagram; d) RRD azimuth rose diagram

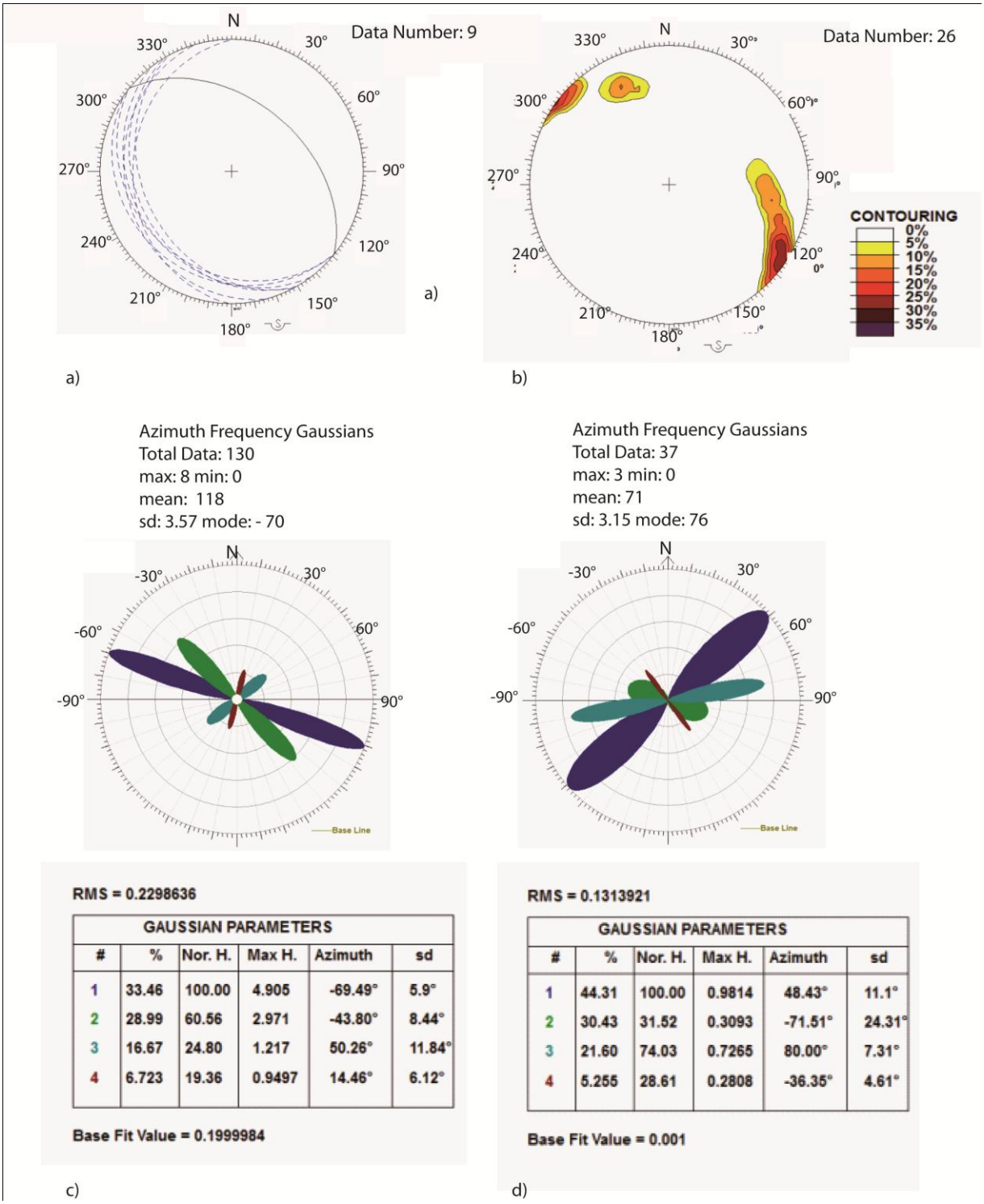

Fig. 5.14 – Structural data analysis of the Ienne fault. a) Fault and bedding stereoplot; b) FRD rotax contour; c) FRD azimuth rose diagram; d) RRD azimuth rose diagram

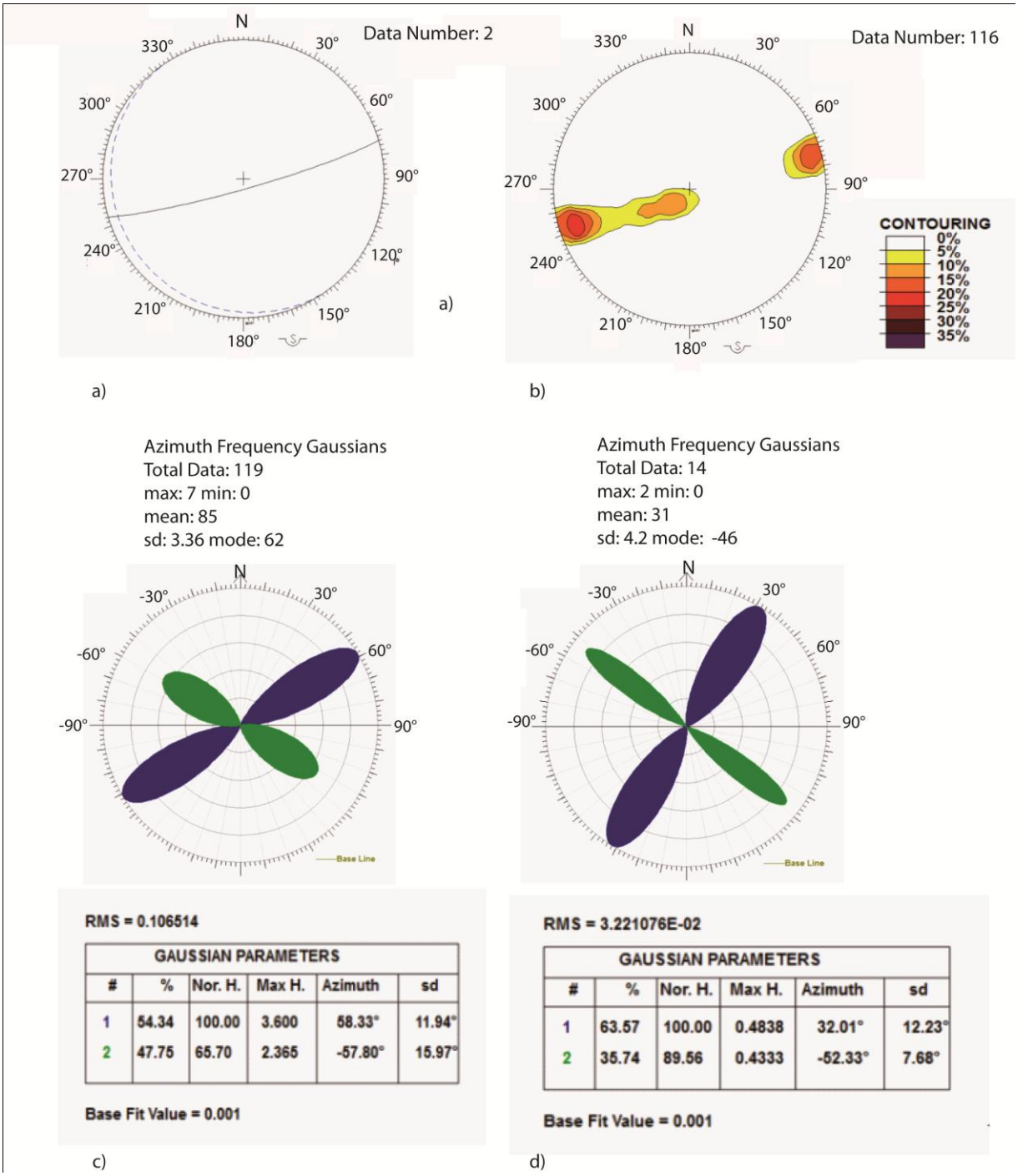

Fig. 5.15 – Structural data analysis of the Pietrasecca fault. a) Fault and bedding stereoplot; b) FRD rotax contour; c) FRD azimuth rose diagram; d) RRD azimuth rose diagram

5.1.3 Velino-Sirente Mountains

A total number of 5 faults have been studied in two different areas of the Velino-Sirente structure: **Tornimparte 1 fault**, **Tornimparte 2 fault**, **Tornimparte 3 fault**, **Tornimparte 4 fault**, and **Tornimparte 5 fault** (Fig. 5.16, 5.17, and Tab. 5.1).

The **Tornimparte 1 fault** is a segment of a seismic scale fault bounded the Campo Felice extensional plain for a length of 1 Km. The fault development occurs at surface level which formation is related to the post-orogenic extension of the Apenninic chain and the expected fault deformation age was 3 Ma. The fault footwall is characterized by an alternation of micritic carbonate and marls, with common red bauxitic horizons. This lithology consists in an oolitic packestone of a carbonatic platform deposition environment, Medium Cretacic in age. The average bed thickness is 0.6 m. The hangingwall of the fault is covered by alluvial quaternary deposits. The fault strikes N 130°, 62° (Fig. 5.23 a). The deformation pattern is characterized by extensional fractures. This abundance is probably related to the fault exhumation, which can open all the type of fractures, hence the pressure-solution fractures too. The rose diagram shows the presence of two main FRF systems oriented NE-SE and NW-SE respectively (Fig. 5.23 c). The rotax value (Fig. 5.23 b) is almost horizontal, suggesting a dip movement of the fault. The shear features related to fault indicate a normal movement.

The fault-core appears continuous and recemented (Fig. 5.18). This recementation is related to the fluid circulation. The fault-core average thickness is 1 m. It is very thin respect the dimension of the fault. Maybe, the major part of fault-core is in the fault hangingwall, which is covered by recent deposits of the plane. The regional deformation pattern is characterized by three main fracture systems oriented NE-SW and NW-SE.

The other 4 faults: **Tornimparte 2, Tornimparte 3, Tornimparte 4 and Tornimparte 5** are subseismic scale faults located on alternation of micritic carbonate and marls, with common red bauxites horizons, Medium Cretacic in age. The rocks are well stratified with an average bed thickness of 0.3 m. These faults are related to a regional tear fault as the regional the thrust.

The **Tornimparte 2 fault** strikes N 277°, 78° (Fig. 5.23 a). Two main fracture systems have been measured (Fig. 5.23 c). The contour analysis of shear planes rotax shows two main values: 28° and 50°. The first value indicates a dip movement, while the second value indicates a lateral movement.

The Tornimparte 3 fault strikes N 69°, 65° (Fig. 5.24 a). The main fracture set strikes N 62° (Fig. 5.24 c). The rotax contour analysis shows a value of 15° (Fig. 5.24 b), suggesting a prevalent dip movement of the fault.

The **Tornimparte 4 fault** strikes N 82°, 66° (Fig. 5.25 a). This fault is characterized by two main fracture systems, the N 50° and the N 74° (Fig. 5.25 c). The rotax contour analysis shows a value of 60° (Fig. 5.25 b), suggesting a prevalent lateral movement of the fault.

The Tornimparte 5 fault strikes N 81°, 86° (Fig. 5.26 a). Two main fracture systems have been measured (Fig. 5.26 c). The rotax contour analysis shows two main values (Fig. 5.26 c): the 20° one indicates a dip movement, while the 50° one suggests the occurrence of some lateral movement of the fault.

All these faults are located in an intensely deformed strike-slip tectonic contest, characterized by two main fracture systems, oriented W-E and NW-SE (Fig. 5.26 d).
Tornimparte 2, Tornimparte 3, and Tornimparte 4 faults show a continuous and thin fault-core (Fig. 5.19, Fig. 5.20). Otherwise, Tornimparte 5 fault shows a continuous and recemented fault-core, which thickness is 1 m (Fig. 5.21).

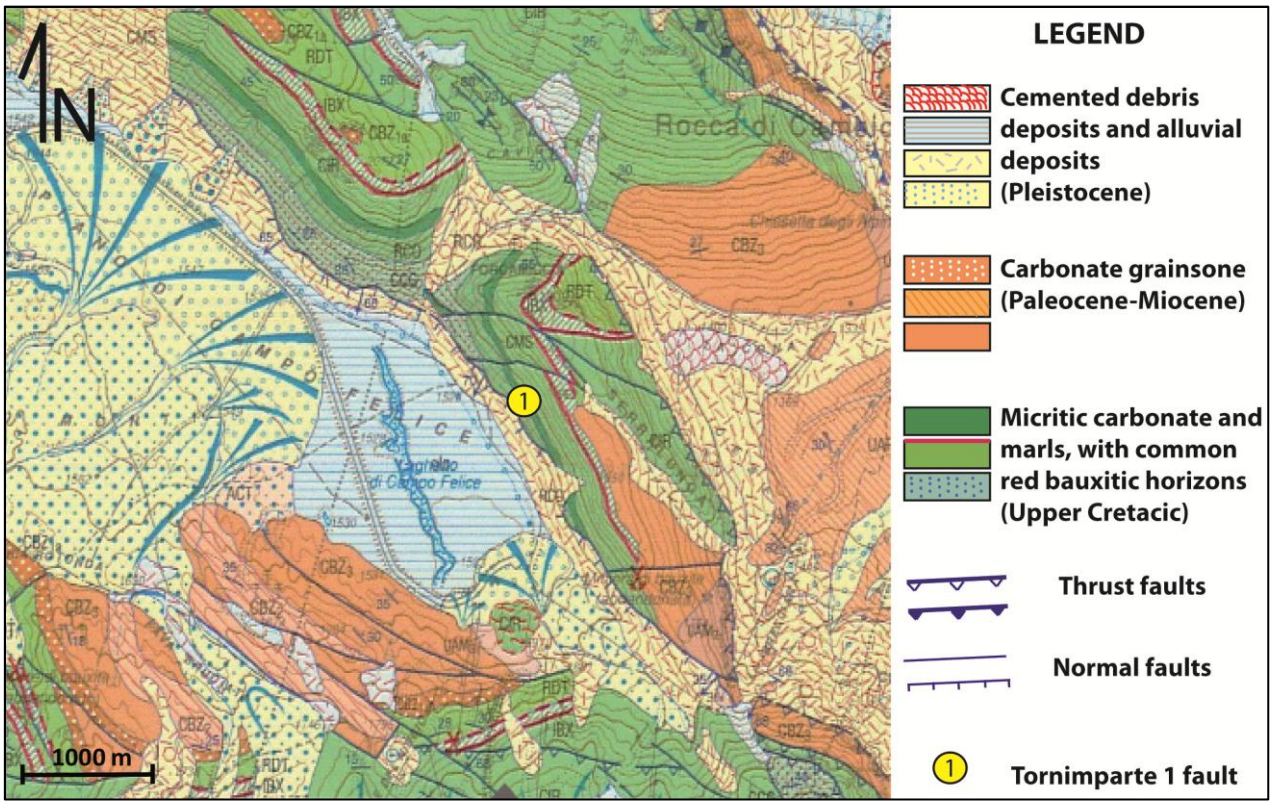

Fig. 5.16 – Geological map of Campo Felice area and location of Tornimparte 1 fault (Modified from "Carta geologica d'Italia 1:50000, Foglio L'AQUILA - 359)

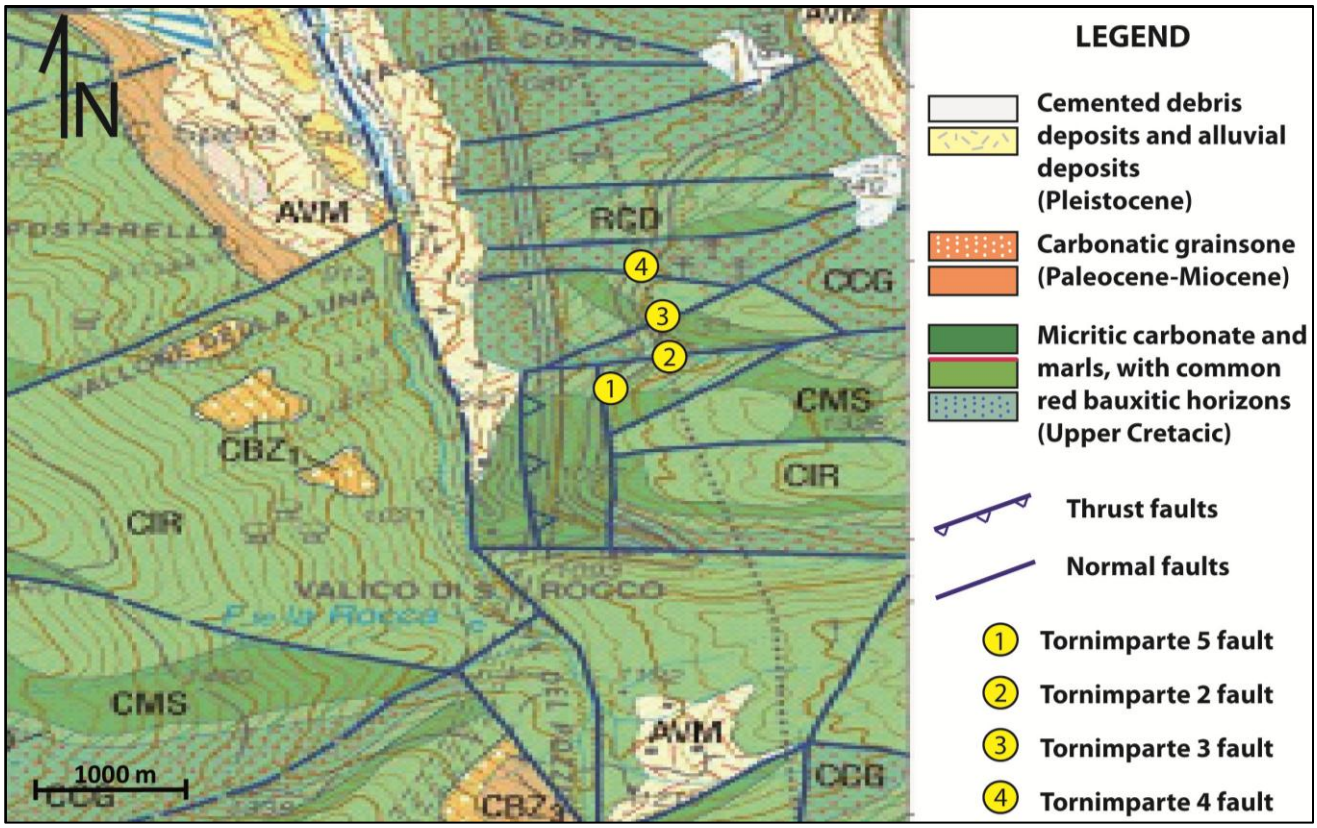

Fig. 5.17 – Geological map of Tornimparte area and location of Tornimparte 2 fault, Tornimparte 3 fault, Tornimparte 4 fault, and Tornimparte 5 fault (Modified from "Carta geologica d'Italia 1:50000, Foglio PESCOROCCHIANO – 358)

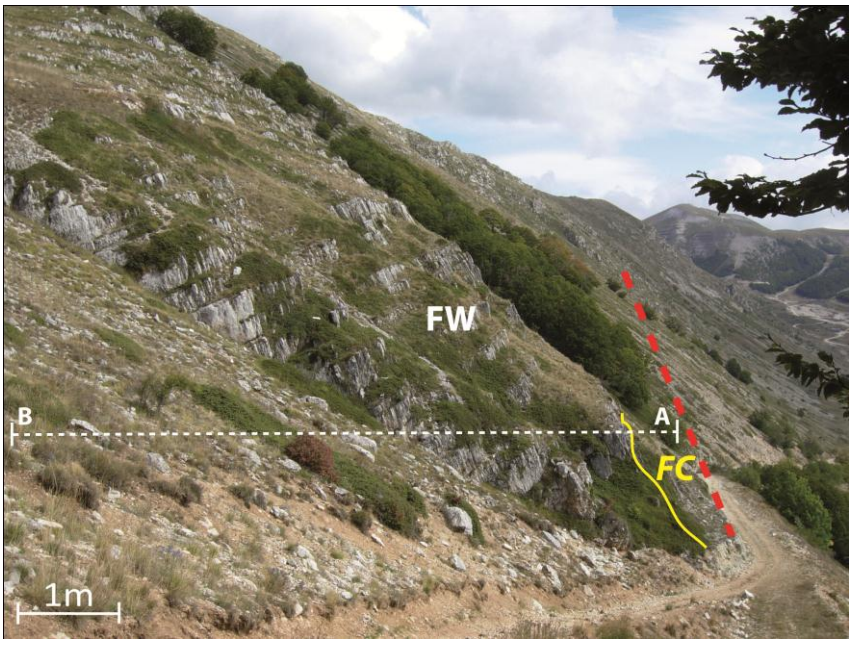

Fig. 5.18 - Tornimparte 1 fault; the red dashed line corresponds to the master fault plane; HW is the fault hangingwall; the yellow line are the fault-core (FC) boundaries; the white dashed line corresponds to the trace of the scan line (A-B)

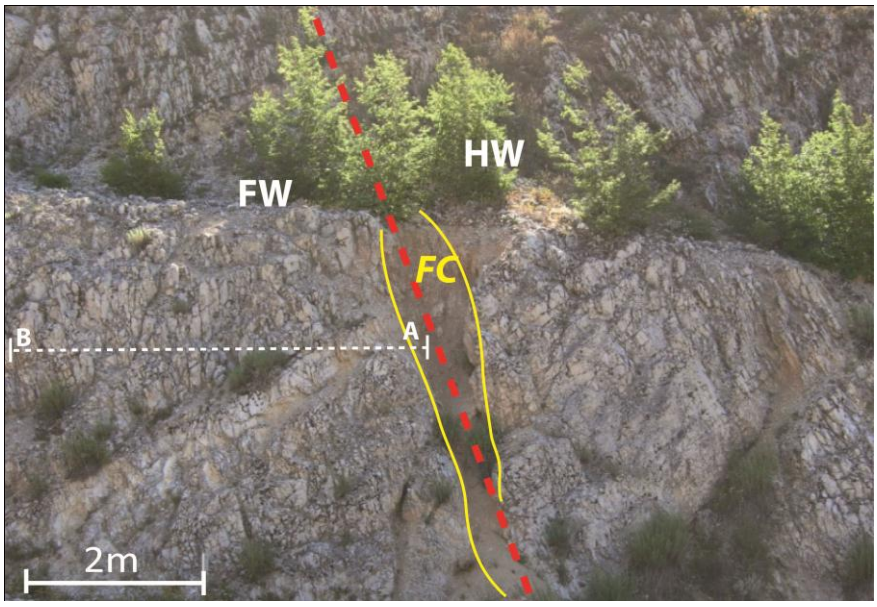

Fig. 5.19 - Tornimparte 2 fault; the red dashed line corresponds to the master fault plane; HW and FW are the fault hangingwall and the footwall respectively; the yellow lines are the fault-core (FC) boundaries; the white dashed line corresponds to the trace of the scan line (A-B)

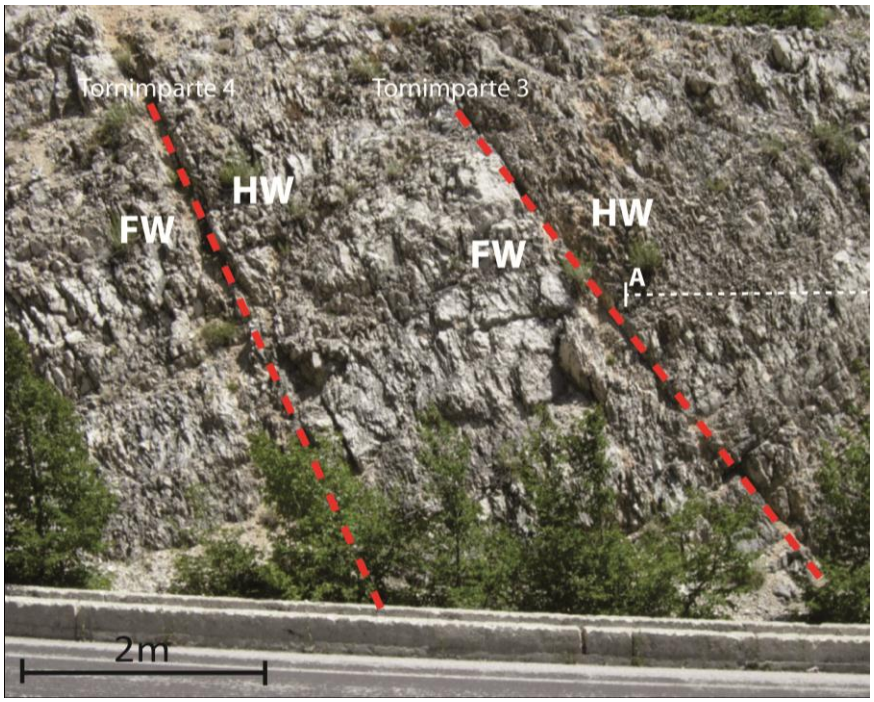

Fig. 5.20 - Tornimparte 3 fault and Tornimparte 4 fault; the red dashed line corresponds to the master fault planes; HW and FW are the fault hangingwall and footwall respectively; the white dashed line corresponds to the trace of the scan line (A-B)

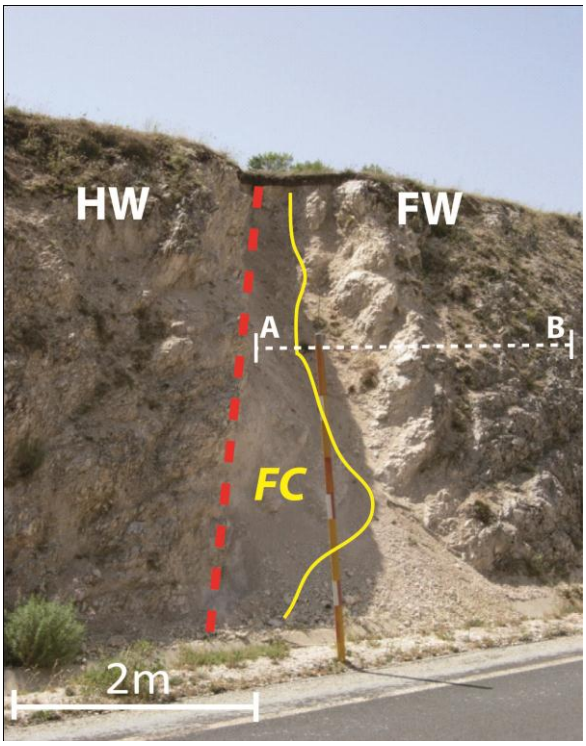

Fig. 5.21 - Tornimparte 5 fault; the red dashed line corresponds to the master fault plane; HW and FW are the fault hangingwall and footwall respectively; the yellow lines are the fault-core (FC) boundaries; the white dashed line corresponds to the trace of the scan line (A-B)

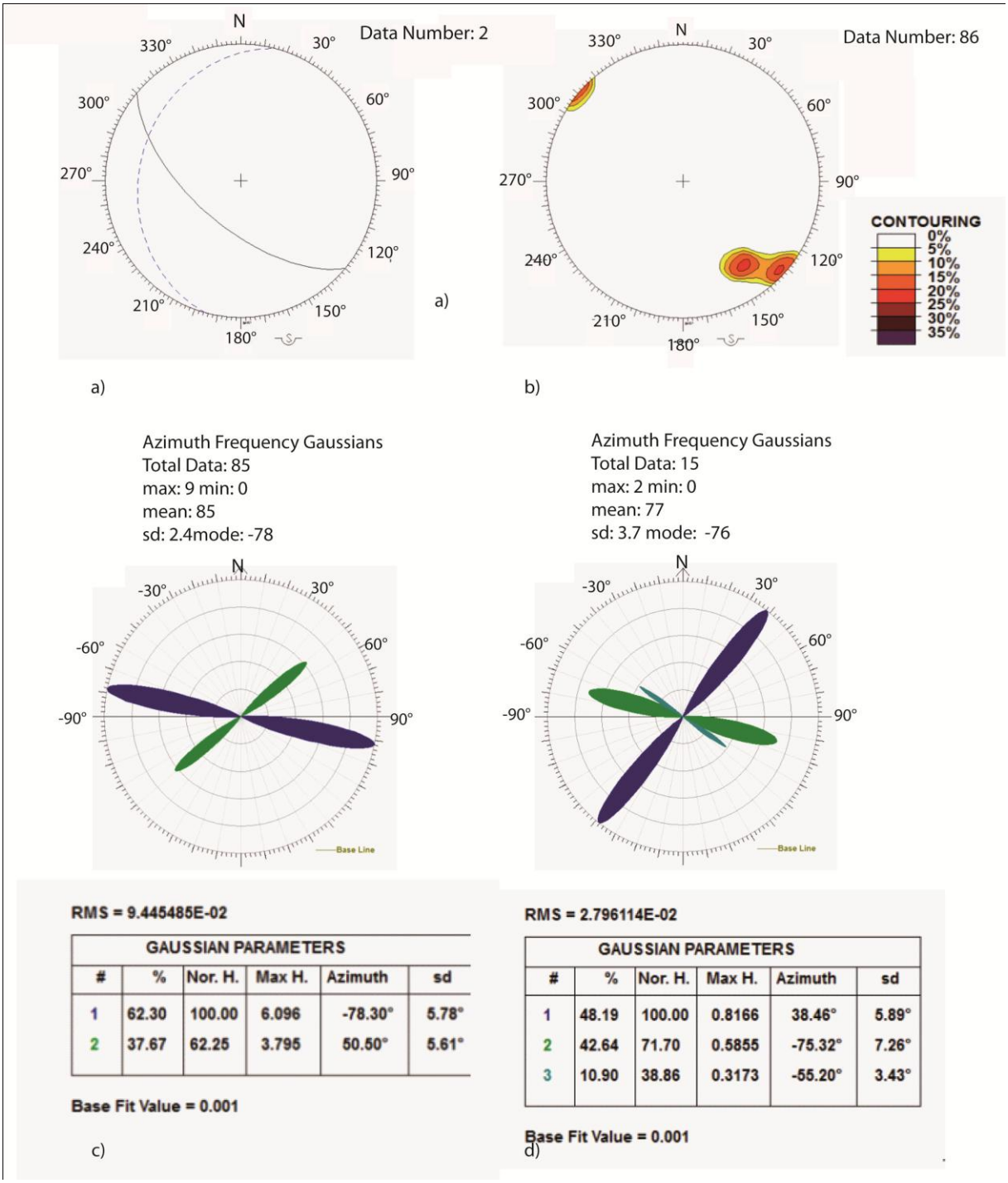

Fig. 5.22 – Structural data analysis of the Tornimparte 1 fault. a) Fault and bedding stereoplot; b) FRD rotax contour; c) FRD azimuth rose diagram; d) RRD azimuth rose diagram

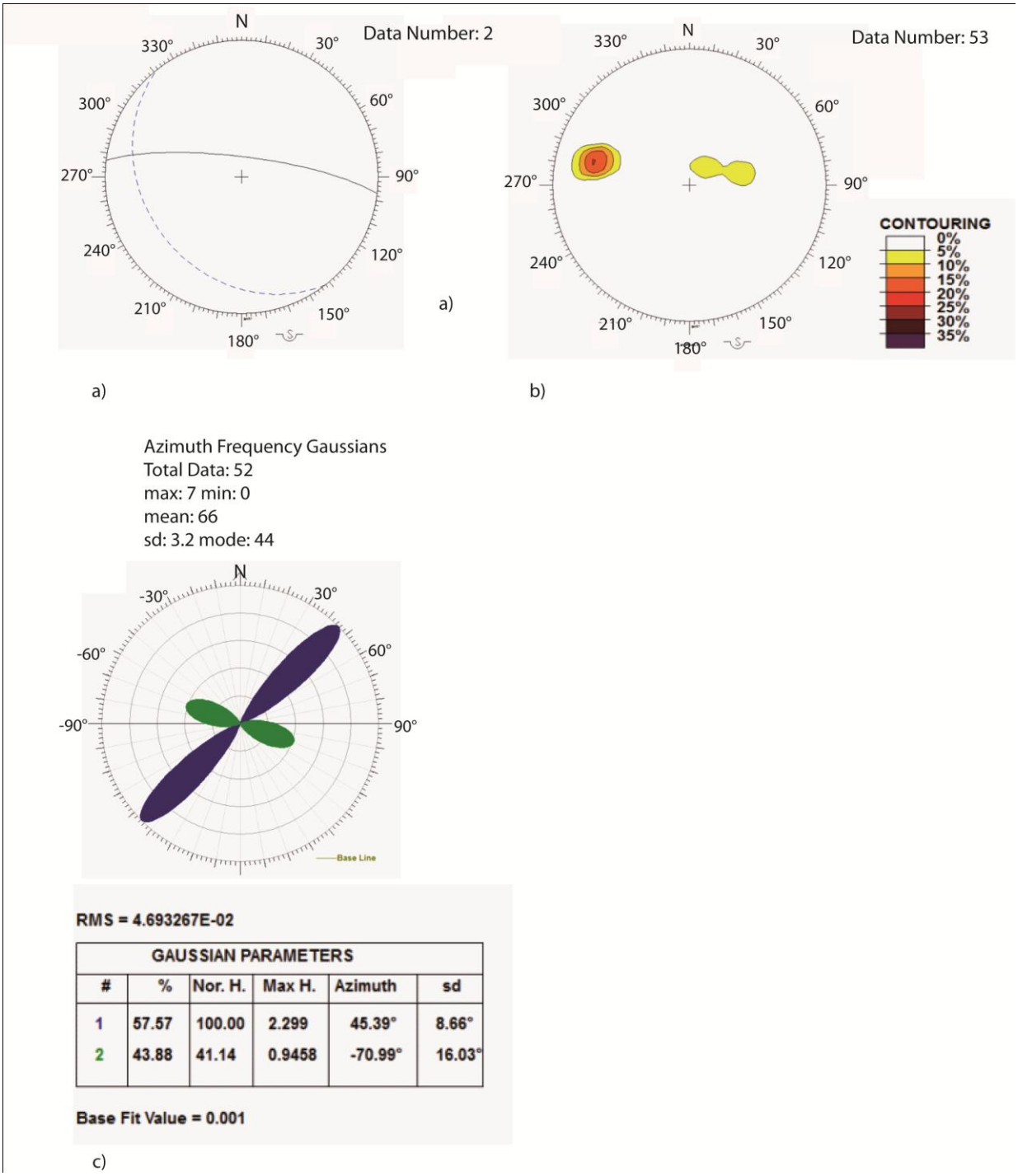

Fig. 5.23 – Structural data analysis of the Tornimparte 2 fault. a) Fault and bedding stereoplot; b) FRD rotax contour; c) FRD azimuth rose diagram

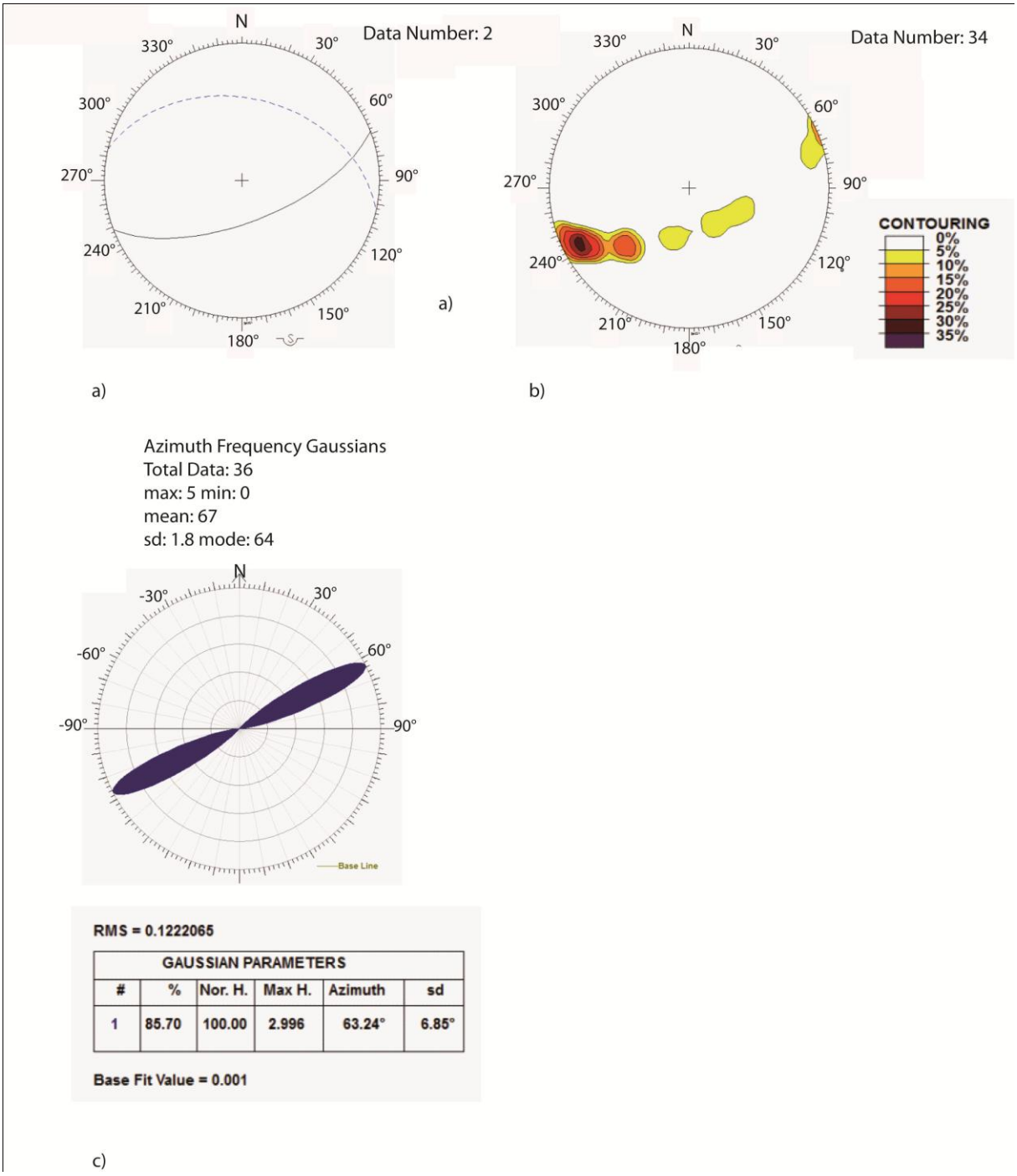

Fig. 5.24 – Structural data analysis of the Rocca di Cave 3 fault. a) Fault and bedding stereoplot; b) FRD rotax contour; c) FRD azimuth rose diagram

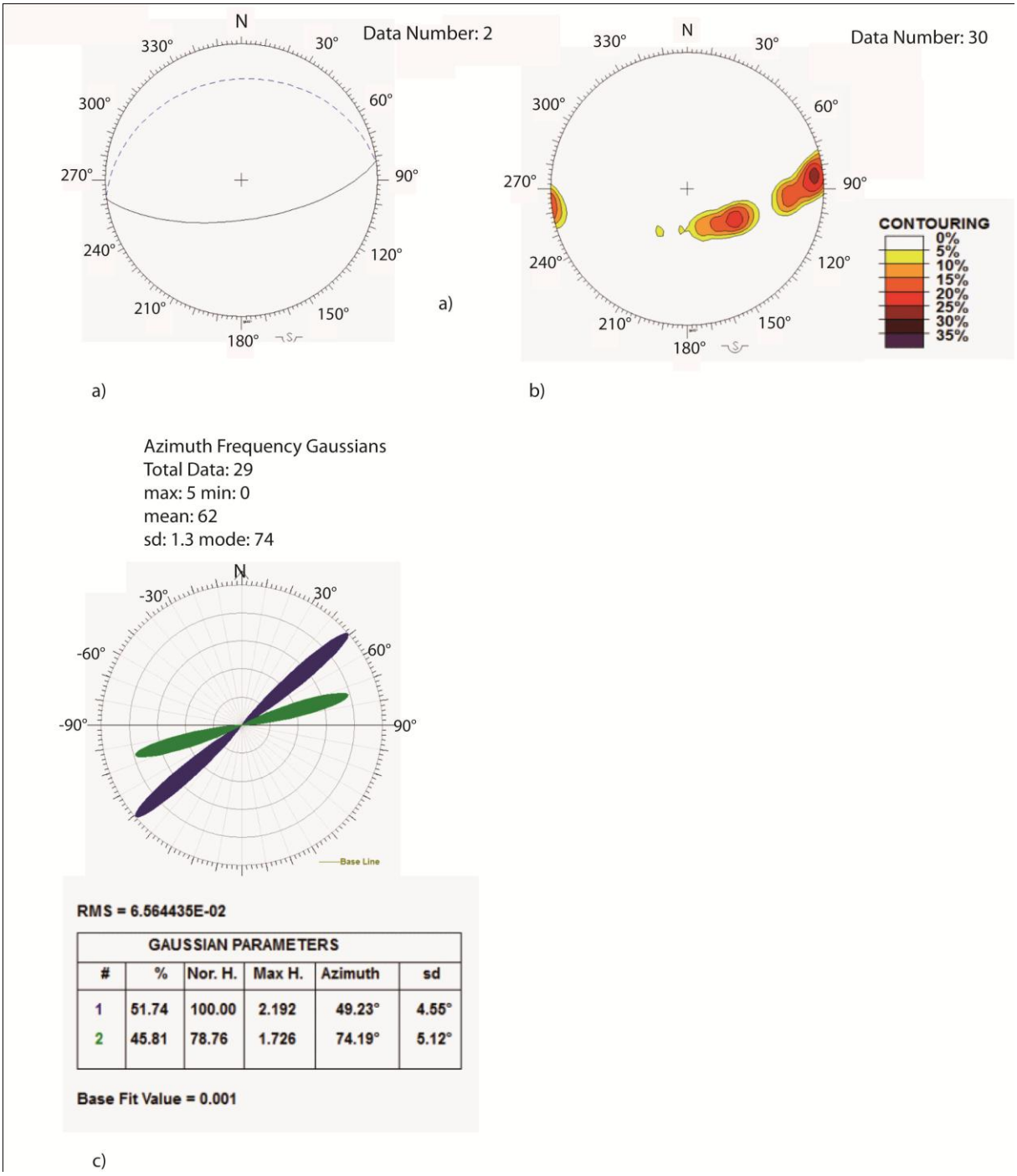

Fig. 5.25 – Structural data analysis of the Tornimparte 4 fault. a) Fault and bedding stereoplot; b) FRD rotax contour; c) FRD azimuth rose diagram

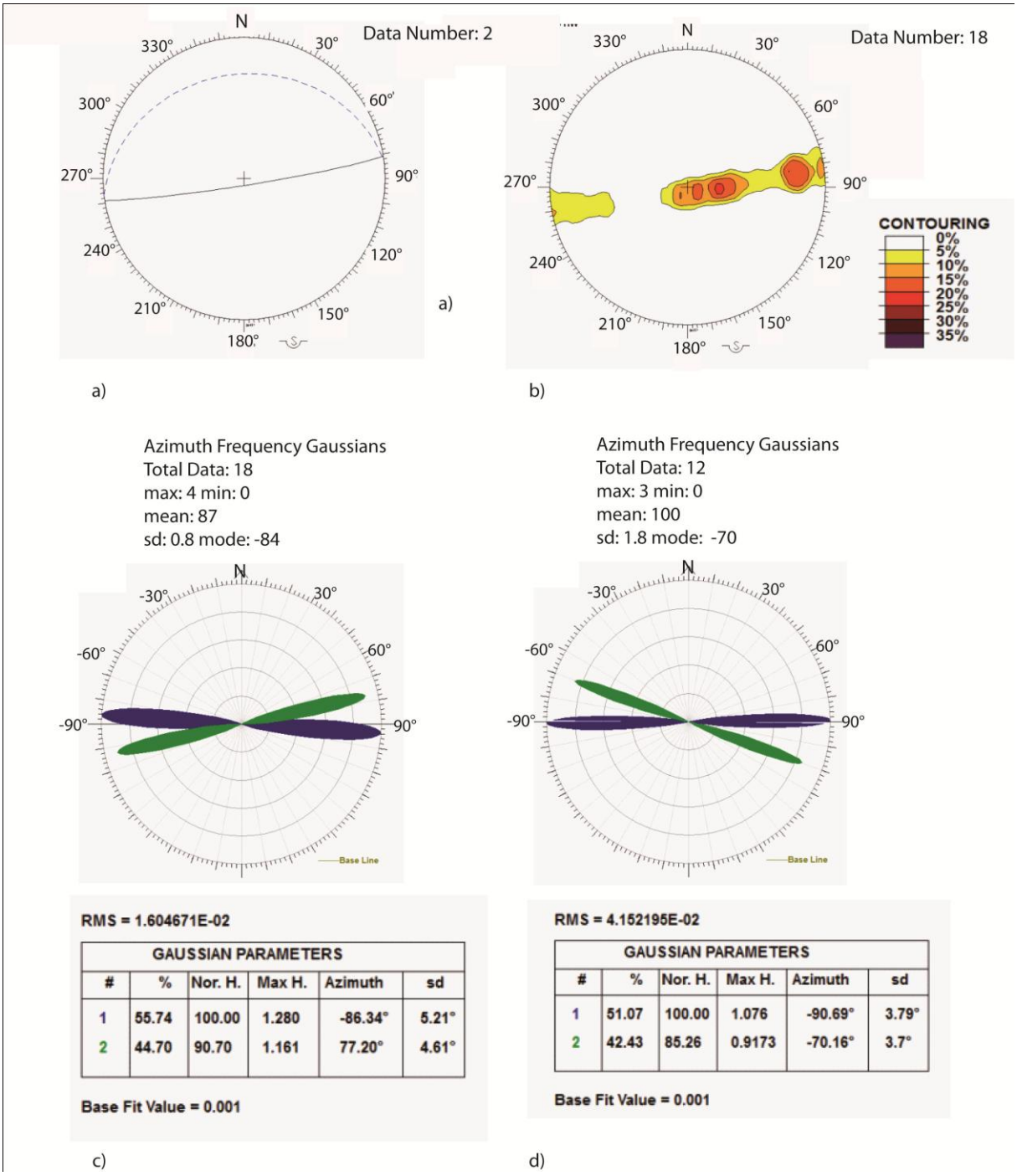

Fig. 5.26 – Structural data analysis of the Tornimparte 5 fault. a) Fault and bedding stereoplot; b) FRD rotax contour; c) FRD azimuth rose diagram; d) RRD azimuth rose diagram

5.1.4 Fucino Basin

A total number of 2 faults have been studied in the Fucino area: **Lecce dei Marsi 1 fault** and **Lecce dei Marsi 2 fault** (Fig. 5.28).

Both the faults are located on well stratified micritic carbonates Lower Cretacic in age and belonging of platform environments. The average bed thickness is 0.4 m. The development of both faults is related to the post-orogenic extension of the area, which causes the development of Fucino Basin (Fig. 3.2). The expected deformation age was 3 Ma.

The **Lecce dei Marsi 1** is a subseismic scale fault located on the hangingwall of the master fault Lecce dei Marsi 2. It strikes N 154°, 81° (Fig. 5.31 a). The rose diagram shows the presence of one main fault related fracturing system, oriented N-S (Fig. 5.31 c). The rotax analysis (Fig. 5.31 b) is almost horizontal (10°), suggesting a pure-dip movement. The fault does not show a fault-core (Fig. 5.29). The extensional fractures are predominant on pressure-solution cleavage.

The **Lecce dei Marsi 2** is a seismic scale normal fault, located along the south-eastern margin of the Fucino Basin. The fault strikes N 190°, 70° (Fig. 5.33 a). The rose diagram shows the presence of several fracture systems (Fig. 5.33 c). The rotax analysis shows a value of 10°, suggesting a prevalent dip movement for this fault. The deformation pattern is characterized by an intense pressure-solution cleavage nearby the fault plane, which frequency decrease with the distance from the master fault plane. The fault hangingwall appears more deformed than the footwall. The fault shows a non-continuous recemented fault-core, which average value is 1.79 m (Fig. 5.30).

The regional deformation is characterized by 4 main fracture systems (Fig. 5.32). The most frequent has the same orientation of the main regional lineament.

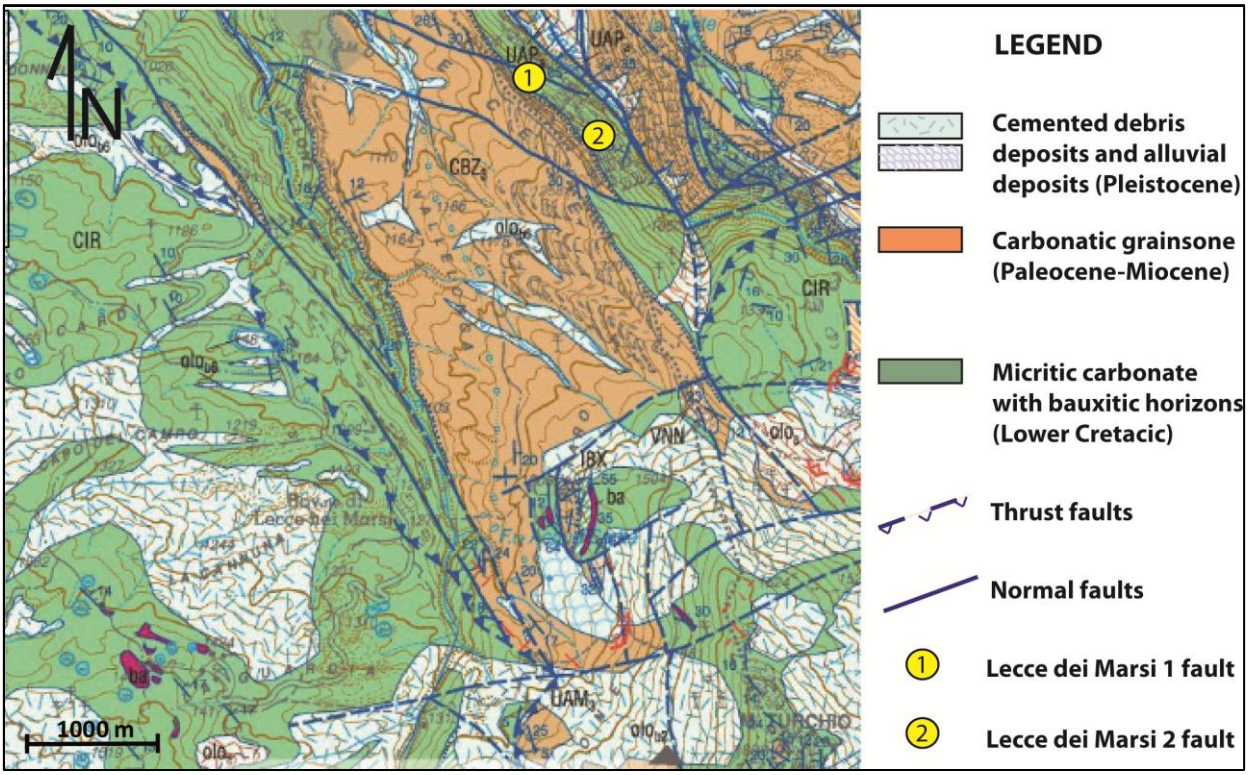

Fig. 5.28 – Geological map Fucino Basin area and location of Lecce dei Marsi 1 and Lecce dei Marsi 2 faults (Modified from "Carta geologica d'Italia 1:50000, Foglio SCANNO – 378)

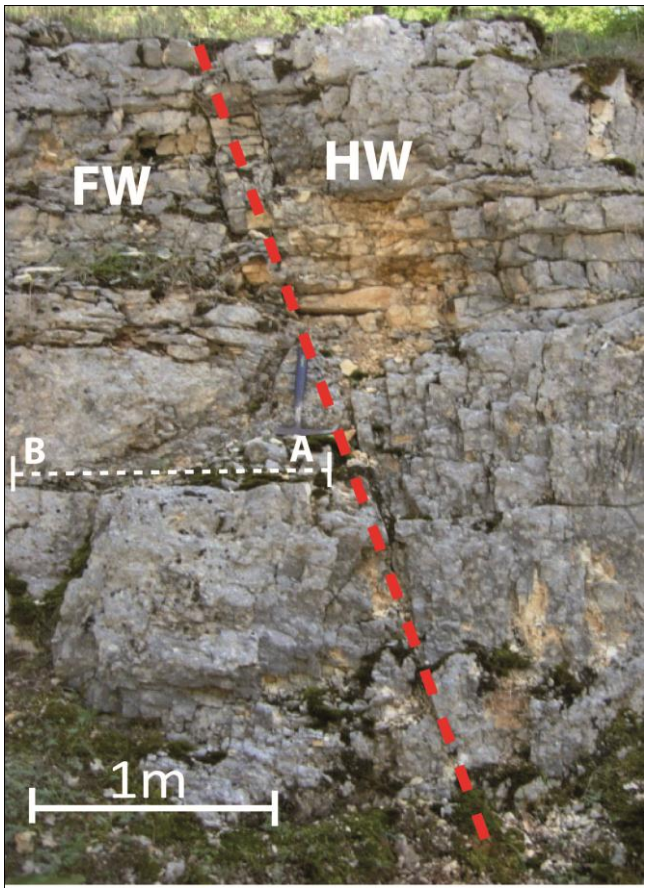

Fig. 5.29 Lecce dei Marsi fault; the red dashed lines correspond to the master fault planes; HW and FW are the fault hangingwall and footwall respectively; the yellow lines are the fault-core boundaries (FC); the white dashed line correspond to the trace of the scan line (A-B)

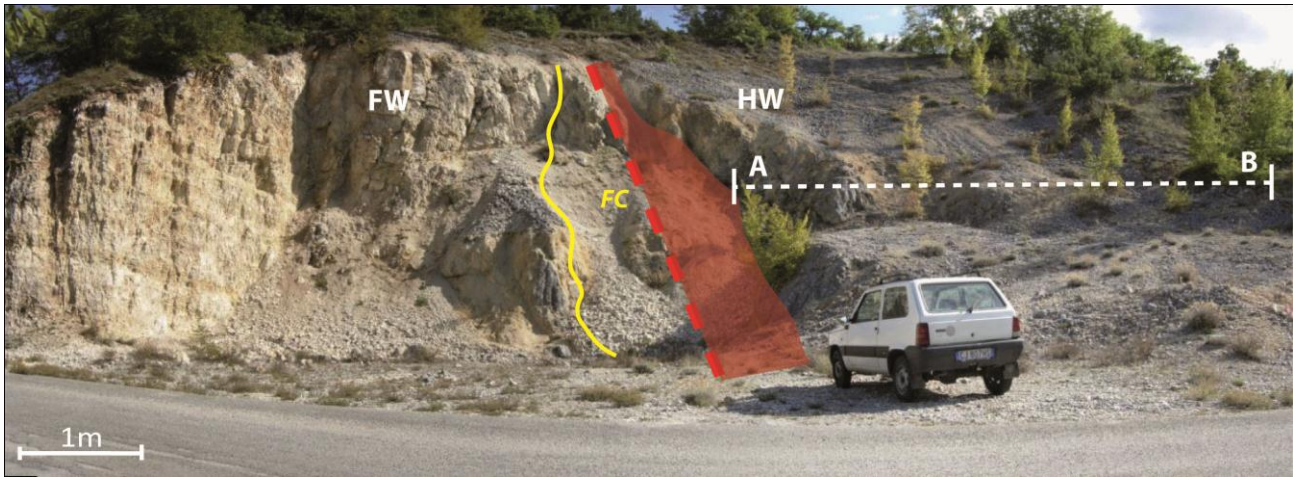

Fig. 5.30 Lecce dei Marsi 2 fault; the red dashed lines correspond to the master fault planes; HW and FW are the fault hangingwall and footwall respectively; the yellow lines are the fault-core boundaries (FC); the white dashed line correspond to the trace of the scan line (A-B)

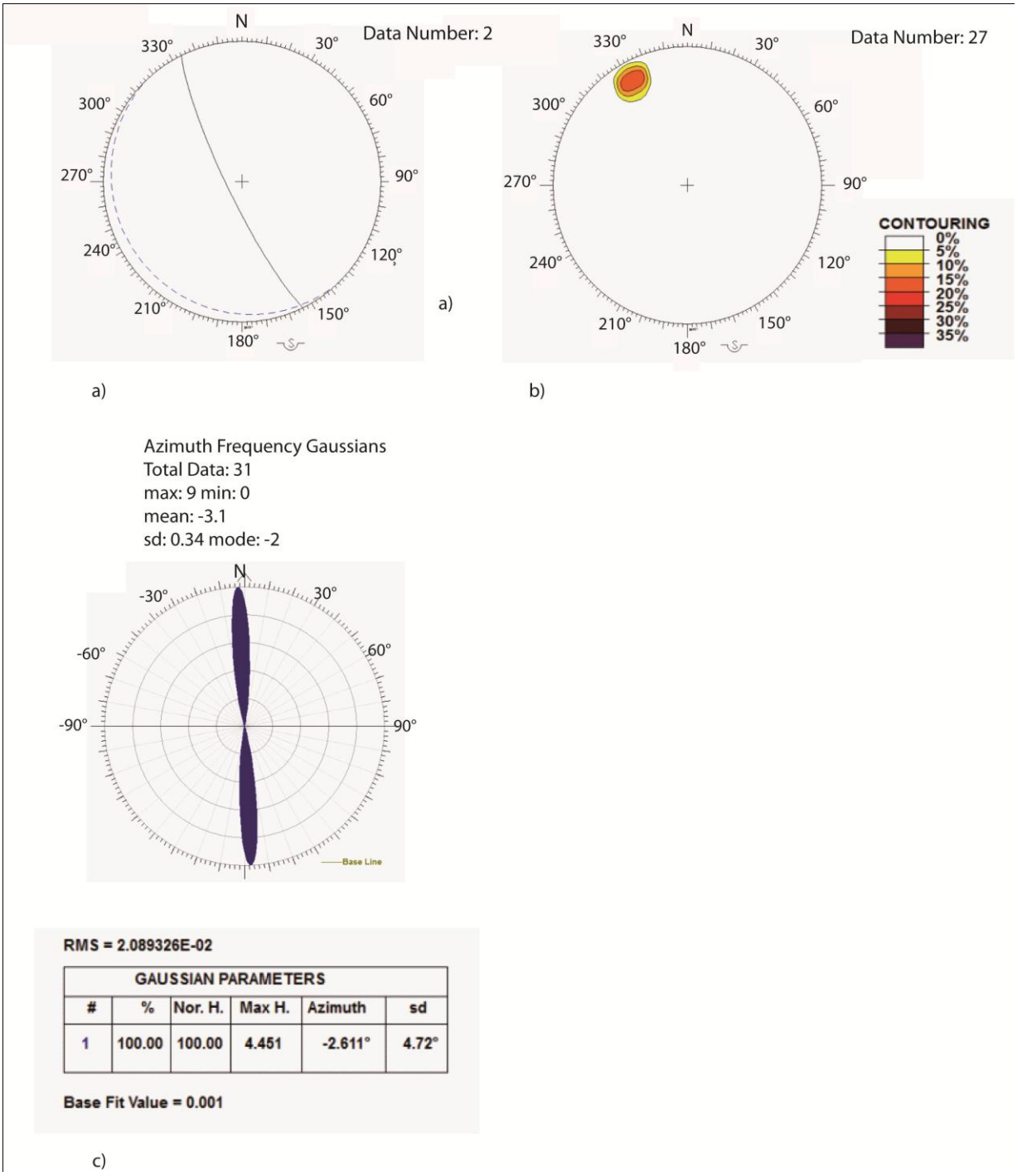

Fig. 5.31 – Structural data analysis of the Lecce dei Marsi 1 fault. a) Fault and bedding stereoplot; b) FRD rotax contour; c) FRD azimuth rose diagram

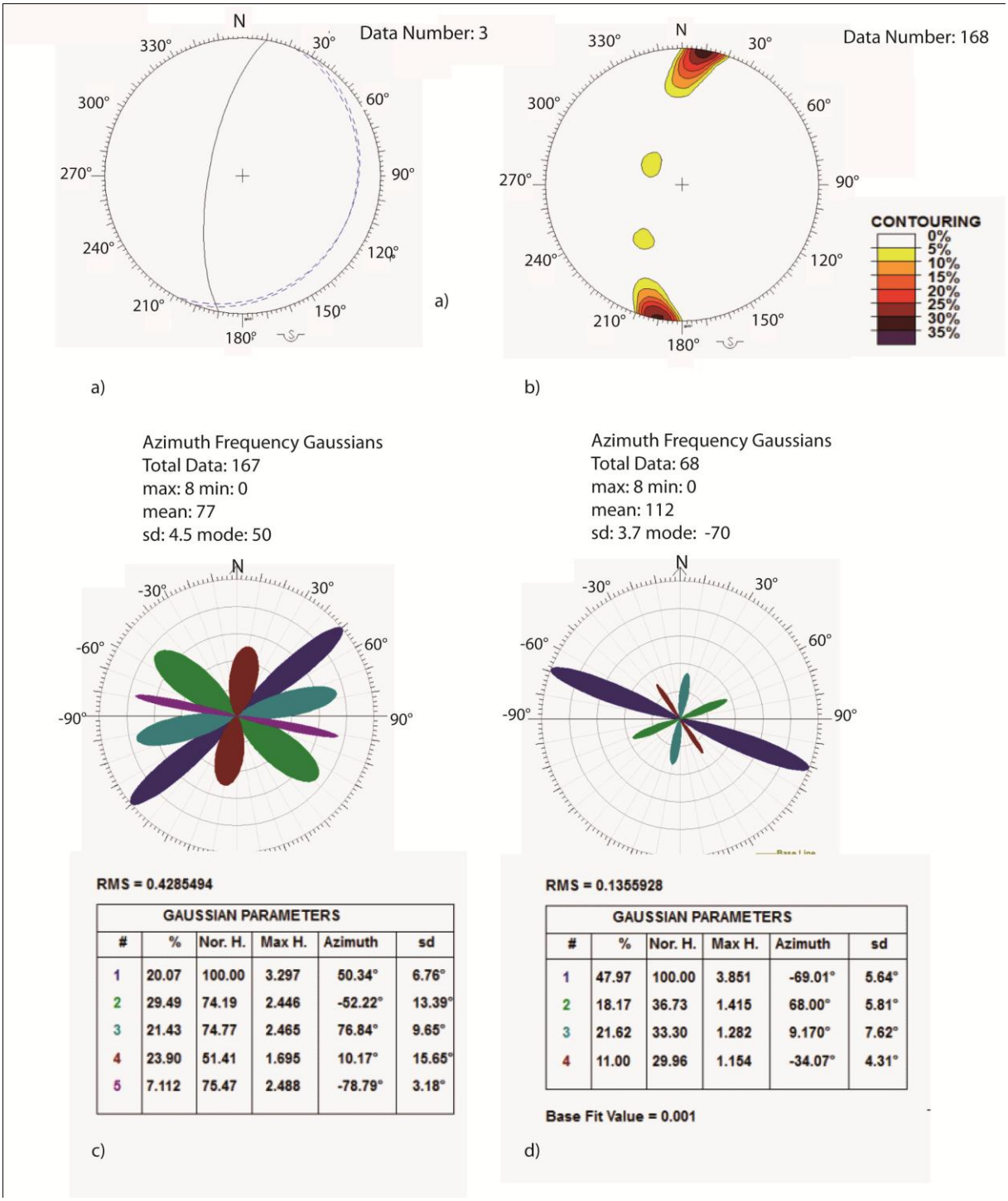

Fig. 5.32 – Structural data analysis of the Lecce dei Marsi 2fault. a) Fault and bedding stereoplot; b) FRD rotax contour; c) FRD azimuth rose diagram; d) RRD azimuth rose diagram

5.1.5 Sagittario Gully

The Sagittario fault is a seismic scale fault located on shallow marine carbonate limestone Jurassic in age (Fig. 5 .33). In particular, the Sagittario fault developed within this strike-slip brittle shear zone, initially as normal fault and then was reactivated with a left lateral component (Billi et al., 2003). This favoured karst erosion and the development of the Sagittario Gully.

The rocks are well stratified with an average thickness of 0.5 m. The master slip surface strikes N 135°, 53° (Fig. 5.35 a) and is fully exposed for approximately 50 m along-strike, and up to 25 m across-strike in the Cava di Rena quarry. The master fault surface bounds the fault-core on the hangingwall, which thickness is 12 m and it is characterized by a rock intensely cataclasited (Fig. 5.34). On the other side, the fault-core grades upward into the damage zone. The footwall shows no extension-related damage, but preserves a well- developed fracture pattern inherited from previous thrust and strike-slip faulting. The expected fault deformation age was contemporary to the main fault thrust movement (10 Ma.) The rose diagram shows four main fracture systems. The more frequent system strikes NE-SW (Fig. 5.35 c). The rotax analysis of the riddle planes shows two main values (Fig. 5.35 b). The 40° value is related to the strike-slip movement, while the 0° value is related to the dip movement of the faults. The regional deformation strikes NE-SW (Fig. 5.35 d).

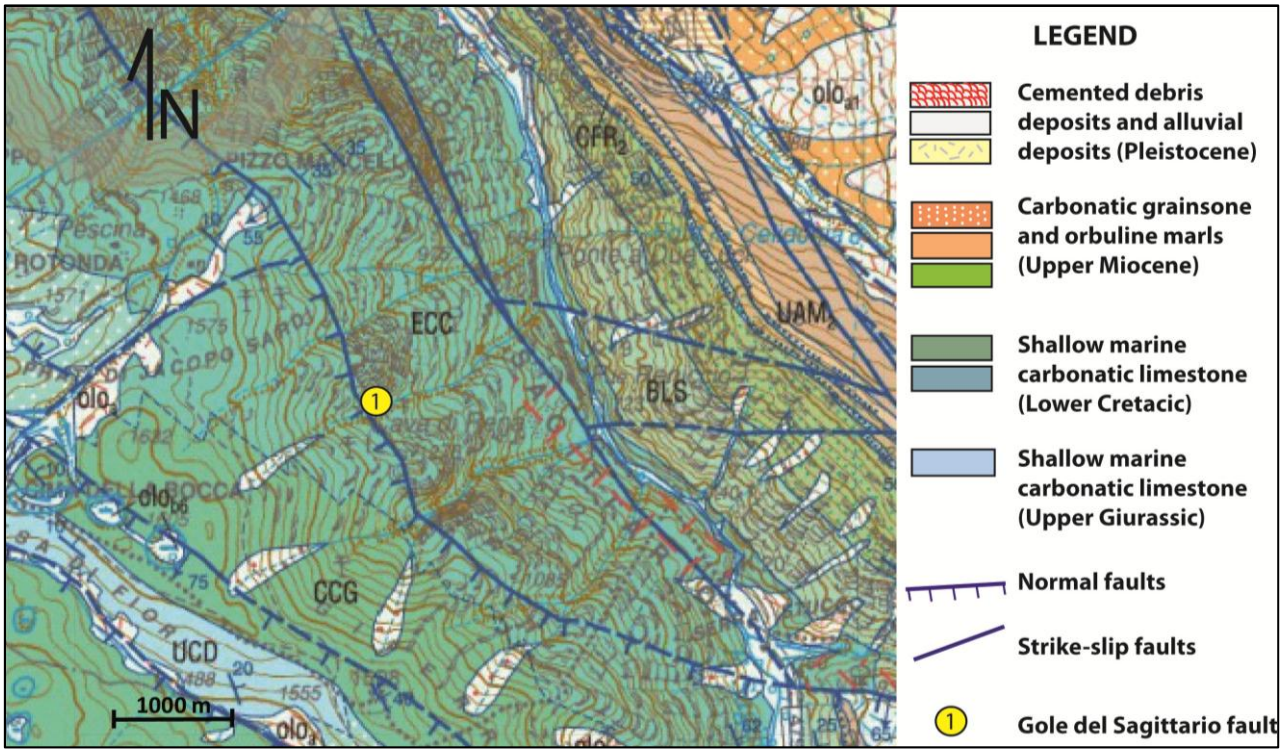

Fig. 5.33 – Geological map of Sagittario Gully area. (Modified from "Carta geologica d'Italia 1:50000, Foglio SCANNO - 378)

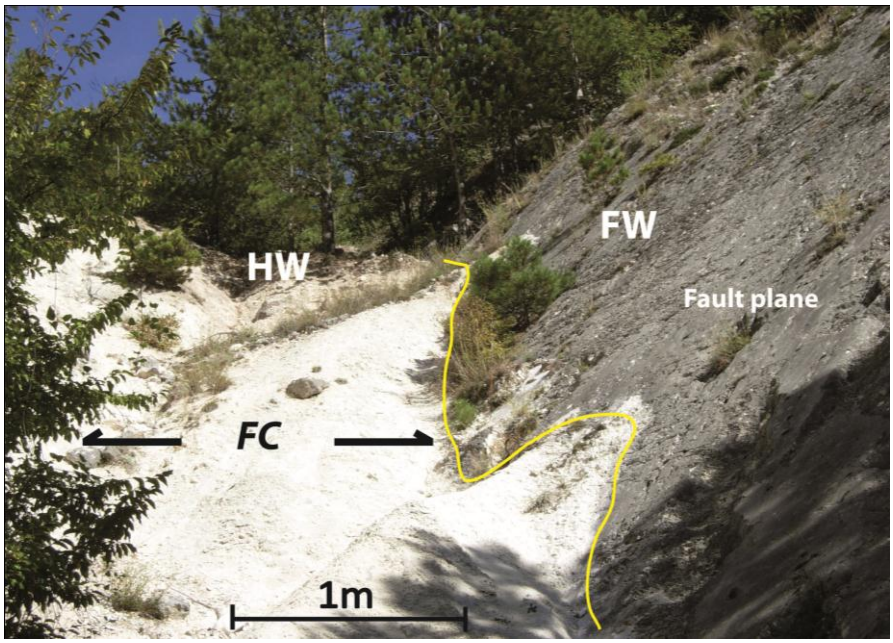

Fig. 5.34 - Gole del Sagittario fault; the yellow line corresponds to the limit between the fault-core (FC) and the fault plane; HW and FW are the fault hangingwall and footwall respectively

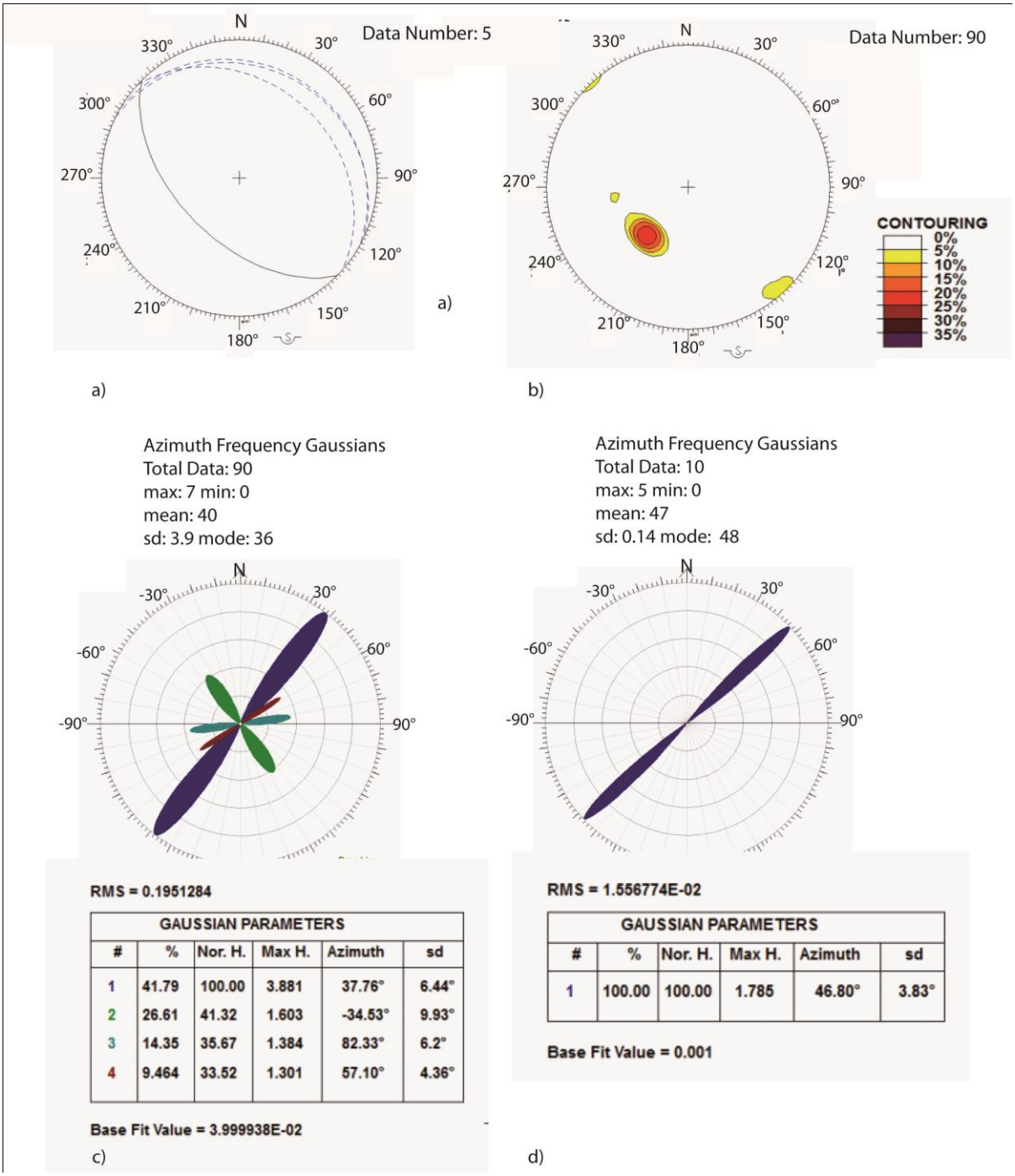

Fig. 5.35 – Structural data analysis of the Sagittario fault. a) Fault and bedding stereoplot; b) FRD rotax contour; c) FRD azimuth rose diagram; d) RRD azimuth rose diagram

5.1.6 Subequana Plain

Castel di Ieri fault is a seismic scale fault located between the villages of Goriano Sicoli and Castel di Ieri (Fig. 5.36). In an abandoned quarry a very good exposure of fault hangingwall can be observed. The fault is located on the carbonate limestone and grainstone of platform-basin transition depositional environment, Lower Cretacic in age. The rocks are well stratified and the average bed thickness is 0.3 m. The deformation of the fault occurred at superficial level and the expected fault age is 3 Ma. The fault strikes is N 146°, 46° (Fig. 5.38 a) and the footwall damage-zone is intensely fractured and is dislocated by several number of secondary faults. The abundance pressure-solution cleavage suggests an intense fluid circulation. The more frequent FRF system strikes NW-SE (Fig. 5.38 c). The rotax analysis of shear planes shows two main values (Fig. 5.38 b). The 10° value is related to a prevalent dip-movement, while the 30° value is related to a lateral movement. The fault-core is continuous and recemented, and its thickness is 3 m (Fig. 5.37). The main regional related fracturing set strikes NE-SE (Fig. 5.38 d).

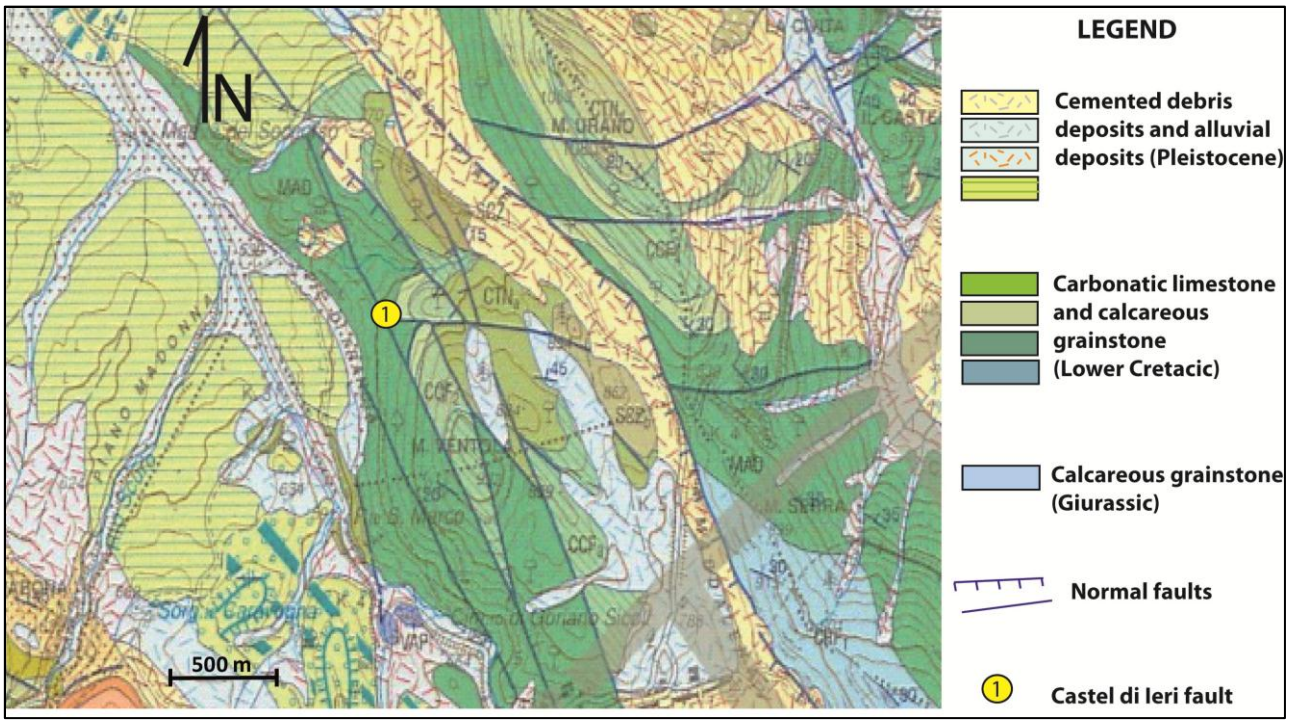

Fig. 5.36 – Geological map of Subequana Plain and location of Castel di Ieri fault (Modified from "Carta geologica d'Italia 1:50000, FOGLIO L'Aquila - 359)

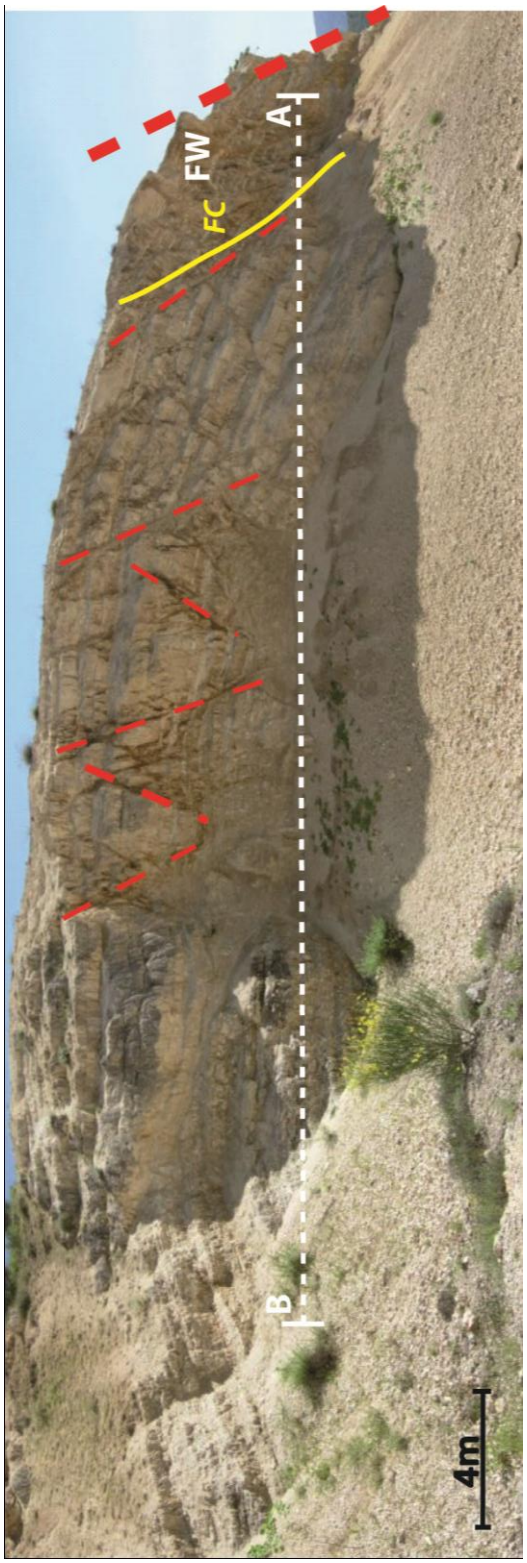

Fig. 5.37 - Castel di Ieri fault; the red dashed lines correspond to the master fault planes; HW and FW are the fault hangingwall and footwall respectively; the yellow lines are the fault-core boundaries (FC); the white dashed line correspond to the trace of the scan line (A-B)

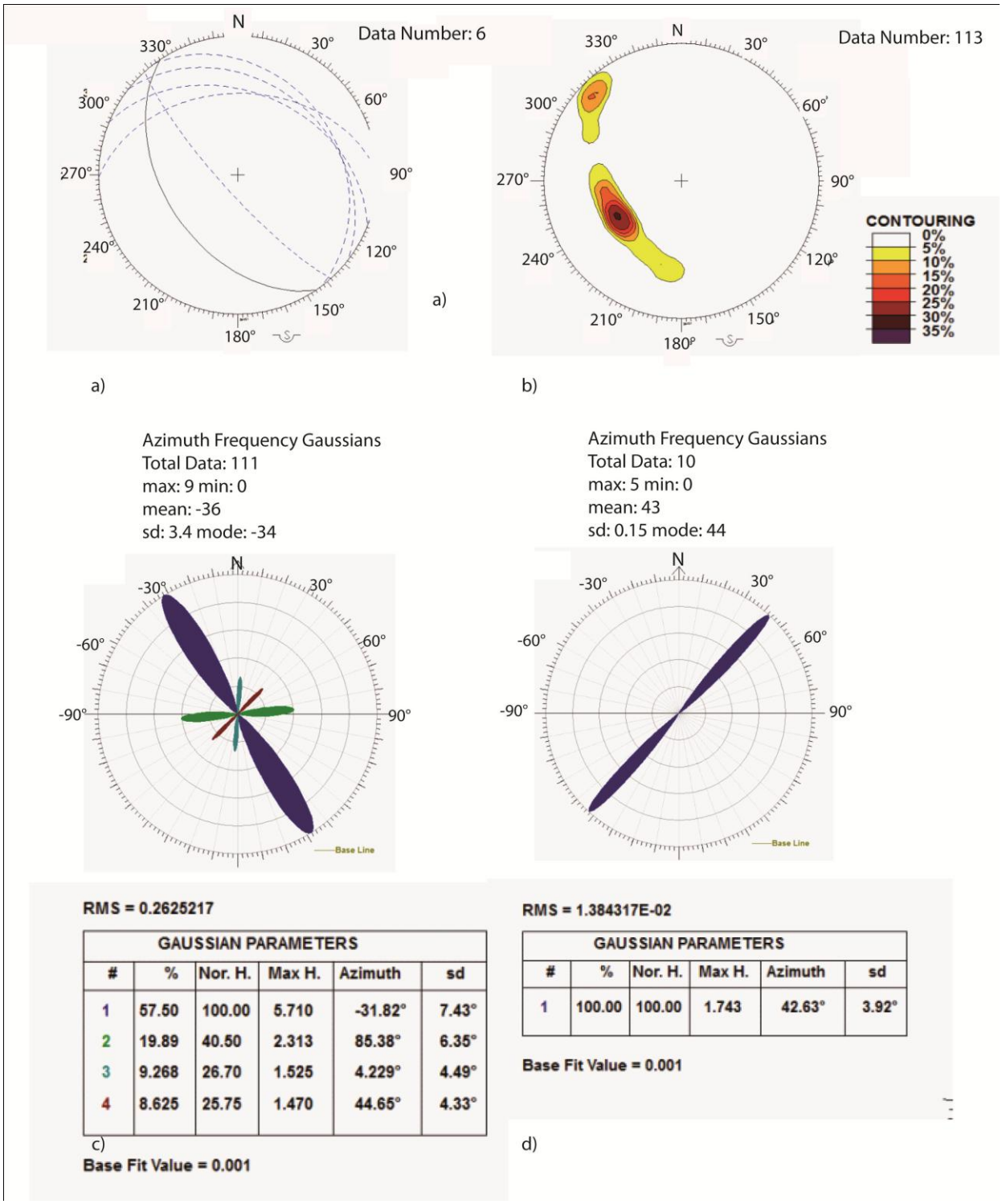

Fig. 5.38 – Structural data analysis of the Castel di Ieri fault. a) Fault and bedding stereoplot; b) FRD rotax contour; c) FRD azimuth rose diagram; d) RRD azimuth rose diagram

5.1.7 Maiella Mountain

A total of 7 faults have been studied in two different areas of Maiella structure (Fig. 3.2). The expected age of deformation is 20 Ma for all the faults of the Maiella area, which correspond to the age of thrust sheet movement.

A total of 5 subseismic faults have been studied on the front of the anticline, near the village of Fara S. Martino, in the Santo Spirito Valley (Fig. 5.39**): Fara 1 faults**, **Fara 2 faults**, **Fara 3 faults, Fara 4 fault**, and **Fara 6 faults**. This Valley provides many vertical outcrops of normal-strike slip faults of different scales that formed through mechanical processes strictly in a compressional regime (Graham et al., 2003). These faults are located on carbonatic wackestone-packstone rocks of platform depositional environment. Along the thrust front the beds plunge from 30° to 85° and strike N-S. The average bed thickness is 0.5-0.7 m in this area.

Fara 1 fault attitude is N 188°, 31° (Fig. 5.46 a). This fault is characterized by two main fracture systems striking NW-SW and N-S respectively (Fig. 5.46 c). The rotax plunges 10° and suggests a dip-slip movement (Fig. 5.46 b). The Fara 2 fault attitude is N 353°, 72° (Fig. 5.47 a). Two main fracture systems are related to fault, striking NW-SE and NE-SW (Fig. 5.47 c). The rotax plunges 45° (Fig. 5.47 b), suggesting a prevalent strike-slip movement. The Fara 3 fault attitude is N 312°, 89° (Fig. 5.48 a). The rose diagram shows the presence of three main fracture systems (Fig. 5.48 c). The NE-SW-1 and the NE-SW-2 are related to fault. The rotax plunges 80° (Fig. 5.48 b), suggesting a prevalent strike-slip movement. The Fara 4 fault attitude is N 183°, 46° (Fig. 5.49 a). Only one fracture system has been measured (Fig. 5.49 c). The rotax value is 30° (Fig. 5.48 b), suggesting a prevalent normal movement of the fault. The Fara 6 fault attitude is N 164°, 61° (Fig. 5.50 a). Three main fracture systems have been measured. The NW-SE-2 and the NE-SW systems are related to fault (Fig. 5.50 c). The rotax plunges 30° (Fig. 5.50 b) and indicates a prevalent dip movement of the fault. Fara 2 fault, Fara 3 fault, Fara 4 fault, and Fara 6 fault do not show a developed fault-core. They show only some little lenses that could be related to stress concentration due to the local asperities of fault plane. The Fara 1 fault shows a developed non-continuous fault-core, which lenses dimension vary from 0.10 to 0.30 m.

The other 2 faults**: Palena 3** and **Palena 4** are located near Palena village on the carbonatic grainstone of carbonate ramp deposits, Miocene in age. The bed thickness is 0.7 m. Both the faults do not show the development of a fault-core. The faults are located on the backlimb of the main thrust system.

The Palena 3 fault attitude is N 152°, 63° (Fig. 5.51 a). The FRF system strikes NNW-SSE (Fig. 5.51 c). The rotax plunges 14° (Fig. 5.51 b), suggesting a prevalent dip-slip movement for this fault.

The Palena 4 fault attitude is N 273°, 70° (Fig. 5.52 a). The FRF system strikes NW-SE (Fig. 5.52 c). The rotax plunges 66° (Fig. 5.52 c), suggesting a prevalent strike-slip movement for this fault.

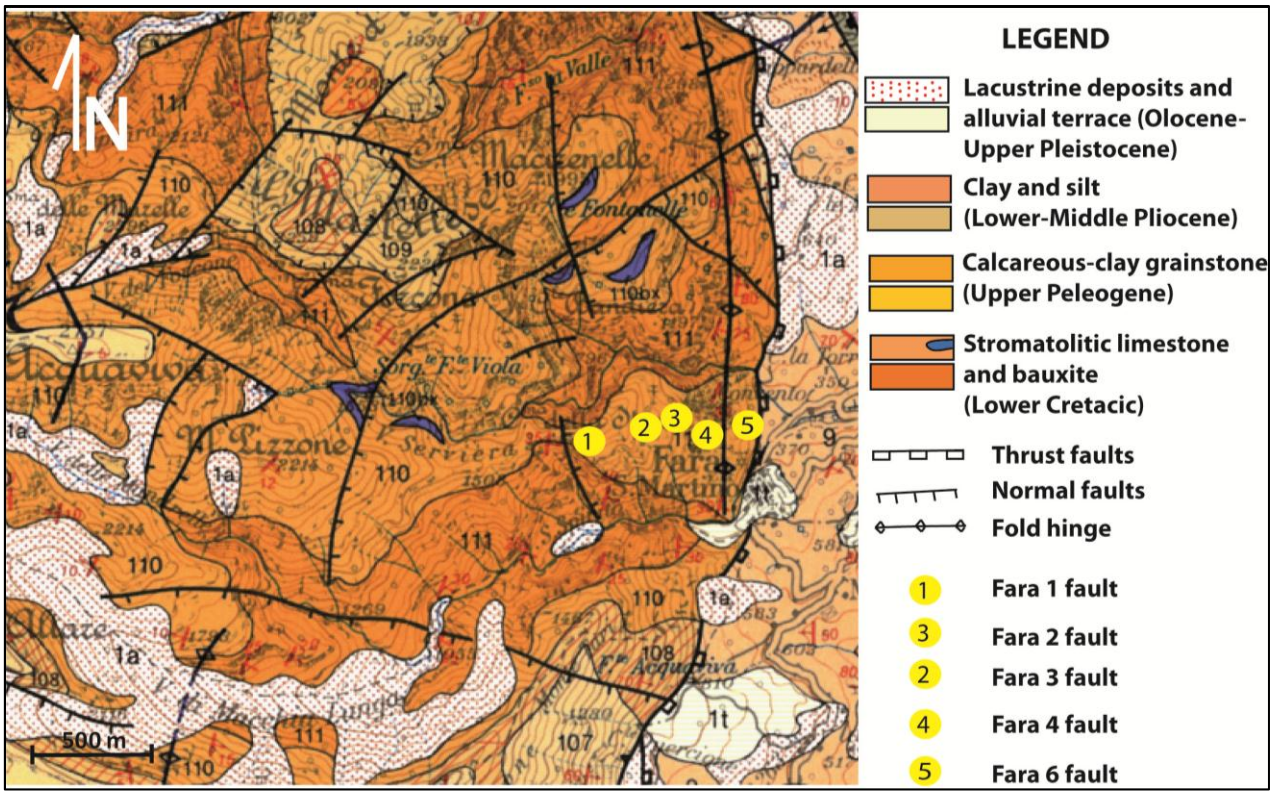

Fig. 5.39 – Geological map of Fara S. Martino area (Maiella Mnt. See Fig. 3.2) and location of Fara 1, Fara 2, Fara 3, Fara 4, and Fara 6 faults. (Modified from "Carta Geologica dell'Abruzzo" 1:100000, Vezzani et al. 1998)

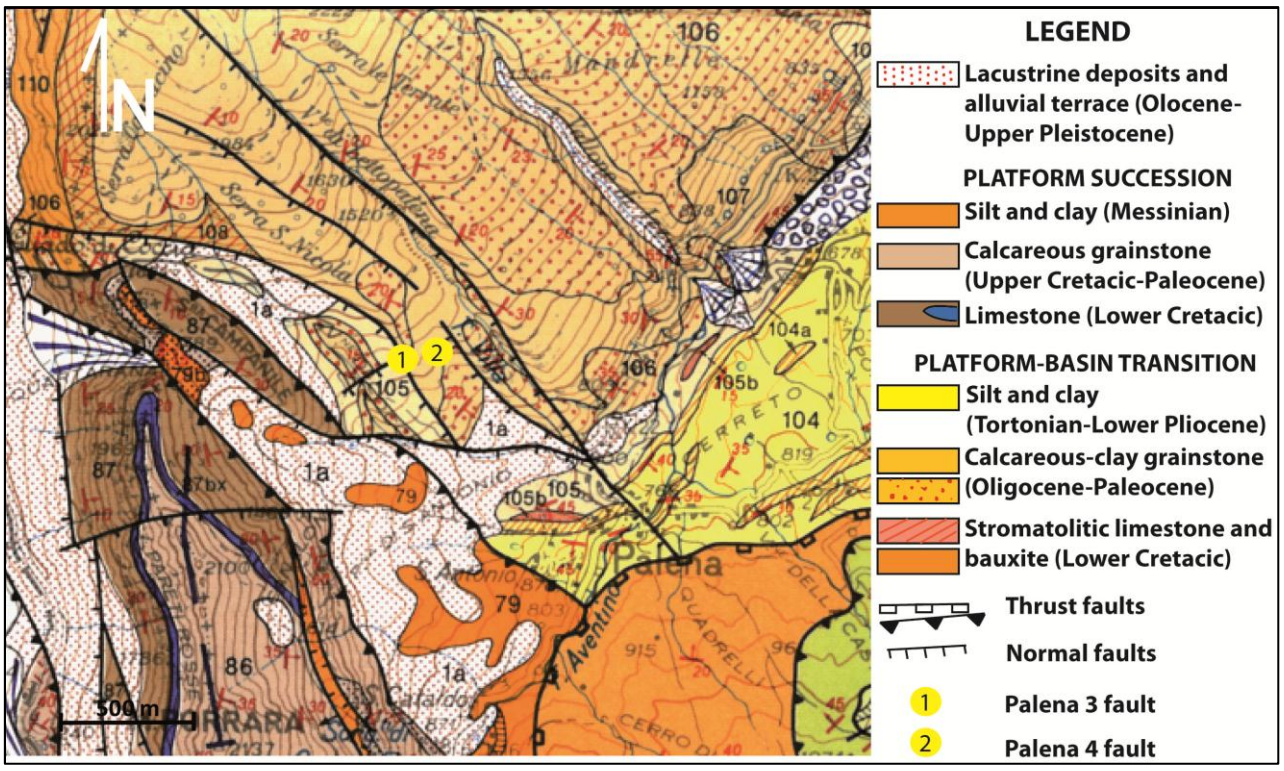

Fig. 5.40 – Geological map of Palena area and location of Palena 3 and Palena 4 faults (Maiella Mnt. See Fig. 3.2) (Modified from "Carta Geologica dell'Abruzzo" 1:100000, Vezzani et al. 1998)

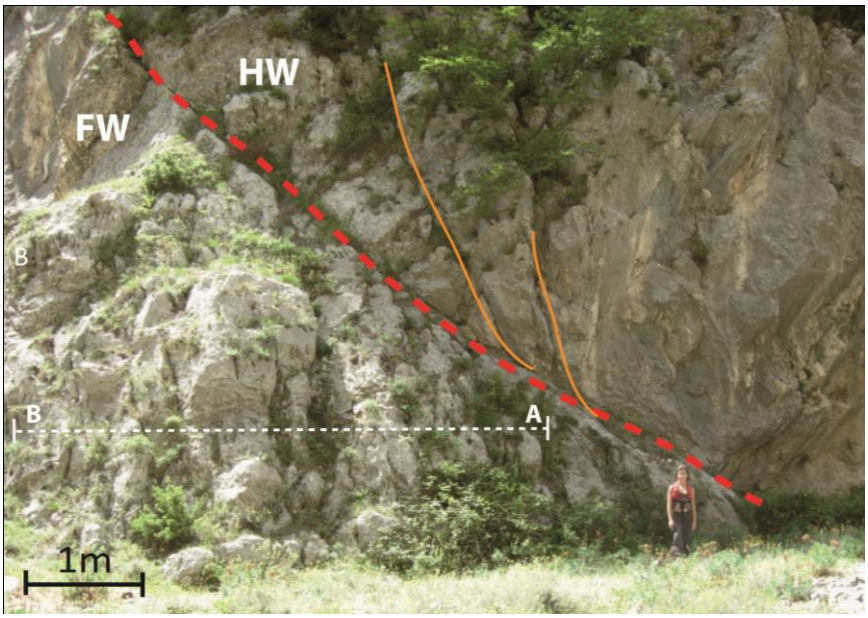

Fig. 5.41 - Fara 1 fault the red dashed lines correspond to the master fault planes; HW and FW are the fault hangingwall and footwall respectively; the orange lines are traces of synthetic planes; the white dashed line correspond to the trace of the scan line (A-B)

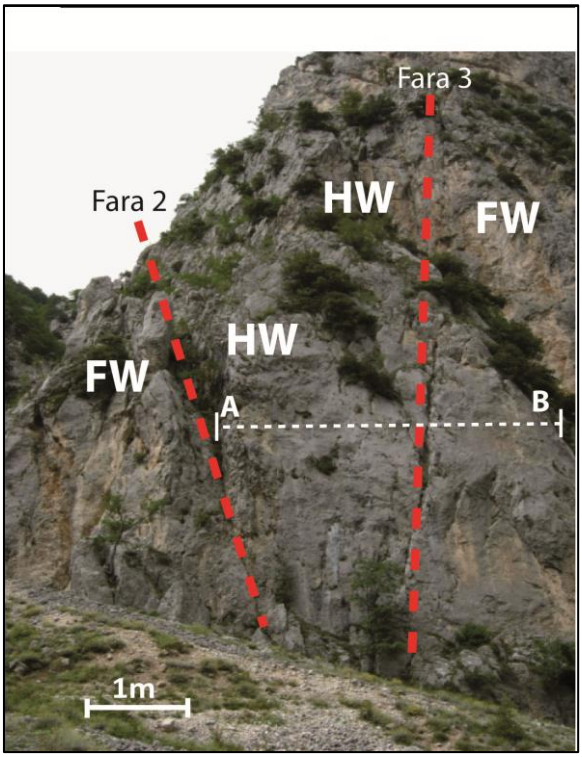

Fig. 5.42 - Fara 2 fault and Fara 3 fault the red dashed lines correspond to the master fault planes; HW and FW are the fault hangingwall and footwall respectively; the white dashed line correspond to the trace of the scan line (A-B)

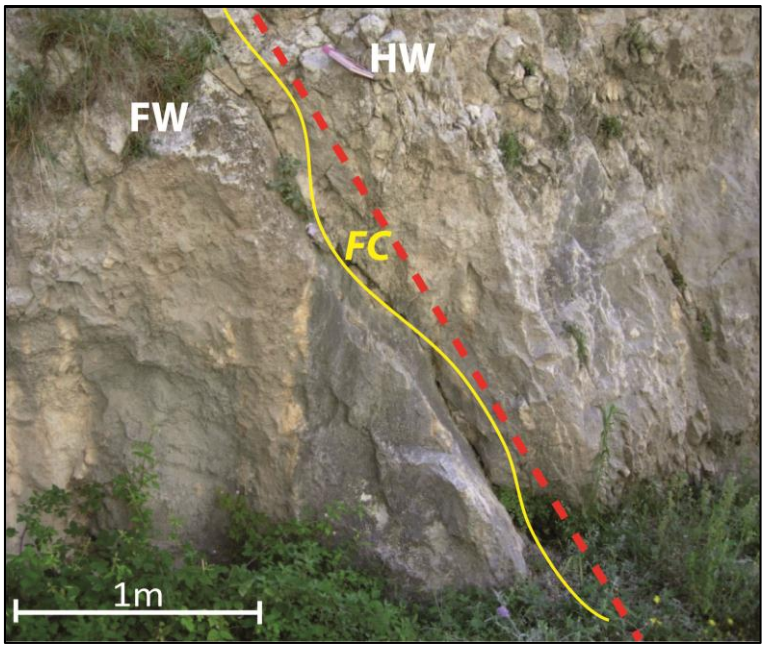

Fig. 5.43 - Fara 4 fault the red dashed lines correspond to the master fault planes; HW and FW are the fault hangingwall and footwall respectively; the yellow lines are the fault-core boundaries (FC); the white dashed line correspond to the trace of the scan line (A-B)

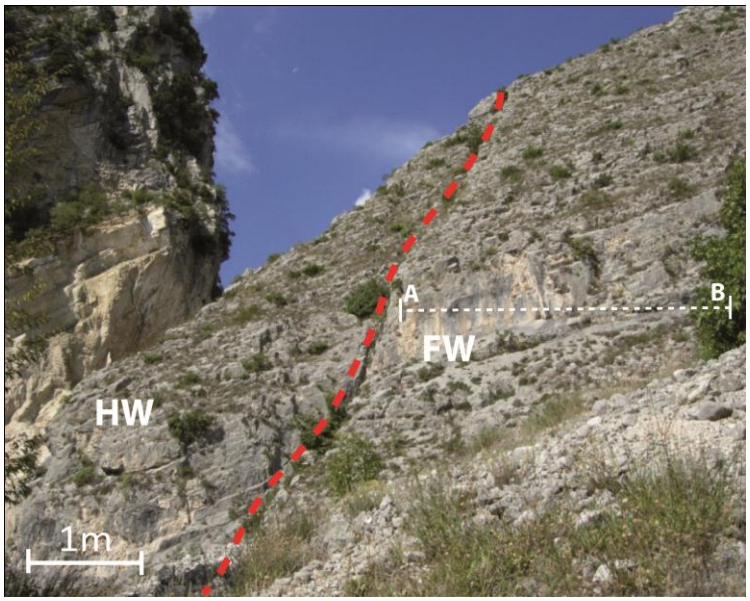

Fig. 5.44 - Fara 6 fault; the red dashed lines correspond to the master fault planes; HW and FW are the fault hangingwall and footwall respectively; the yellow lines are the fault-core boundaries (FC); the white dashed line correspond to the trace of the scan line (A-B)

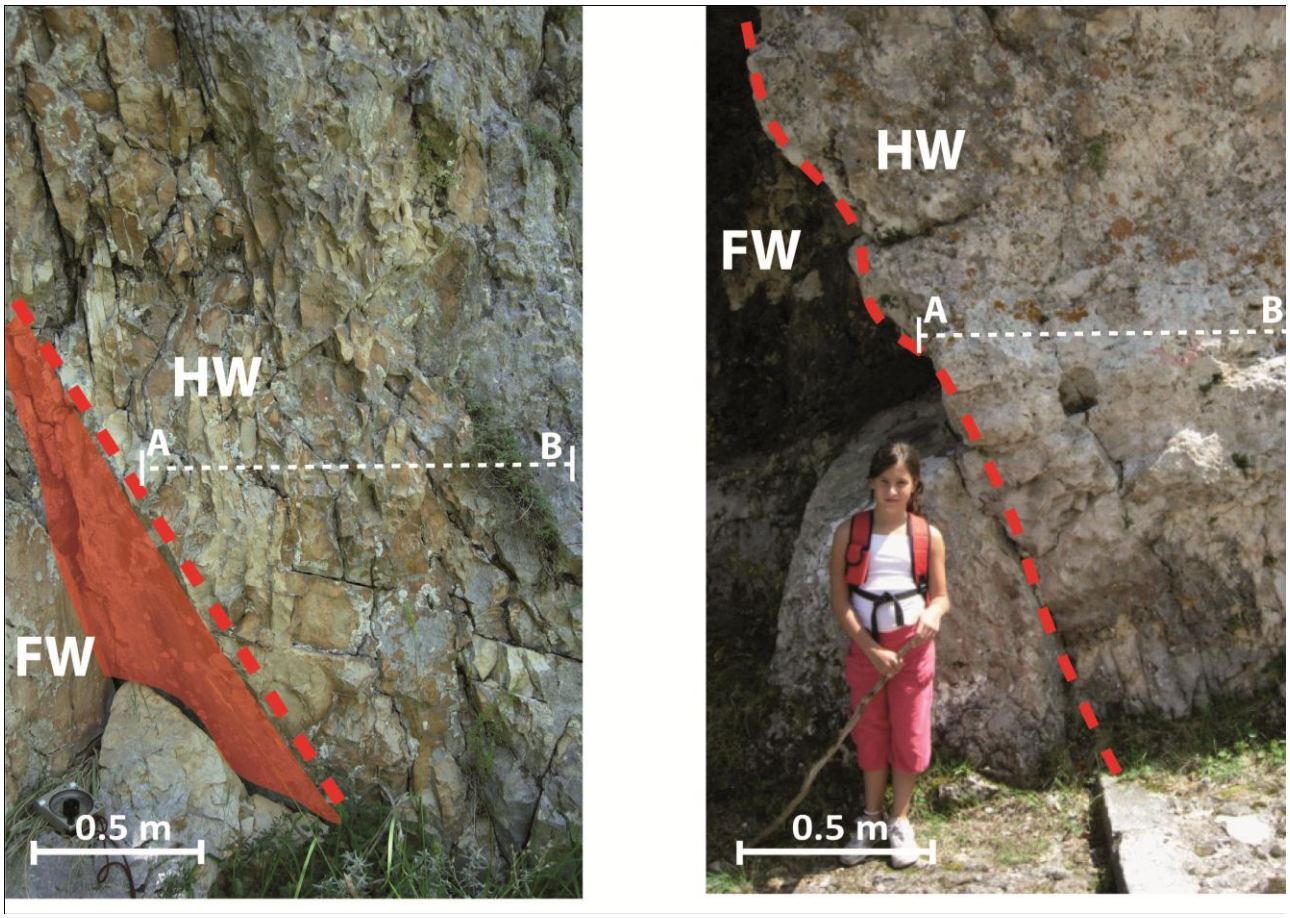

b)

Fig. 5.45 - Palena 3 fault (a) and Palena 4 fault (b); the red dashed lines correspond to the master fault planes; HW and FW are the fault hangingwall and footwall respectively; the white dashed line correspond to the trace of the scan line (A-B)

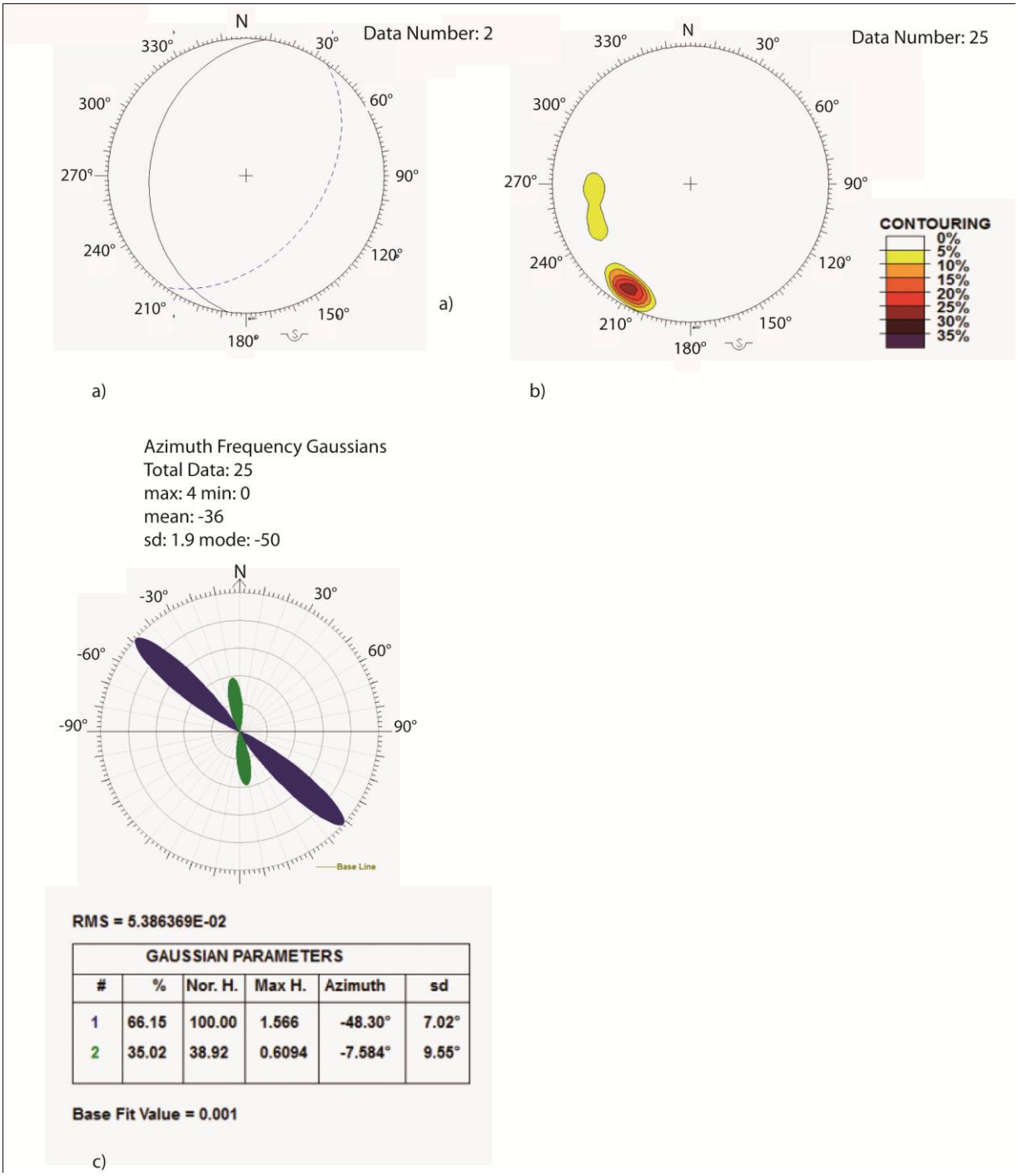

Fig. 5.46 – Structural data analysis of the Fara 1 fault. a) Fault and bedding stereoplot; b) FRD rotax contour; c) FRD azimuth rose diagram

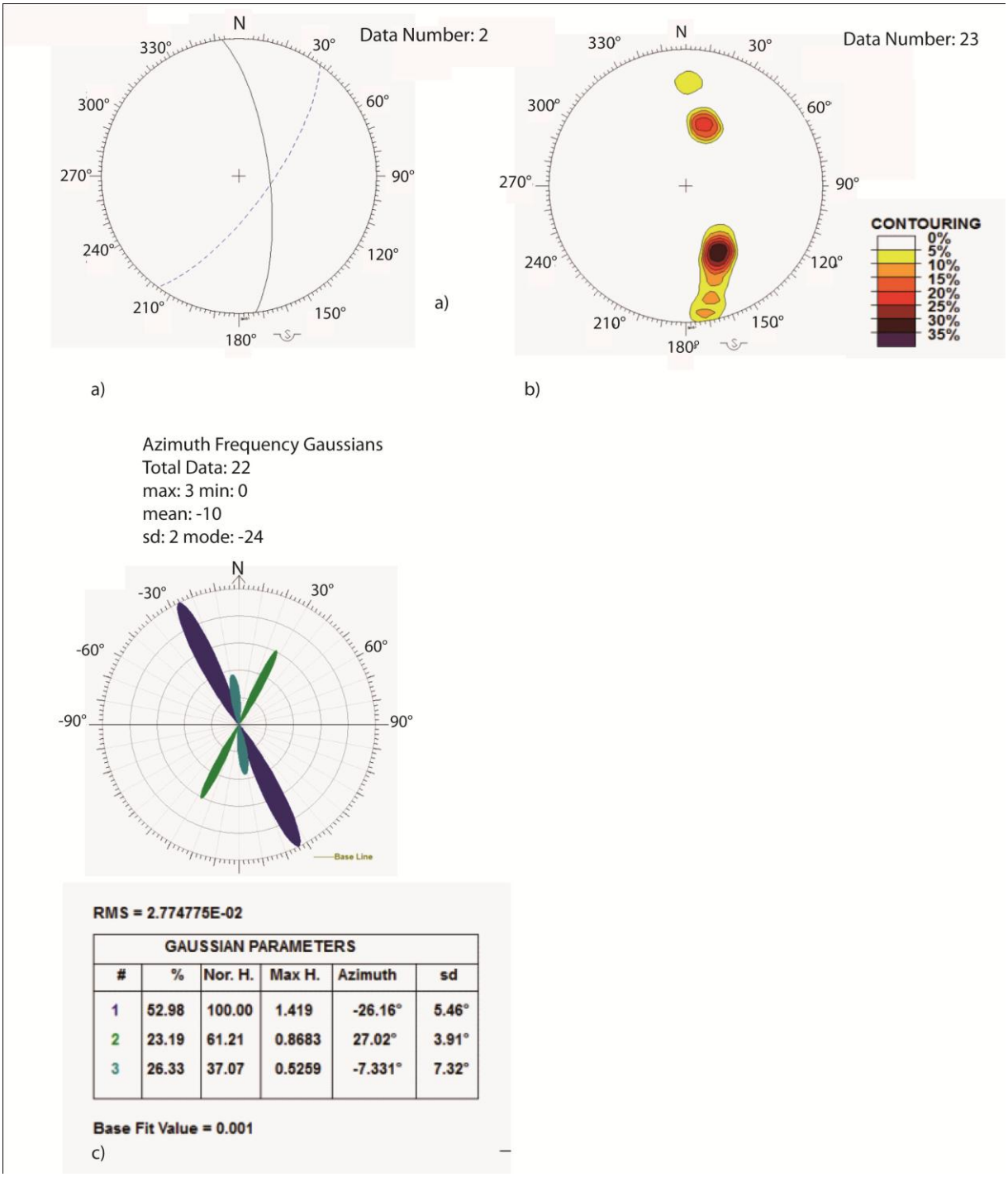

Fig. 5.47 – Structural data analysis of the Fara 2 fault. a) Fault and bedding stereoplot; b) FRD rotax contour; c) FRD azimuth rose diagram

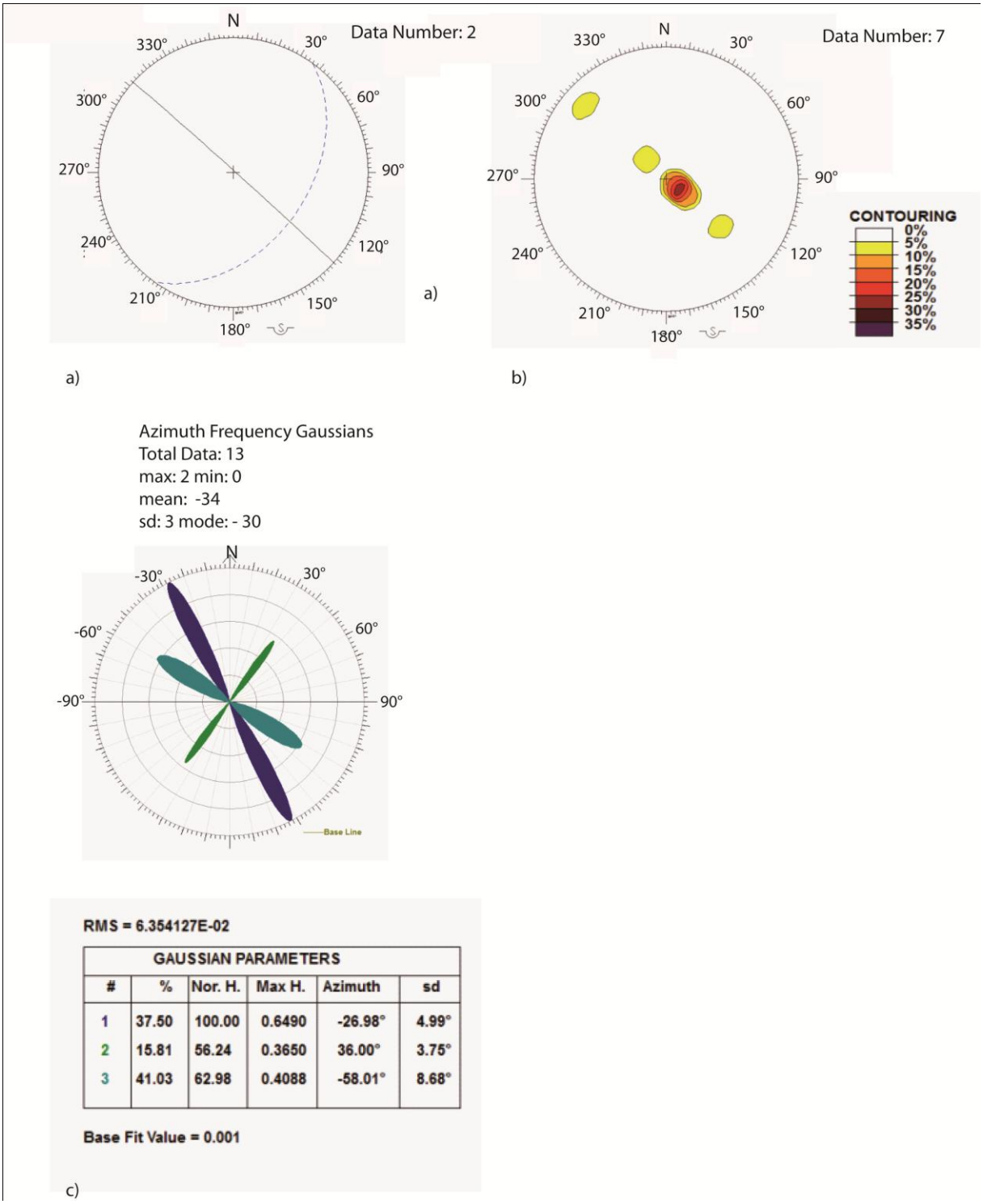

Fig. 5.48 Structural data analysis of the Fara 3 fault. a) Fault and bedding stereoplot; b) FRD rotax contour; c) FRD azimuth rose diagram

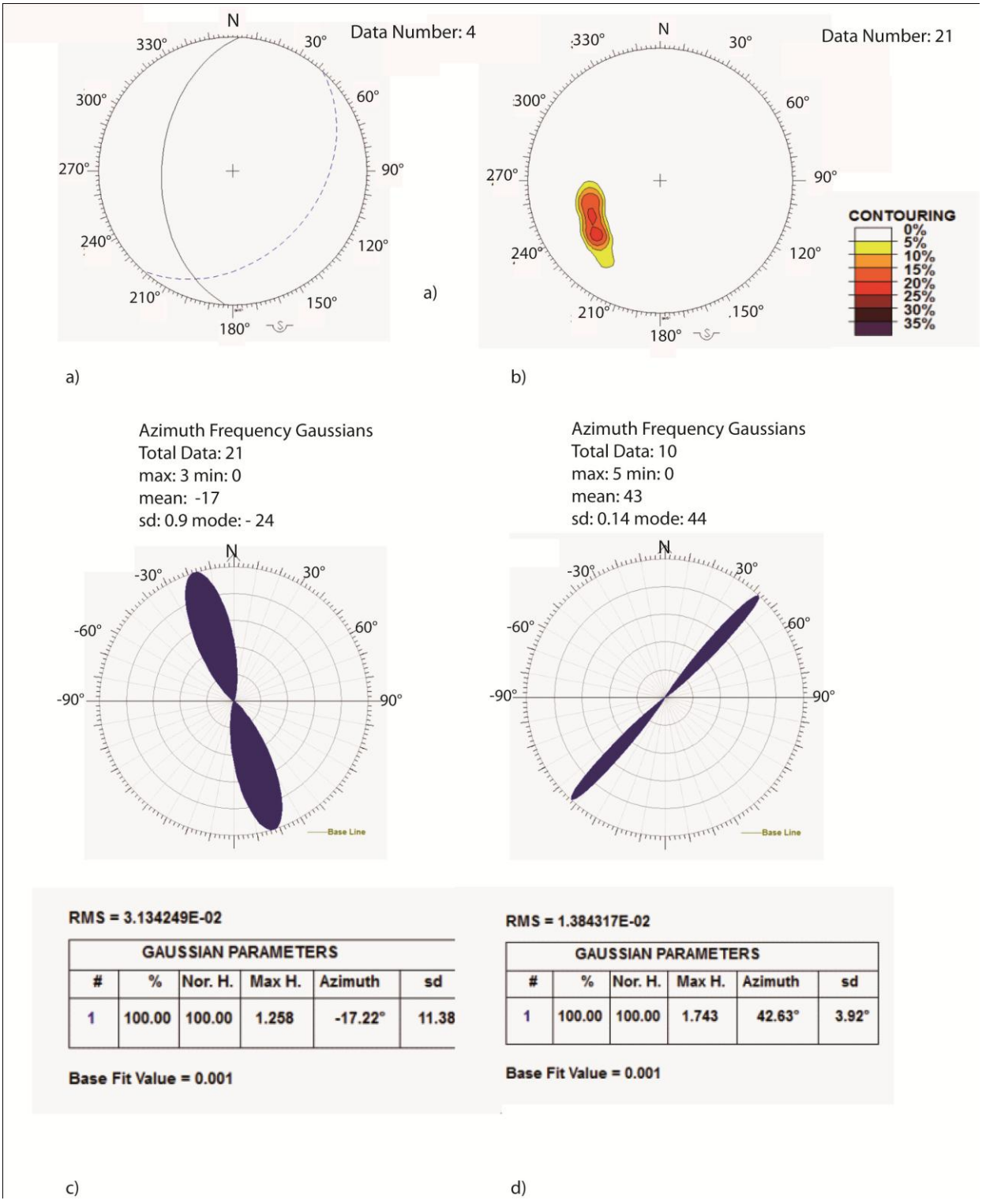

Fig. 5.49 – Structural data analysis of the Fara 4 fault. a) Fault and bedding stereoplot; b) FRD rotax contour; c) FRD azimuth rose diagram; d) RRD azimuth rose diagram

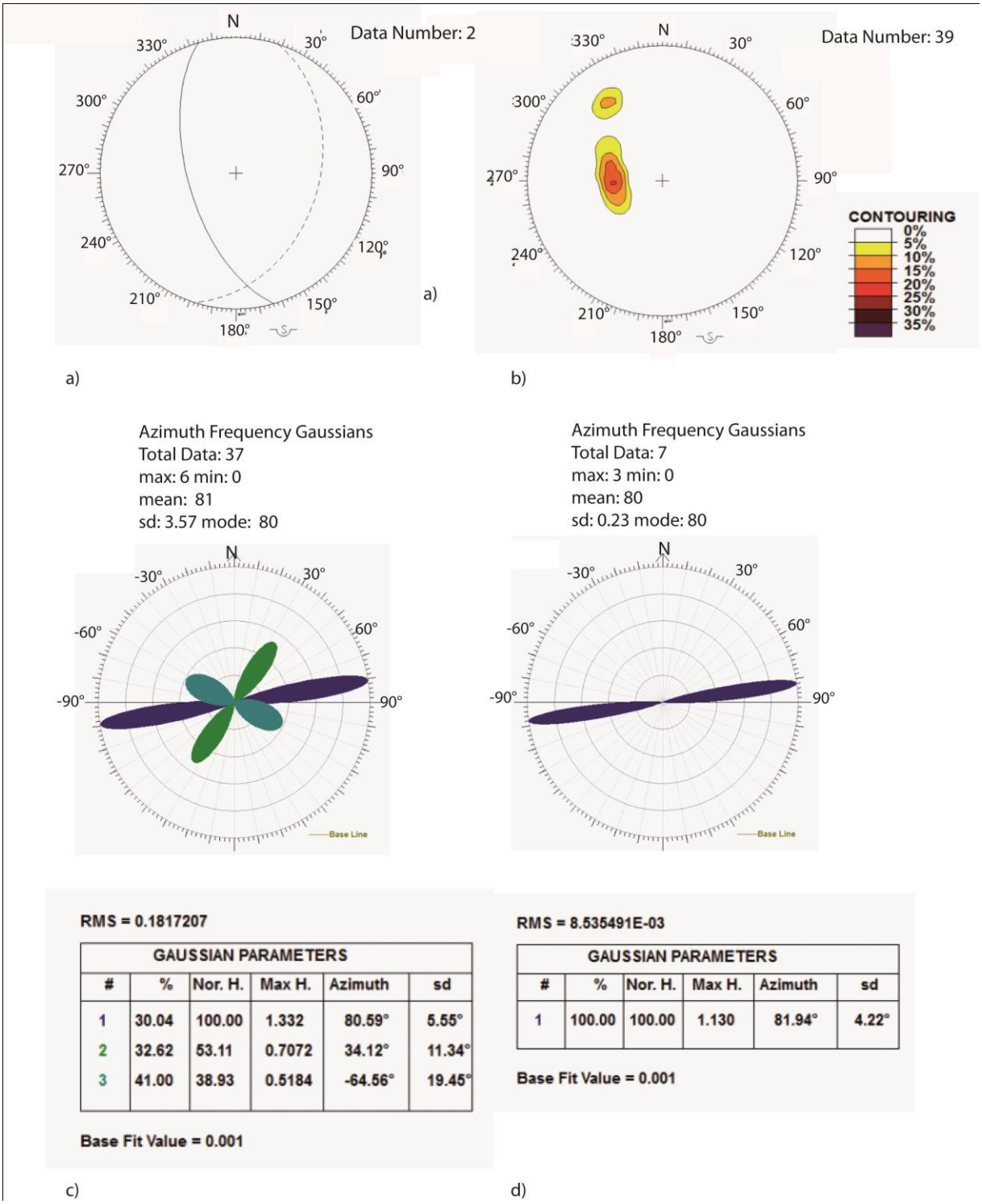

Fig. 5.50 – Structural data analysis of the Fara 6 fault. a) Fault and bedding stereoplot; b) FRD rotax contour; c) FRD azimuth rose diagram; d) RRD azimuth rose diagram

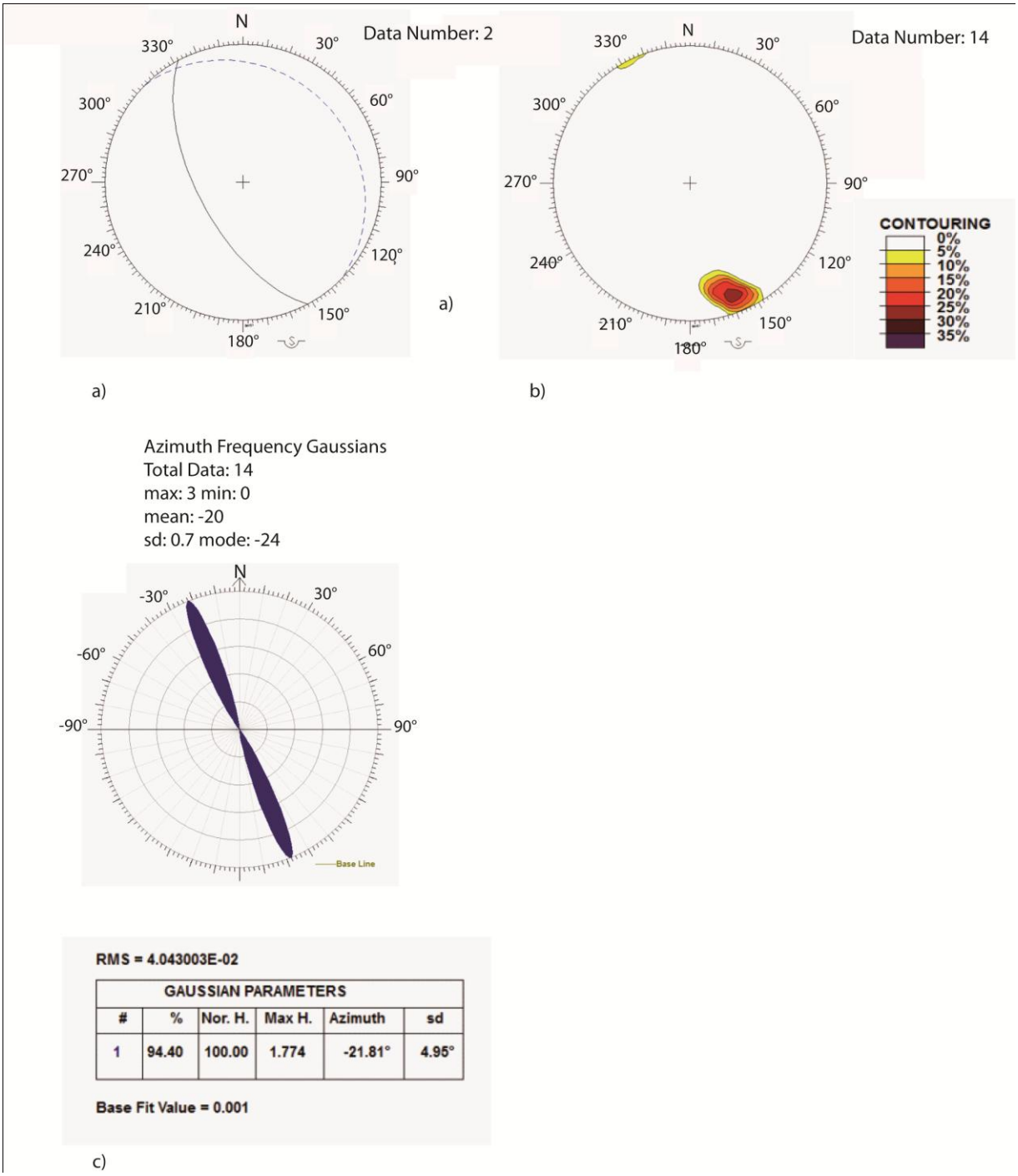

Fig. 5.51– Structural data analysis of the Palena 3 fault. a) Fault and bedding stereoplot; b) FRD rotax contour; c) FRD azimuth rose diagram

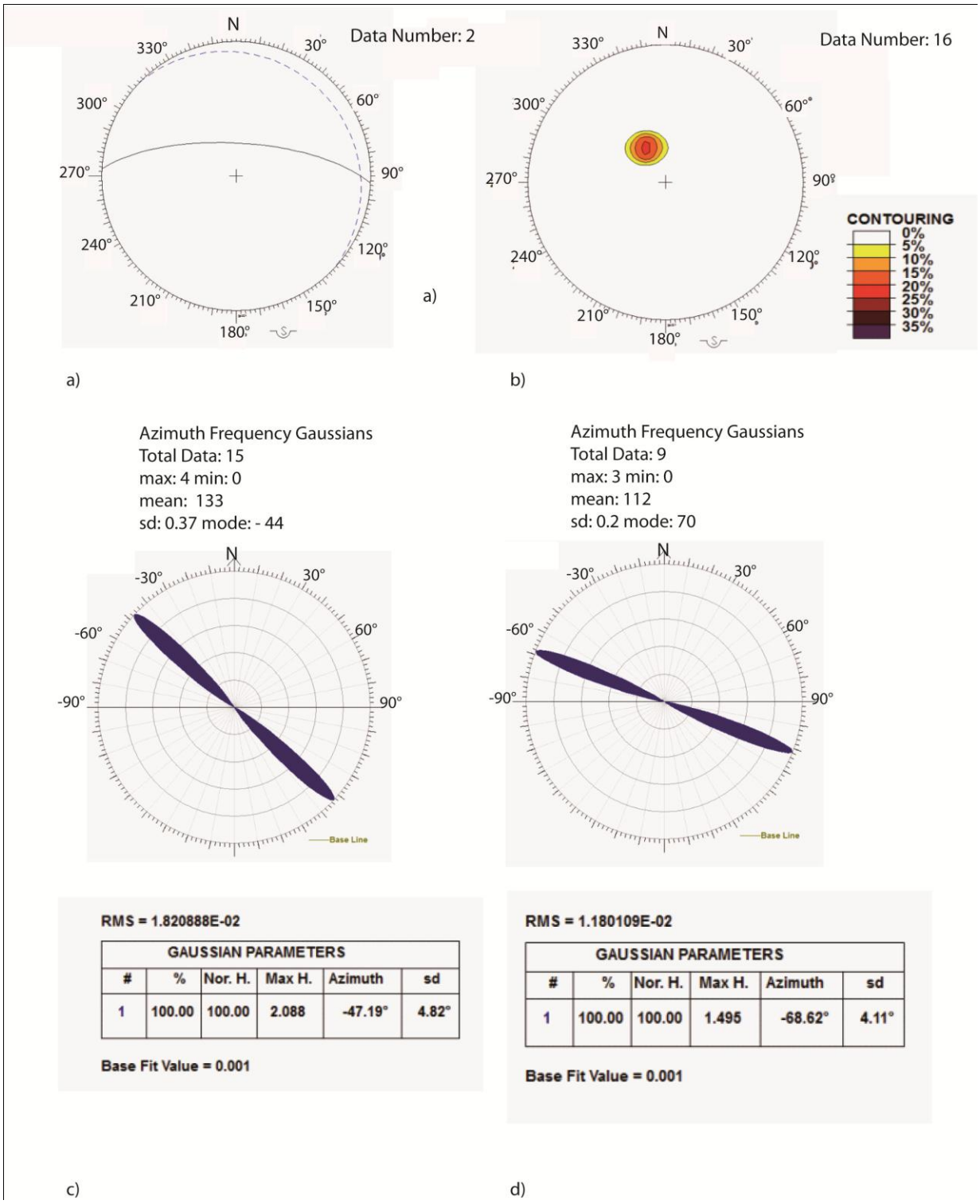

Fig. 5.52 – Structural data analysis of the Palena 4 fault. a) Fault and bedding stereoplot; b) FRD rotax contour; c) FRD azimuth rose diagram; d) RRD azimuth rose diagram

5.2 The total throw computations

When the outcrop does not allow measuring the throw its computation was performed using the Schliche et al. (1996) relation:

$$THROW = 0.03*(Fault\ Length)^{1.06} \quad \text{(eq. 5.1)}$$

The fault length is:

$$Fault\ Length = Fault\ High*2 \quad \text{(eq. 5.2)}$$

As explained in the section 4.1.5.1, the rotax values have been used to compute the "Total Throw", which take into account the strike-slip component of throw. The studied faults do not show a substantial difference between the total throw and the throw. Otherwise, the total throw is higher than the throw (Fig. 5.53 and Tab. 5.4), for the faults which have a strike slip component. The computation of the total amount of throw is important because the throw is directly related to the kinematic stress and therefore rules the development of the fault deformation pattern.

5.3 The deformation depth computations

The fault deformation depth has been computed using the relation of the section 4.1.5.2 and the results are showed in Tab. 5.5. The erosion rate used for the computation is 0.0016 mm/a how suggest Scrocca et al. 2006, that corresponds to the typical uplift rate in active chain.

5.4 Insoluble content analysis

In order to better characterize the rocks and to quantify the rehology, the insoluble content analysis have been performed both on the pristine rock and on the fault rock. For the detailed procedure see the section 4.1.5.3 of the current work.

The graph of Fig. 5.54 shows the result of this analysis and the relation between the insoluble content of the pristine rock and the fault one (maximum value). The pristine rock insoluble content values range between 9.4 and 1.6 (%), while the fault insoluble content values range between 11 and 0.2 (%). A good correlation exists between the Pristine rock insoluble content and the fault insoluble content, except for the case of Ienne fault, Filettino fault and Rocca di Cave 1 fault, which show higher values of pristine rock insoluble content. These data suggest that the insoluble content depends The fault clay content depends primarily on the pristine rock initial clay content and secondarily on the development of the pressure solution at advanced stage of fault deformation.

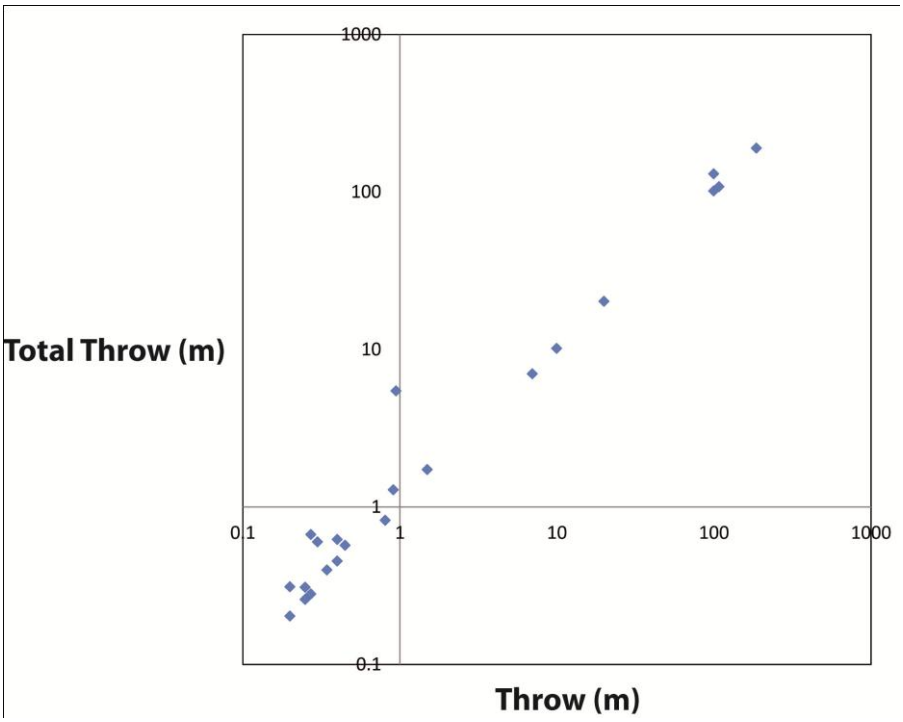

Fig. 5.53 - Relation between the throw and the total throw. The total throw is higher than the throw for the faults which have a strike slip component

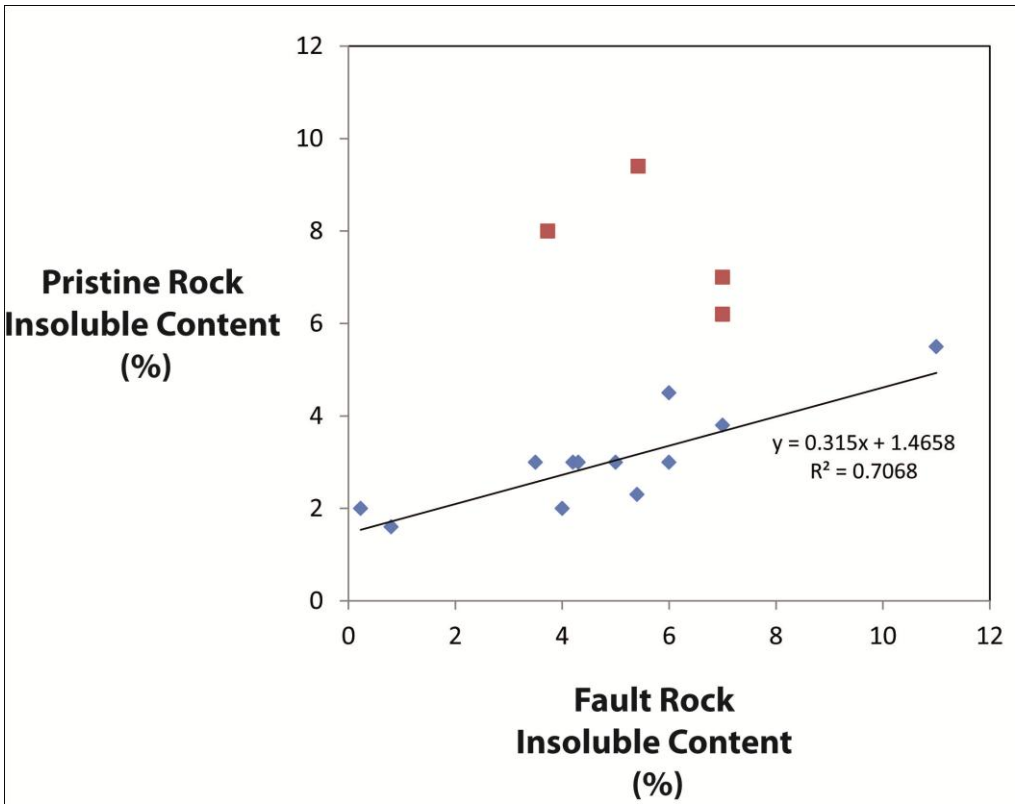

Fig. 5.54 – Comparison between the insoluble content of the fault rock sample and the pristine rock sample

SITE	NAME	LAT	LONG
Prenestini Mts.	RoccadiCave 1	N 41°50'50.54"	E 12°50'50.45"
	RoccadiCave 2	N 41°50'26.0"	E 12°56'26.6"
	RoccadiCave 3	N 41°50'26.0"	E 12°56'26.6"
Simbruini Ernici Mts.	Filettino	N 41°53'07.82"	E 13°18'36.86"
	Ienne	N 41°53'55.9"	E 13°09'47.1"
	Pietrasecca	N 42°08'10.8"	E 13°06'56.7"
Velino-Sirente Mts.	Tornimparte 1	N 42°12'48.9"	E 13°27'36.3"
	Tornimparte 2	N 42°16'05.4"	E 13°19'41.0"
	Tornimparte 3	N 42°16'05.4"	E 13°19'41.0"
	Tornimparte 4	N 42°16'05.4"	E 13°19'41.0"
	Tornimparte 5	N 42°16'05.4"	E 13°19'41.0"
Fucino Basin	LeccedeiMarsi 1	N41°54'08.4"	E13°40'58.3"
	LeccedeiMarsi 2	N41°54'59.9"	E13°40'22.5"
Sagittario Gully	Gole Sagittario	N41°58'12.3"	E13°48'53.1"
Subequana Plain	Castel di Ieri	N42°05'52.2"	E13°45'41.6"
Maiella Mts.	Fara 1	N42°05'18.08"	E14°11'50.98"
	Fara 2	N42°05'03.8"	E14°10'33.4"
	Fara 3	N42°05'03.8"	E14°10'33.4"
	Fara 4	N42°5'20.73"	E14°11'34.72"
	Fara 6	N42°5'19.83"	E14°11'42.54"
	Palena 3	N41°56'43.4"	E14°07'09.3"
	Palena 4	N41°56'43.4"	E14°07'09.3"

Tab. 5.1 – Fault locations divided by sites. For the location of each sites see Fig. 3.2

SITE	NAME	DEPOSITION ENVIROMENT	TECTONIC ENVIROMENT	STRUCTURAL POSITION
Prenestini Mnt.	RoccadiCave 1	Carbonatic ramp	Thrust and strike-slip	Backlimb
	RoccadiCave 2	Carbonatic platform	Thrust and strike-slip	Bac-limb
	RoccadiCave 3	Carbonatic platform	Thrust and strike-slip	Backlimb
Simbruini Ernici Mnt.	Filettino	Carbonatic platform	Thrust-fold belt	Forelimb
	Ienne	Carbonatic platform	Thrust-fold belt	Backlimb
	Pietrasecca	Carbonatic ramp	Thrust-fold belt	Forelimb
Velino-Sirente Mnt.	Tornimparte 1	Carbonatic Platform	Post-orogenic extension	-
	Tornimparte 2	Carbonatic Platform	Strike-slip	-
	Tornimparte 3	Carbonatic Platform	Strike-slip	-
	Tornimparte 4	Carbonatic Platform	Strike-slip	-
	Tornimparte 5	Carbonatic Platform	Strike-slip	-
Fucino Basin	LeccedeiMarsi 1	Carbonatic platform	Post-orogenic extension	-
	LeccedeiMarsi 2	Carbonatic platform	Post-orogenic extension	-
Sagittario Gully	Gole del Sagittario	Carbonatic Platform	Thrust and strike-slip	-
Subequana Plain	Castel di Ieri	Platform-Basin transition	Post-orogenic extension	-
Maiella Mnt.	Fara 1	Carbonatic platform	Thrust-fold belt	Forelimb
	Fara 2	Carbonatic platform	Thrust-fold belt	Forelimb
	Fara 3	Carbonatic platform	Thrust-fold belt	Forelimb
	Fara 4	Carbonatic platform	Thrust-fold belt	Forelimb
	Fara 6	Carbonatic platform	Thrust-fold belt	Forelimb
	Palena 3	Carbonatic ramp	Thrust-fold belt	Backlimb
	Palena 4	Carbonatic ramp	Thrust-fold belt	Backlimb

Tab. 5.2 – Summary of fault and rock characteristics

SITE	NAME	AVERAGE BED THICKNESS (m)	FAULT-CORE FEATURES	FAULT-CORE WIDTH (m)	DEFORMATION AGE (Ma)
Prenestini Mnt.	RoccadiCave 1	0.2	non-continuous	0.10 - 0.15	52
	RoccadiCave 2	0.33	-	0	52
	RoccadiCave 3	0.33	-	0	52
Simbruini Ernici Mnt.	Filettino	0.6	recemented	7	67
	Ienne	0.2	continuous	1.9	67
	Pietrasecca	0.4	continuous	3.46	67
Velino-Sirente Mnt.	Tornimparte 1	0.6	continuous-recemented	1	3
	Tornimparte 2	0.3	continuous	0.4	23
	Tornimparte 3	0.3	continuous	0.04	23
	Tornimparte 4	0.3	continuous	0.02	23
	Tornimparte 5	0.3	continuous-recemented	1	23
Fucino Basin	LeccedeiMarsi 1	0.1	-	0	3
	LeccedeiMarsi 2	0.4	non-continuous recemented	1.79	3
Sagittario Gully	Gole del Sagittario	0.5	continuous cataclastic	12	10
Subequana Plain	Castel di Ieri	0.3	continuous-recemented	3	3
Maiella Mnt.	Fara 1	0.6	non-continuous	0.3	20
	Fara 2	0.6	-	-	20
	Fara 3	0.6	-	-	20
	Fara 4	0.7	-	-	20
	Fara 6	0.5	-	-	20
	Palena 3	0.7	-	-	20
	Palena 4	0.7	-	-	20

Tab. 5.3 – Summary of fault and rock characteristics

NAME	THROW (m)	ROTAX (°)	TOTAL THROW (m)
RoccadiCave 1	0.45	38	0.57
RoccadiCave 2	0.20	50	0.31
RoccadiCave 3	0.25	36	0.31
Filettino	20.00	8	20.20
Ienne	107.94	2	108.01
Pietrasecca	7.00	2	7.00
Tornimparte 1	186.94	10	189.82
Tornimparte 2	0.40	28	0.45
Tornimparte 3	0.25	15	0.26
Tornimparte 4	0.30	60	0.60
Tornimparte 5	0.40	50	0.62
LeccedeiMarsi 1	0.20	10	0.20
LeccedeiMarsi 2	10.00	10	10.15
GoleSagittario	100.00	40	130.53
CasteldiIeri	100.00	10	101.54
Fara 1	0.81	10	0.82
Fara 2	0.91	45	1.29
Fara 3	0.95	80	5.45
Fara 4	0.34	30	0.40
Fara 6	1.50	30	1.73
Palena 3	0.27	14	0.28
Palena 4	0.27	66	0.67

Tab. 5.4 –Total throw and rotax plunge values

NAME	AGE (Ma)	EROSION RATE (mm/a)	DEFORMATION DEPTH (m)
RoccadiCave 1	52	0.000016	832
RoccadiCave 2	52		832
RoccadiCave 3	52		832
Filettino	67		1072
Ienne	67		1072
Pietrasecca	67		1072
Tornimparte 1	3		48
Tornimparte 2	23		368
Tornimparte 3	23		368
Tornimparte 4	23		368
Tornimparte 5	23		368
Leccedei Marsi 1	3		48
Leccedei Marsi 2	3		48
GoleSagittario	10		160
CasteldiIeri	3		48
Fara 1	20		320
Fara 2	20		320
Fara 3	20		320
Fara 4	20		320
Fara 6	20		320
Palena 1	20		320
Palena 4	20		320

Tab. 5.5 – Fault age and deformation depth values

5.5 Quantitative analyses of fault and regional related deformation intensity

5.5.1 Spatial analysis of the deformation intensity in fault damage-zones

As it has been outlined in the introduction of this work, the development and the evolution of the deformation patterns in fault damage-zone depends on multiple geological factors. Therefore, in order to investigate this issue, it is necessary a spatial quantification of the deformation intensity. For each faults have been performed the H/S scan-lines through the distance from the fault plane. The data have been analysed using the transect technique (see section 4.1.3 of the current work). A total of 20 faults have been analysed, which have essentially a dip-slip movement (Rotax < 60°). In the next section the main results of the analysis will be presented and discussed separately for each site.

5.5.1.1 Prenestini Mountains

The **Rocca di Cave 1 fault** (Throw: 2.58 m) hangingwall scan line (A-B see Fig. 5.2) length is 3.5 m (Fig. 5.55 *a*). The H/S spatial analysis shows that the more frequent value near the fault plane is 1.6. The frequency of higher value of H/S increases at the distance of 2.8 m up to 7-5 and then decreases to 2-4.5. The regional deformation is very intense with a mean value of 5.1 (Fig 5.55 *b*).
The **Rocca di Cave 2 fault** (Throw: 0.50 m) fault hangingwall scan line length is 3 m (A-B see Fig. 5.3). The H/S spatial analysis that nearby the fault plain the most frequent H/S value is 3.3, then occurs an increase to 5 and a decrease to 1.2 at a distance of 2.9 m from the fault plane (Fig. 5.56 *a*).
The **Rocca di Cave 3 fault** (Throw: 1.43 m) fault hangingwall scan line length is 5 m (A-B see Fig. 5.3). The H/S mean value show a decrease from high value nearby the fault plain to lower value at 2.6 m from the master fault plane (Fig. 5.57 *b*). This scan line intercepts the Rocca di Cave 2 fault (Fig. 5.57 a), in fact at the distance of 1.8 m from the fault plane there is a local increase of H/S frequency (3.3), which corresponds to the H/S values detected on the Rocca di Cave 2 fault.
At a distance of 4 m the H/S frequency reach the regional H/S mean value, that is 3.5 both for the Rocca di Cave 3 and the Rocca di Cave 2 faults (Fig. 5.57 *b*).

5.5.1.2 Simbruini-Ernici Mountains

The **Filettino fault** (Throw: 20 m) fault footwall scan line length is 50 m (A-B see Fig. 5.10). A transect analysis was performed for each set related to fault. The cumulative H/S transect Gaussian analysis (Fig. 5.58 *a*) shows a decrease of the H/S from 4 down to 2 at the distance of 18 m. Then an increase of the value occurs, due to the presence of a secondary fault and a new decrease down to the mean regional value at the distance of 30 m, which is of 2.7 (Fig. 5.58 *b*).
The **Ienne fault** (Throw: 108 m) hangingwall scan line length is 30 m (A-B see Fig. 5.11). The transect analysis was performed for the fault-related fracture sets (NW-SE-1; NW-SE-2). The cumulative Gaussian transect analysis shows H/S mean value around 3.3-4.1 on the fault plane (Fig. 5.59 *a*). This value is constant for 8 m and then increases up to 4.5 and then decrease down to the regional mean value, which is 1.9 (Fig. 5.59 *b*). The increase of H/S value is related to the presence of a secondary fault located at 12 m from the main fault plane.

The **Pietrasecca fault** (Throw: 8 m) hangingwall scan line length is 50 m (A-B see Fig. 5.12). The scan line intercepts a sequence of secondary faults, which presence causes the local increase of the H/S value. For this fault the vertical scale used is 0-20. That means that this fault is intensely deformed. The Gaussian fit transect analysis (Fig. 5.60 *a*) shows a decrease of H/S values from 10 to 3.3-6. The regional deformation mean value is 2.4 for this fault (Fig. 5.60 *b*).

5.5.1.3 Velino-Sirente Mountains

The **Tornimparte 1 fault** (Throw: 198 m) fault footwall scan line length is 20 m (A-B see Fig. 5.18). Due to the high values of H/S it was used the scale 0-20 (Fig. 5.61 *a*). The more frequent H/S value nearby the fault plane is the peak 17. It remains constant for 8 m and then decreases down to 7. The regional H/S mean value is 3.1 (Fig. 5.61 *b*).

The **Tornimparte 2 fault** (Throw: 0.4 m) footwall scan line length is 3 m (A-B see Fig. 5.19). The H/S value decreases from 4 down to 2.5 at 3 m from the fault plane (Fig. 5.62 *a*).

The **Tornimparte 3 fault** (Throw: 0.3 m) hangingwall scan line length is 3 m (A-B see Fig. 5.20). The peaks of H/S are three on the fault plane, which values range from 8-5-2.6 respectively. The number of the peak decrease to one at 2.7 m from the fault plane, which value is 2 (Fig. 5.63 *a*).

The **Tornimparte 5 fault** (Throw: 0.6 m) footwall scan line length is 3 m (A-B see Fig. 5.21). The number of peaks decreases from 4 on the fault plane to 1 at a distance of 2 m from the fault plane. The more intense H/S value is 7 on the fault plane, then it decrease to 3.3 at 0.50 m and to 2 at 1 m (Fig. 5.64 *a*).

The regional H/S mean value is 3.5 for the Tornimparte 2-3-5 faults (Fig. 5.64 *b*).

5.5.1.4 Fucino Basin

The **Lecce dei Marsi 1 fault** (Throw: 2 m) hangingwall footwall length is 2 m (A-B see Fig. 5.29). The number of peak decreases from 2 to 1 along the distance, but we there is not any decrease of the value with the distance (Fig. 5.65 *a*).

The **Lecce dei Marsi 2 fault** (Throw: 114 m) hangingwall scan line length is 25 m (A-B see Fig. 5.30). The H/S transect analysis shows 4 main peak nearby the fault plane (Fig. 5.66 *a*). The number of the peak decreases with the distance from the fault plane. The more frequent H/S value is 7 on the fault plane. It increases for the presence of secondary faults. It decreases down to 3 at the distance of 8 m from the fault plane. The regional deformation H/S mean value is 2 for both the faults (Fig. 5.66 *b*).

5.5.1.5 Sagittario Gully

The **Gole del Sagittario fault** (Throw: 130 m) footwall scan line length is 25 m (Fig. 5.67 *a*). The number of peaks is 3 on the fault plane and it decrease with the increase of distance (Fig. 5.67 *a*). It increases locally for the presence of a secondary fault. The H/S value decreases from high values on the fault plane (8) down to 1 at a distance of 22 m from the fault plane. The regional deformation H/S mean value is 2 (Fig. 5.67 *b*).

5.5.1.6 Subequana Plain

The **Castel di Ieri fault** (Throw: 106 m) footwall scan line length is 25 m (Fig. 5.37). The H/S transect analysis shows the presence of two peaks on the fault plane (Fig. 5.68 *a*). The value of H/S initially increases reaching a value of 5. Then it decreases down to the regional value, which is 2.2 (Fig. 5.68 *b*).

5.5.1.7 Maiella Mountain

The **Fara 1 fault** (Throw: 2.3 m) footwall scan line length is 7 m (A-B see Fig. 5.41). The Gaussian fit analysis shows the presence of two peaks on the fault plane (Fig. 5.69 *a*). The number of the peak decreases down to one at a distance of 5 m from the fault plane. The more frequent value is 3 on the fault plane. At the distance of 1.10 m an increase occurs and then a new decrease down to 3.1 at a distance of 5 m.

The **Fara 2 fault** (Throw: 1.8 m) footwall scan line length is 4 m (A-B see Fig. 5.41). The Gaussian fit analysis shows the presence of two main peaks on the fault plane (Fig. 5.70 *a*). The number of the peak increase to two at a distance of 3 m from the fault plane, due to the presence of Fara 2 fault. The H/S show high value nearby the fault (5.3-7.2). The value increases and then decrease down to 3.6 at 3 m from the fault plane.

The **Fara 4 fault** (Throw: 0.4 m) footwall scan line length is 3 m (A-B see Fig. 5.43). The Gaussian fit analysis shows the presence of one peak which value is 6 on the fault plane. It decreases down to 3.1 at 3 m from the fault plane (Fig. 5.71 *a*). The regional deformation H/S mean value is 2.2 for Fara 1, Fara 2, and Fara 4 faults (Fig. 5.71 *b*).

The **Fara 6 fault** (Throw: 4.3 m) footwall scan line length is 12 m (A-B see Fig. 5.44). The Gaussian fit analysis shows the presence of one peak on the fault plane. The H/S value on the fault plane is 3.4 and it remains constant for 4 m. It increase at 4.8 m from the fault plane up to 5 but here there are no evidence of any secondary fault on the field (Fig. 5.72 *a*). Then it decreases down the regional mean that is 2.5 (Fig. 5.72 *b*).

The **Palena 3 fault** (Throw: 0.2 m) hangingwall scan line length is 4 m (A-B see Fig. 5.45). The Gaussian fit analysis shows 3 peaks on the fault plane and 4 peak at a distance of 2 m. The H/S value is 4.1. (Fig. 5.73 *a*) Then it increase up to 6.1 at 3.8 m from the fault plane. The general trend is characterized by an increase of the H/S value.

The **Palena 4 fault** (Throw: 1.56 m) hangingwall scan line length is 3 m (A-B see Fig. 5.45). The H/S values are very high for this fault (Fig. 5.74 *a*). The values are constant with one variation at 2.2 m from the fault plane (Fig. 5.74 *b*).

The regional deformation H/S mean value is 3.9 for both the faults (Fig. 5.66 *b*).

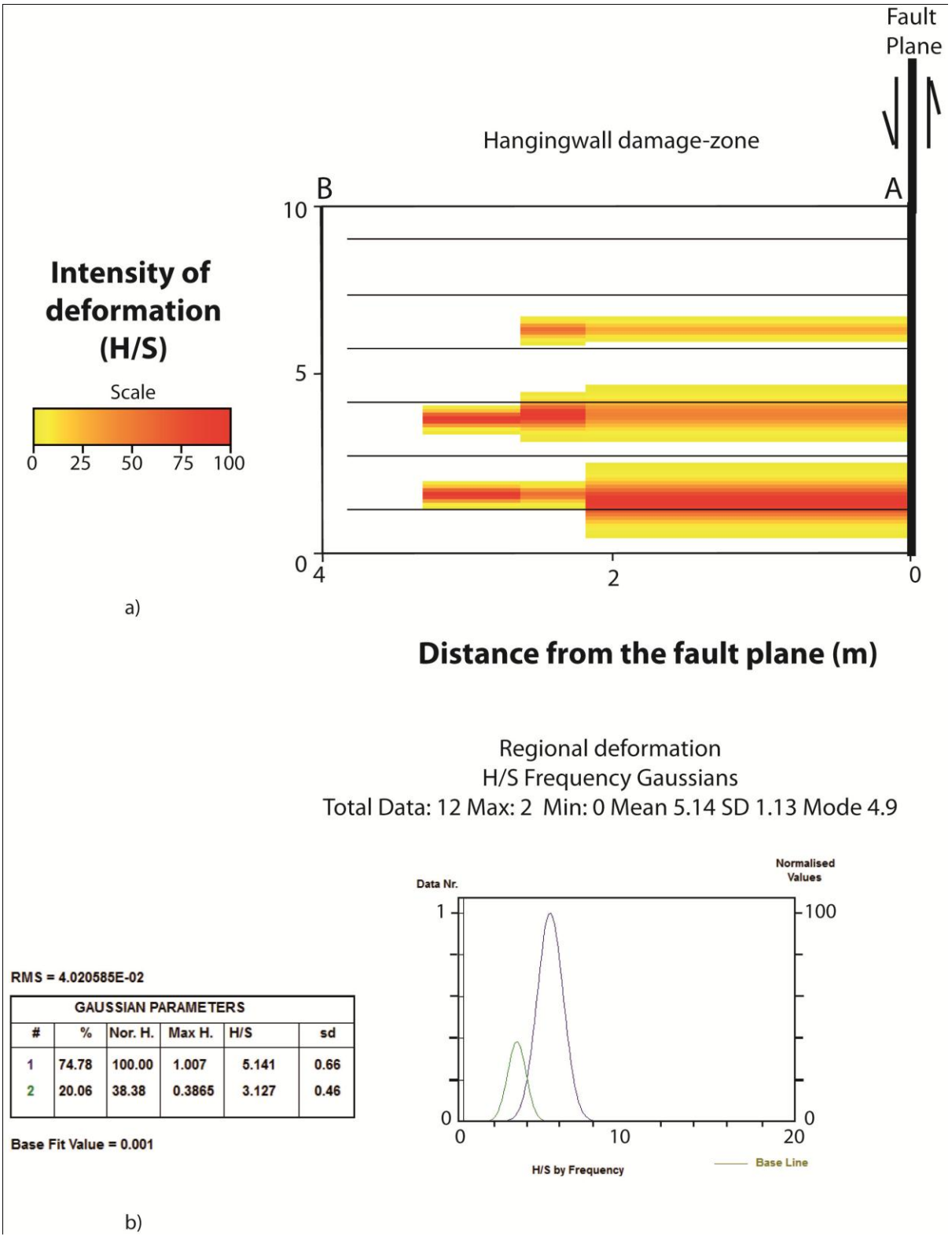

Fig. 5.55 – *a)* Gaussian fit transect analysis of the Rocca di Cave 1 fault hangingwall (scan line A-B see Fig. 5.2) *b*) Regional deformation mean value

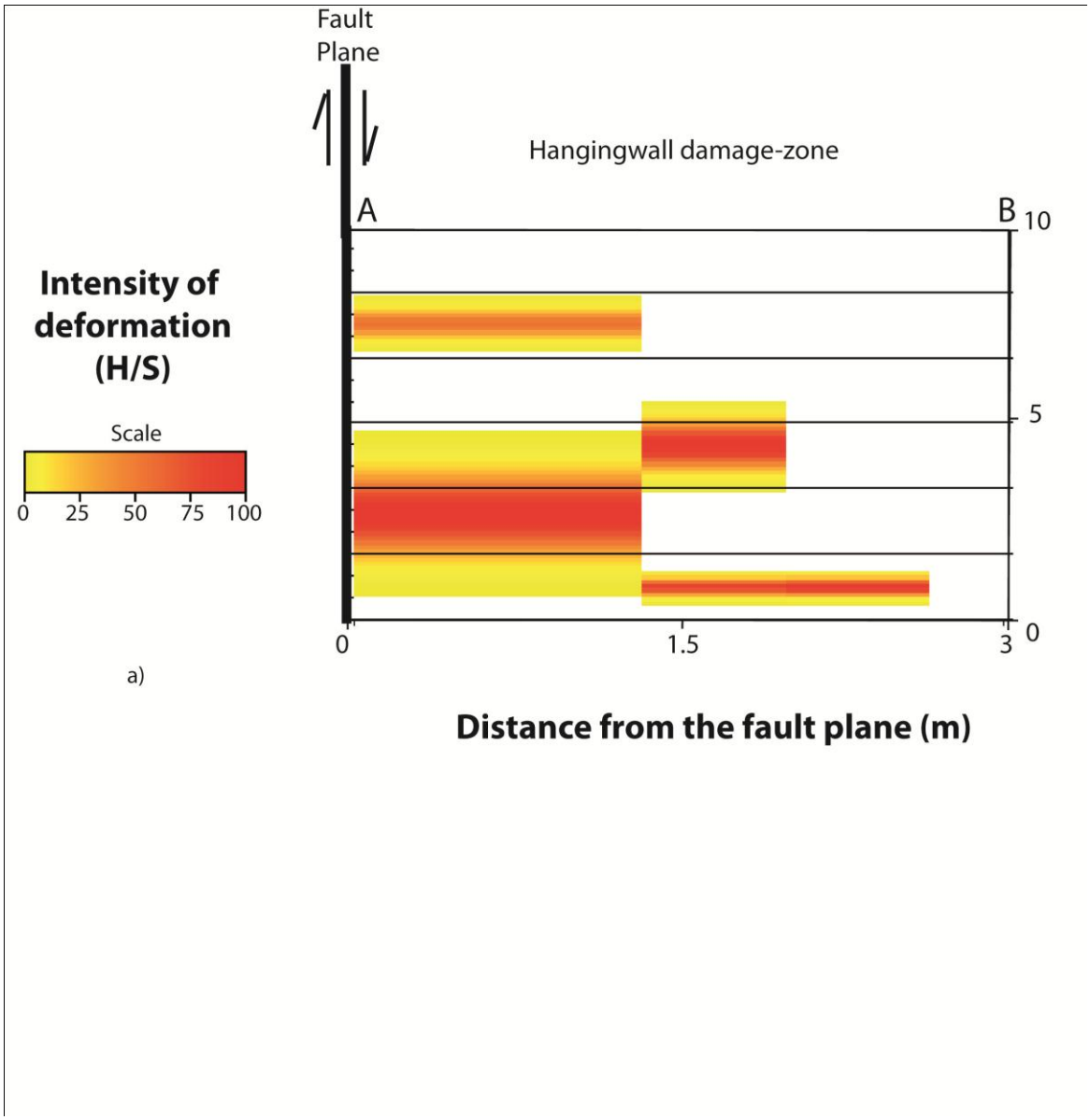

Fig. 5.56 – *a)* Gaussian fit transect analysis of the Rocca di Cave 2 fault hangingwall (scan line A-B see Fig. 5.3)

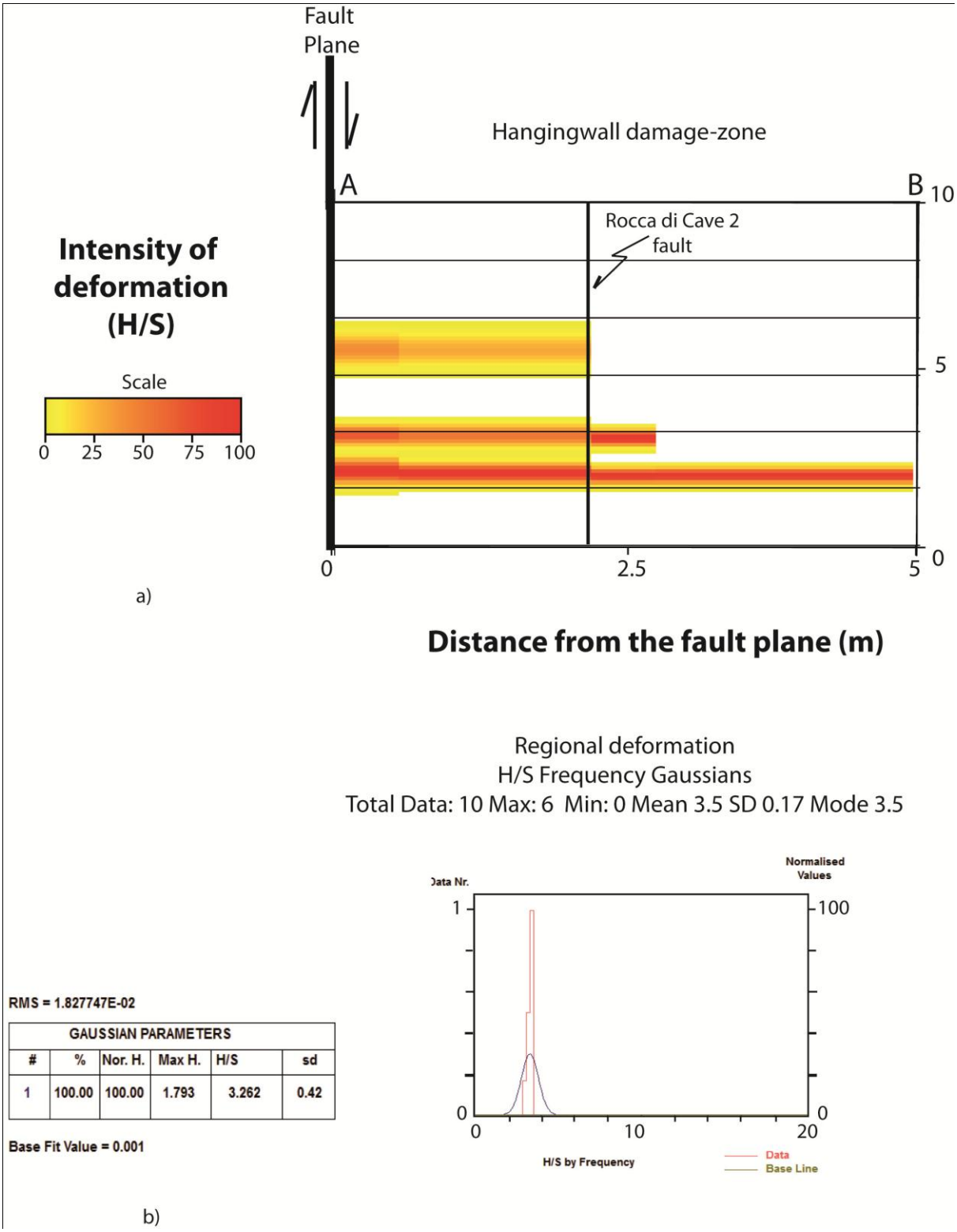

Fig. 5.57 – *a)* Gaussian fit transect analysis of the Rocca di Cave 3 fault hangingwall (scan line A-B see Fig. 5.3); *b)* Regional deformation mean value

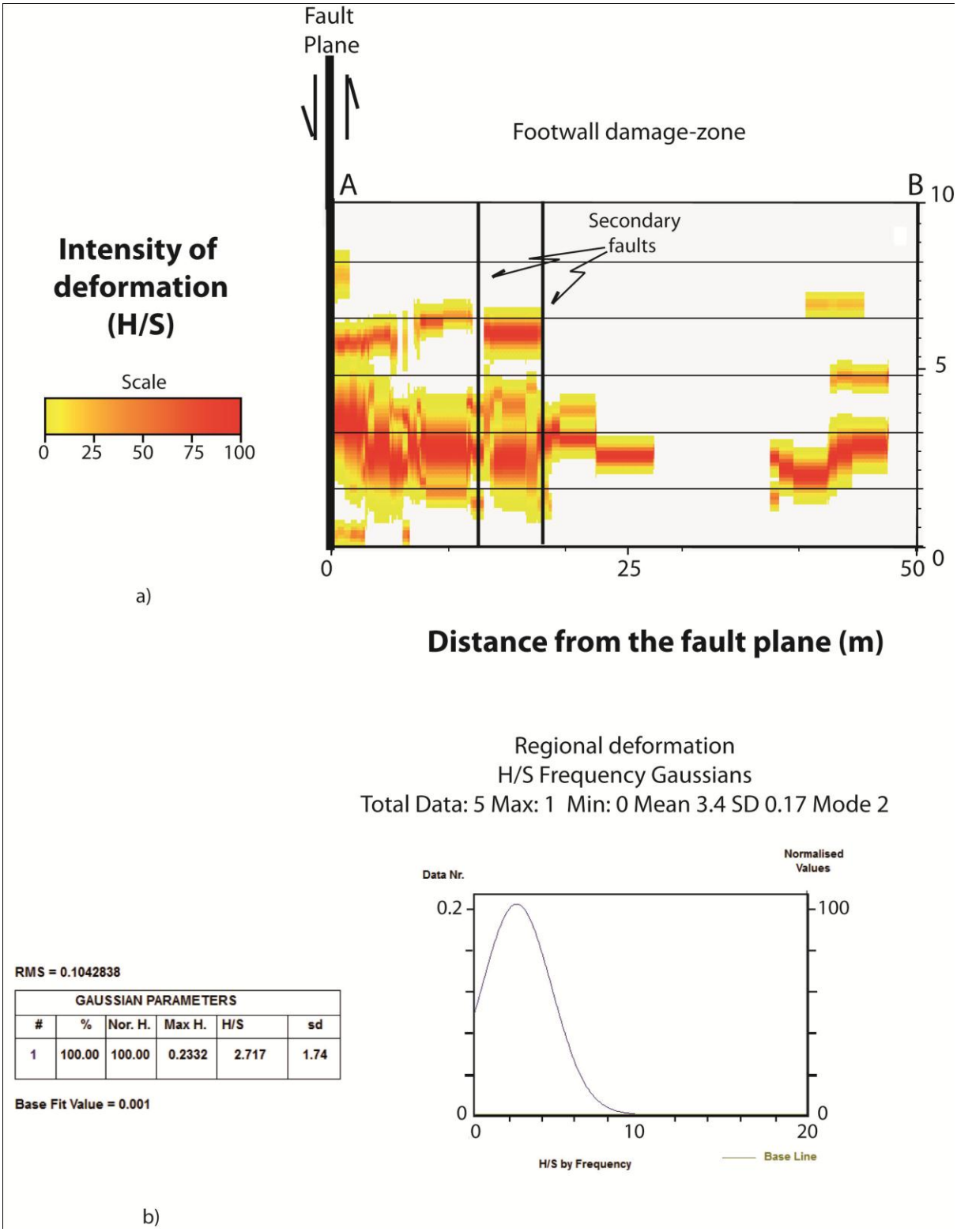

Fig. 5.58 - Gaussian fit transect analysis of Filettino fault footwall (scan line A-B see Fig. 5.10); *b)* Regional deformation mean value

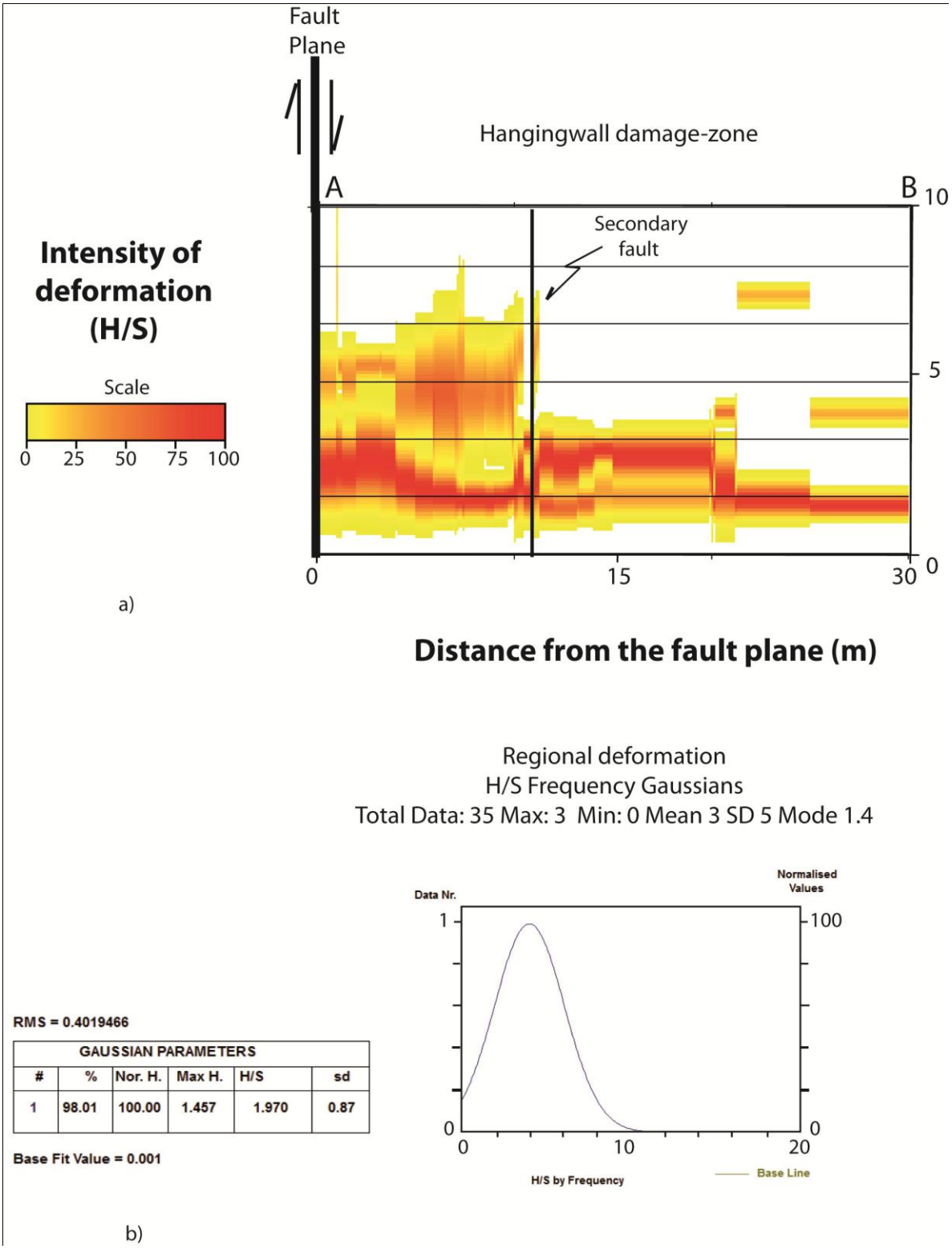

Fig. 5.59 - Gaussian fit transect analysis of the Ienne fault hangingwall (scan line A-B see Fig. 5.11); *b)* Regional deformation mean value

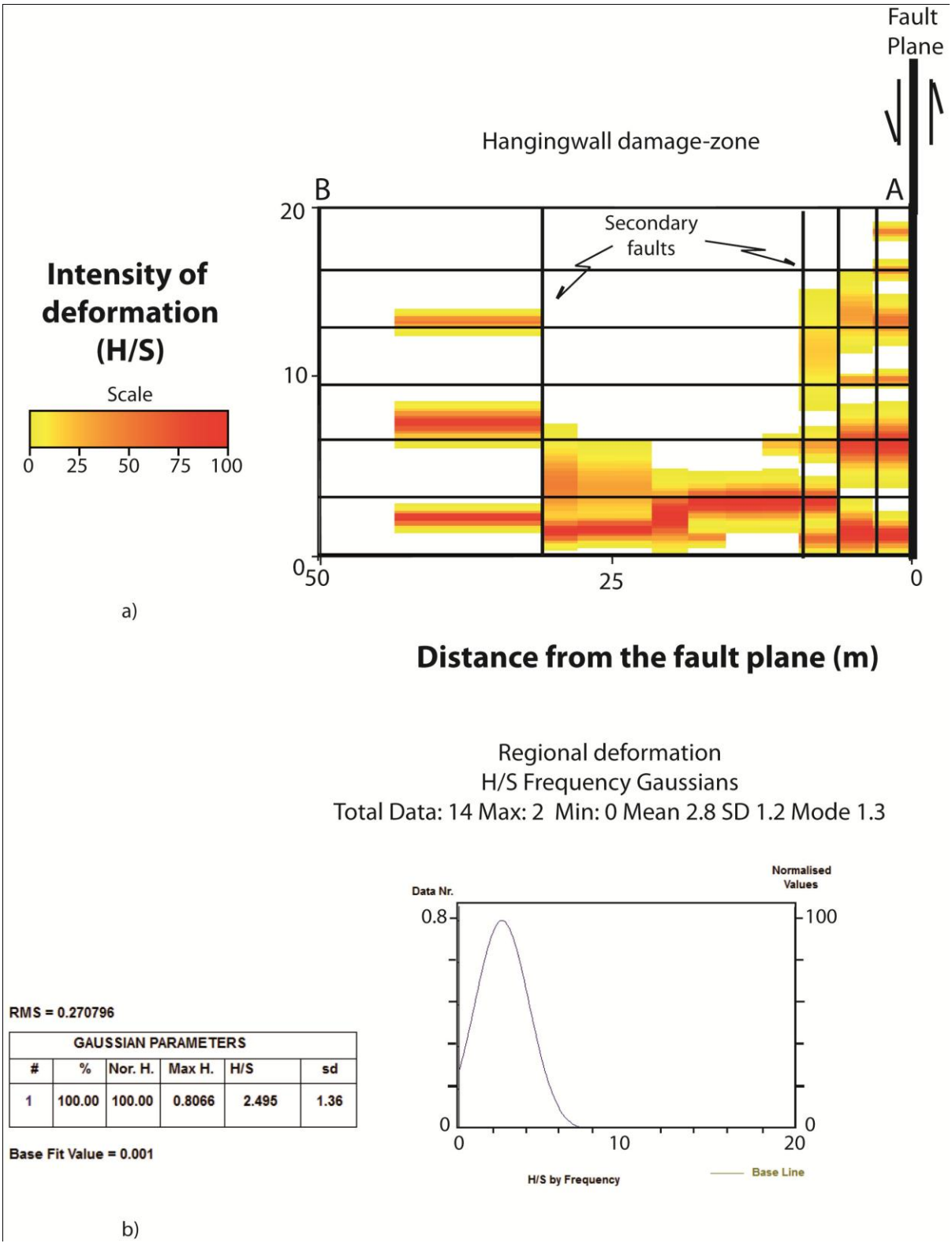

Fig. 5.60 - Gaussian fit transect analysis of the Pietrasecca fault hangingwall (scan line A-B see Fig. 5.12); *b)* Regional deformation mean value

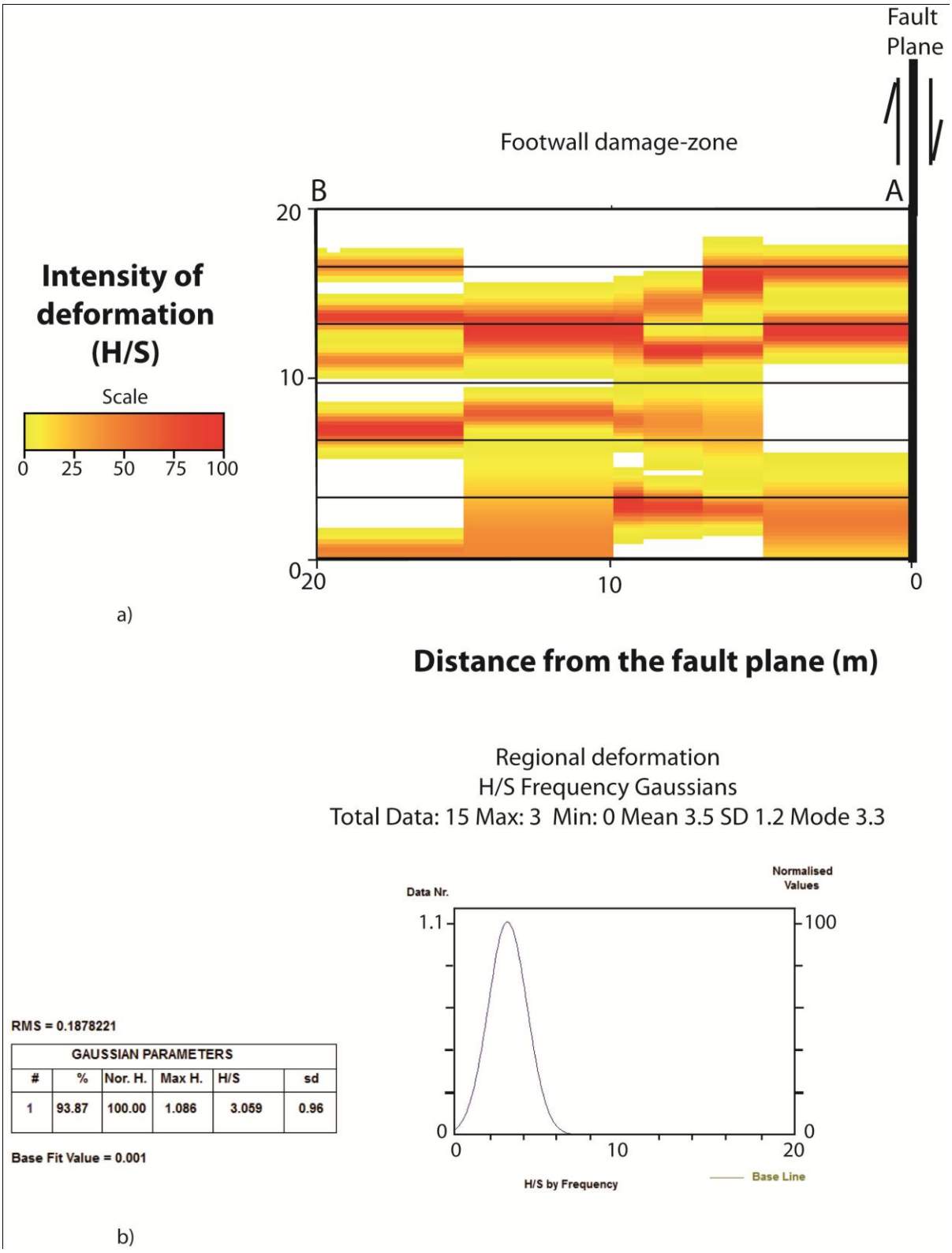

Fig. 5.61 - Gaussian fit transect analysis of the Tornimparte 1 fault footwall (scan line A-B see Fig. 5.18); *b)* Regional deformation mean value

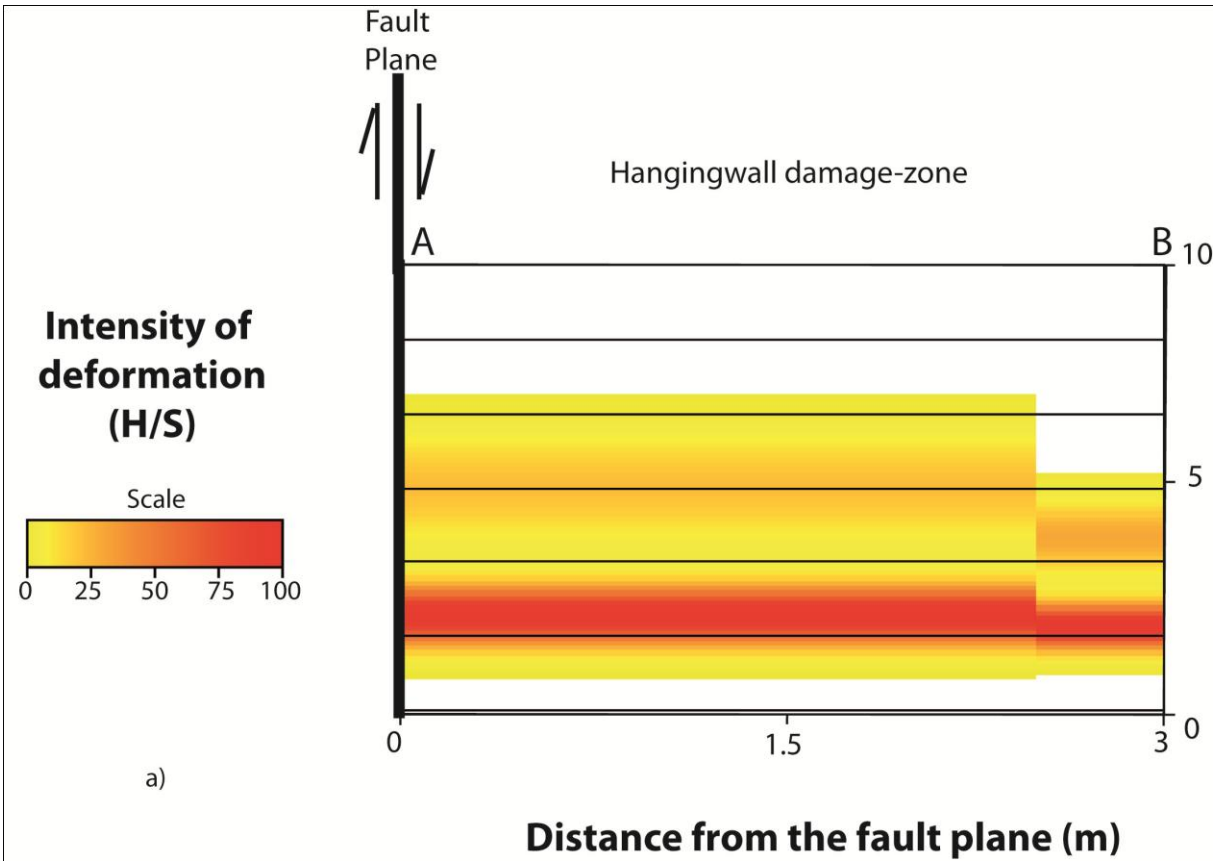

Fig. 5.62 - Gaussian fit transect analysis of the Tornimparte 2 fault hangingwall (scan line A-B see Fig. 5.19)

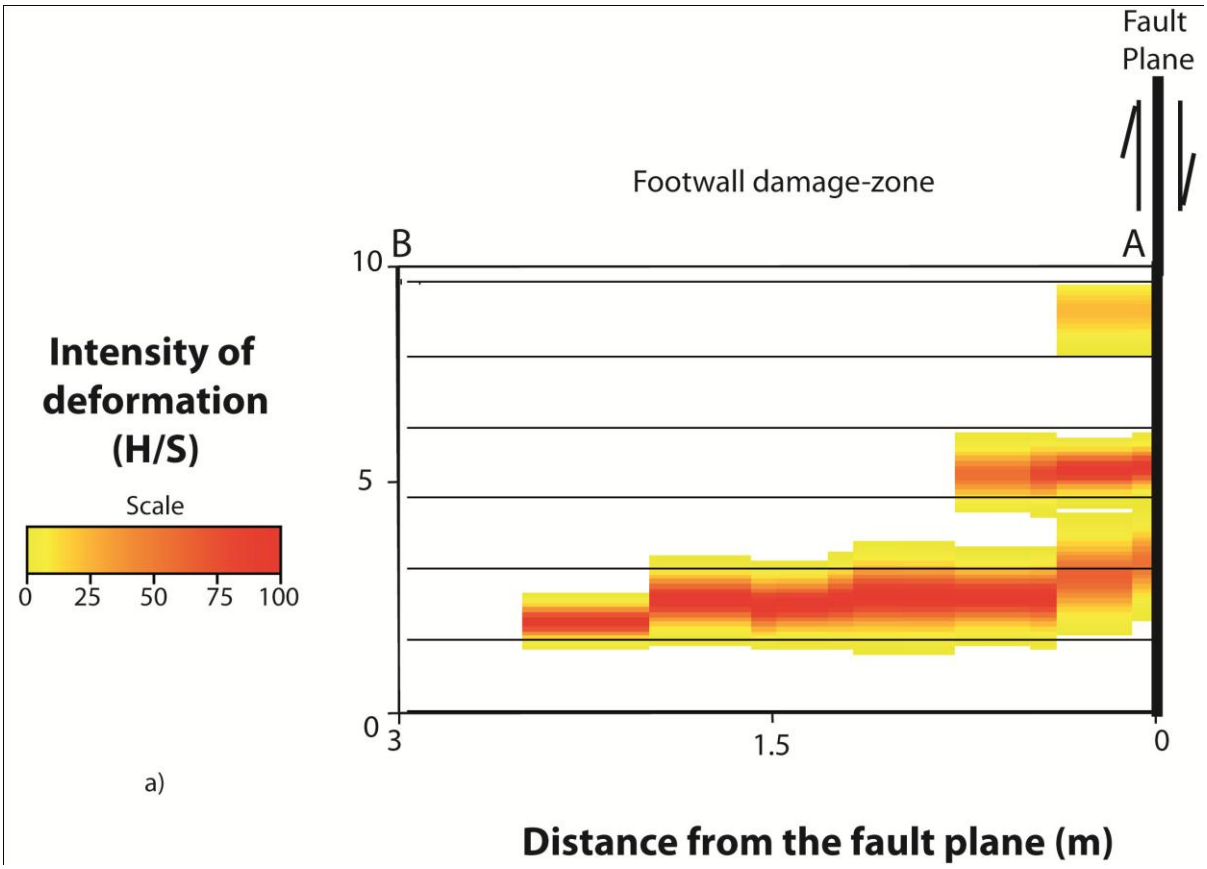

Fig. 5.63 - Gaussian fit transect analysis of the Tornimparte 3 fault footwall (scan line A-B see Fig. 5.20)

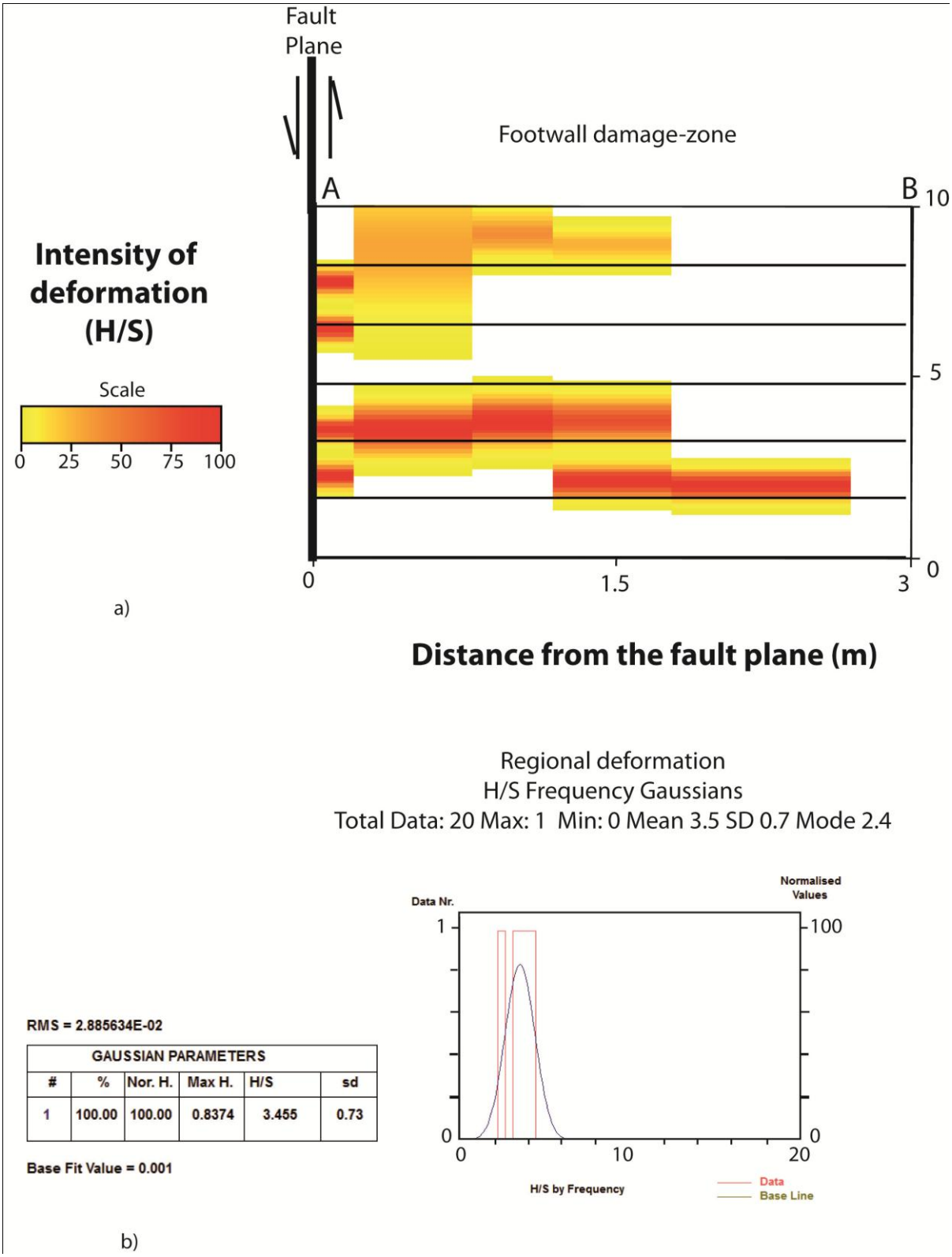

Fig. 5.64 - Gaussian fit transect analysis of the Tornimparte 5 fault footwall scan line (A-B see Fig. 5.21); *b)* Regional deformation mean value

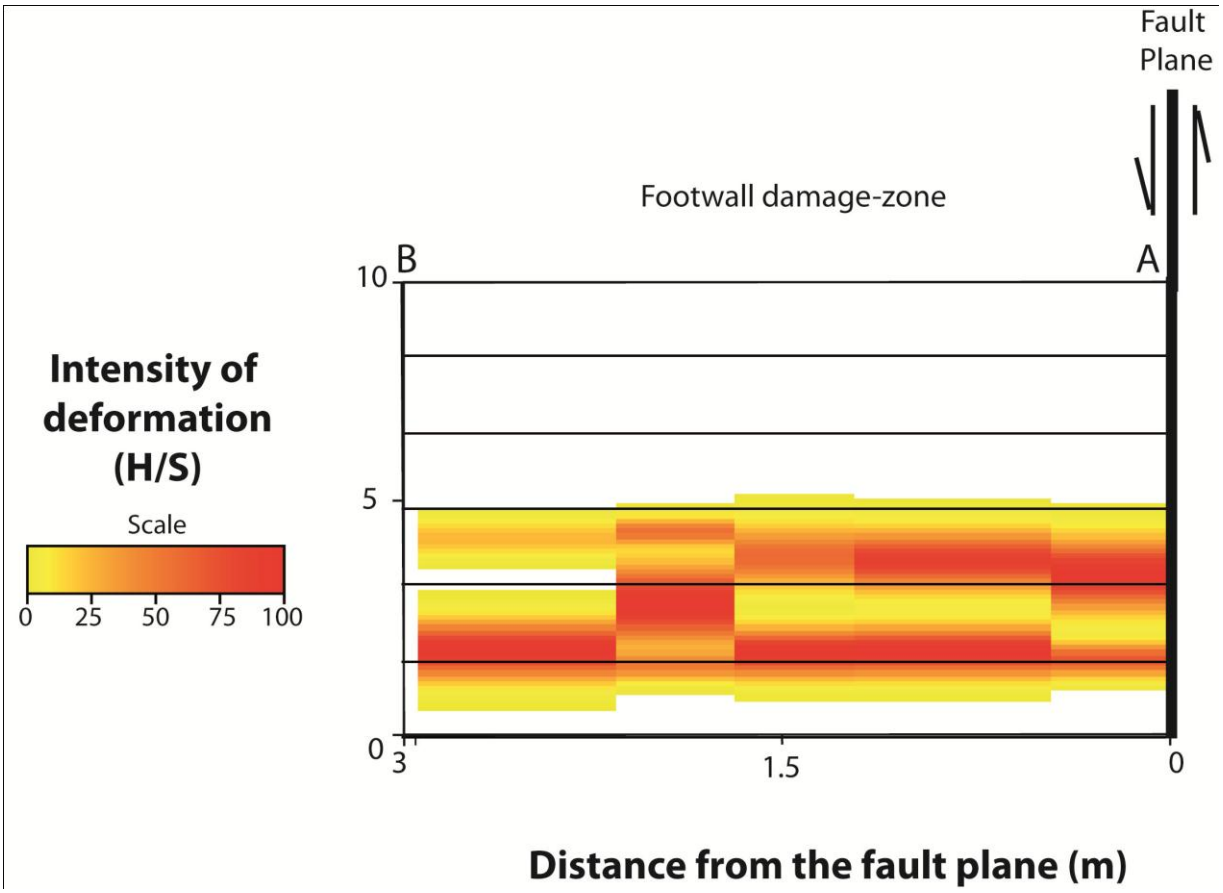

Fig. 5.65 - Gaussian fit transect analysis of the Lecce dei Marsi 1 fault footwall (scan line A-B Fig. 5.29)

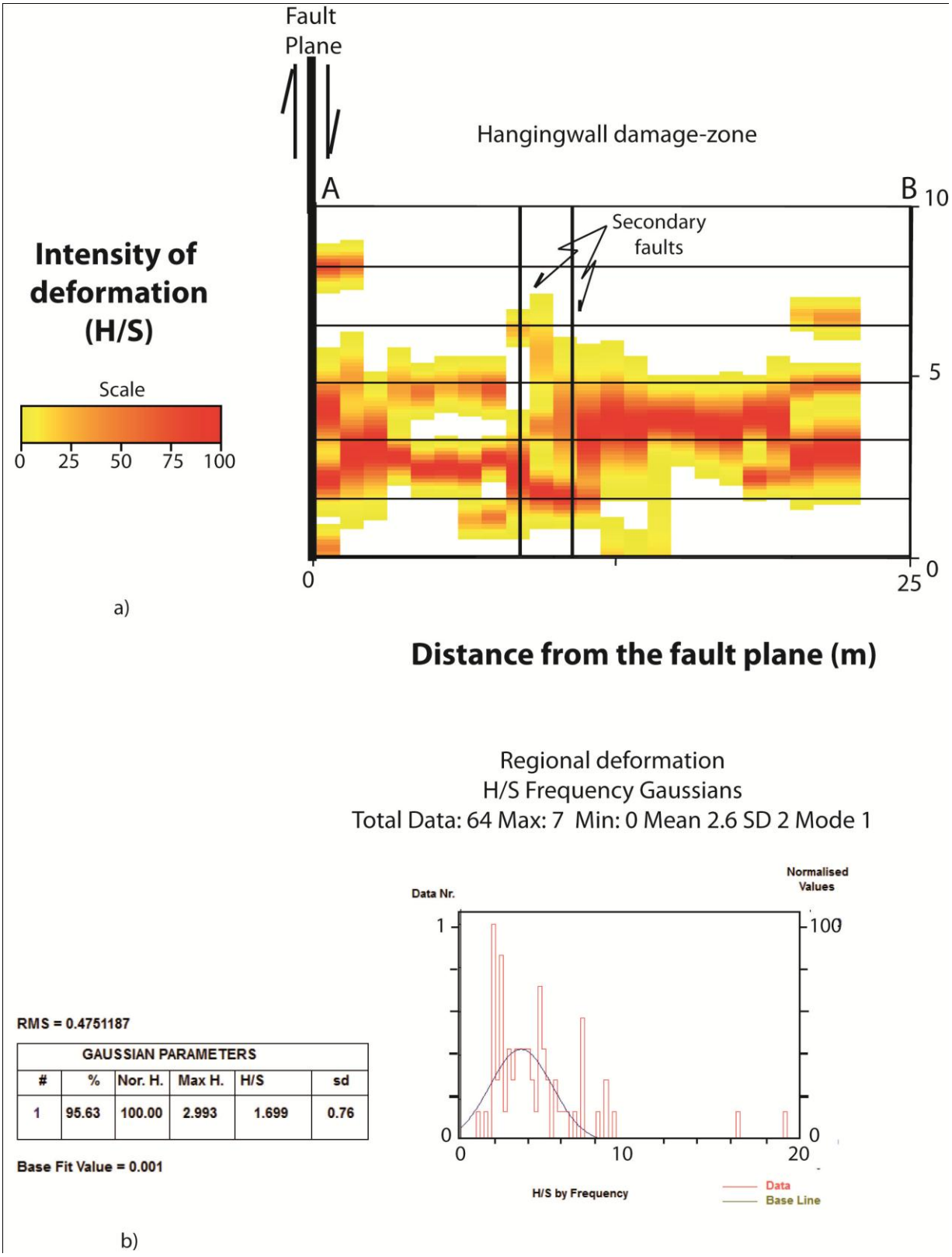

Fig. 5.66 - Gaussian fit transect analysis of the Lecce dei Marsi 2 fault hangingwall scan line (A-B see Fig. 5.30); *b)* Regional deformation mean value

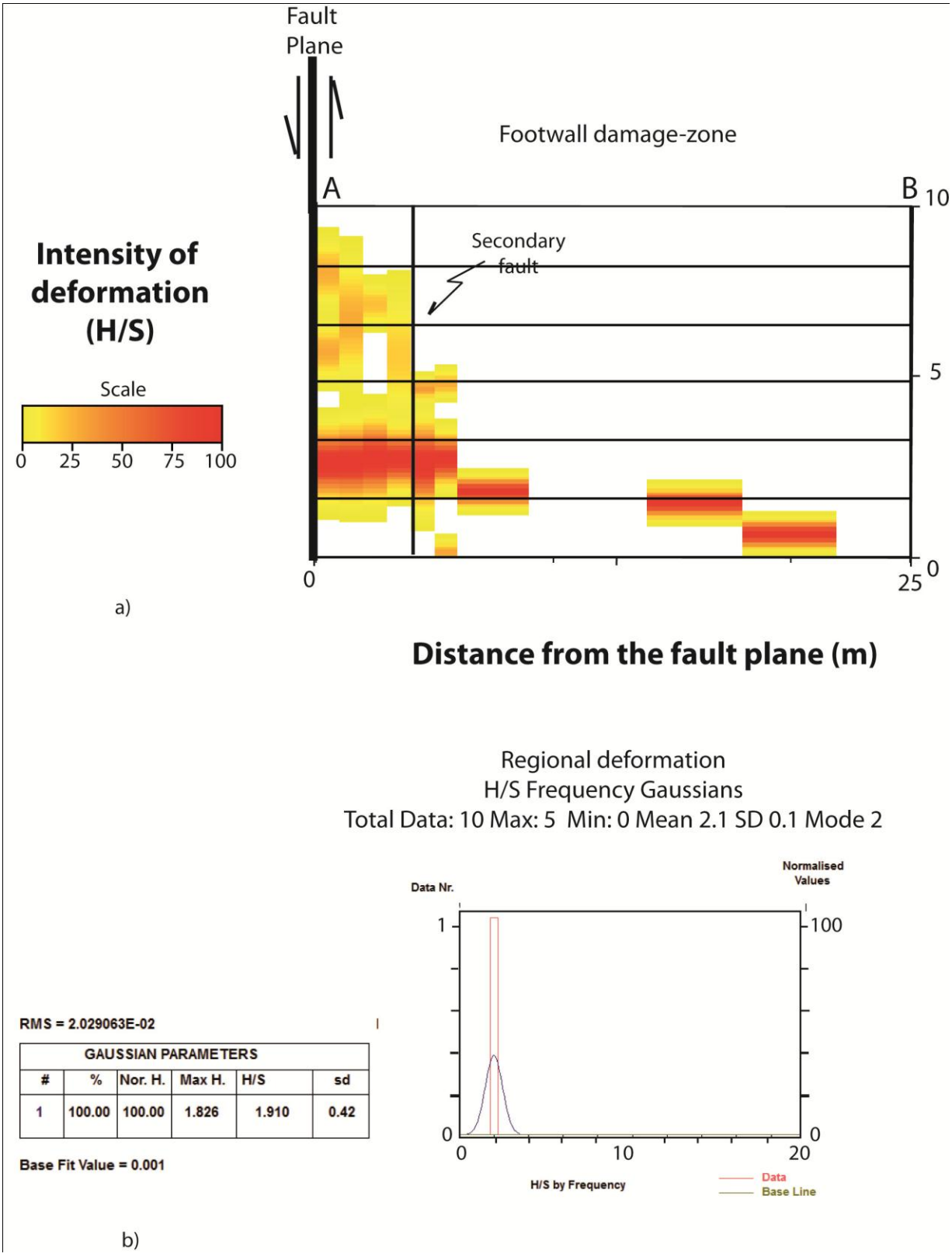

Fig. 5.67 - Gaussian fit transect analysis of the Gole del Sagittario fault footwall (scan line A-B see Fig. 5.34); *b)* Regional deformation mean value

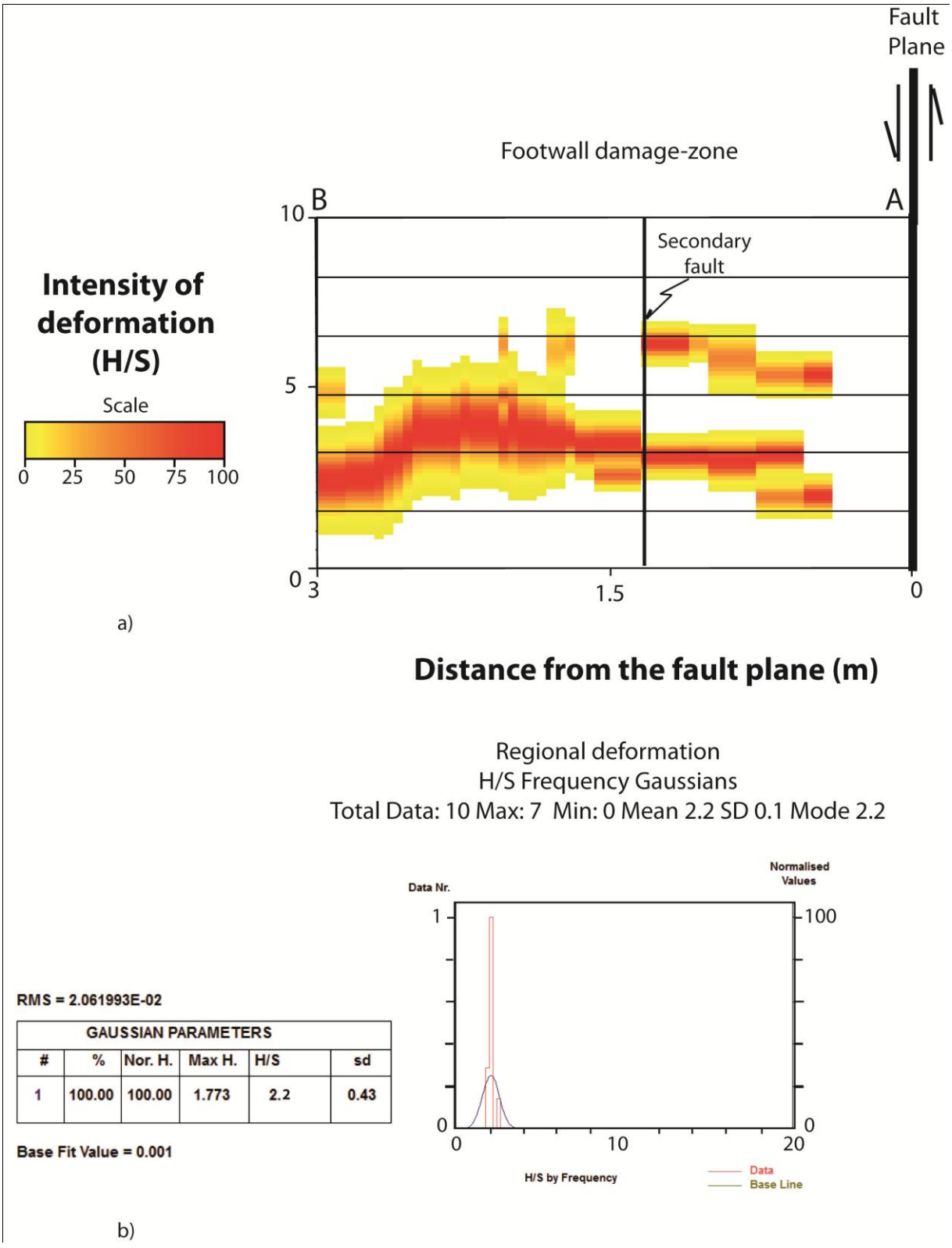

Fig. 5.68 - Gaussian fit transect analysis of the Castel di Ieri fault footwall (scan line A-B see Fig. 5.37); *b)* Regional deformation mean value

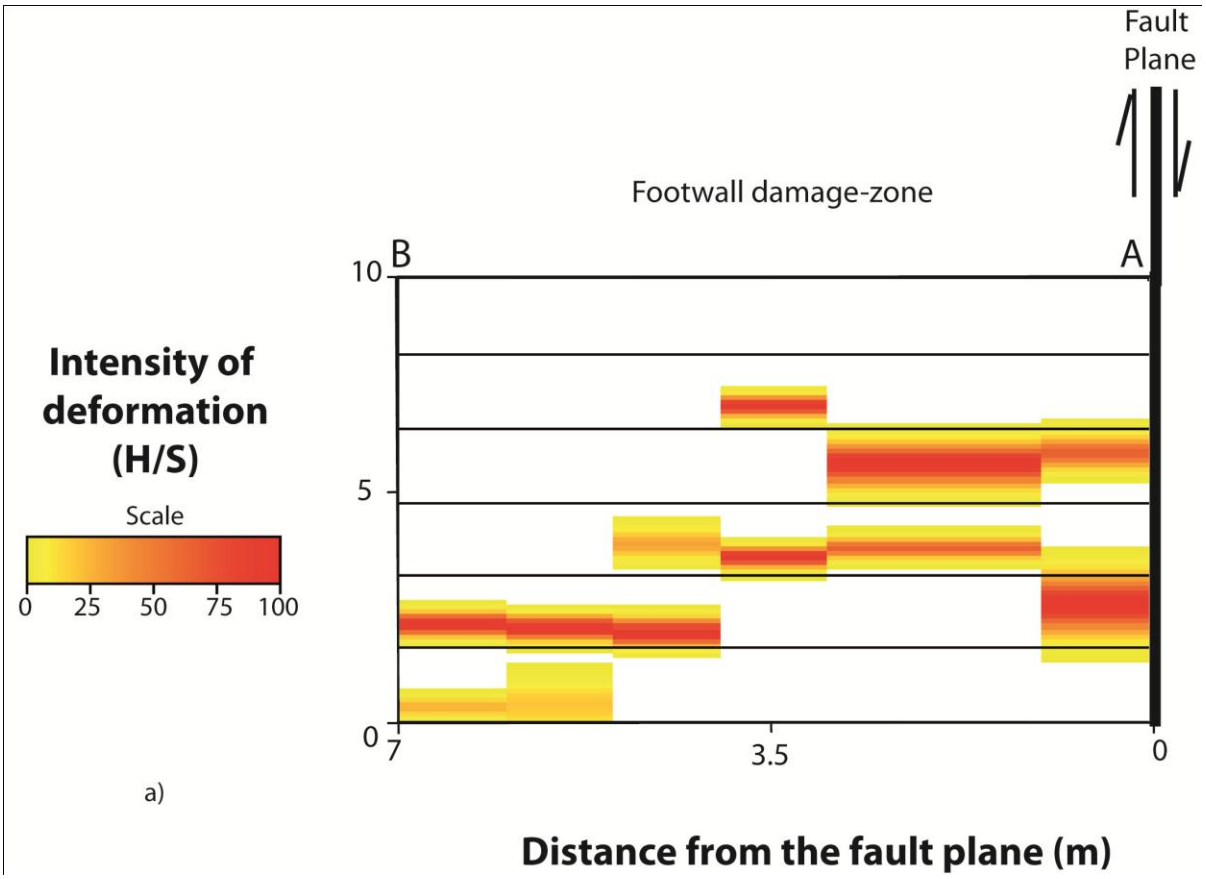

Fig. 5.69 - Gaussian fit transect analysis of the Fara 1 fault footwall (scan line A-B see Fig. 5.41)

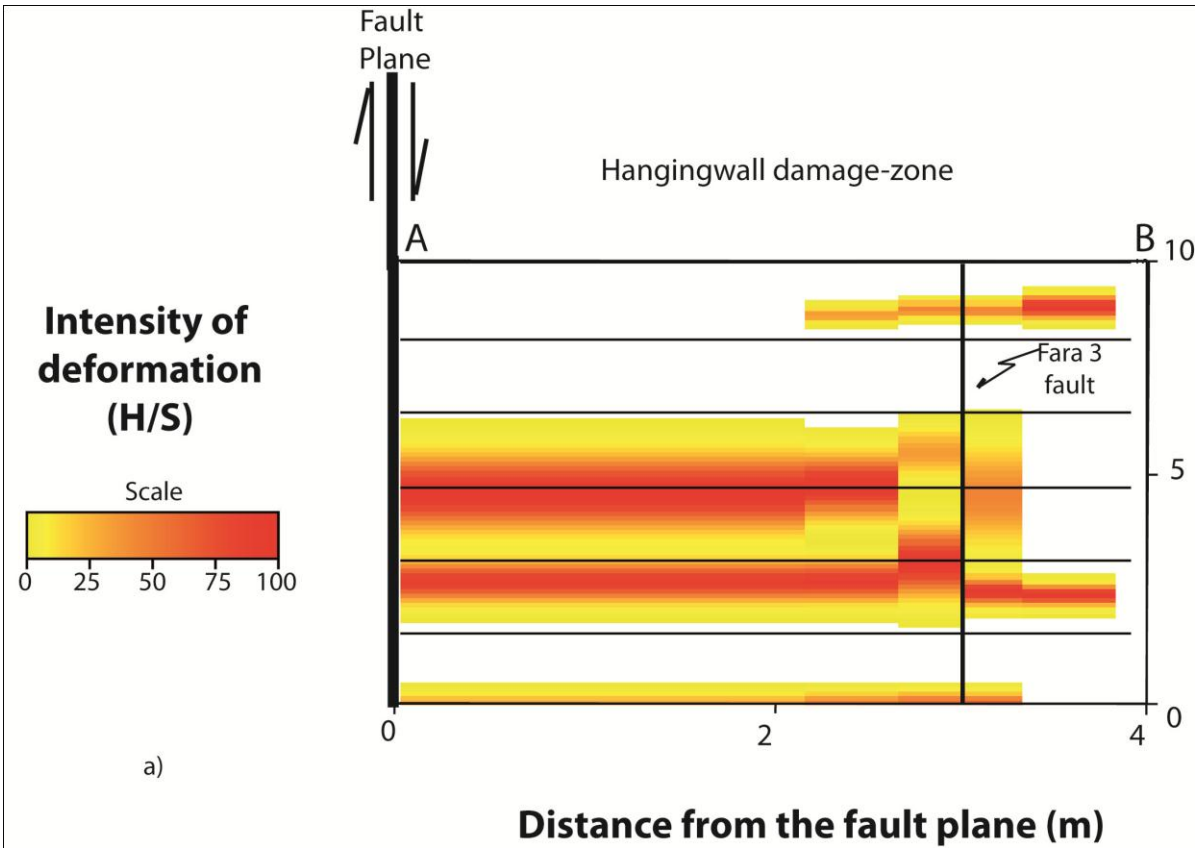

Fig. 5.70 - Gaussian fit transect analysis of the Fara 3 fault hangingwall scan line (A-B see Fig. 5.42)

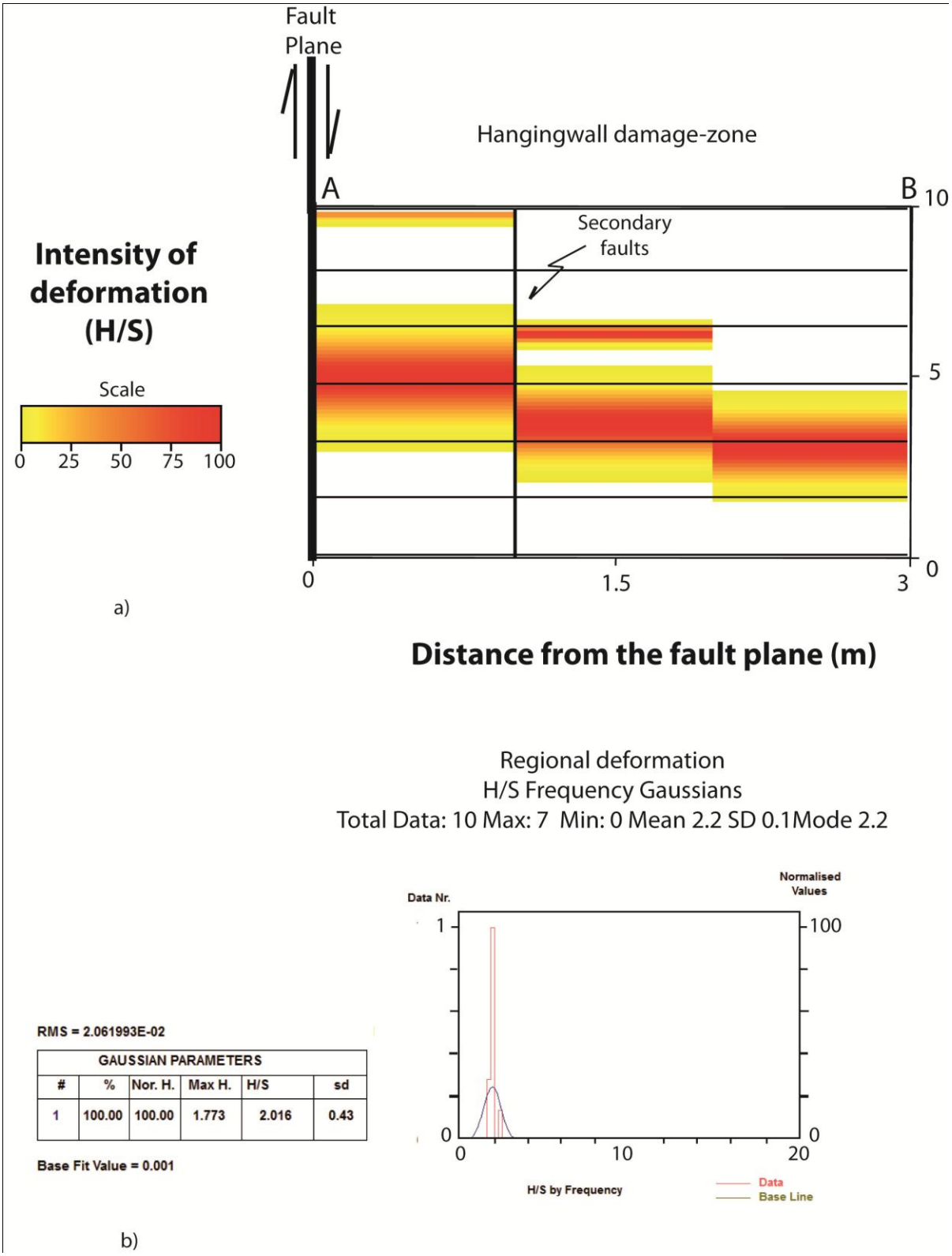

Fig. 5.71 - Gaussian fit transect analysis of the Fara 4 fault hangingwall (scan line A-B see Fig. 5.43); *b)* Regional deformation mean value

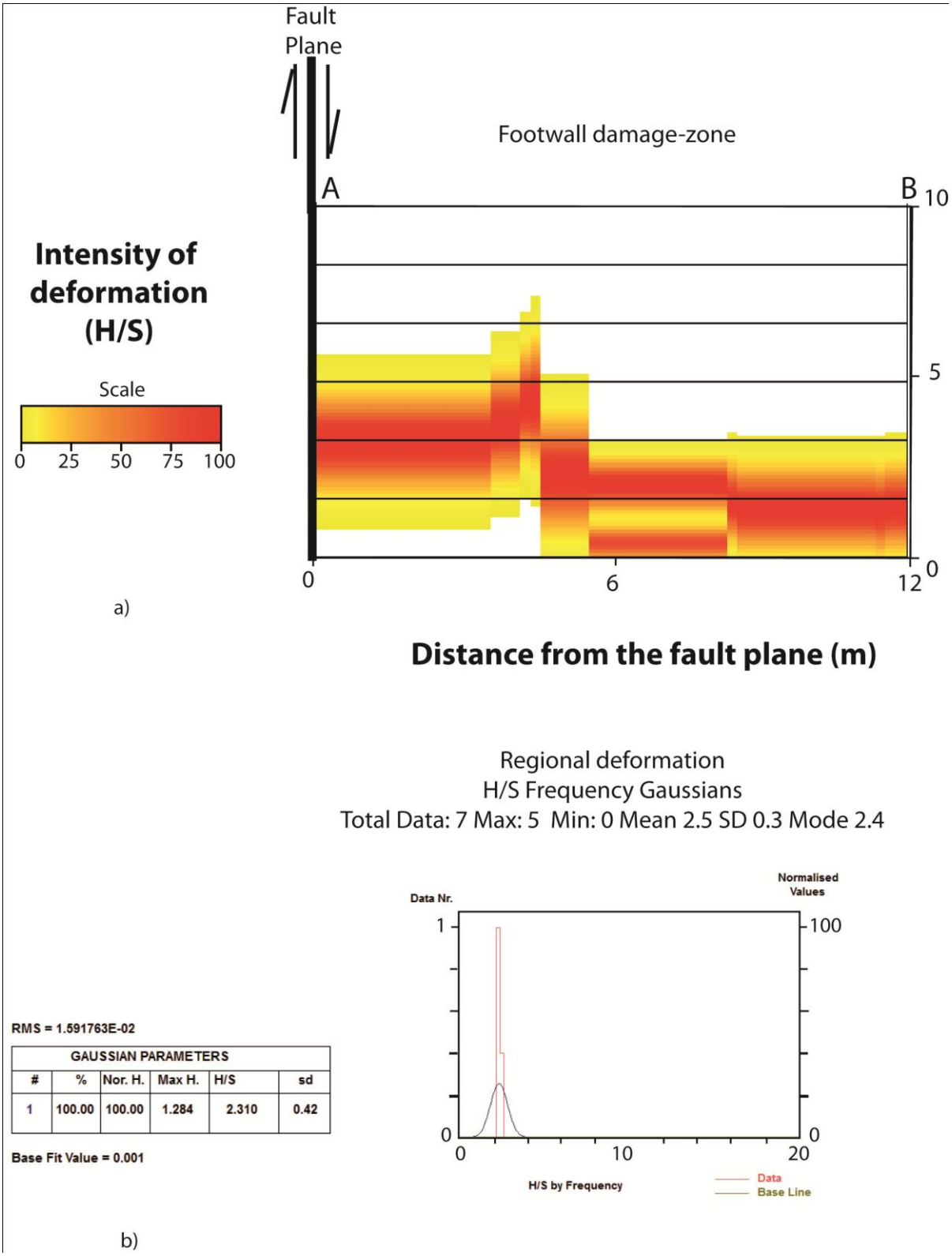

Fig. 5.72 - Gaussian fit transect analysis of the Fara 6 fault footwall scan line (A-B see Fig. 5.44); *b)* Regional deformation mean value

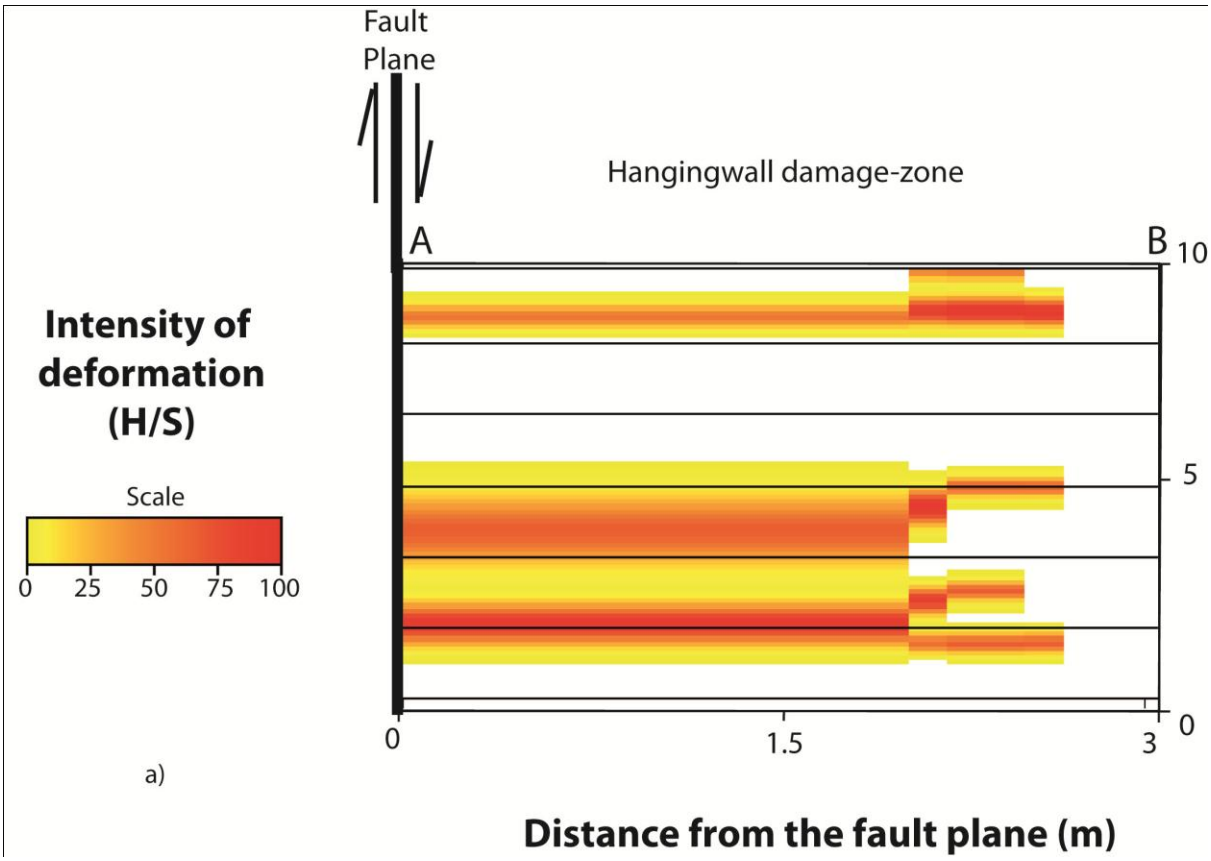

Fig. 5.73 - Gaussian fit transect analysis of the Palena 3 fault hangingwall scan line (A-B see Fig. 5.45)

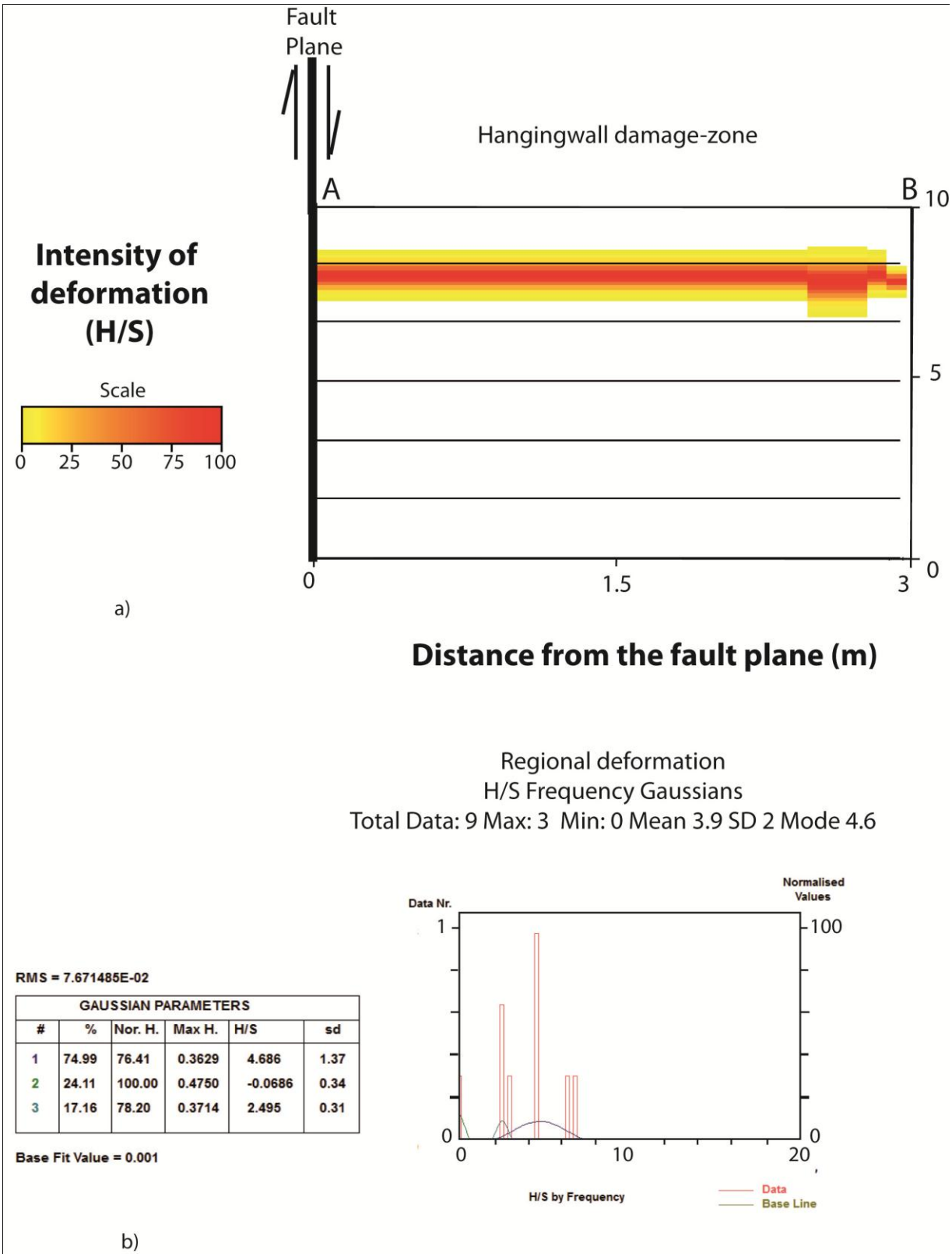

Fig. 5.74 - Gaussian fit transect analysis of the Palena 4 fault hangingwall (scan line A-B see Fig. 5.45); *b)* Regional deformation mean value

5.5.2 Damage-zone width

A new methodology was prepared to define the limit between the fault rock and the pristine rock. In particular, in the current work the limit between the damage-zone and the pristine rock was fixed at the distance where both the azimuth and the H/S stabilize on the regional values.
The methodology was tested on the complete fault database. In this section will be presented and discussed the results of 6 faults (Ienne fault, the Pietrasecca fault, the Filettino fault, the Fara 1 fault, the Fara 4 fault and the Rocca di Cave fault), which represent a sample of the fault variability in term of throw and dimension.

Rocca di Cave 1 fault

The FRF azimuth rotates increasing the distance from the fault plane (Fig. 5.75 *b*). The frequency of the regional fracture system E 15° increases at the distance of 2.2 m from the fault plane. The H/S stabilizes the regional value of 5 H/S at 2.7 m from the fault plane (Fig. 5.75 *a*). The limit between the damage-zone and the pristine rock is fixed at 2.5 m from the fault plane.

Filettino fault

The FRF azimuth rotates increasing the distance from the fault plane (Fig. 5.76 *b*). The frequency of the regional fracture system E 81° increases at the distance of 27 m from the fault plane. The H/S stabilizes the regional value of 2.7 H/S at 20 m from the fault plane (Fig. 5.76 *a*). The limit between the damage-zone and the pristine rock is fixed at 24 m from the fault plane.

Ienne fault

The FRF azimuth and the H/S spatial analysis one have been compared and the results are showed in Fig. 5.77. The azimuth rotates increasing the distance from the fault plane. The frequency of the regional fracture system E 48° increases at the distance of 18 m from the fault plane (Fig. 5.77 *b*). The H/S stabilizes the regional value of 2.7 H/S at 22.5 m from the fault plane (Fig. 5.77 *a*). The limit between the damage-zone and the pristine rock is fixed at 20.2 m from the fault plane.

Pietrasecca fault

The FRF azimuth rotates increasing the distance from the fault plane (Fig. 5.78 *b*). The frequency of the regional fracture system increases at the distance of 6.5 m from the fault plane. The H/S stabilizes the regional value of 2.2 H/S between 6.5 and 12.5 m from the fault plane (Fig. 5.78 *a*). The limit between the damage-zone and the pristine rock is fixed at 9 m from the fault plane.

Fara 1 fault

The FRF azimuth rotates increasing the distance from the fault plane (Fig. 5.79 *b*). The frequency of the regional fracture system increases at the distance of 4.5 m from the fault plane. The H/S stabilizes the regional value of 2.2 H/S at 6 m from the fault plane (Fig. 5.79 *a*). The limit between the damage-zone and the pristine rock is fixed at 5.5 m from the fault plane.

Fara 4 fault

The FRF azimuth rotates increasing the distance from the fault plane (Fig. 5.79 *b*). The frequency of the regional fracture system increases at the distance of 1.8 m from the fault plane. The H/S stabilizes to the regional value of 2.2 H/S at 1.8 m from the fault plane (Fig. 5.79 *a*). The limit between the damage-zone and the pristine rock is fixed at 1.8 m from the fault plane.

The computed damage-zone widths of the fault complete database, including both seismic and subseismic faults, are compared with the fault H/S deformation values (Fig. 5.81 *a*). The data show a poor correlation having R^2= 0.09. Otherwise, considering the subseismic scale faults (Fig. 5.81 *b*), the data are plotted by a linear trend having R^2= 0.72. This result suggests that the increase of the stress intensity produces an increase of the deformation intensity (H/S), and also an increase of the damage-zone width.

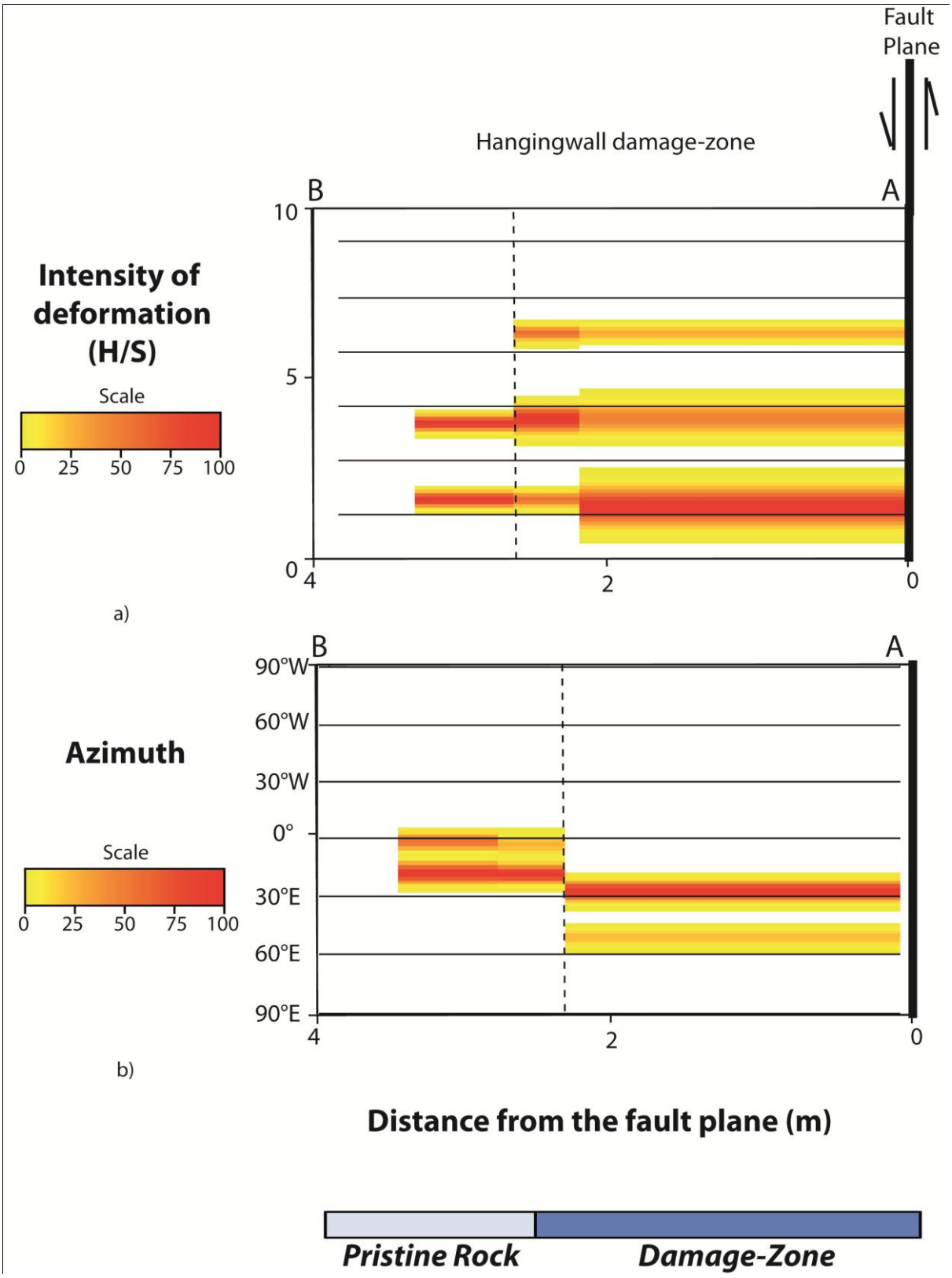

Fig. 5.75 – Limit between the damage zone and the pristine rock for the Rocca di Cave 1 fault; *a)* H/S spatial analysis; *b)* Azimuth spatial analysis. The dashed lines correspond to the limits between the damage-zone and the pristine rock.

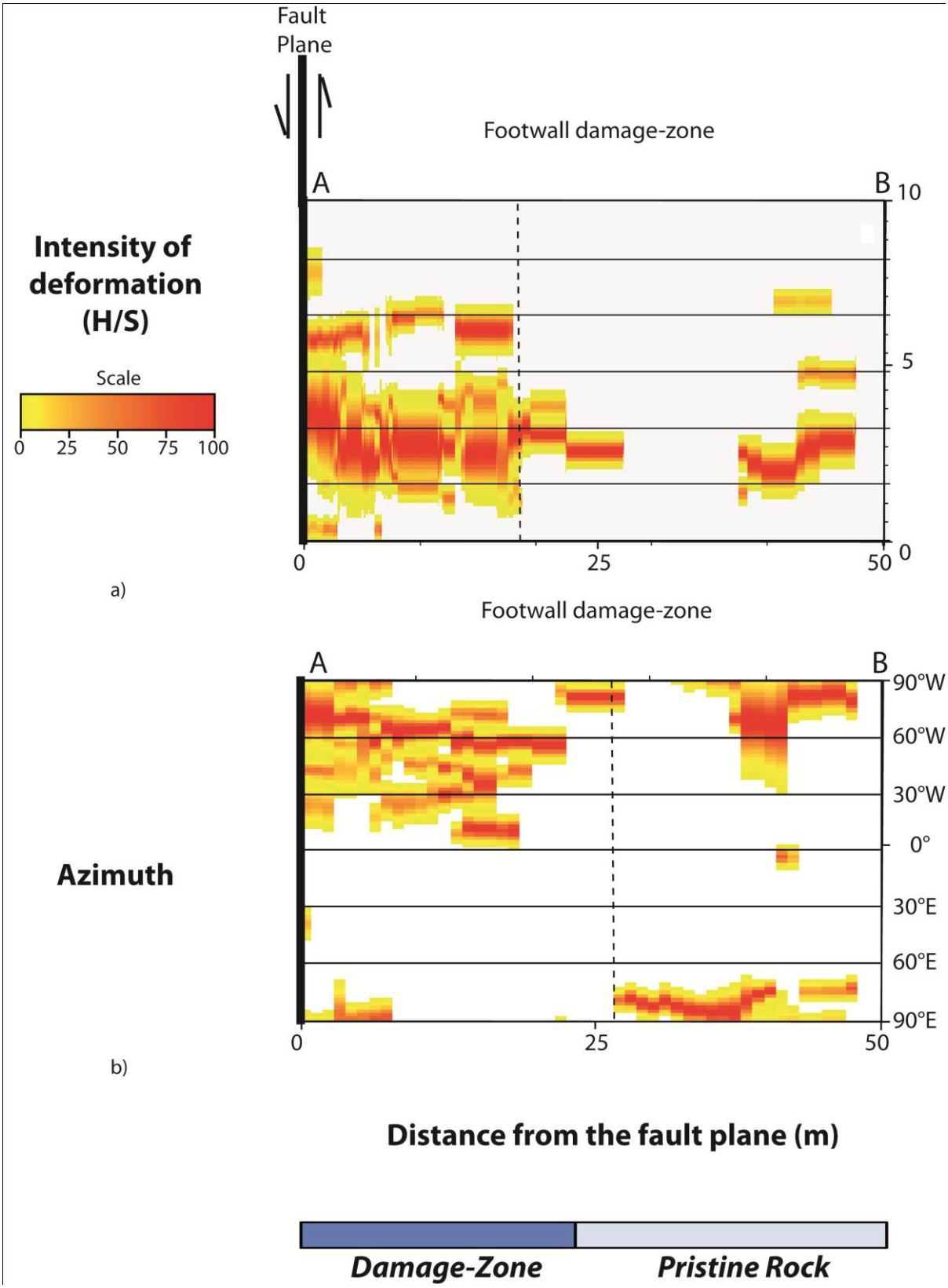

Fig. 5.76 - Limit between the damage zone and the pristine rock for the Filettino fault; *a)* H/S spatial analysis; *b)* Azimuth spatial analysis. The dashed lines correspond to the limits between the damage-zone and the pristine rock.

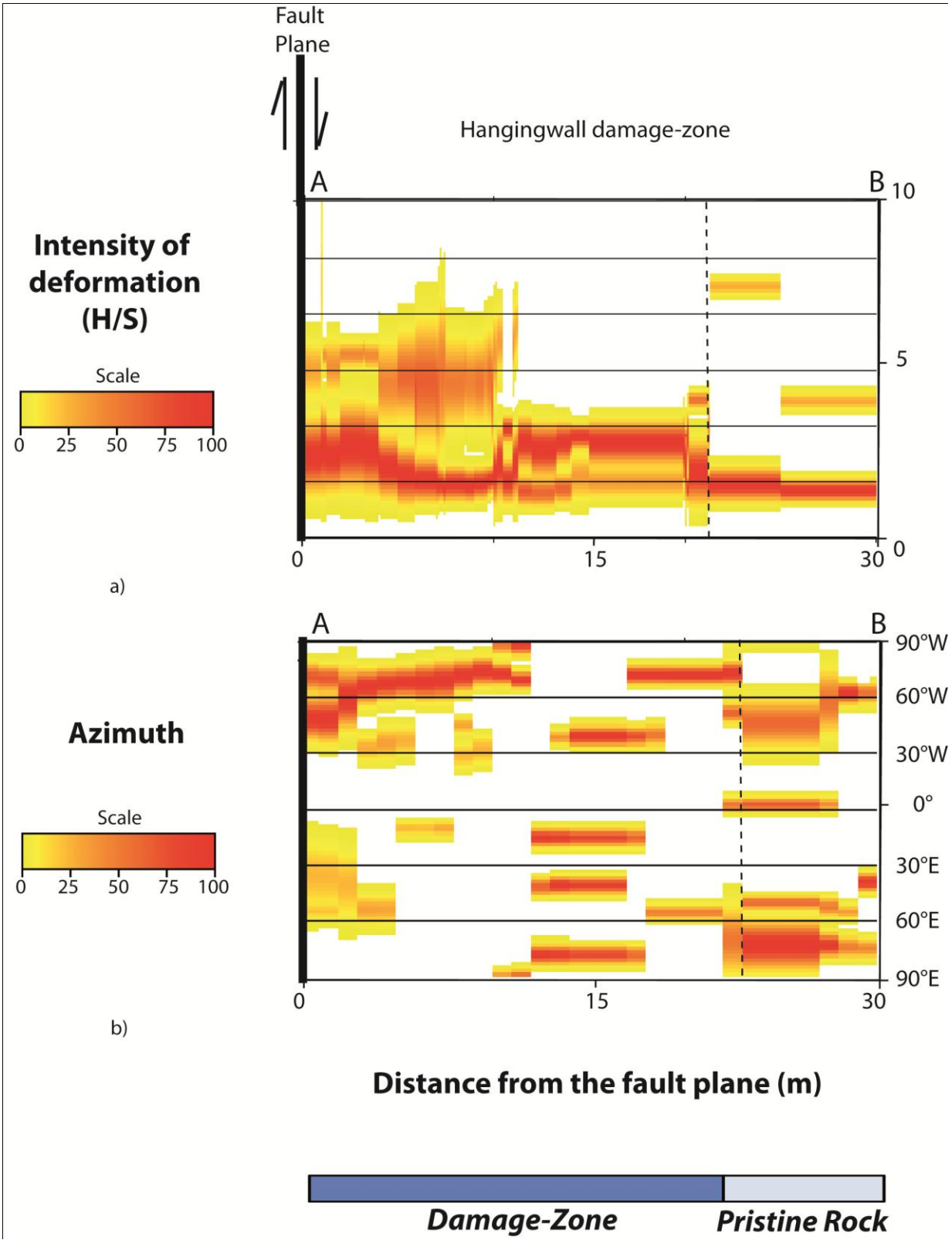

Fig. 5.77 - Limit between the damage zone and the pristine rock for the Ienne fault; *a)* H/S spatial analysis; *b)* Azimuth spatial analysis. The dashed lines correspond to the limits between the damage-zone and the pristine rock.

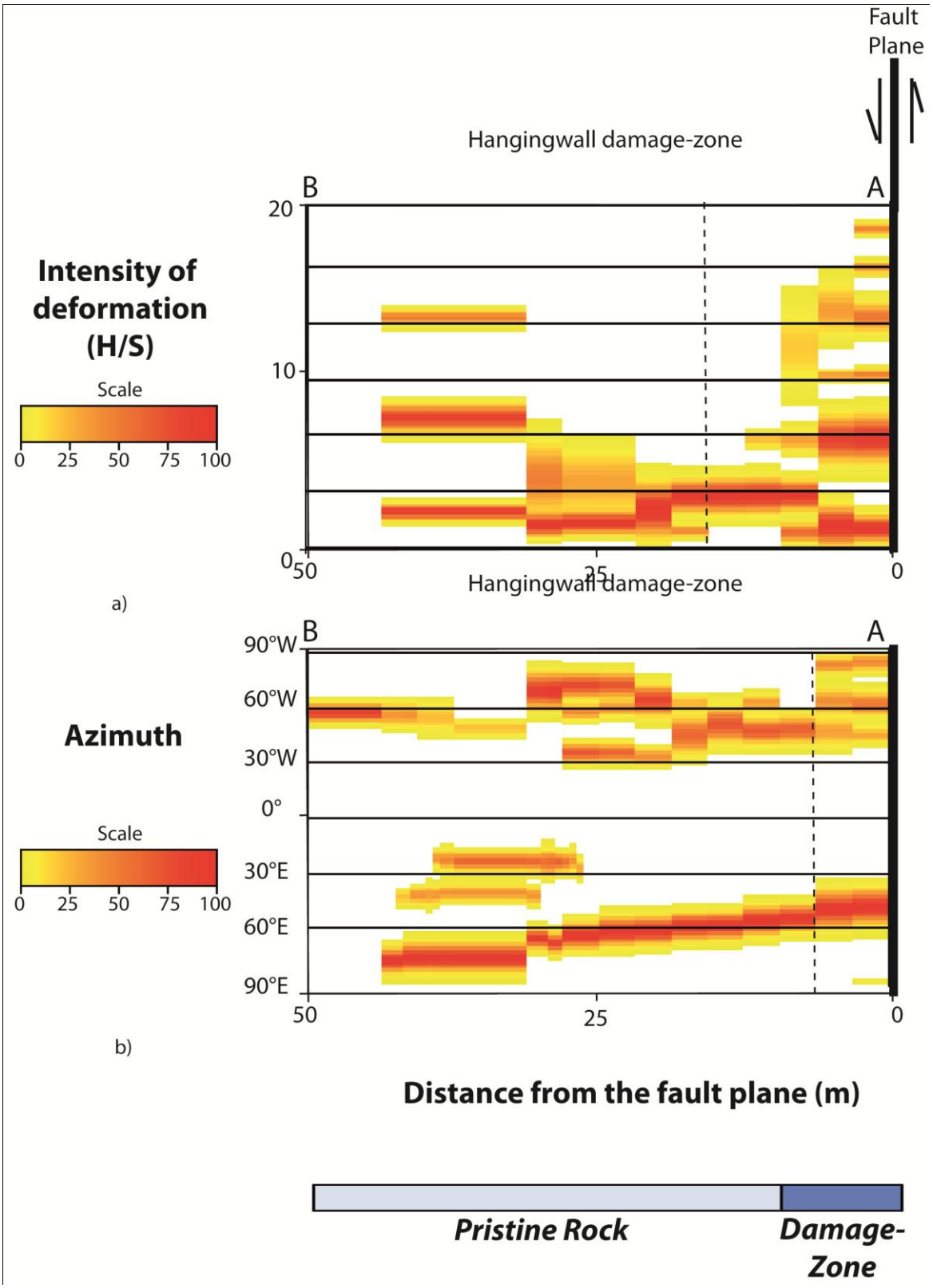

Fig. 5.78 - Limit between the damage zone and the pristine rock for the Pietrasecca fault; *a)* H/S spatial analysis; *b)* Azimuth spatial analysis. The dashed lines correspond to the limits between the damage-zone and the pristine rock.

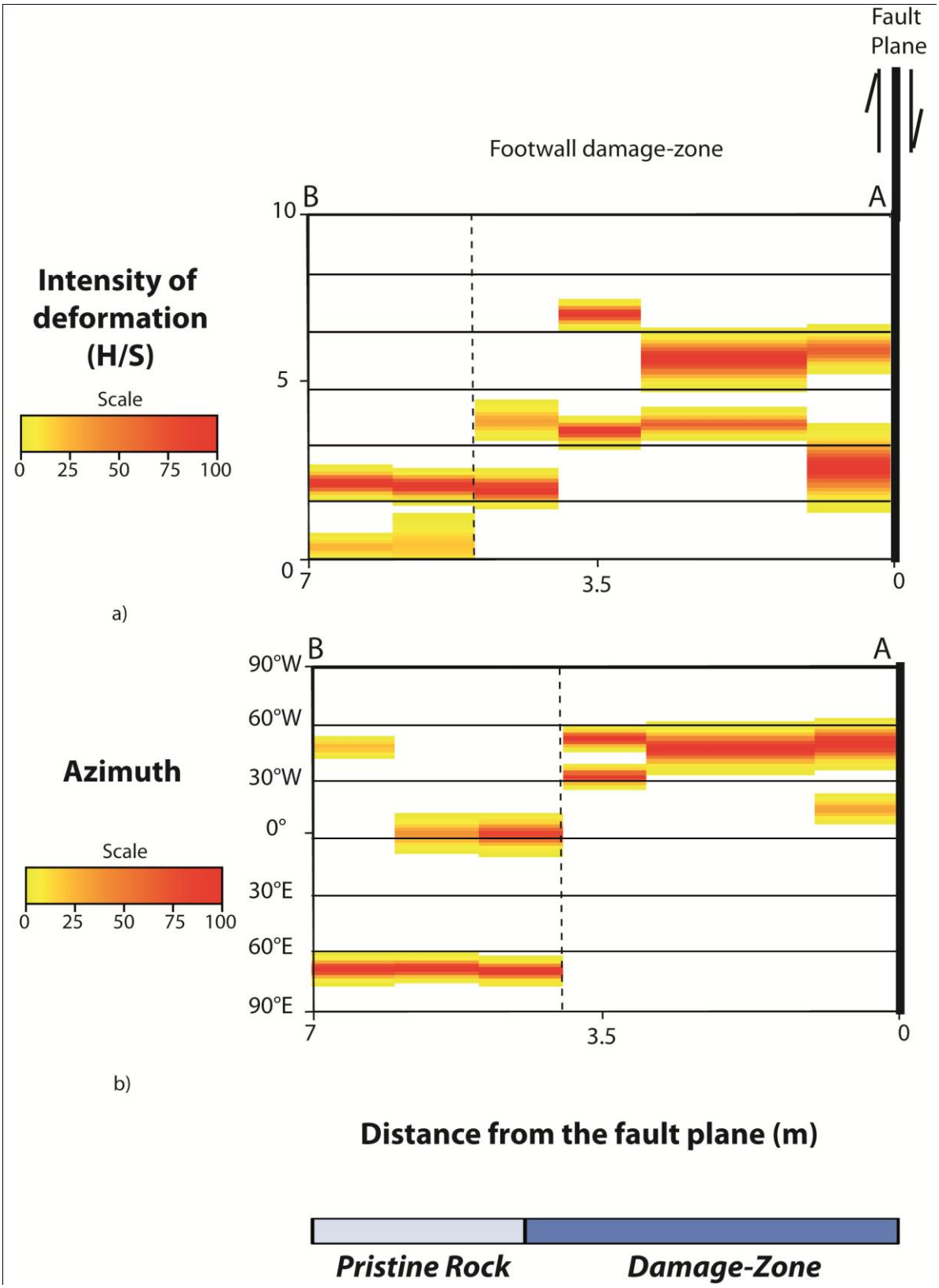

Fig. 5.79 - Limit between the damage zone and the pristine rock for the Fara 1 fault; *a)* H/S spatial analysis; *b)* Azimuth spatial analysis. The dashed lines correspond to the limits between the damage-zone and the pristine rock.

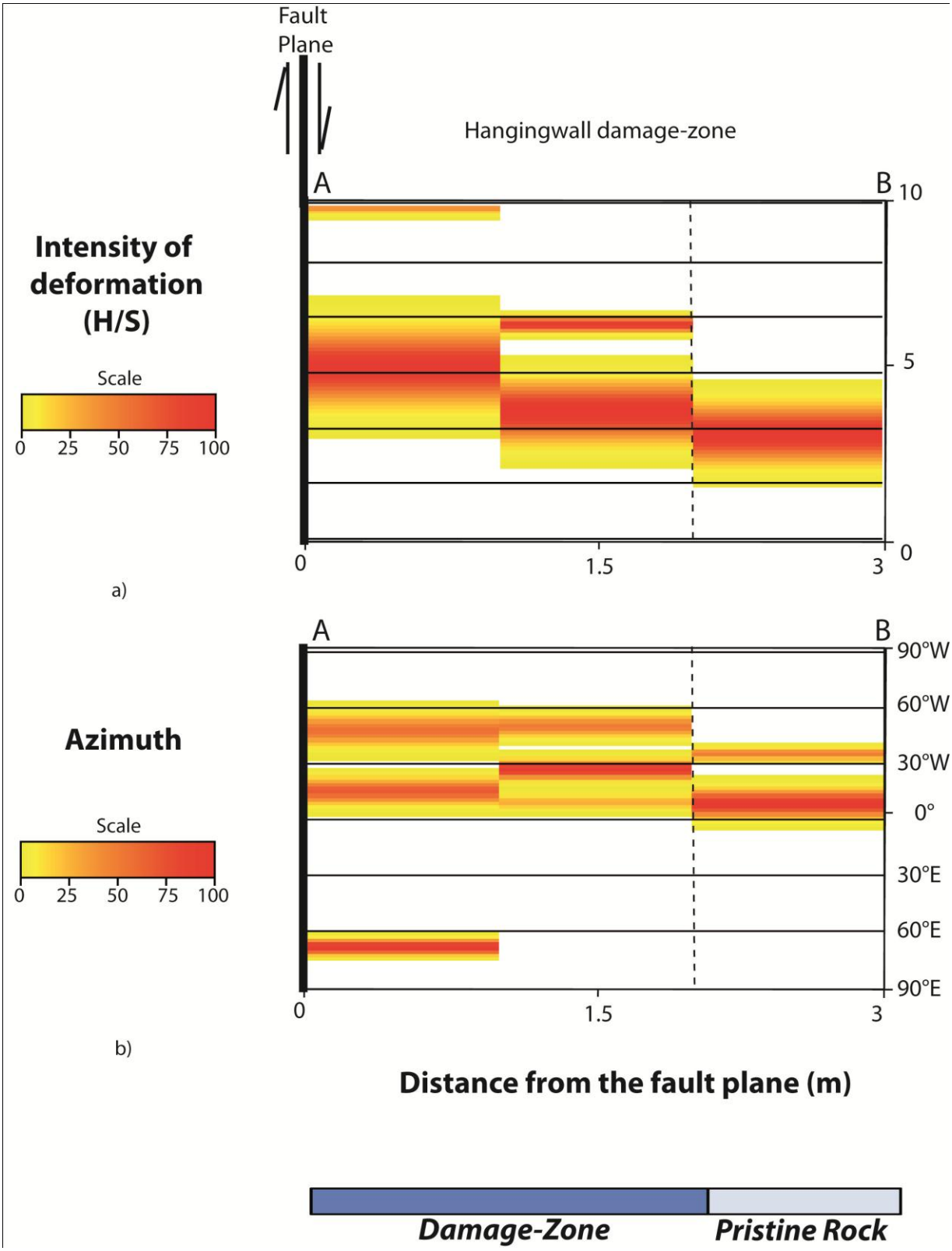

Fig. 5.80 - Limit between the damage zone and the pristine rock for the Fara 4 fault; *a)* H/S spatial analysis; *b)* Azimuth spatial analysis. The dashed lines correspond to the limits between the damage-zone and the pristine rock.

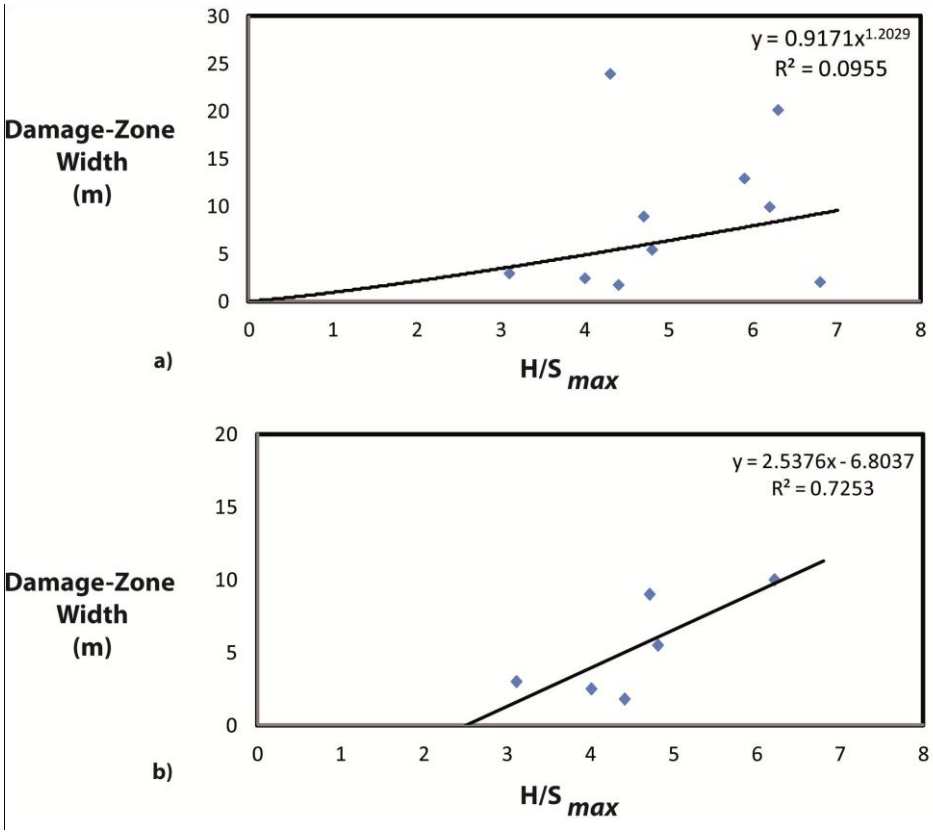

Fig. 5.81 – Damage-zone widths versus H/S maximum values; *a)* Seismic and subseismic scale faults; *b)* Subseismic scale faults

5.5.2.2 Fault core and damage-zone width

All of the analysed faults contain damage-zones, but only some of that have fault-cores. The fault-cores have been described (see the section 5.1) and their thickness has been measured (Tab. 5.3). The studied faults can be divided in 3 main groups basing on the fault-core type:

1) No Fault-Core
2) Recemented Fault-Core
3) Continuous Fault-Core

The seismic scale faults are characterized essentially by a recemented fault-core, except the case of the Gole del Sagittario fault. The recementation process is related to the fluid circulation, which in turn is probably related to the recent activity of faults. Also the fault-core thickness is probably related to the fault activity. For example, the Castel di Ieri fault is a seismic scale active fault which fault-core is recemented with a thick value of 20 m. On the other hand, the Filettino fault is a seismic scale inactive fault characterized by lower value of fault-core width (7 m).

5.5.3 Hangingwall and footwall deformation

The fault hangingwall (HW) and footwall (FW) deformation patterns have been investigated where the outcrop exposure allows studying both the zones. This analysis has been performed on 7 faults are presented.

5.5.3.1 H/S spatial analysis

In this section by the Gaussian fit and the Mean value transect analysis results are presented.

Filettino fault

The HW and the FW show the same H/S mean value on the fault plane, that is 4.8 (Fig. 5.82 *b*). On the other hand, the Gaussian fit analysis shows different most frequent highest H/S values, that are 7 and 5 respectively (Fig. 5.82 *a*), suggesting that the HW is more deformed than the FW. The damage-zones show different widths as well: 24 m for the footwall and 20 m for the hangingwall.

Tornimparte 2 fault

The HW and the FW show the same H/S mean value on the fault plane, that is 6.6 (Fig. 5.83 *b*). The Gaussian fit analysis shows different most frequent highest H/S values, that are 3.5 for the HW and 2 for the FW (Fig. 5.83 *a*).

Tornimparte 3 fault

The HW and the FW show the different H/S mean values on the fault plane (Fig. 5.84 *b*), that are 5.3 for the HW and 4.8 for the FW. The Gaussian fit analysis shows that the most frequent highest H/S values are 5.3 for the HW and 3.3 for the FW (Fig. 5.84 *a*).

Tornimparte 5 fault

The mean value analysis (Fig. 5.85 *b*) shows that on the fault plane the HW is more deformed then the FW (6.8-3.3 respectively). The Gaussian fit analysis shows that the highest most frequent H/S value is 8 for the HW and 3.3 for the FW (Fig. 5.85 *a*).

Fara 1 fault

The mean value analysis (Fig. 5.86 *b*) shows higher value in the HW (5.7) than the FW (4.6). The Gaussian fit analysis shows that the most frequent highest H/S value is 8.4 for the HW and 7 for the FW (Fig. 5.86 *a*).

Fara 2 fault

The mean value analysis (Fig. 5.87 *b*) shows a HW more deformed then the FW (5-3.5 respectively). The Gaussian fit analysis shows that the most frequent highest H/S value is 5 for the HW and 2.7 for the FW (Fig. 5.87 *a*).

Fara 3 fault

The mean value analysis (Fig. 5.88 *b*) shows a HW more deformed then the FW (4.2-2.5 respectively) The Gaussian fit analysis shows that the most frequent highest H/S value is 8.4 for the HW and 7 for the FW (Fig. 5.88 *a*).

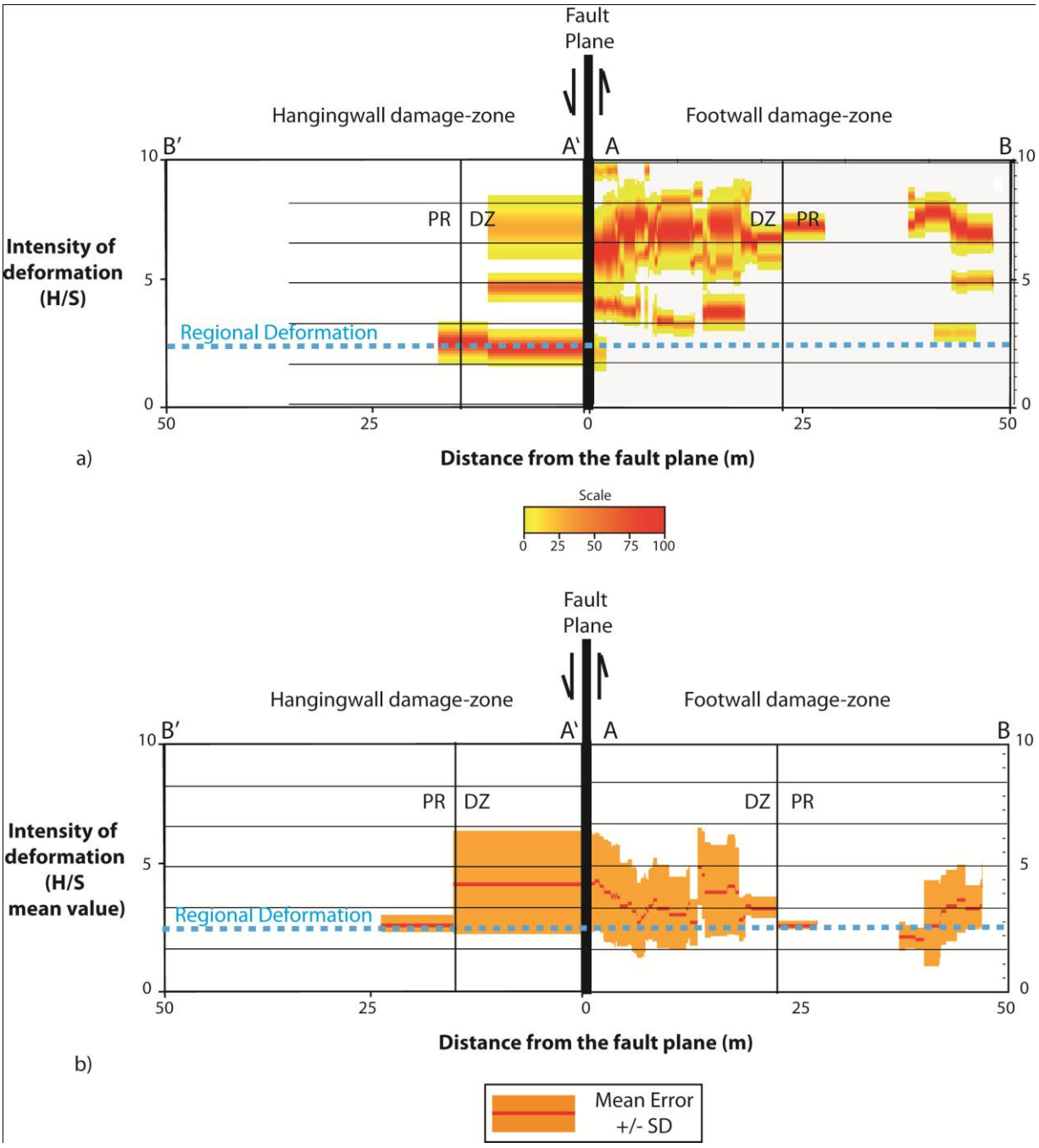

Fig. 5.82 – Comparison between the HW and FW deformation of the Filettino fault; *a)* H/S Gaussian Fit transects analysis; *b)* H/S Mean Value transects analysis. The dashed blue line corresponds to the regional deformation value; the black thin line corresponds to the limit between the damage-zone (DZ) and the pristine rock (PR)

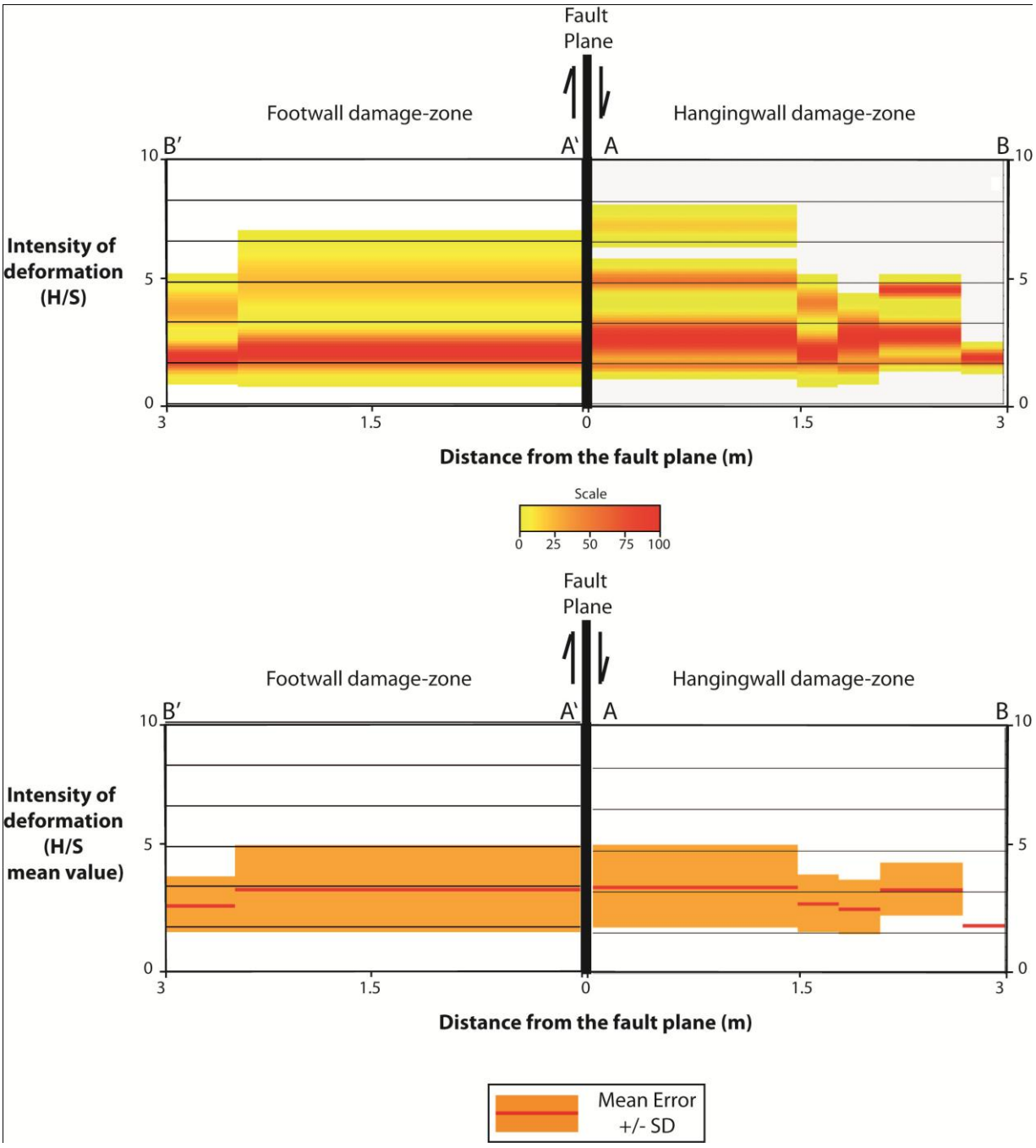

Fig. 5.83 – Comparison between the HW and FW deformation of the Tornimparte 2 fault; *a)* H/S Gaussian Fit transect analysis; *b)* H/S Mean Value transect analysis

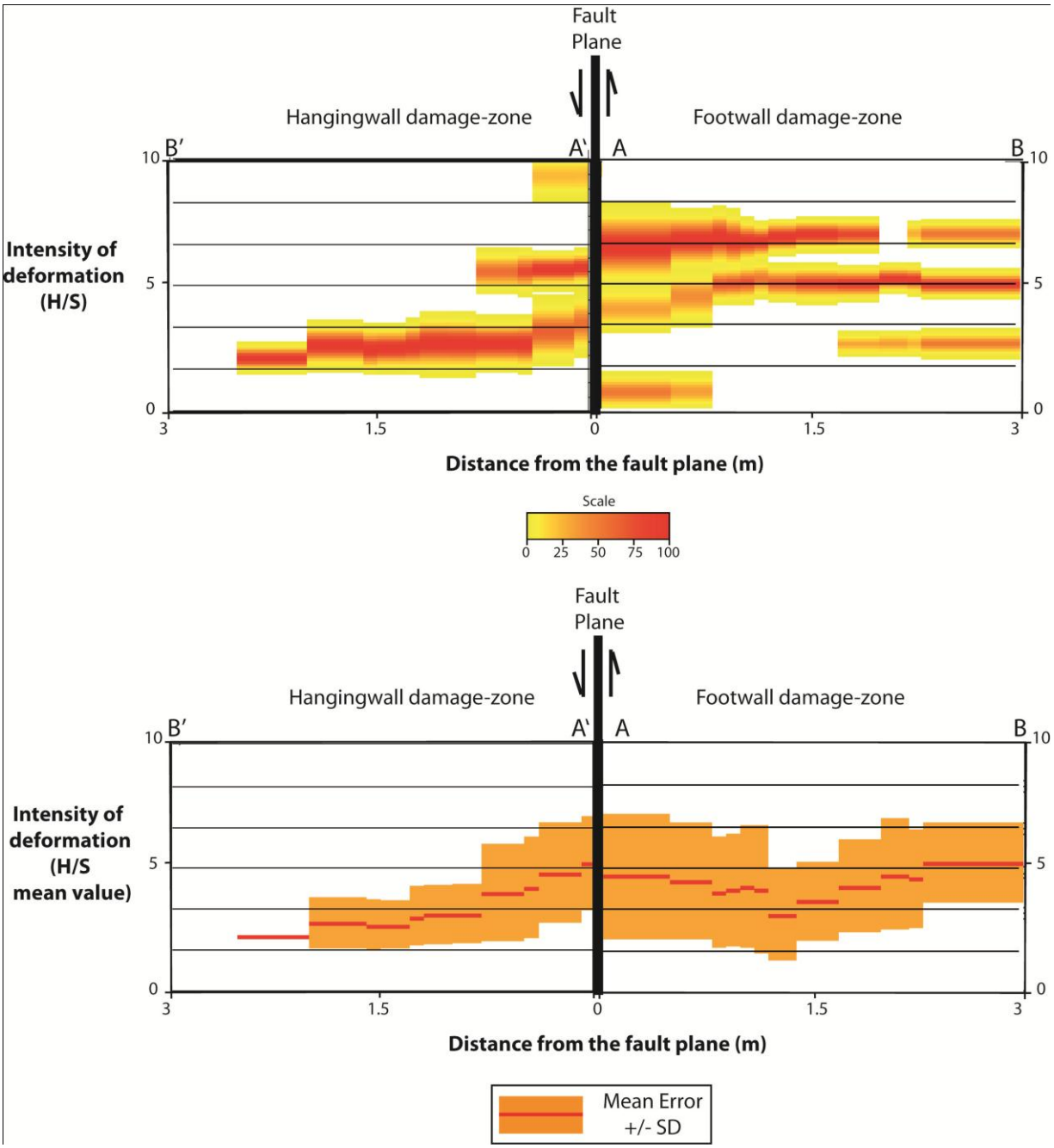

Fig. 5.84 - Comparison between the HW and FW deformation of the Tornimparte 3 fault; a) H/S Gaussian Fit transect analysis; b) H/S Mean Value transect analysis

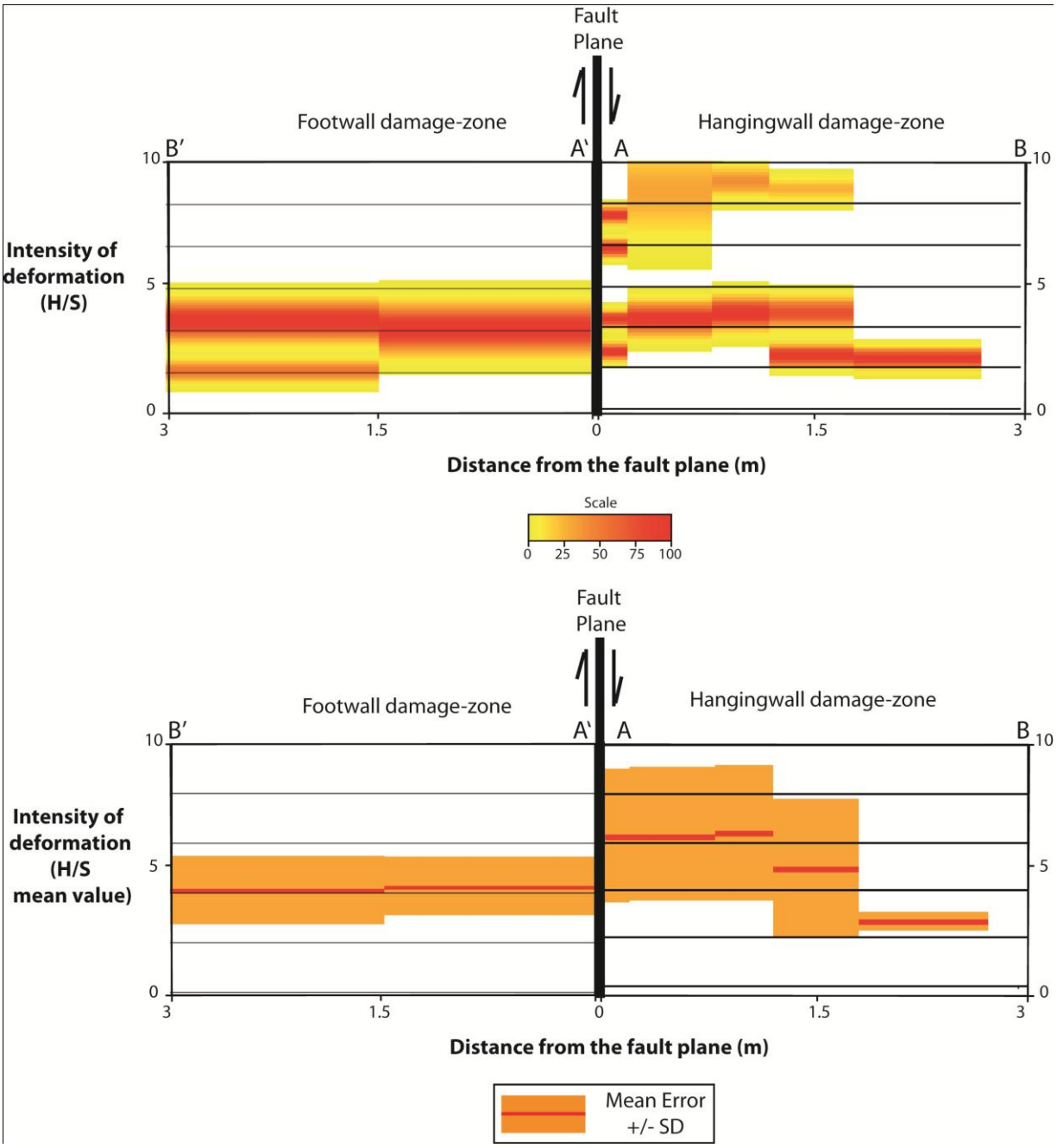

Fig. 5.85 - Comparison between the HW and FW deformation of the Tornimparte 5 fault; a) H/S Gaussian Fit transect analysis; b) H/S Mean Value transect analysis

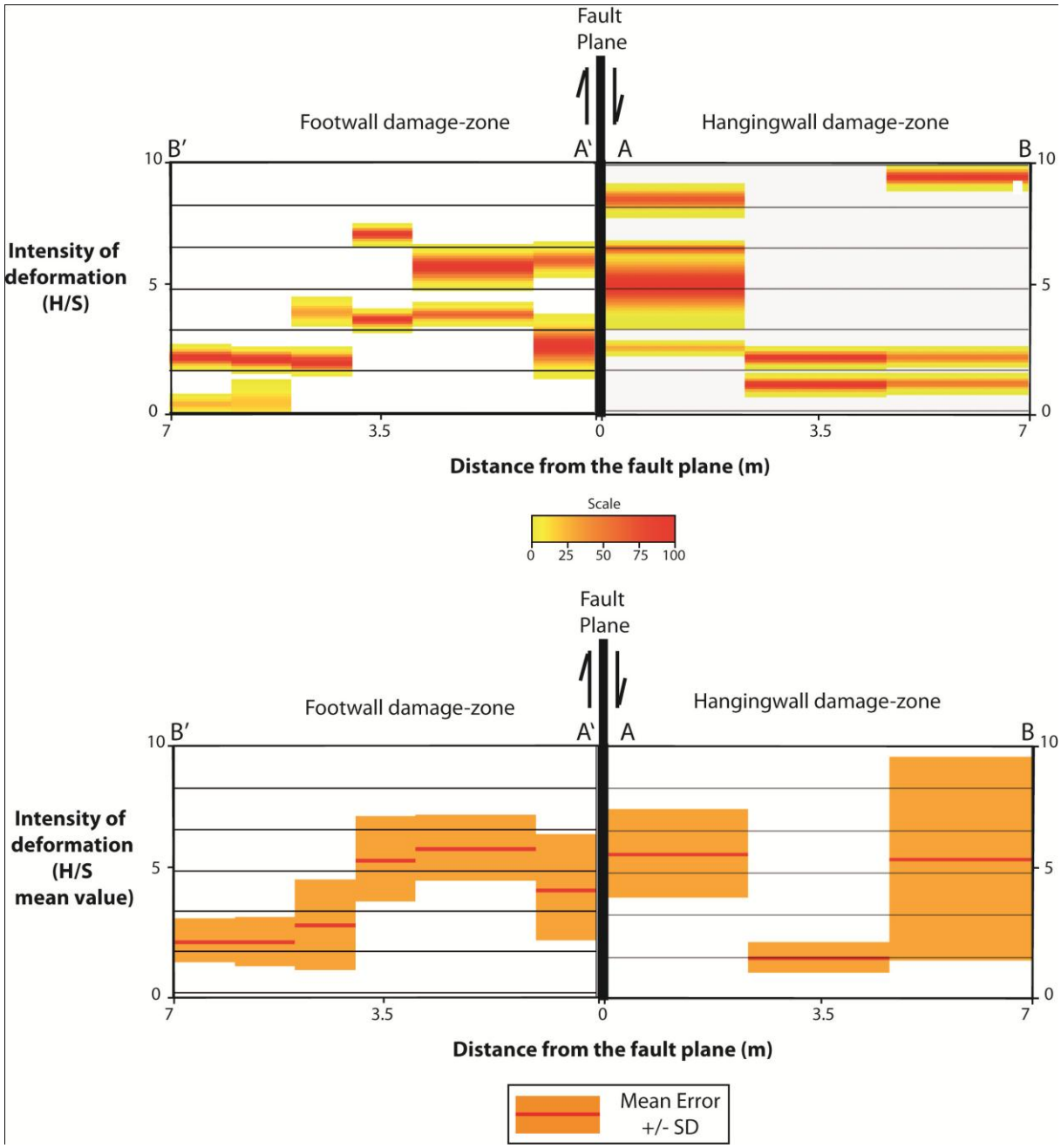

Fig. 5.86 - Comparison between the HW and FW deformation of the Fara 1 fault; a) H/S Gaussian Fit transect analysis; b) H/S Mean Value transect analysis

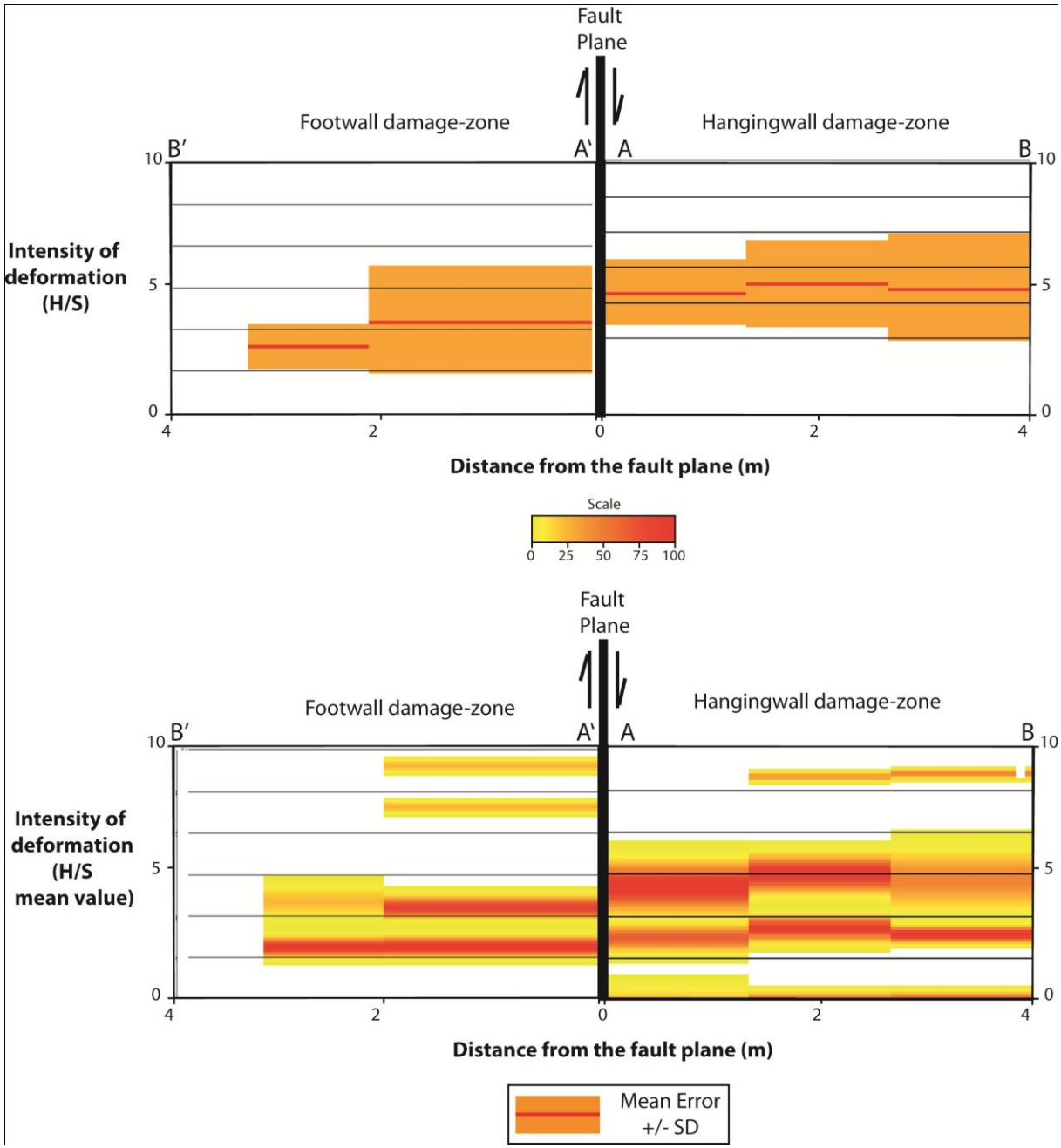

Fig. 5.87 - Comparison between the HW and FW deformation of the Fara 2 fault; a) H/S Gaussian Fit transect analysis; b) H/S Mean Value transect analysis

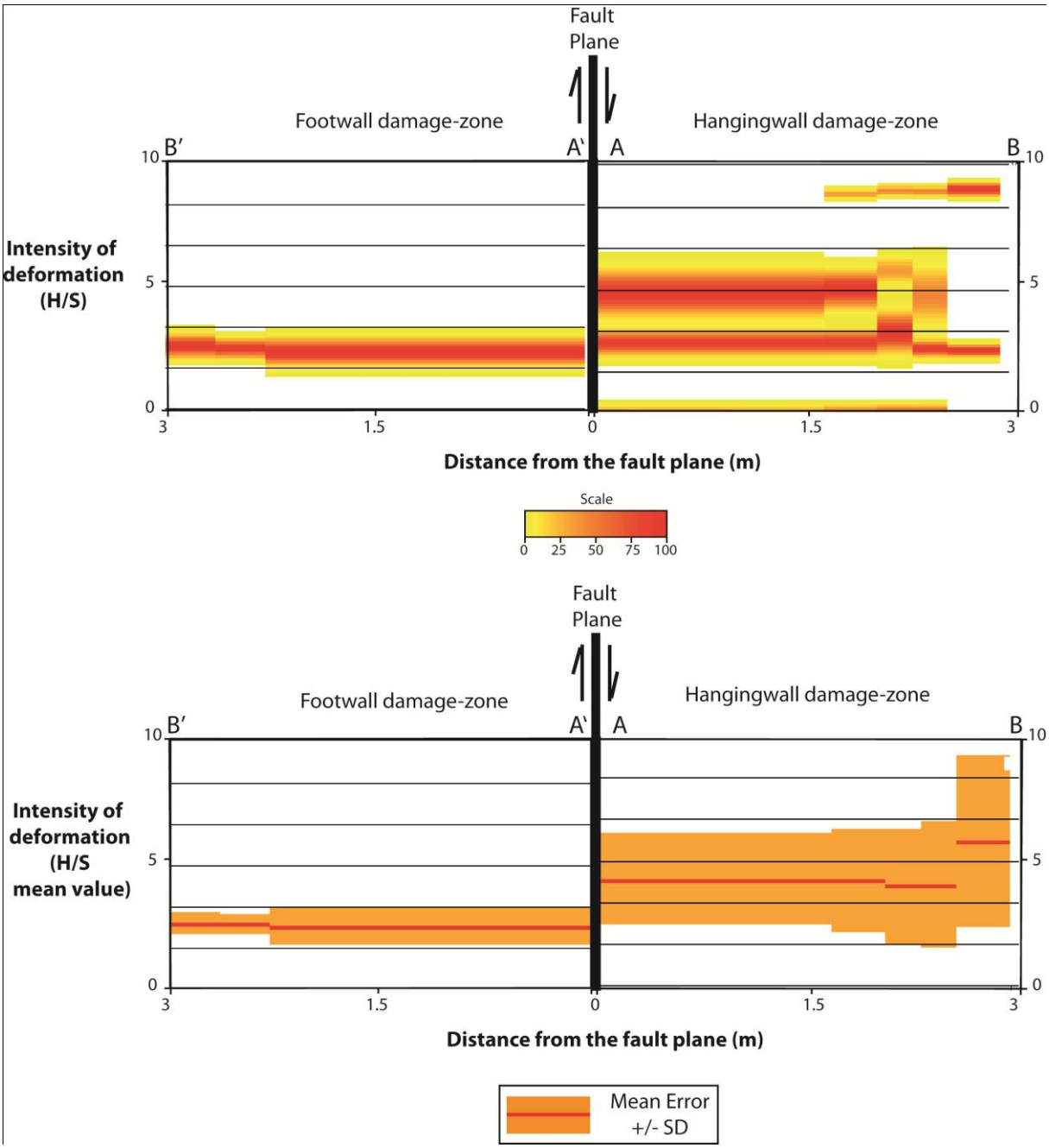

Fig. 5.88 - Comparison between the HW and FW deformation of the Fara 3 fault; a) H/S Gaussian Fit transect analysis; b) H/S Mean Value transect analysis

5.5.3.2 Maximum values of deformation intensity

The graph of Fig. 5.89 shows the comparison between the HW and the FW deformation intensity measured as maximum value of H/S. In the graph the right columns correspond to the fault HW, while the left columns to the fault FW.

The data show that the faults HW are more deformed than the FW. The HW H/S values range between 9 and 4.8, while the FW H/S value between 7 and 3, and that difference is not related to the juxtaposition of different lithologies. This is true except for the case of the Filettino fault, which is characterized by dolostone lithology at the HW and carbonate at FW. The higher value of FW deformation intensity (H/S_{max}=7), respect to the HW (H/S_{max}=5) one, is probably related to the weaker mechanical behaviour of dolostone.

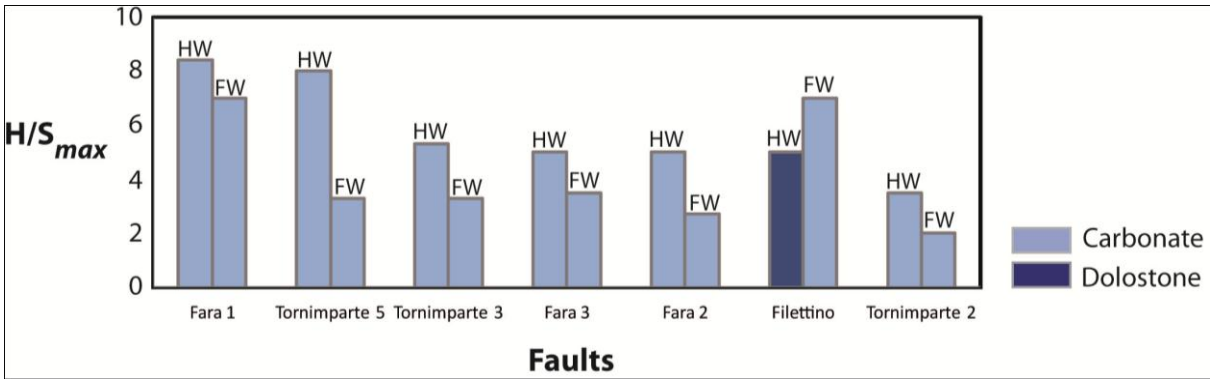

Fig. 5.89 –Comparison between the H/S maximum values of the footwall (FW) and hangingwall (HW)

5.5.4 Stratabound and non-stratabound fault-related fractures

The connectivity, in a layered succession of rocks, strongly depends on the connection between layers. The connectivity is enhanced by the presence of non-stratabound fault related fractures, so that the quantification of their abundance is extremely important to define an expected degree of connectivity.

In order to investigate that issue the fracture height (H) has been compared with the average bedding thickness. This analysis has been performed on the total of 21 faults. The results are presented in the graph of Fig. 5.91 and 5.92, where the y-axis corresponds to the height fracture (H), the x-axis to the distance from the fault plane, and the red line is the average bedding thickness. The faults can be divided in two groups. The first group is composed by 10 faults, which are characterized essentially by stratabound fractures (Fig. 5.91). All these faults are subseismic scale faults, with the exception of the Castel di Ieri fault. The second group is characterized by both seismic and subseismic scale faults for a total number of 9 faults (Fig. 5.92).

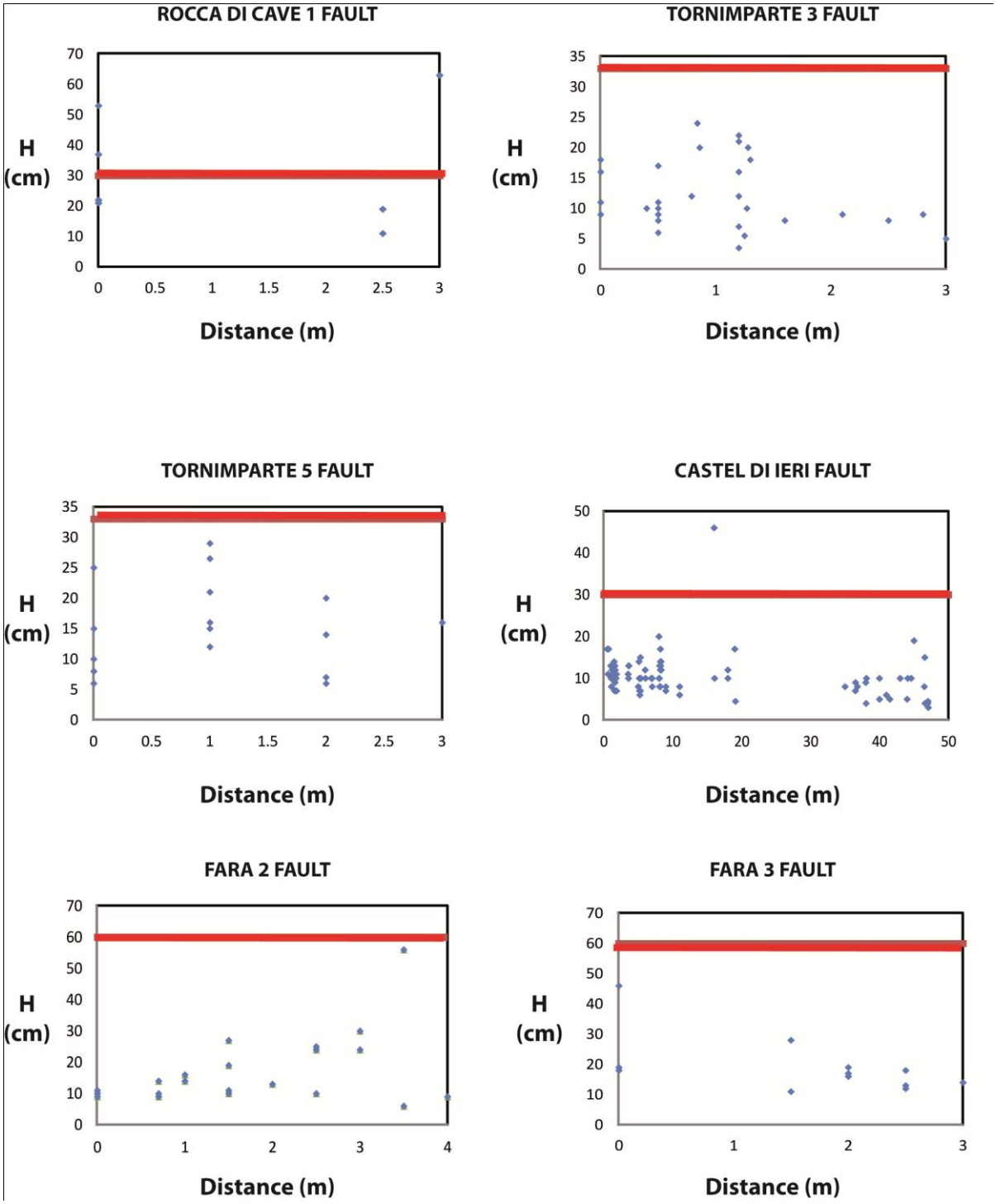
ROCCA DI CAVE 1 FAULT
H (cm)
Distance (m)
TORNIMPARTE 3 FAULT
H (cm)
Distance (m)
TORNIMPARTE 5 FAULT
H (cm)
Distance (m)
CASTEL DI IERI FAULT
H (cm)
Distance (m)
FARA 2 FAULT
H (cm)
Distance (m)
FARA 3 FAULT
H (cm)
Distance (m)

(continued from previous page)

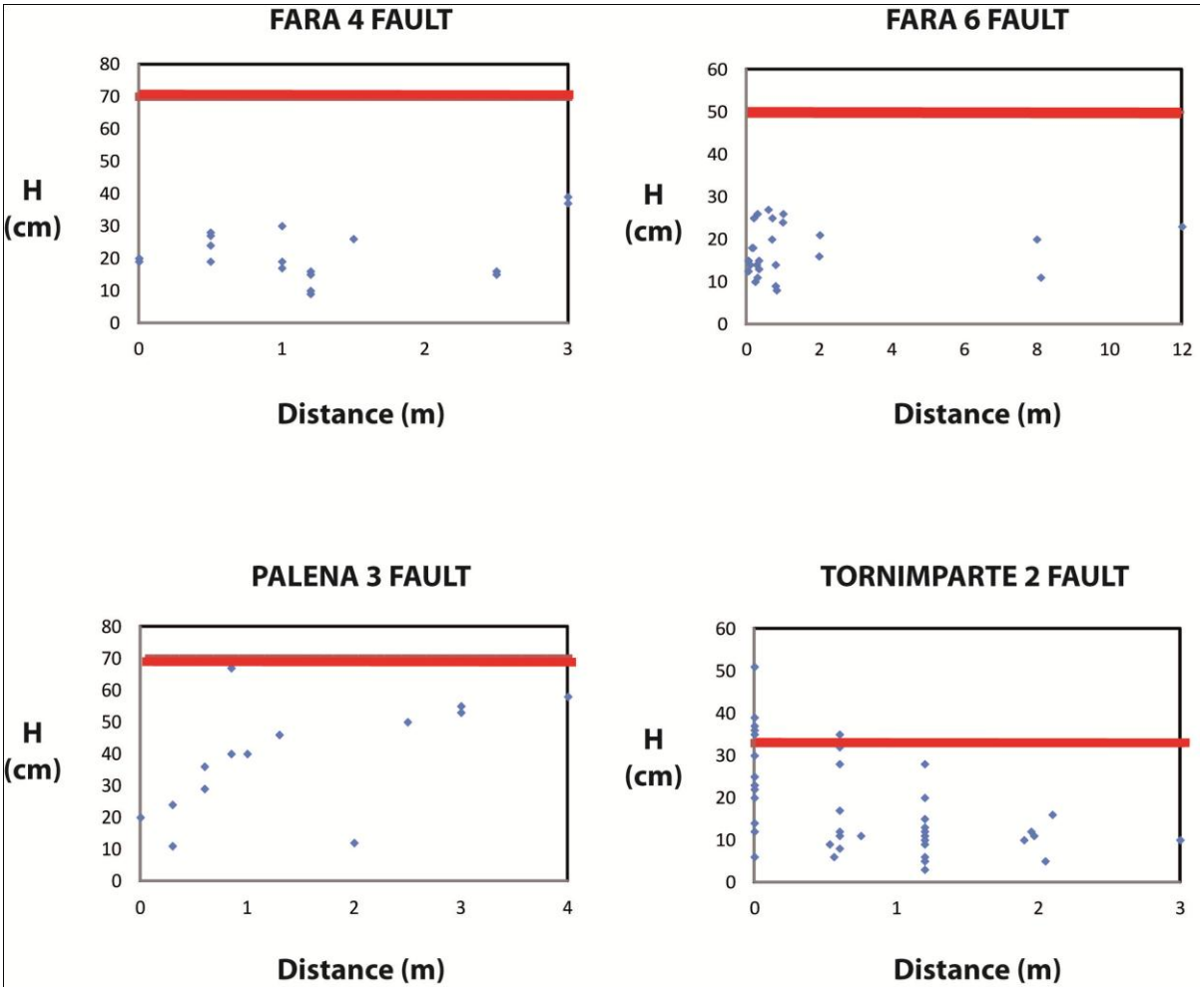

Fig. 5.91 – Height of fractures versus distance from the fault plane; the y-axis corresponds to the fracture height (H), and the x-axis to the distance from the fault plane. The red line corresponds to the average bedding thickness

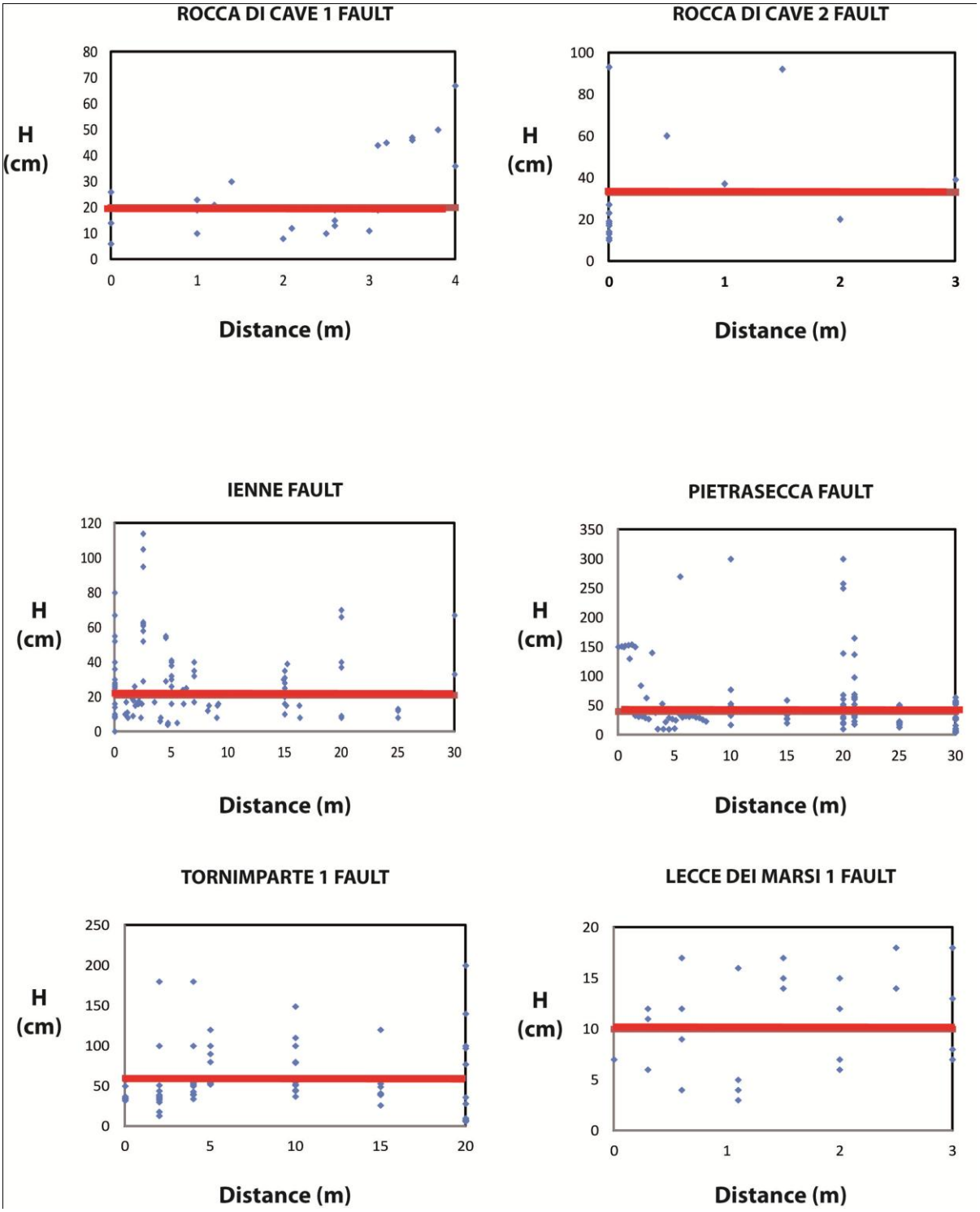
ROCCA DI CAVE 1 FAULT
H (cm)
Distance (m)
ROCCA DI CAVE 2 FAULT
H (cm)
Distance (m)
IENNE FAULT
H (cm)
Distance (m)
PIETRASECCA FAULT
H (cm)
Distance (m)
TORNIMPARTE 1 FAULT
H (cm)
Distance (m)
LECCE DEI MARSI 1 FAULT
H (cm)
Distance (m)

(continued from previous page)

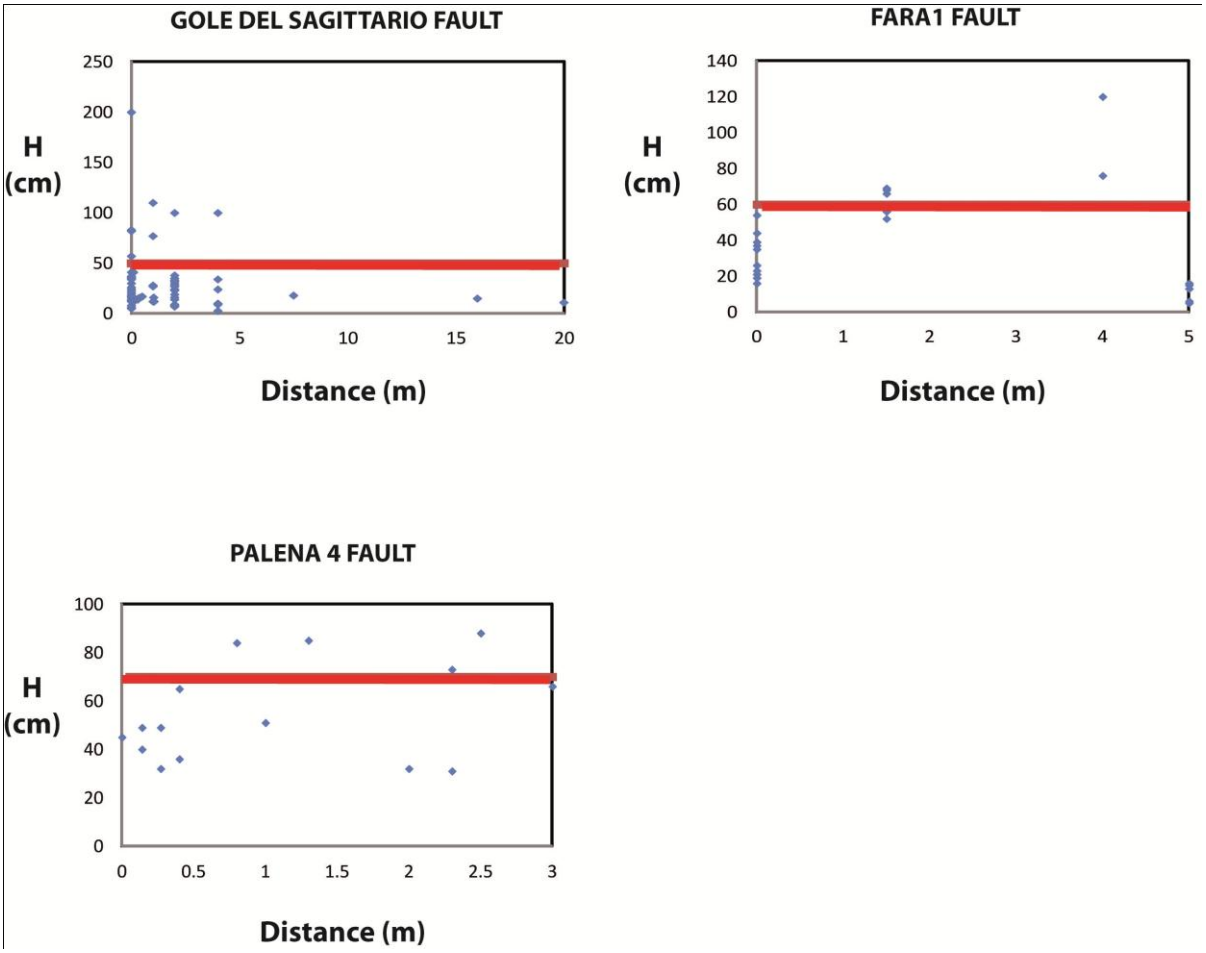

Fig. 5.92– Height of fractures versus distance from the fault plane; the y-axis corresponds to the fracture height (H), and the x-axis to the distance from the fault plane. The red line corresponds to the average bedding thickness

NAME	H/S max FAULT	H/S max REGIONAL
RoccadiCave 1 HW	9	5
RoccadiCave 2 FW	9.5	3.5
RoccadiCave 3 HW	6.6	3.5
Filettino FW	7	2.7
Filettino HW	4.8	2.7
Ienne HW	8.3	2
Pietrasecca HW	7.2	2.5
Tornimparte 1 FW	9	3.1
Tornimparte 2 FW	4.5	3.5
Tornimparte 2 HW	7	3.5
Tornimparte 3 FW	7	3.5
Tornimparte 3 HW	9	3.5
Tornimparte 5 FW	3.3	3.5
Tornimparte 5 HW	9	3.5
LeccedeiMarsi 1 FW	2.7	2.4
LeccedeiMarsi 1 HW	3	2.4
LeccedeiMarsi 2 FW	8.3	2
GoleSagittario FW	8.3	2.1
Casteldileri FW	6.6	2.2
Fara 1 FW	7	2.2
Fara 1 HW	8.4	2.2
Fara 2 FW	5.5	2.2
Fara 2 HW	9	2.2
Fara 4 HW	6.6	2.2
Fara 6 FW	4	2.5
Palena 3 HW	8.5	3.9
Palena 4 HW	8.3	3.9

Tab. 5.6 – Summary of the fault tectonic environments, structural position, fault H/S max, and regional H/S max

NAME	COMPUTED D-Z WIDTH (m)	NAME	MEASURED D-Z WIDTH (m)
RoccadiCave 2 FW	17.3	RoccadiCave 1 HW	2.5
RoccadiCave 3 HW	9.9	Filettino FW	24.0
Filettino HW	5.4	Ienne HW	20.0
Tornimparte 1 FW	15.0	Pietrasecca HW	9.0
Tornimparte 2 HW	11.0	Fara 1 FW	5.5
Tornimparte 2 FW	4.6	Fara 4 HW	1.8
Tornimparte 3 HW	16.0		
Tornimparte 3 FW	11.0		
Tornimparte 5 HW	16.0		
Tornimparte 5 FW	7.0		
Lecce dei Marsi 2 FW	14.3		
Gole del Sagittario FW	14.3		
Casteldileri FW	40.0		
Fara 1 HW	14.5		
Fara 2 HW	5.9		
Fara 2 FW	2.0		
Fara 6 FW	3.3		
Palena 3 HW	14.8		

Tab. 5.7 –Summary of the damage-zone widths

5.6 Analytical model of deformation intensity distribution in fault damage-zones

In this section are presented statistical analyses performed on the field data in order to provide a quantitative model of the deformation intensity distribution in fault damage-zones. The model was performed on a data set including the faults that are characterized essentially by a normal movement (Rotax value < 50° see chapter 4.2.2.1 of this work) for a total number of 17 faults.

5.6.1 The smoothing of H/S field data

The smoothing procedure applied on the H/S data, was realized in order to prepare the row field data to be analysed via Monte Carlo. A Smooth Software package, prepared for this work, allows computing the H/S mean value in order to remove the local noise due to the presence of secondary faults and the casual fluctuation to better visualize the general deformation trends. In particular, the procedure, setting the smooth range and the sampling pace, consists of two main steps. The first smooth was focussed to compute the H/S mean values; the second smooth was focussed both to remove the local noise and to add the regional deformation values. For this secondary smooth the regional deformation values have been added to the fault dataset. The setting parameters, namely the smoothing range and the sampling pace, have been tuned for each fault, considering the dimension of the damage-zone width.

5.6.1.1 Presentation of the smoothed data

The **Rocca di Cave 1 fault** data were smoothed using an interval width of 0.2 and a sampling pace of 0.1. The resulting H/S mean value (Fig. 5.93 *c*) increases with the distance from the fault plane. At the distance of 1 m from the fault plane the trend reaches a peak, and then it decreases to the regional value at the distance of 2.5 m from the fault plane.

The **Rocca di Cave 2 fault** data were smoothed using an interval width of 0.4 and a sampling pace of 0.1. The resulting H/S mean value (Fig. 5.94 *c*) shows a trend characterized by a very narrow and height. Then the values stabilized to the regional at a distance of 17 m from the fault plane.

The **Rocca di Cave 3 fault** data were smoothed using an interval width of 0.2 and a sampling pace of 0.1. The resulting H/S mean value (Fig. 5.95 *c*) shows an exponential decrease of H/S values down to the regional at a distance of 17 m from the fault plane.

The **Filettino fault** data were smoothed using an interval width of 3 and a sampling pace of 0.5. The resulting H/S mean value (Fig. 5.96 *c*) is constant for 10 m; then it stabilizes to the regional H/S value at a distance of 24 m from the fault plane.

The **Ienne fault** data were smoothed using an interval width of 3 and a sampling pace of 1. The resulting H/S mean value (Fig. 5.97 *c*) increases reaching a peak and stabilizes to the regional H/S value at a distance of 20 m from the fault plane.

The **Pietrasecca fault** data were smoothed using an interval width of 3 and a sampling pace of 0.5. The resulting H/S mean value (Fig. 5.98 *c*) decreases and stabilizes to the regional H/S value at a distance of 9 m from the fault plane.

The **Tornimparte 1 fault** data were smoothed using an interval width of 3 and a sampling pace of 1. The resulting H/S mean value (Fig. 5.99 *c*) increases reaching a peak, which is extremely large

and high. Then the trend stabilizes to the regional H/S value at a distance of 9 m from the fault plane.

The **Tornimparte 2 fault** data were smoothed using an interval width of 1 and a sampling pace of 0.2. The resulting H/S mean value (Fig. 5.100 *c*) shows a decreasing trend down to the regional H/S value at a distance of 11 m from the fault plane.

The **Tornimparte 3 fault** data were smoothed using an interval width of 1 and a sampling pace of 0.3. The resulting H/S mean value (Fig. 5.101 *c*) shows a decreasing trend down to the regional H/S value at a distance of 11 m from the fault plane.

The **Tornimparte 5 fault** data were smoothed using an interval width of 0.5 and a sampling pace of 0.1. The resulting H/S mean value (Fig. 5.102 *c*) shows a decreasing trend down to the regional H/S value at a distance of 7 m from the fault plane.

The **Lecce dei Marsi 2 fault** data were smoothed using an interval width of 3 and a sampling pace of 1. The resulting H/S mean value (Fig. 5.103 *c*) shows a decreasing trend down to the regional H/S value at a distance of 14 m from the fault plane.

The **Gole del Sagittario fault** data were smoothed using an interval width of 1 and a sampling pace of 0.3. The resulting H/S mean value (Fig. 5.104 *c*) shows a trend characterized by an increase of H/S values which reach a peak and by a decreasing down to the regional H/S value at a distance of 14 m from the fault plane.

The **Castel di Ieri fault** data were smoothed using an interval width of 2 and a sampling pace of 2. The resulting H/S mean value (Fig. 5.105 *c*) shows a trend characterized by an increase of H/S values and a decreasing down to the regional H/S value at a distance of 14 m from the fault plane. The peak is very large and high in this fault.

The **Fara 1 fault** data were smoothed using an interval width of 3 and a sampling pace of 0.2. The resulting H/S mean value (Fig. 5.106 *c*) shows a trend characterized by an increase of H/S values and a decreasing down to the regional H/S value at a distance of 5.5 m from the fault plane. The peak is very large and high in this fault.

The **Fara 2 fault** data were smoothed using an interval width of 3 and a sampling pace of 0.2. The resulting H/S mean value (Fig. 5.107 *c*) shows a trend characterized by an increase of H/S values and a decreasing down to the regional H/S value at a distance of 2 m from the fault plane.

The **Fara 4 fault** data were smoothed using an interval width of 3 and a sampling pace of 0.2. The resulting H/S mean value (Fig. 5.108 *c*) shows a decreasing trend down to the regional H/S value at a distance of 1.8 m from the fault plane.

The **Fara 6 fault** data were smoothed using an interval width of 3 and a sampling pace of 0.5. The resulting H/S mean value (Fig. 5.109 *c*) shows a decreasing trend down to the regional H/S value at a distance of 3.3 m from the fault plane.

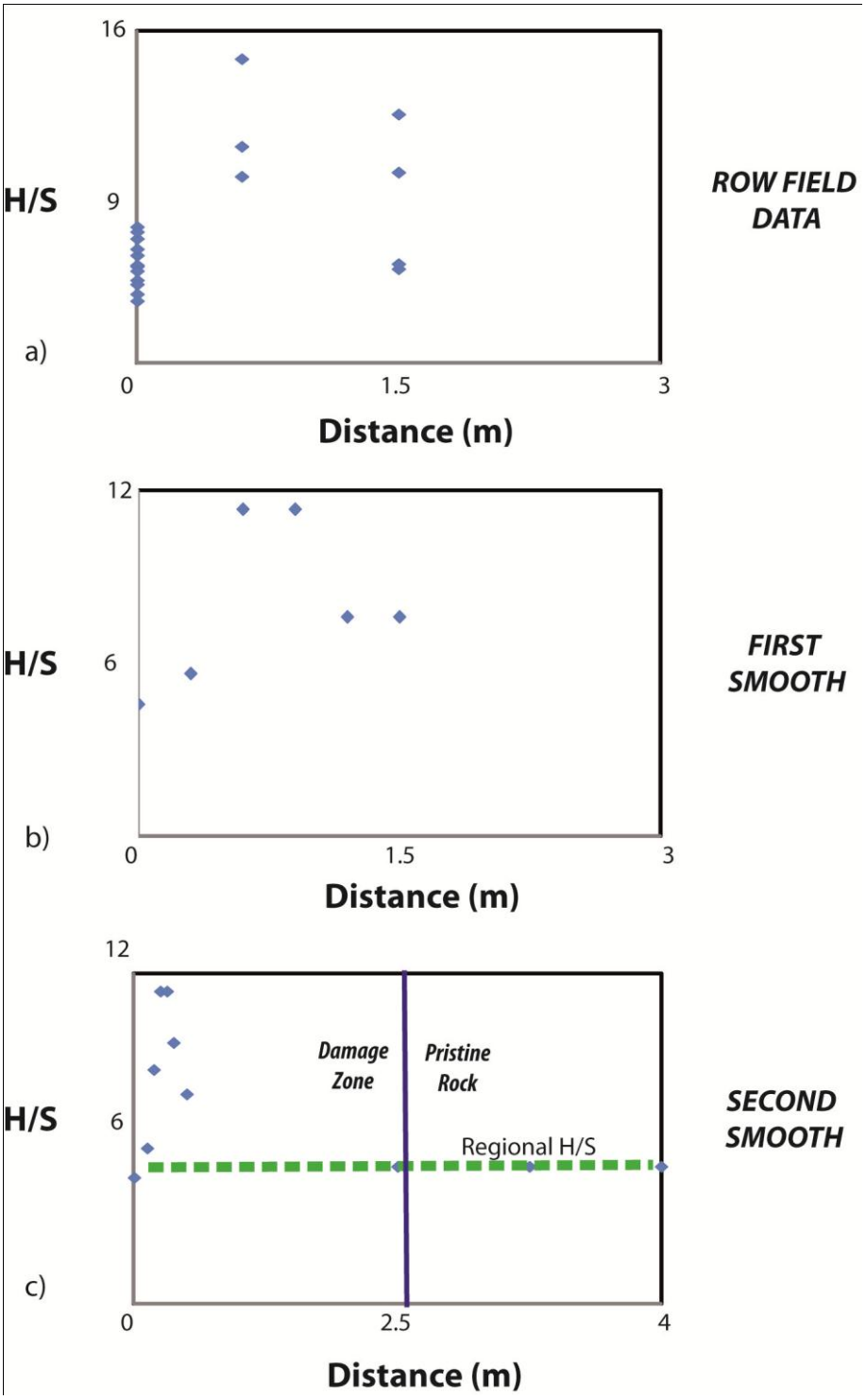

Fig. 5.93 – The smoothing data of the Rocca di Cave 1 fault; a) Scattered row data; b) Resulting of the first smooth; c) Resulting of the second smooth. The green dashed line corresponds to the regional H/S value; the red dashed line corresponds to the secondary fault; the black line corresponds to the damage-zone pristine rock boundary

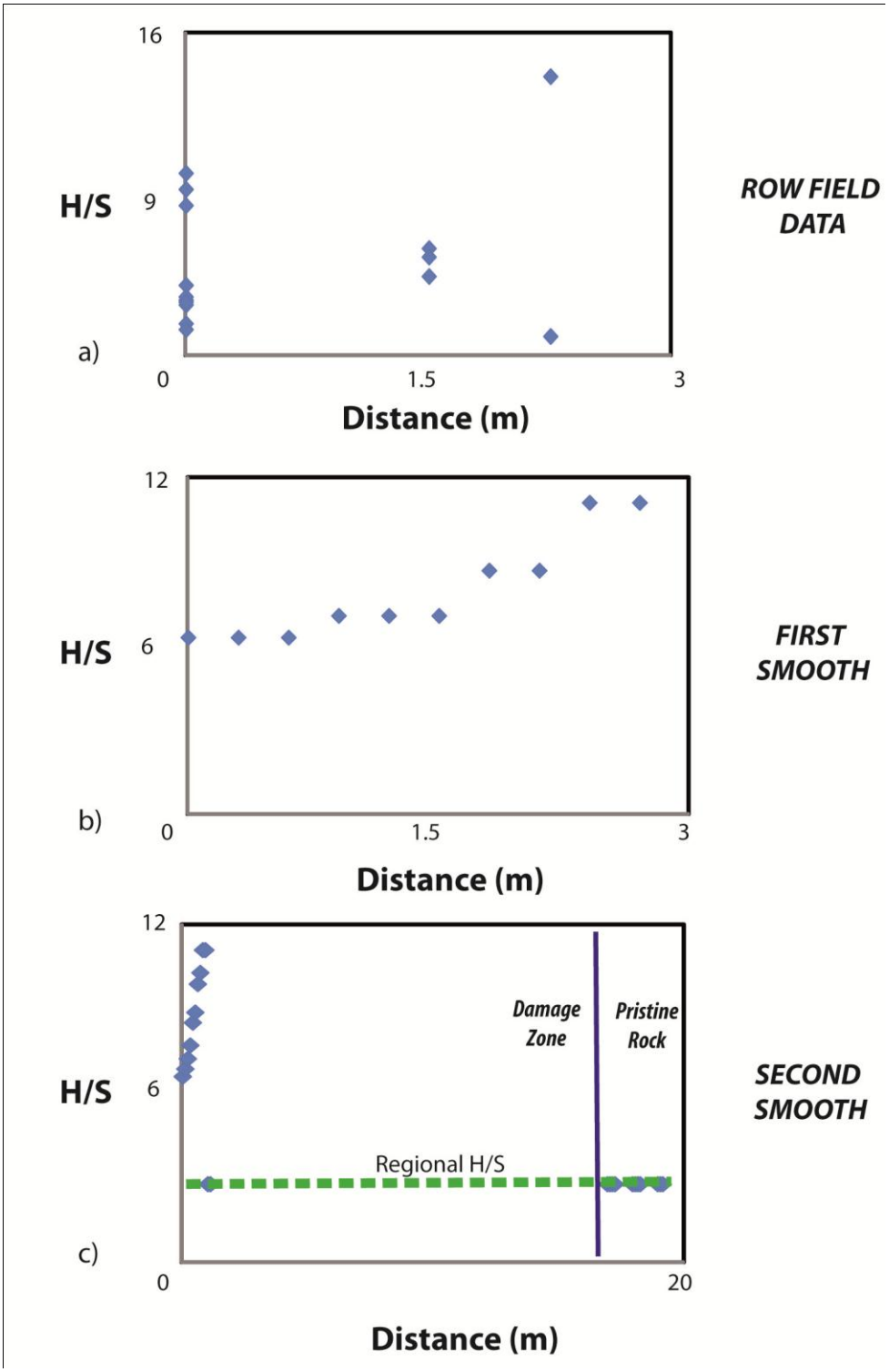

Fig. 5.94 – The smoothing data of the Rocca di Cave 2 fault; a) Scattered row data; b) Resulting of the first smooth; c) Resulting of the second smooth. The green dashed line corresponds to the regional H/S value; the red dashed line corresponds to the secondary fault; the black line corresponds to the damage-zone pristine rock boundary

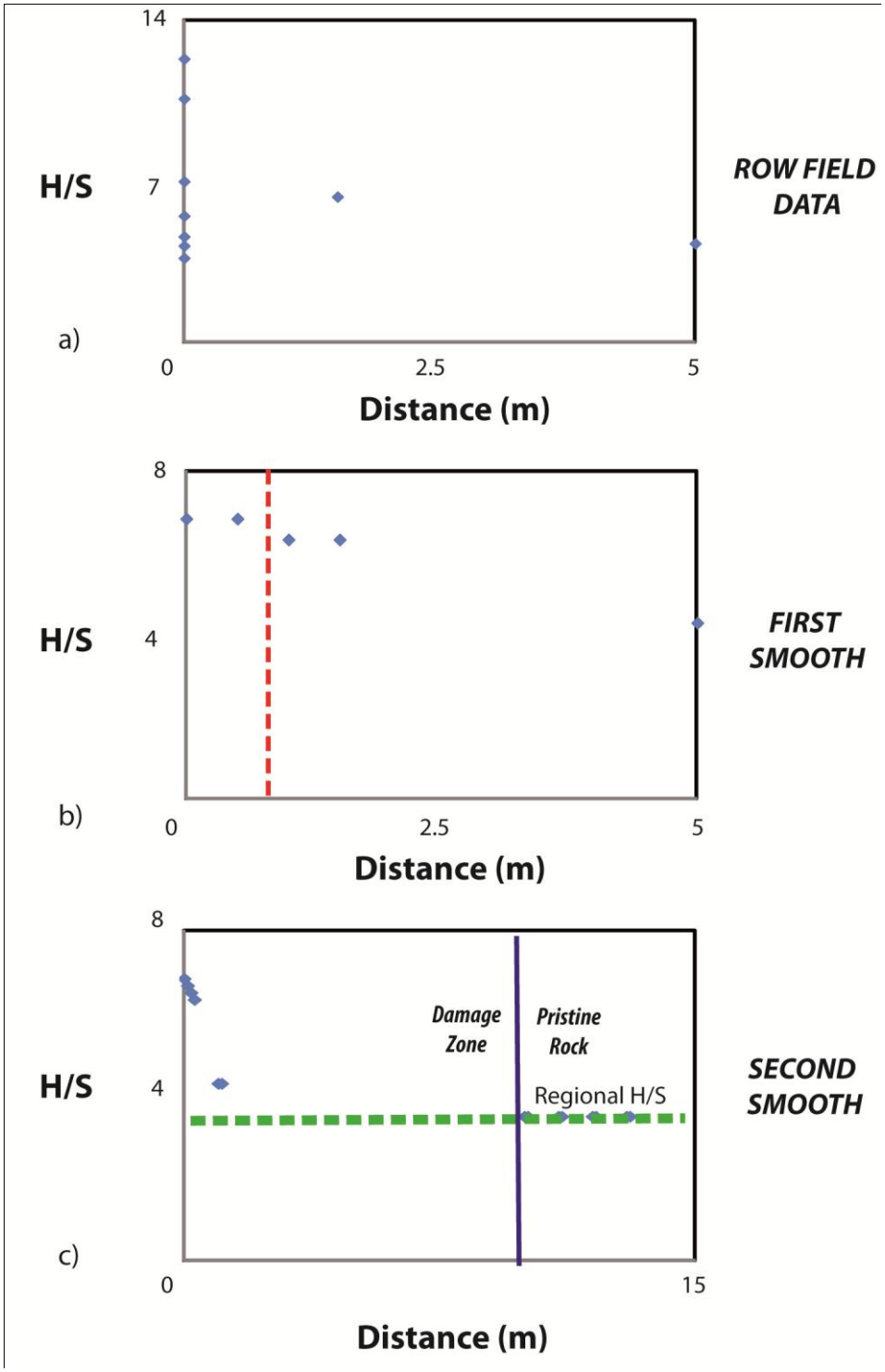

Fig. 5.95 – The smoothing data of the Rocca di Cave 3 fault; a) Scattered row data; b) Resulting of the first smooth; c) Resulting of the second smooth. The green dashed line corresponds to the regional H/S value; the red dashed line corresponds to the secondary fault; the black line corresponds to the damage-zone pristine rock boundary

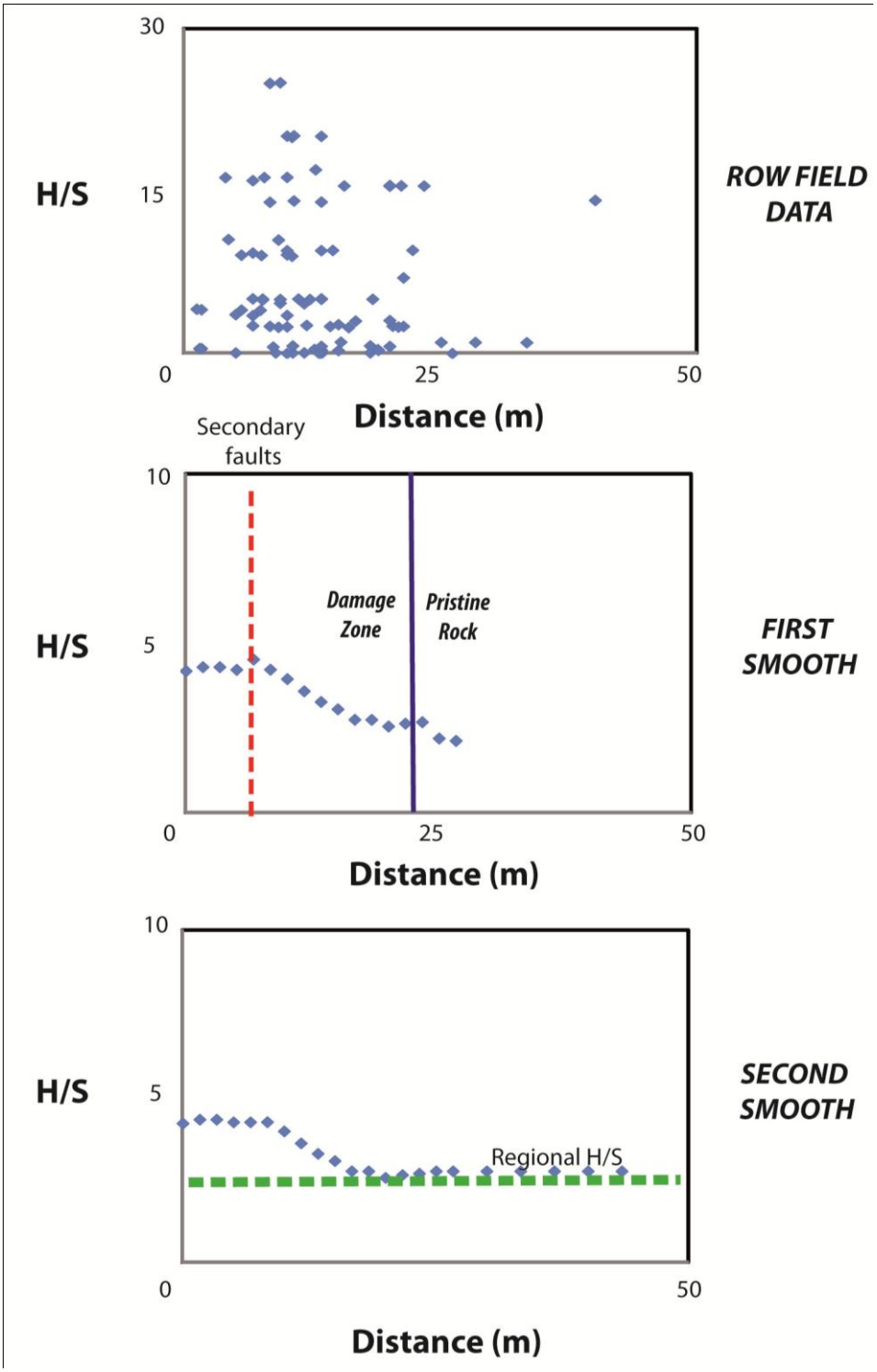

Fig. 5.96 – The smoothing data of the Filettino fault; a) Scattered row data; b) Resulting of the first smooth; c) Resulting of the second smooth. The green dashed line corresponds to the regional H/S value; the red dashed line corresponds to the secondary fault; the black line corresponds to the damage-zone pristine rock boundary

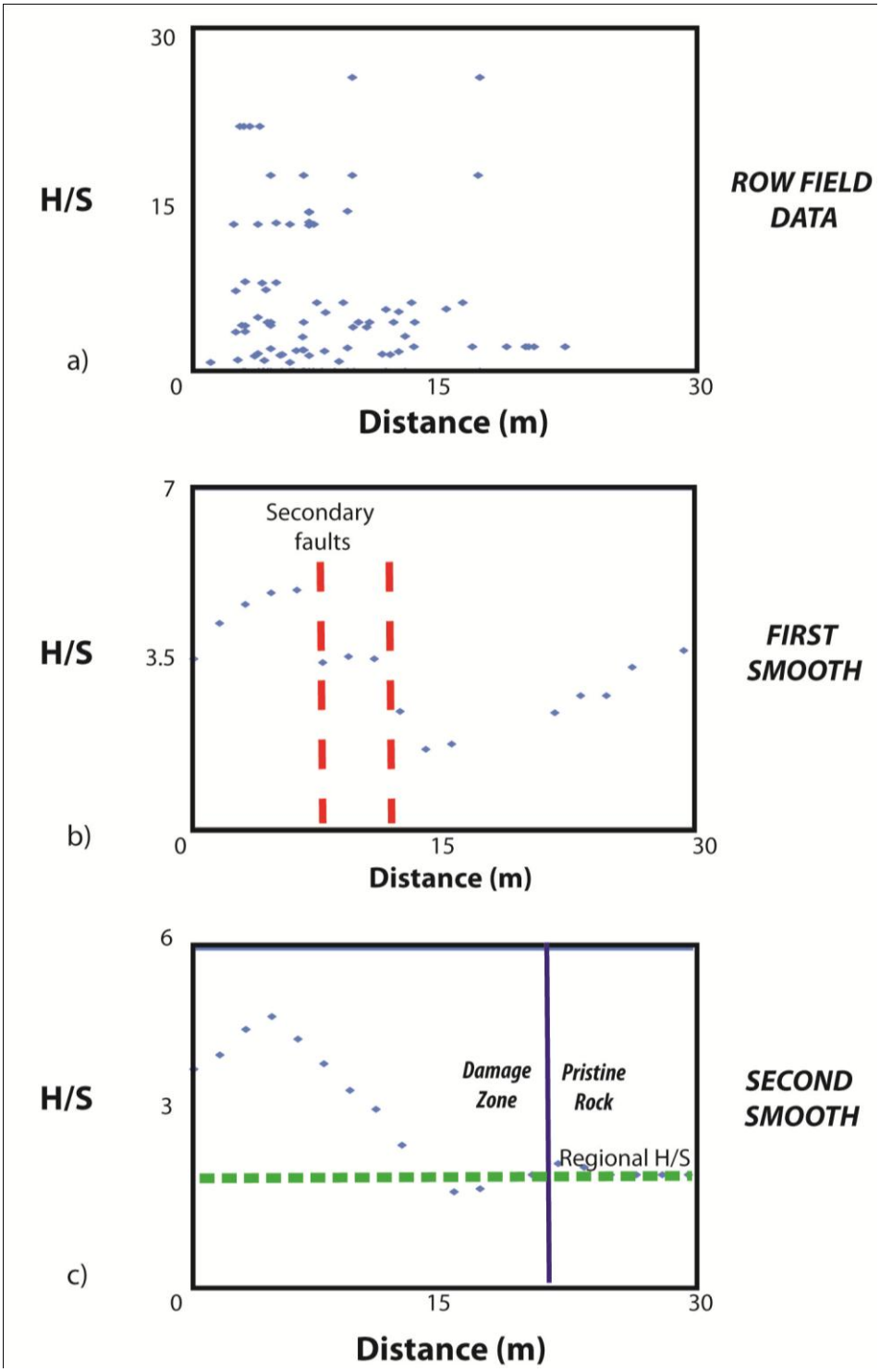

Fig. 5.97 – The smoothing data of the Ienne fault; a) Scattered row data; b) Resulting of the first smooth; c) Resulting of the second smooth. The green dashed line corresponds to the regional H/S value; the red dashed line corresponds to the secondary fault; the black line corresponds to the damage-zone pristine rock boundary

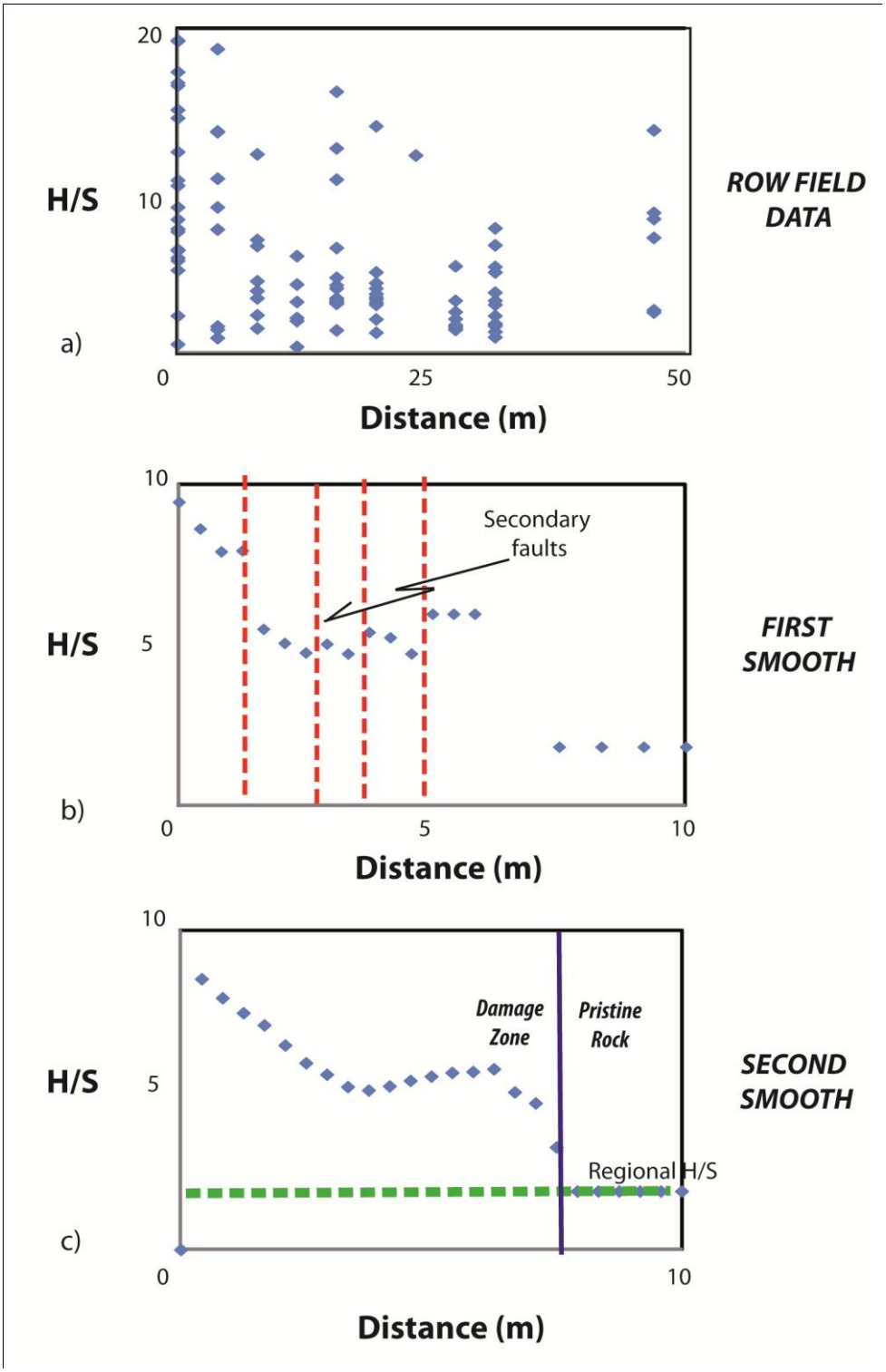

Fig. 5.98 – The smoothing data of the Pietrasecca fault; a) Scattered row data; b) Resulting of the first smooth; c) Resulting of the second smooth. The green dashed line corresponds to the regional H/S value; the red dashed line corresponds to the secondary fault; the black line corresponds to the damage-zone pristine rock boundary

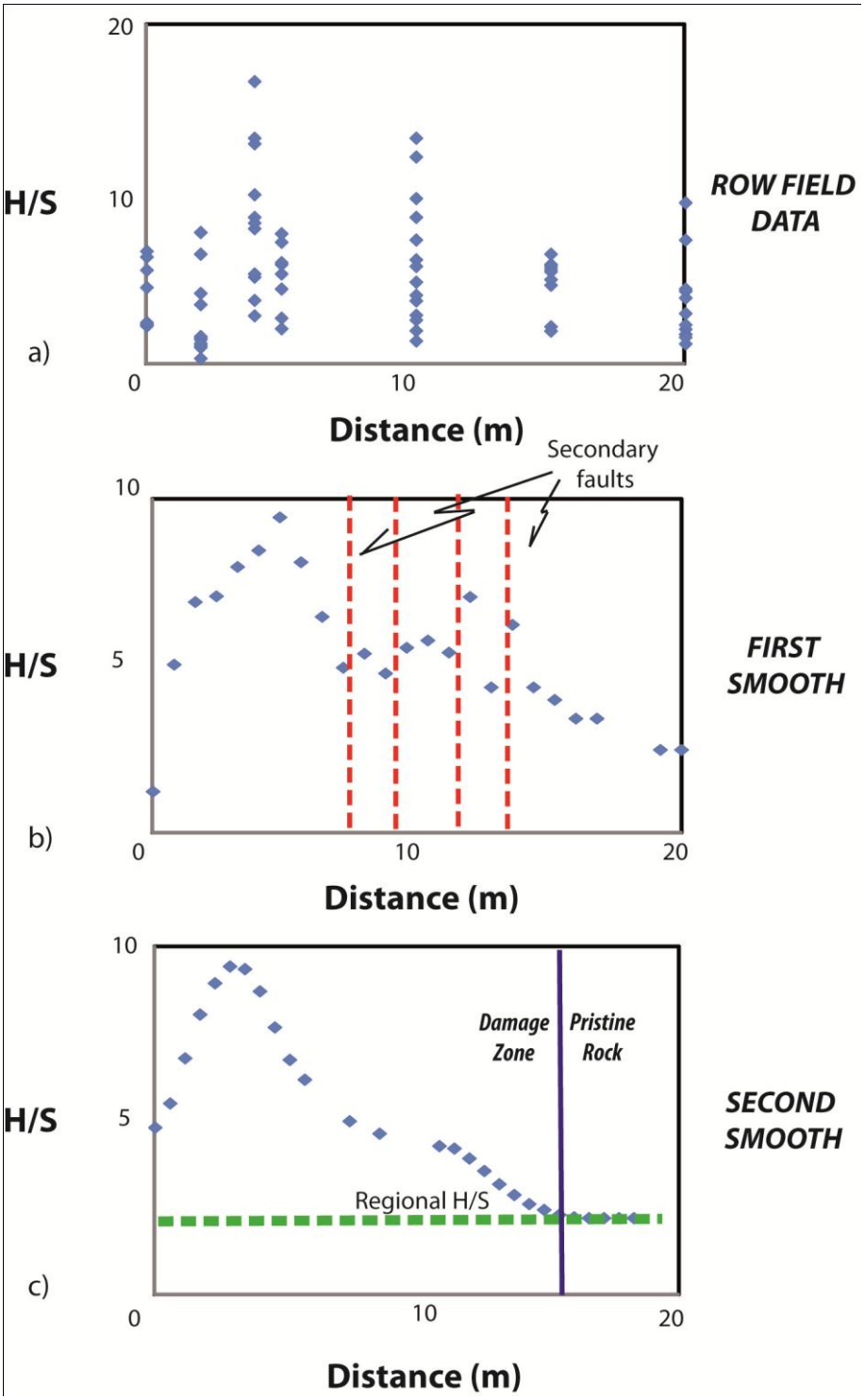

Fig. 5.99 – The smoothing data of the Tornimparte 1 fault; a) Scattered row data; b) Resulting of the first smooth; c) Resulting of the second smooth. The green dashed line corresponds to the regional H/S value; the red dashed line corresponds to the secondary fault; the black line corresponds to the damage-zone pristine rock boundary

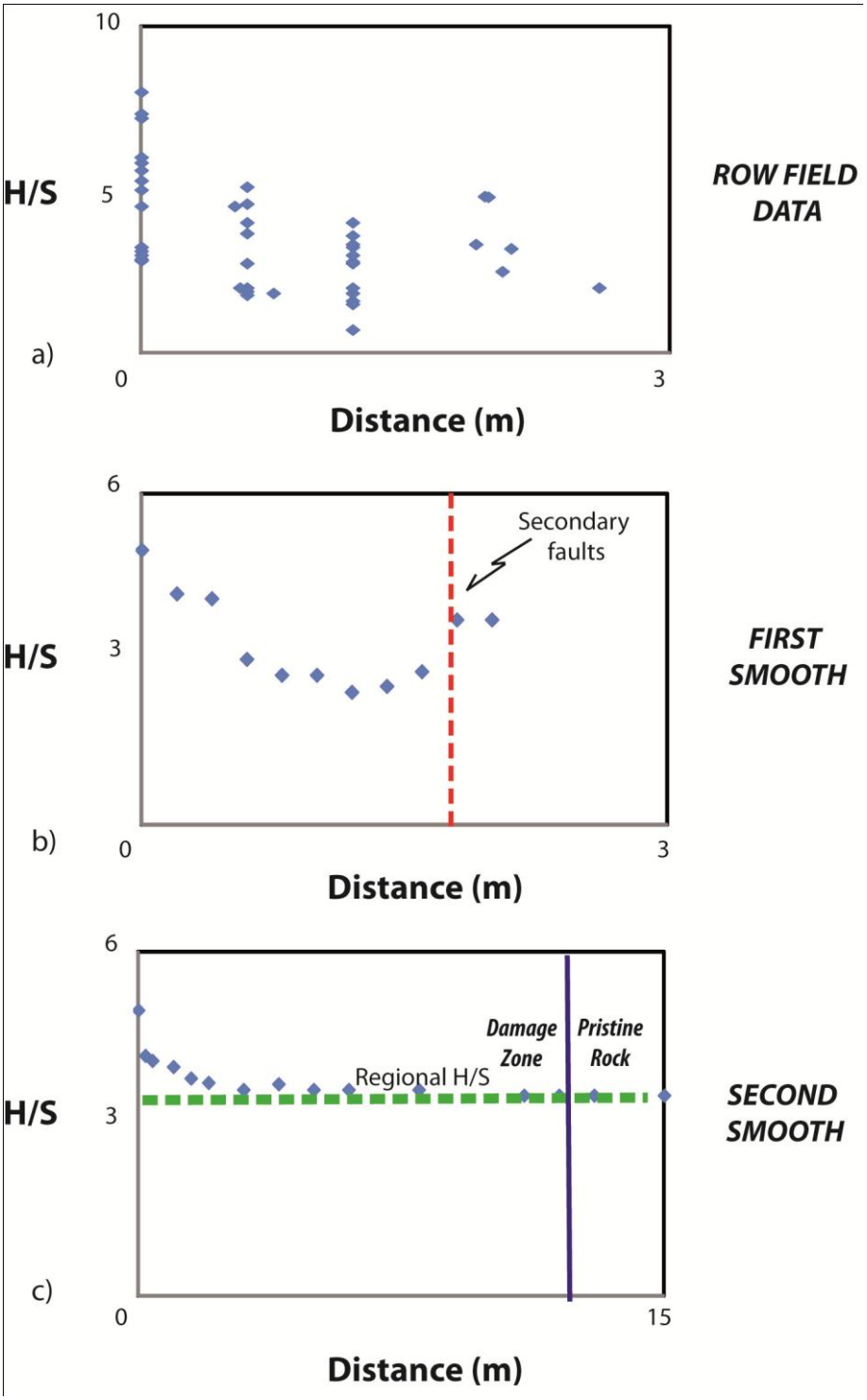

Fig. 5.100 – The smoothing data of the Tornimparte 2 fault; a) Scattered row data; b) Resulting of the first smooth; c) Resulting of the second smooth. The green dashed line corresponds to the regional H/S value; the red dashed line corresponds to the secondary fault; the black line corresponds to the damage-zone pristine rock boundary

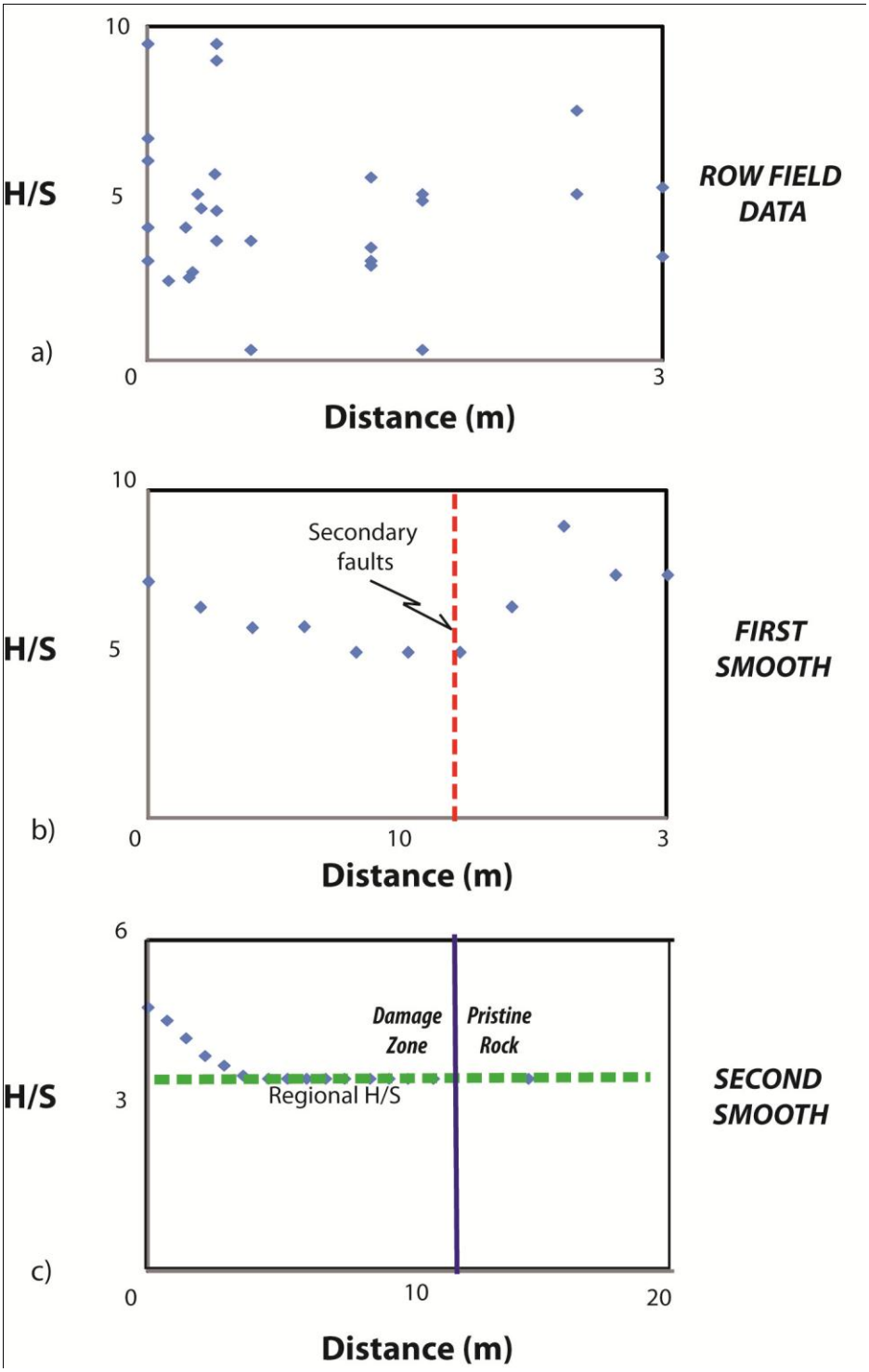

Fig. 5.101 – The smoothing data of the Tornimparte 3 fault; a) Scattered row data; b) Resulting of the first smooth; c) Resulting of the second smooth. The green dashed line corresponds to the regional H/S value; the red dashed line corresponds to the secondary fault; the black line corresponds to the damage-zone pristine rock boundary

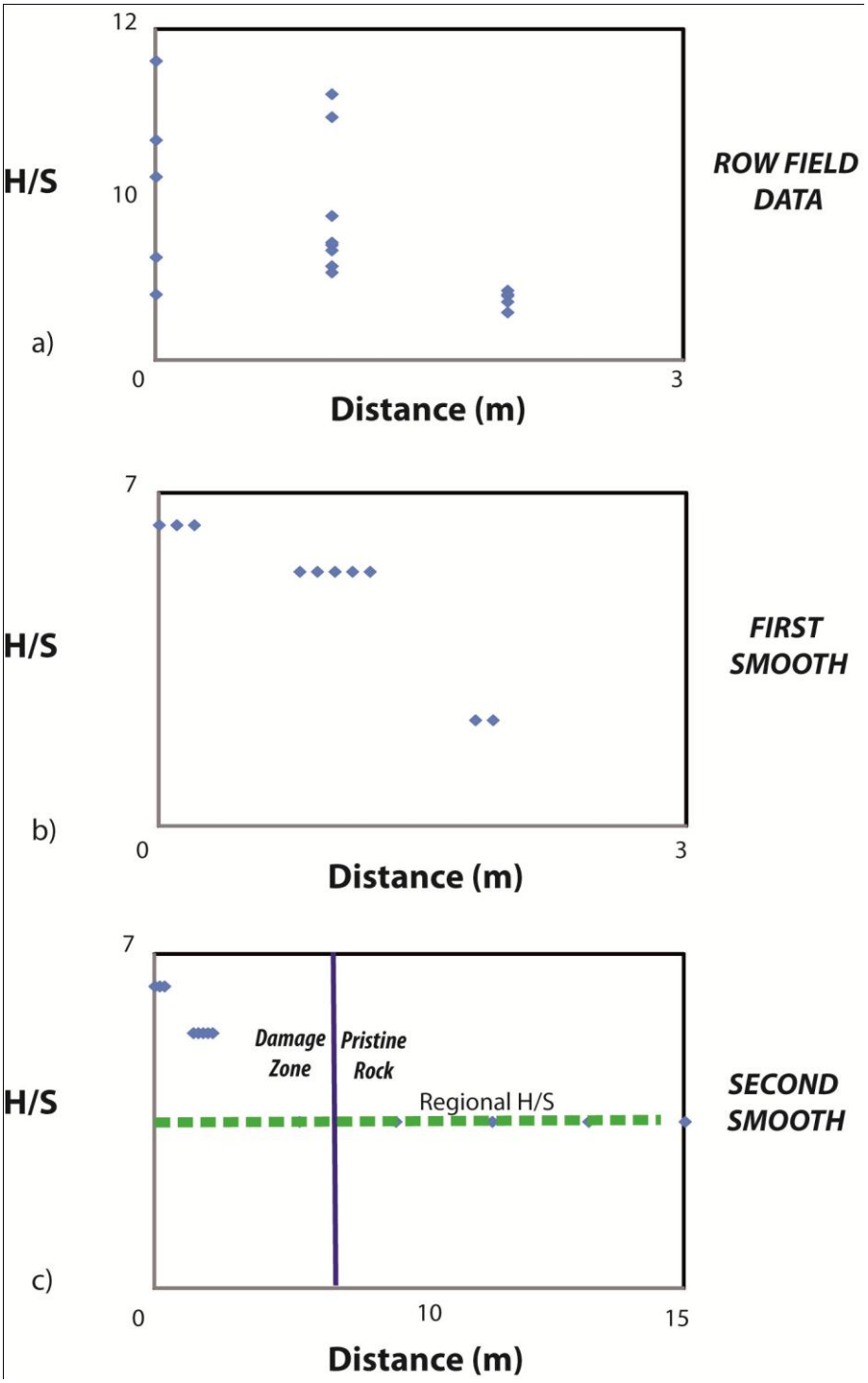

Fig. 5.102 – The smoothing data of the Tornimparte 5 fault; a) Scattered row data; b) Resulting of the first smooth; c) Resulting of the second smooth. The green dashed line corresponds to the regional H/S value; the red dashed line corresponds to the secondary fault; the black line corresponds to the damage-zone pristine rock boundary

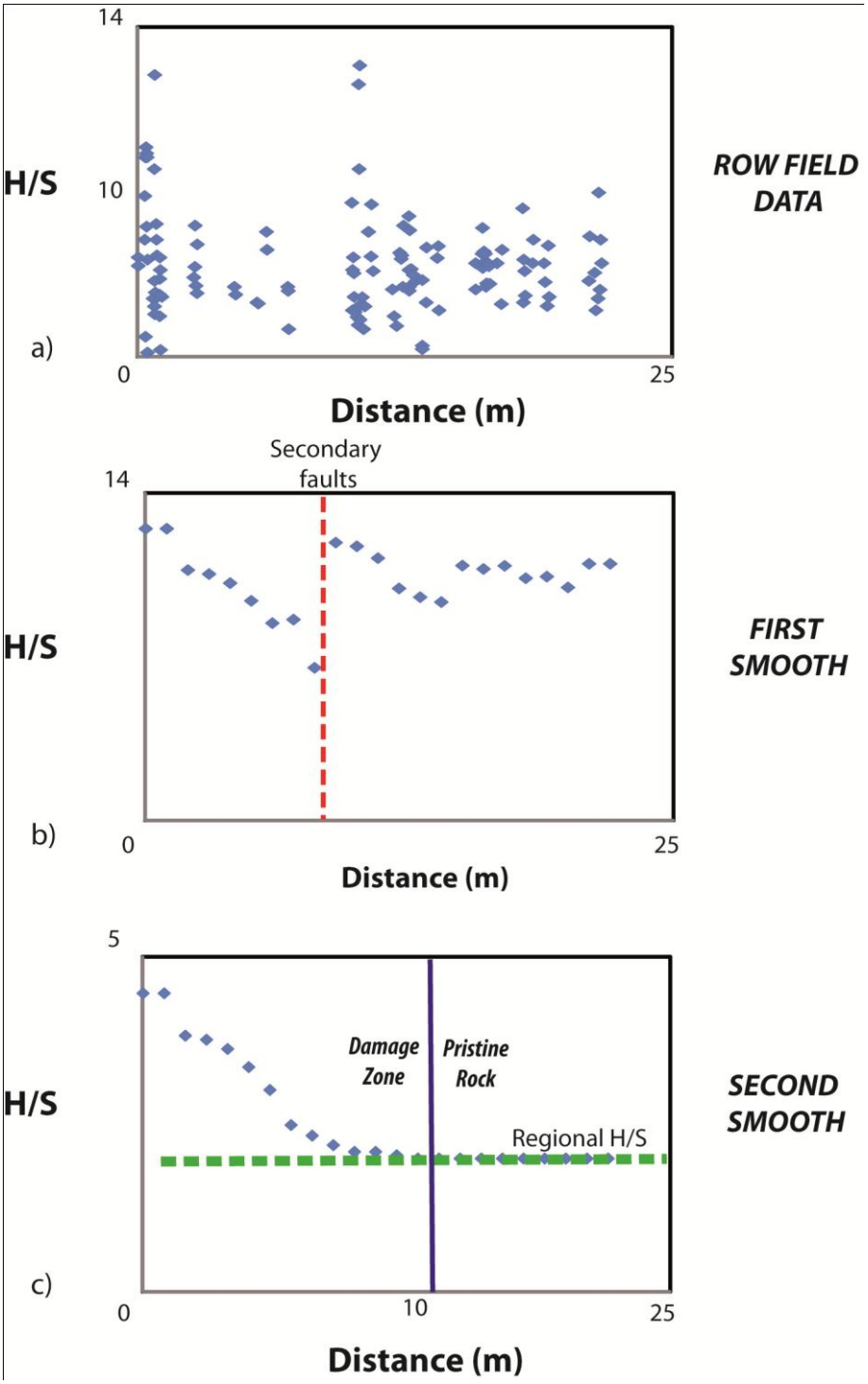

Fig. 5.103 – The smoothing data of the Lecce dei Marsi 2 fault; a) Scattered row data; b) Resulting of the first smooth; c) Resulting of the second smooth. The green dashed line corresponds to the regional H/S value; the red dashed line corresponds to the secondary fault; the black line corresponds to the damage-zone pristine rock boundary

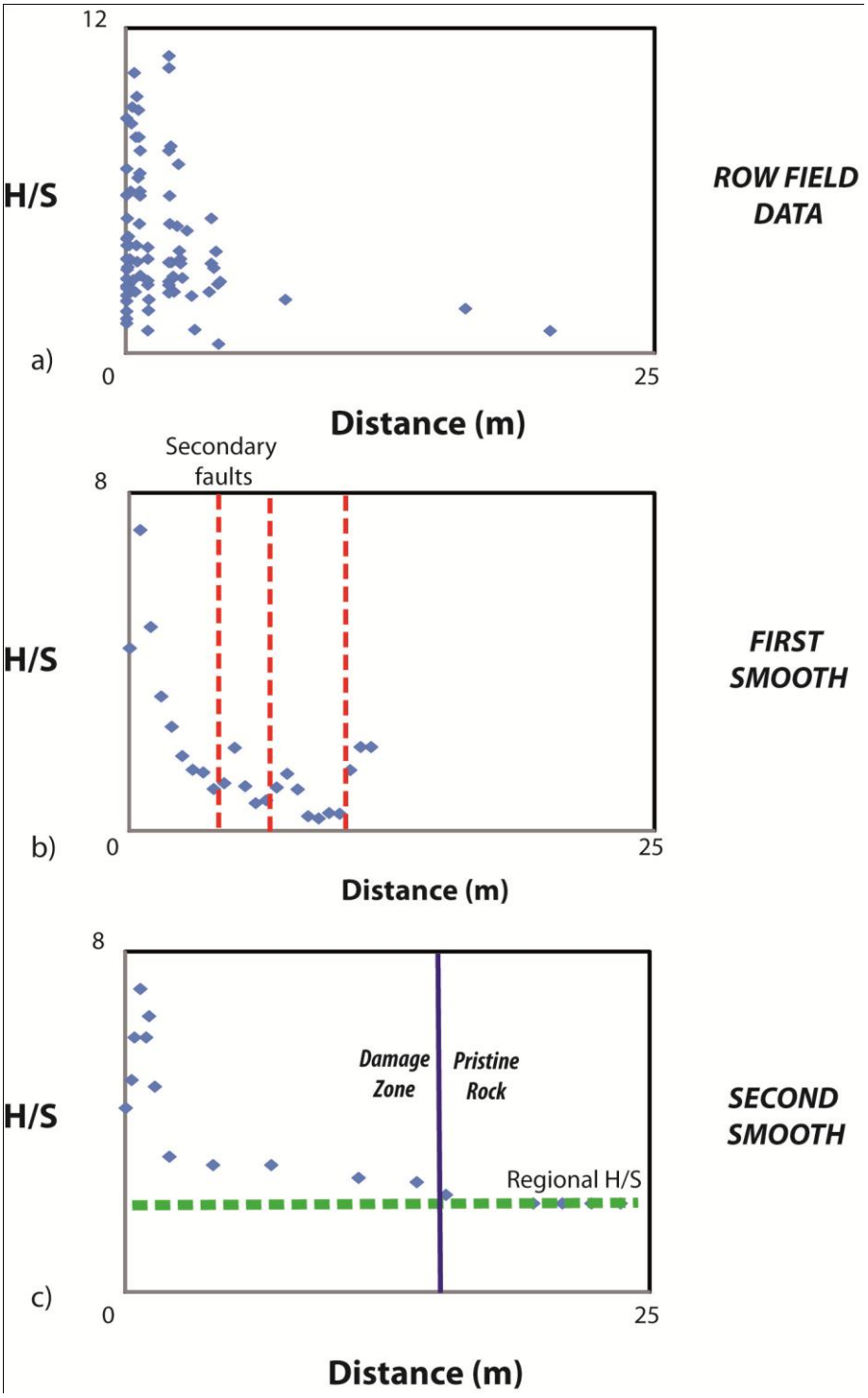

Fig. 5.104 – The smoothing data of the Gole del Sagittario fault; a) Scattered row data; b) Resulting of the first smooth; c) Resulting of the second smooth. The green dashed line corresponds to the regional H/S value; the red dashed line corresponds to the secondary fault; the black line corresponds to the damage-zone pristine rock boundary

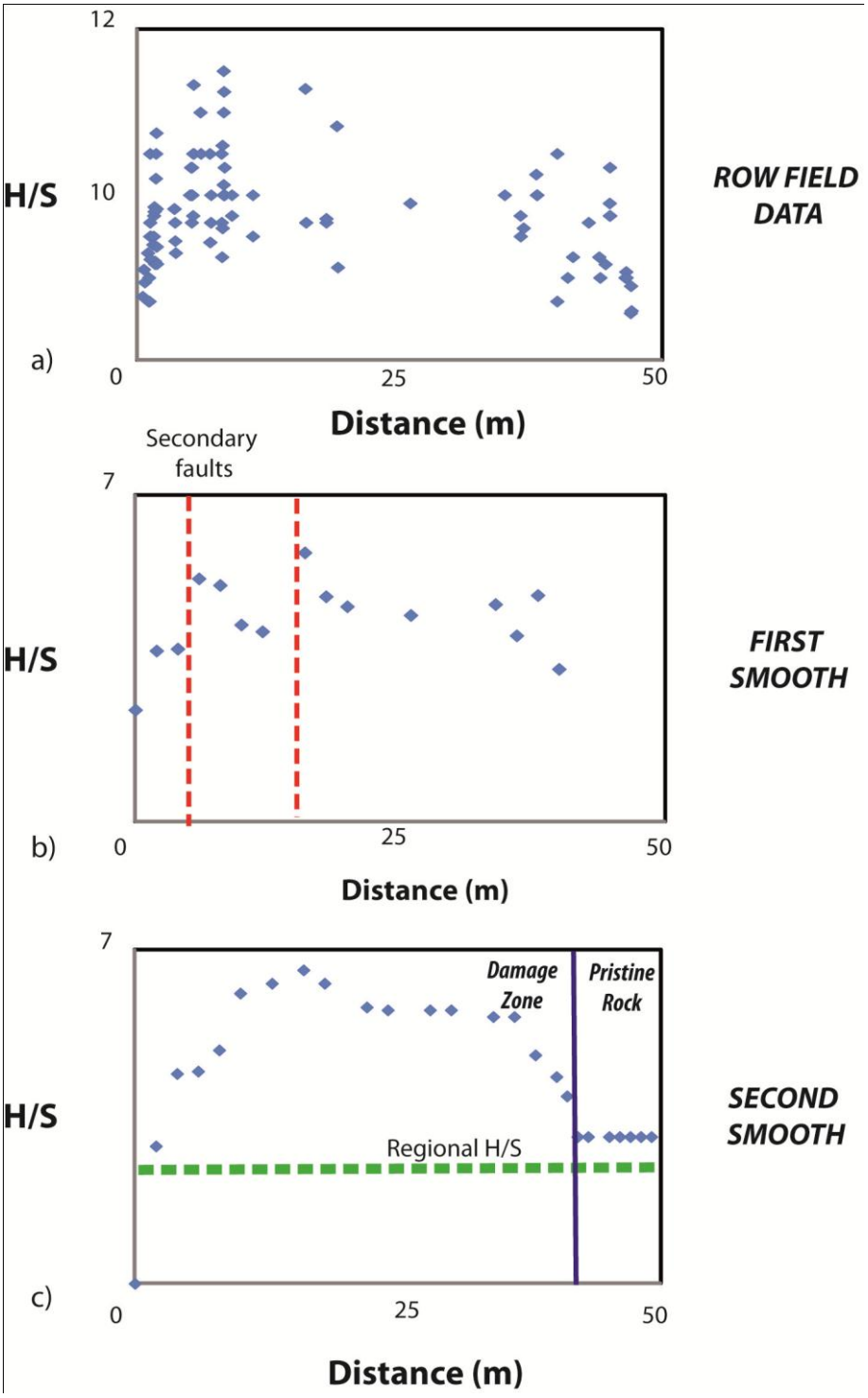

Fig. 5.105 – The smoothing data of the Castel di Ieri fault; a) Scattered row data; b) Resulting of the first smooth; c) Resulting of the second smooth. The green dashed line corresponds to the regional H/S value; the red dashed line corresponds to the secondary fault; the black line corresponds to the damage-zone pristine rock boundary

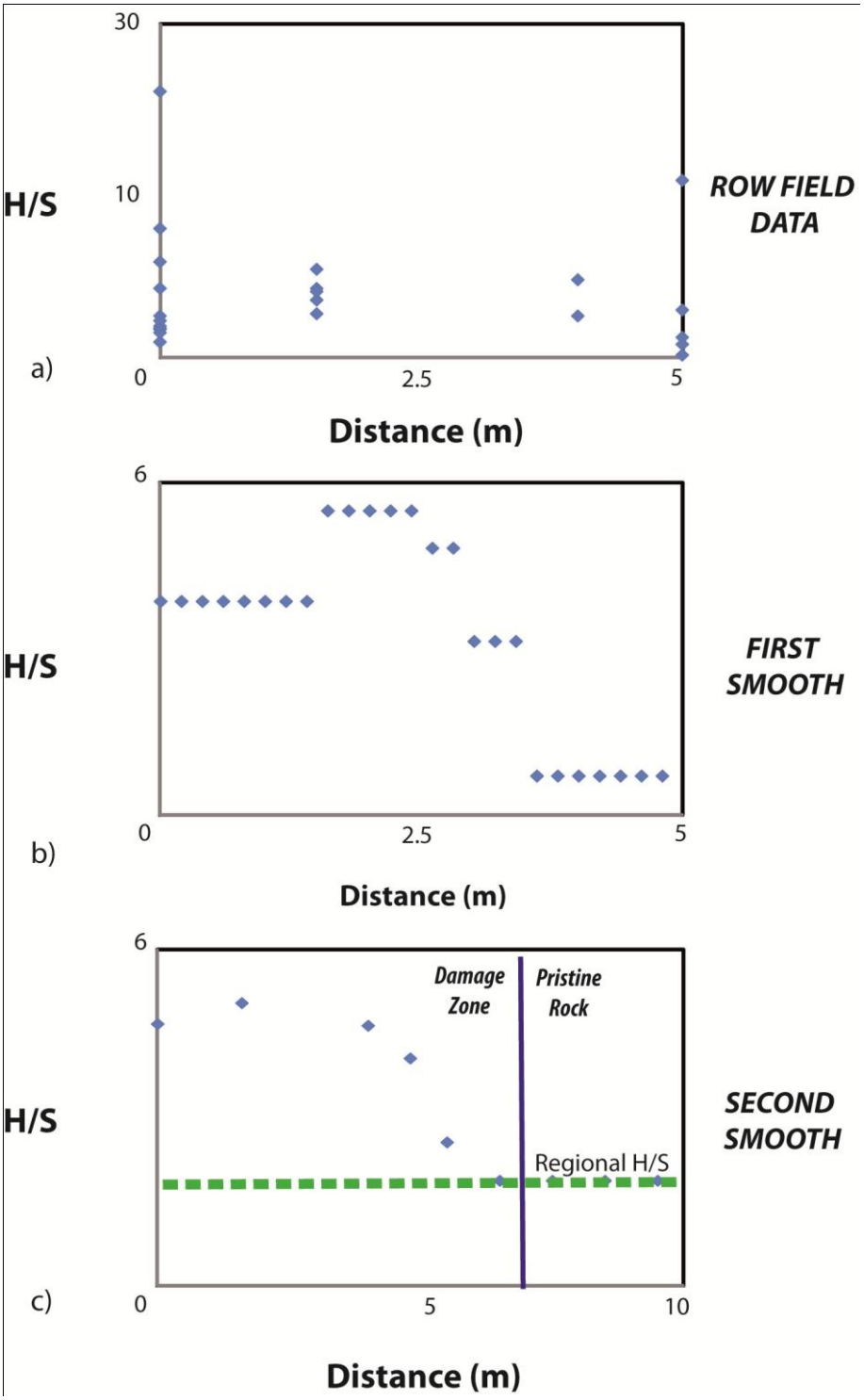

Fig. 5.106 –The smoothing data of the Fara 1 fault; a) Scattered row data; b) Resulting of the first smooth; c) Resulting of the second smooth. The green dashed line corresponds to the regional H/S value; the red dashed line corresponds to the secondary fault; the black line corresponds to the damage-zone pristine rock boundary

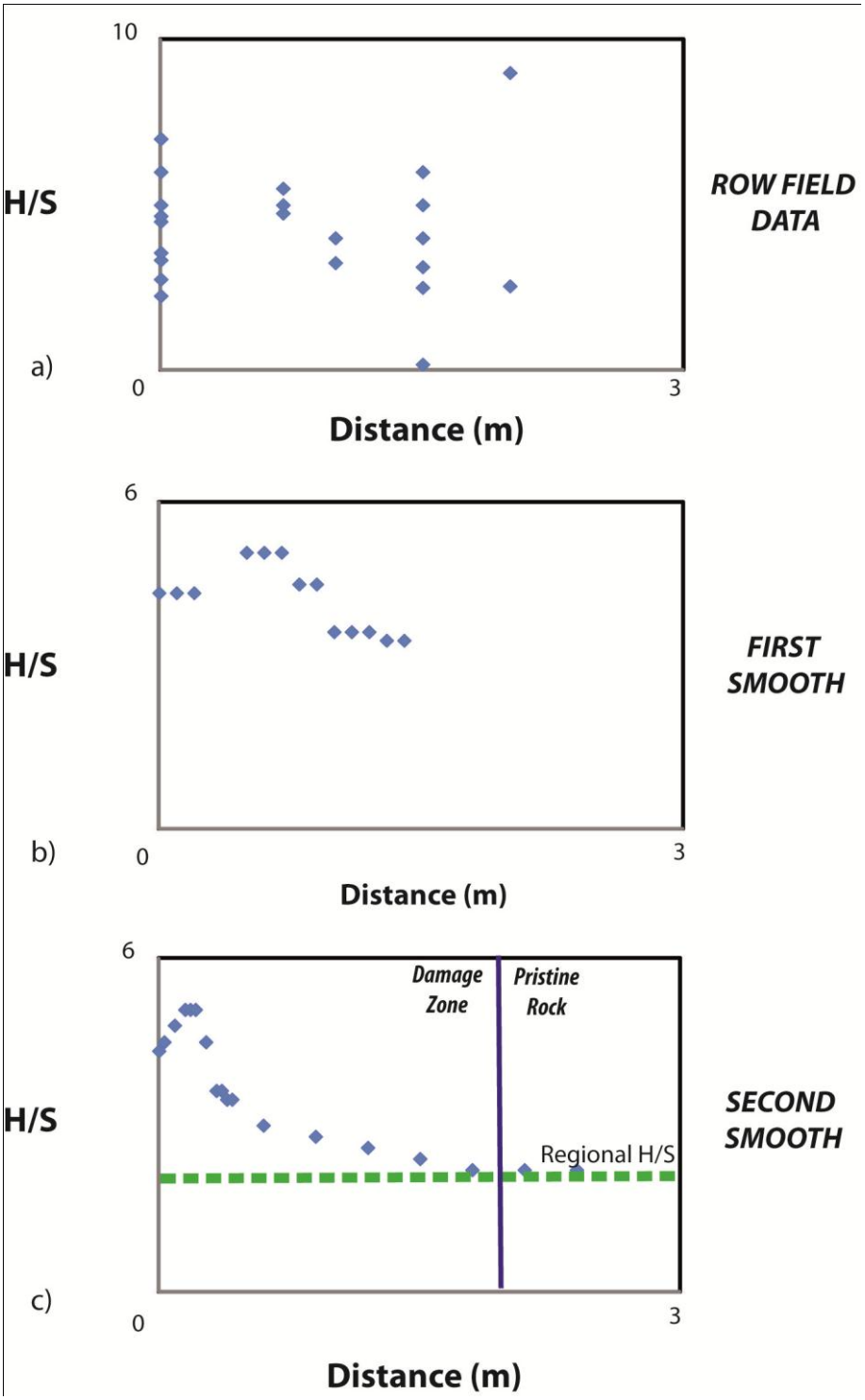

Fig. 5.107 –The smoothing data of the Fara 2 fault; a) Scattered row data; b) Resulting of the first smooth; c) Resulting of the second smooth. The green dashed line corresponds to the regional H/S value; the red dashed line corresponds to the secondary fault; the black line corresponds to the damage-zone pristine rock boundary

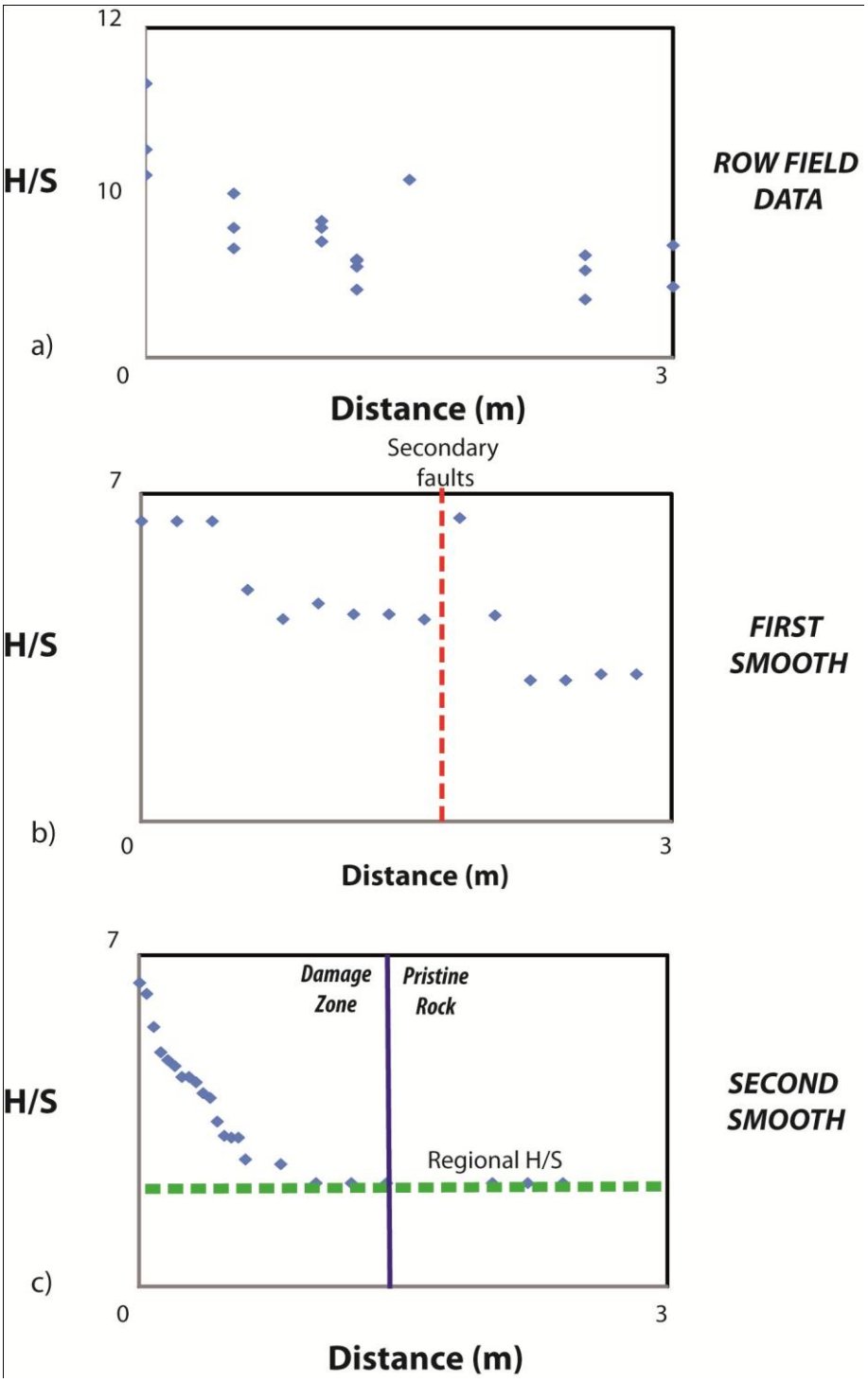

Fig. 5.108 –The smoothing data of the Fara 4 fault; a) Scattered row data; b) Resulting of the first smooth; c) Resulting of the second smooth. The green dashed line corresponds to the regional H/S value; the red dashed line corresponds to the secondary fault; the black line corresponds to the damage-zone pristine rock boundary

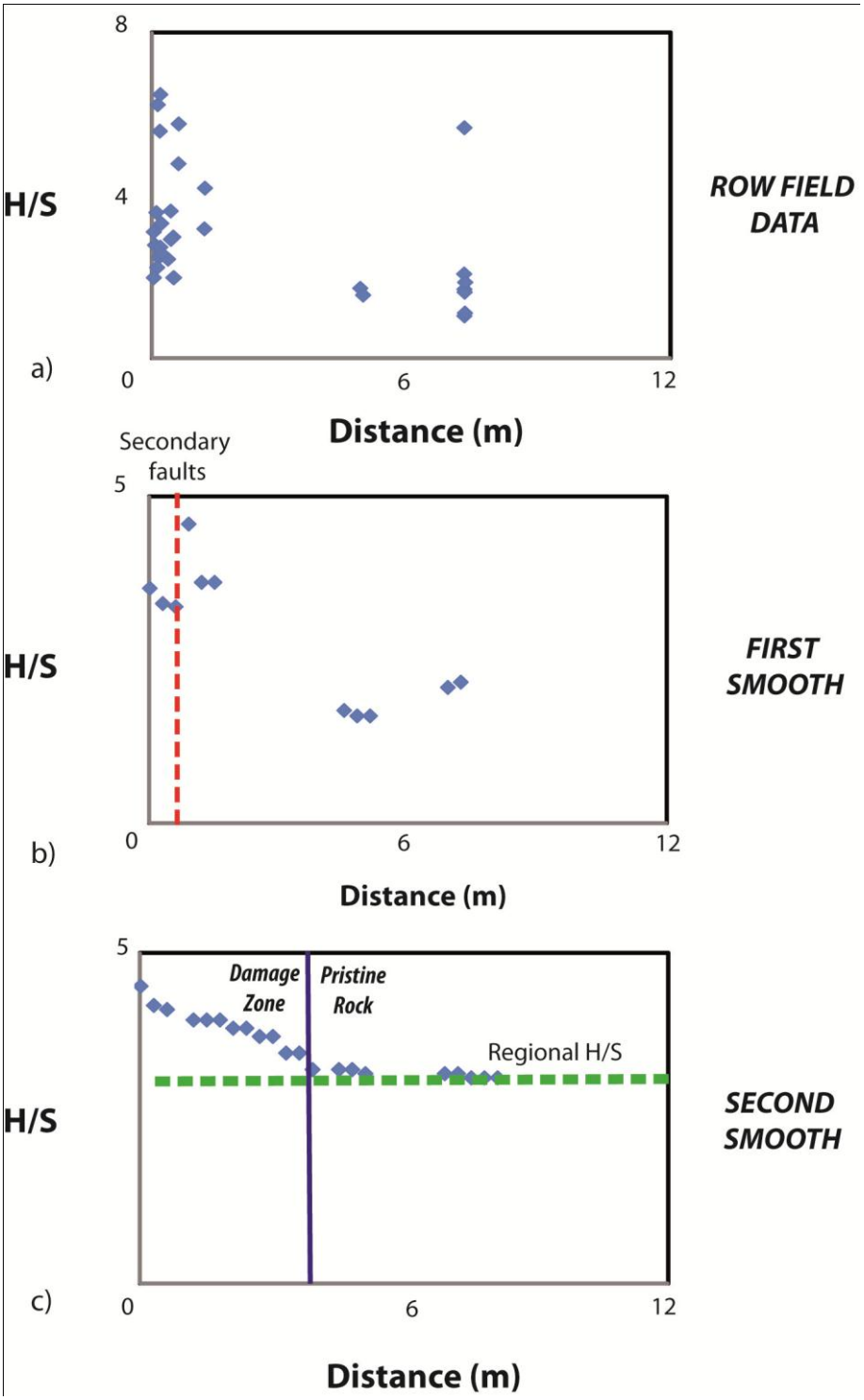

Fig. 5.109 –The smoothing data of the Fara 6 fault; a) Scattered row data; b) Resulting of the first smooth; c) Resulting of the second smooth. The green dashed line corresponds to the regional H/S value; the red dashed line corresponds to the secondary fault; the black line corresponds to the damage-zone pristine rock boundary

5.6.1.2 Interpretation of the smoothed data

The quantitative analysis of the smoothed H/S curves shows the presence of three main trend typologies. A total number of 9 faults are characterized by a decreasing trend of H/S value with the increase of distance from the fault plane. This decrease can be exponential such as the case of the Pietrasecca fault, the Tornimparte 2 fault, the Tornimparte 3 fault, the Tornimparte 5 fault, the Fara 4 fault, or can be a Semi-Gaussian, such as the case of Lecce dei Marsi 2 and the Fara 1 faults. On the other hand, a total of 8 faults show a Gaussian trend. It is characterized by an increase of H/S values through the distance from the fault plane and then a decrease down to the regional value. Therefore, this trend is characterized by a peak, where position, height, and width depend on the fault characteristic. Hence, one or more geological process produces the decrease of H/S value nearby the fault plane. We can observe that the subseismic scale faults prevalently show an exponential or a semi-Gaussian decrease, while the seismic scale faults are characterized by a trend that shows the peak. This evidence suggests that this particular trend is probably related to the evolution of the faults in time and space. In addition, these faults show the presence of a fractured rock on a cataclastic and recemented matrix in proximity of the fault plane. In this way, it is reasonable to ascribe this trend to the occurrence of a recementation process.

5.6.2 The equation study: Monte Carlo first stage

The model was prepared to find a predictive equation of the expected H/S value in the fault damage zones from the geological characteristics of a fault. The geological characteristics of a fault in carbonates that have been considered in the physical model were: the displacement, the deformation depth, the regional deformation and the rock mechanical characteristics including clay content during the fault activity.

The first series of tests results in a log-normal equation. It is a probability distribution of a random variable whose logarithm is normally distributed. If X is a random variable with a normal distribution, then $Y = e(X)$ has a log-normal distribution; likewise, if Y is log-normally distributed, then $X = \log(Y)$ is normally distributed. The equation shape depends on three parameters: a) H, the height of the peak; b) P, the position of the peak; c) W, the width of the peak. The regional intensity of deformation (x / x + 1) was added to the equation.

This initial approach was not completely satisfying when compared to the geological, since it was not possible to obtain a significant relation between the parameters and the given geological parameters. A different equation was then prepared to introduce a more probabilistic distribution of fracturing, i.e. by considering that a more favourable stress conditions would result in a higher fracturing probability. This new equation takes this in consideration and is based on the Normalized Standard Error distribution curve (i.e. Gaussian Curve) (Fig. 5.110):

$$\mathbf{H/S} = (\textit{Term 1} + \text{Regional H/S}) * \textit{Term 2} \qquad \text{(eq. 5.3)}$$

Term 1 is:

$$\textit{Term 1} = \mathbf{H}*e\,[-1.383*(\text{Distance} / \mathbf{W})\text{^}\mathbf{M}) \quad \text{(eq. 5.4)}$$

The *Term 2* is:

$$\textit{Term 2} = \text{Distance} / (\text{Distance} + \mathbf{R}) \quad \text{(eq. 5.5)}$$

With:
H that is the H/S maximum mean value minus the regional H/S and it controls the height of the equation peak (Fig. 5.110 Final equation I Type).
W that is the distance from the fault-plane where the H/S became ½. It controls the width of the curve (Fig. 5.110 Final equation I Type)
R that is the *C-C* Number (Fig. 5.110 Final equation I Type)
M that is the position of the peak. It governs the shape of the curve and the damage-zones maturity (Fig. 5.110 Final equation I Type).

The two terms can be related to the main geological process that controls the distribution of the deformation intensity in fault zone. In particular, the *Term 2* is related to the fault kinematic (K) because increases the H/S value; the Term 2 is related to the pressure solution and the cementation process (C-C), because it causes a decrease of the H/S value. Replacing the term, the equation can be written in following form:

$$\mathbf{H/S} = (K + \text{Regional H/S})*\text{C-C} \quad \text{(eq. 5.6)}$$

The K-factor and the C-C factor include all the geological variables that control the development of fault damage-zone, such as the throw, the deformation depth, and the clay content. To study the relation between this geological factor and the variation of the deformation intensity with the distance from the fault-plane it was used the Monte Carlo statistical approach (see next paragraph).

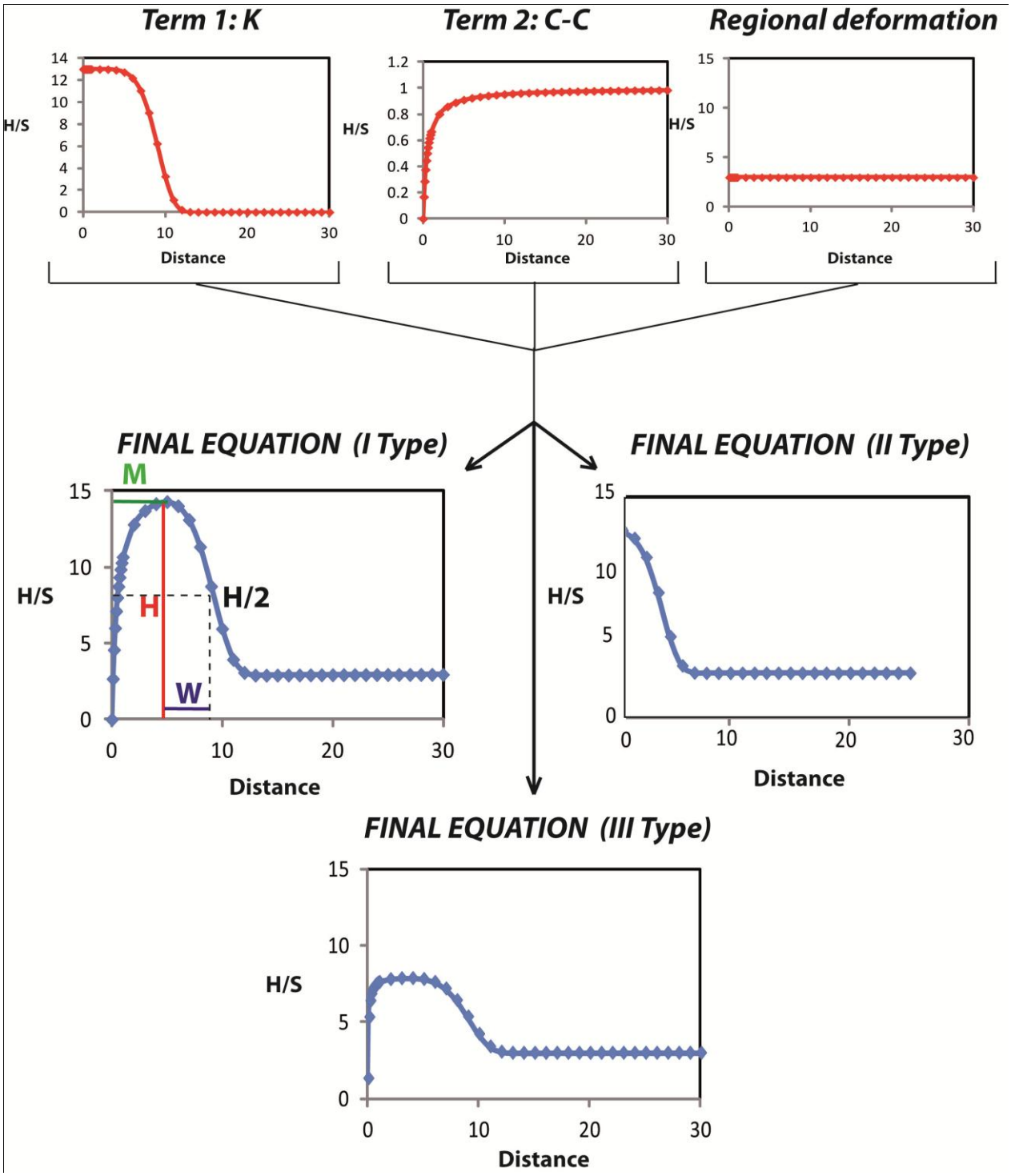

Fig. 5.110 – Scheme of the final equation which is able to reproduce the three trends

5.6.3 The implementation

The method was implemented into an in-house developed software, MONTECARLO_MCM. A further parameter in the Monte Carlo MCM software allows to set the threshold RMS value (**Trms)** to identify and save results with an RMS < **Trms**. This allows obtaining the required statistics for the evaluation of the attractors in the probability/solution space. This parameter was set to **Trms** = 0.1 for the first step.

In this way the software provides graphical windows during the inversion to describe the distribution of preliminary solutions in given sections/surfaces of the multidimensional probabilistic/solution space. It is possible to have a visual check on the convergence of the solution (i.e. the consistency of the solution attractors Fig. 5.112). This allowed controlling the parameters that rules the Monte Carlo MCM inversion to the final values used.

5.6.4 Monte Carlo resulting parameters and the geological variables

The study of the geological factor affecting the intensity of deformation in fault damage-zone was completed by means of the Monte Carlo statistical analysis. In this paragraph are presented the results of the statistical analysis in order to study the geological factor affecting the shape of the curve controlled by the equation parameters H, W, R and M. It is important to remind that the different curves correspond to different deformation patterns and this kind of approach allows finally defining quantitatively the relation between the deformation distribution in fault damage-zones and the geological factor affecting this distribution.

The Monte Carlo results are showed in the Appendix 1. For the analysis it has been used the following parameter search ranges: H 0-10; W 0-20; R 0-0.3; M 0-10, and the following Monte-Carlo parameters: Number of Iterations 10; Number of Cycle per iteration 10000; Converging Factor 0.9. The resulting RMS range from 0.1 to 1.68, and the highest RMS was found for the Rocca di Cave 1 fault, Rocca di Cave 2, Tornimparte 1 fault, and Castel di Ieri fault.

To study this issue a correlation analysis was applied to the resulting Monte-Carlo *H, W, R, M,* and the main geological variables, namely the Insoluble contents (Cl), the throws (Th), the deformation depths (DDf) and the regional H/S values (H/S Regional). The results of the analysis are the correlation number (CN) which absolute value proves the goodness of the correlation. In particular, CN = 0 means a bad correlation, while a CN = 1 indicates a good correlation.

The results of the first correlation analysis are showed in Fig. 5.111 a. We can see that the clay content correlation numbers are always minor than 0.50, suggesting that this variable does not affect the shape of the curve. Otherwise, the throws affect mostly the W parameter (CN = 0.60), which controls to the width of the curve. The regional deformation is mostly related to R and H parameters (CN = 0.50; 0.68), which both control the height of the curve. The deformation depth does not show any evident relation with the equation parameters.

A second correlation analysis was performed on the faults which deformation trend shows an exponential trend (Fig. 5.111 b). For these faults the most important parameters which affect the shape of the curve are the throw, the regional deformation, and the deformation depth. In particular, the throw and the regional deformation control the W parameter (CN = 0.78), hence

the width of the curve. The deformation depth controls the H parameter (CN = 0.58), hence the height of the curve.

A third correlation analysis was performed on the faults showing a Gaussian trend (Fig. 5.111 c). The data show that only the regional deformation affects the sensibly the shape of the curve (CN = 0.85).

	H	W	R	M	CLAY	THROW	REG	DEF DEPTH
H	1.00	0.38	0.63	0.42	0.22	0.30	0.50	0.14
W	0.38	1.00	-0.22	-0.04	0.00	0.61	-0.25	-0.11
R	0.63	-0.22	1.00	0.40	0.30	-0.12	0.68	0.25
M	0.42	-0.04	0.40	1.00	0.35	-0.05	0.13	0.42
CLAY	0.22	0.00	0.30	0.35	1.00	0.29	0.19	0.62
THROW	0.30	0.61	-0.12	-0.05	0.29	1.00	-0.27	-0.25
REG	0.50	-0.25	0.68	0.13	0.19	-0.27	1.00	0.28
DEF DEPTH	0.14	-0.11	0.25	0.42	0.62	-0.25	0.28	1.00

a)

	H	W	R	M	CLAY	THROW	REG	DEF DEPTH
H	1.00	0.29	-0.53	0.40	0.02	0.25	-0.28	0.58
W	0.29	1.00	-0.40	0.68	-0.64	0.78	-0.78	0.10
R	-0.53	-0.40	1.00	-0.13	0.05	-0.29	0.27	-0.33
M	0.40	0.68	-0.13	1.00	-0.24	0.23	-0.51	0.23
CLAY	0.02	-0.64	0.05	-0.24	1.00	-0.56	0.53	0.31
THROW	0.25	0.78	-0.29	0.23	-0.56	1.00	-0.59	0.02
REG	-0.28	-0.78	0.27	-0.51	0.53	-0.59	1.00	0.29
DEF DEPTH	0.58	0.10	-0.33	0.23	0.31	0.02	0.29	1.00

b)

	H	W	R	M	CLAY	THROW	REG	DEF DEPTH
H	1.00	0.15	0.64	0.25	-0.46	-0.10	0.82	-0.25
W	0.15	1.00	-0.48	-0.79	-0.61	0.48	-0.25	-0.45
R	0.64	-0.48	1.00	0.49	0.13	-0.46	0.85	0.24
M	0.25	-0.79	0.49	1.00	0.45	-0.64	0.59	0.49
CLAY	-0.46	-0.61	0.13	0.45	1.00	-0.48	-0.03	0.89
THROW	-0.10	0.48	-0.46	-0.64	-0.48	1.00	-0.55	-0.77
REG	0.82	-0.25	0.85	0.59	-0.03	-0.55	1.00	0.23
DEF DEPTH	-0.25	-0.45	0.24	0.49	0.89	-0.77	0.23	1.00

c)

Fig. 5.111 – Correlation analysis results; a) All the faults; b) Faults showing exponential H/S trend; c) Fault showing the Gaussian H/S trend

5.6.5 The relation with the geological factors: Monte Carlo second stage

In the second step, resulting parameters from each fault were compared and a set of 20 faults representing the main type of damage zone observed. Then their equation parameters were

substituted in equation (Eq. 1) by functions of the geological parameters that would replicate their relations with the geological parameters of the corresponding fault.

Distance = 1.044
Insoluble Content = 6.363e-02
Throw= 1.483
Regional H/S = 0.402
Deformation Depth = 2.701

A second MCM fit was then processed to obtain the final parameters of the equation that relates the H/S values at distance x to the given geological characteristics of the fault.

5.6.6 The resulting model

Eventually, a Monte-Carlo analysis was performed using all the studied faults in order to find the parameter of the final equation that will be implemented in the predictive modelling software. The final numeric results have this form:

$$\mathbf{H/S} = \{Term\ 1 = \mathbf{H} * e\ [-4 * \ln_2 * (\mathbf{x} / \mathbf{W})\hat{}\mathbf{M}] + \text{Regional H/S}) * \mathbf{x}/(\mathbf{x} + \mathbf{R})\} \qquad \text{(eq. 5.7)}$$

With:

H = 1.04
W = 6.36
M = 0.40
R = 1.48

The resulting RMS is 2, which correspond to an error of 2.0 in the computation of H/S. The high value is related to the big variability of trends included in the model.

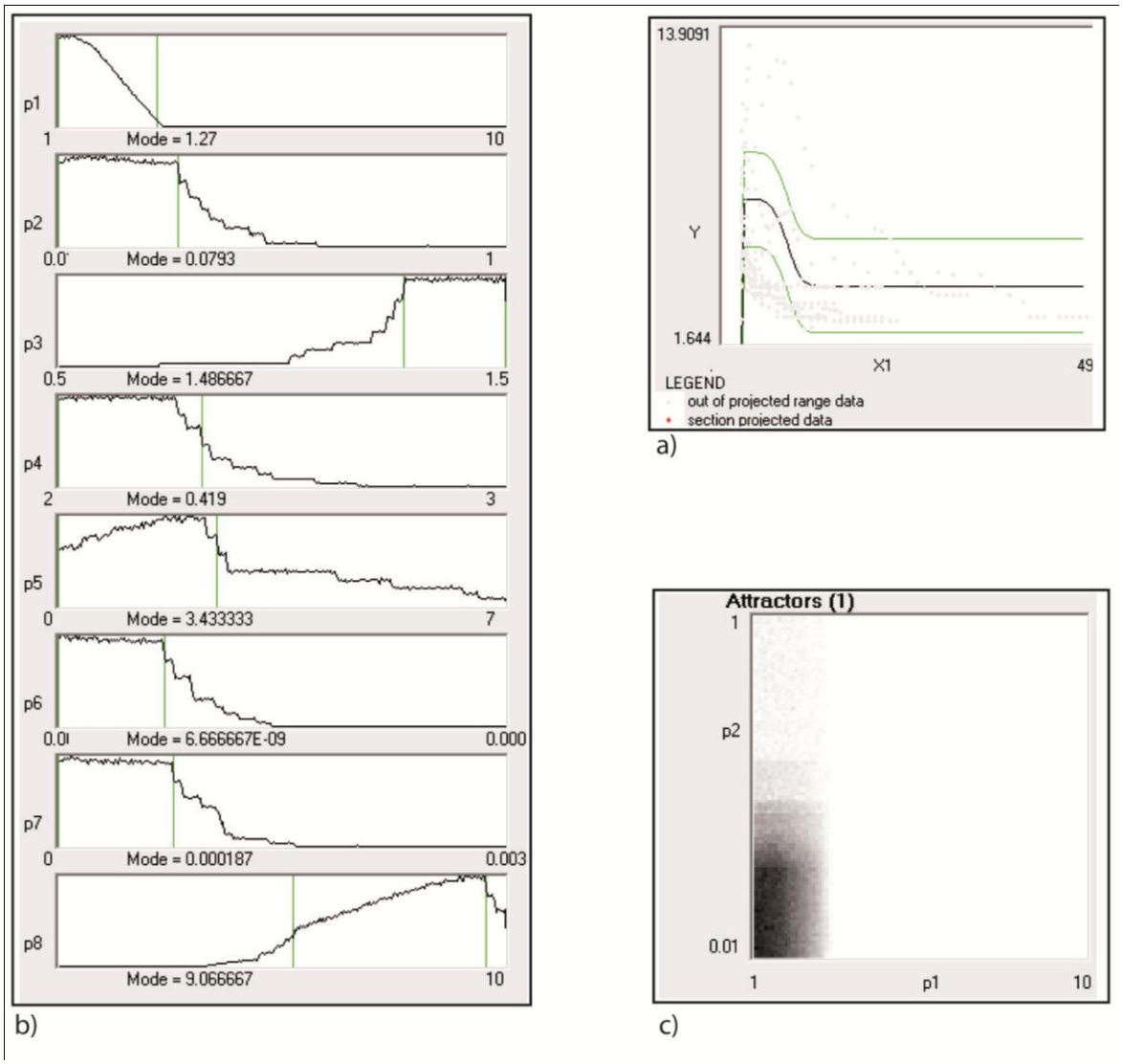

Fig. 5.112 – a) Data Space; b) Parameter Space; c) Parameters Section attractor

5.7 Fracturing predictive modelling

The resulting equation was implemented in an in-house fracturing predictive software (Frap 3) and the models of the following 6 faults have been performed: Filettino, Ienne, Pietrasecca, Tornimparte 1, Tornimparte 2, Fara 4 and Fara 6, which the results are showed in Appendix 2. Each plane corresponds to an H/S plane at an x distance from the fault plane. The colour scale correspond to the H/S scale, hence the deformation intensity scale. These faults have been chosen because they represent a sample of scale variability. The models were compared with the field data in order to test the validity of the prediction.

5.7.1 Physical parameters setting

The same rock mechanical parameters have been used for the modelled faults and the data are summarized in Tab. 5.8. The Poisson Ratio for the consolidated rocks generally ranges between 0.2 and 0.3 and we choose 0.25. The rock density strongly depends on the lithology. It ranges between 2300 and 2700 Kg/cm^3 in limestones and between 2400 and 2800 in shales. The lithologies of the modelled faults consist in carbonate mudstones and grainstones, and we chose 2600 Kg/cm^3. The cohesion value and friction angle are 5 MPa and 30° respectively.

The fault physical parameters data are summarized in Tab 5.9. The Pressure solution threshold depends on the typology of rock. The deformation depth is related to the overburden at fault top and the reactivation critical probability is related to the activity of fault.

NAME	CONDITION	POISSON RATIO	ROCK DENSITY (Kg/cm3)	COHESION (Mpa)	FRICTION ANGLE
Filettino	Kinematic	0.25	2600	5	30
Ienne	Kinematic	0.25	2600	5	30
Pietrasecca	Kinematic	0.25	2600	5	30
Tornimparte 1	Kinematic	0.25	2600	5	30
Tornimparte 2	Kinematic	0.25	2600	5	30
Fara 4	Kinematic	0.25	2600	5	30
Fara 6	Kinematic	0.25	2600	5	30

Tab. 5.8

NAME	PRESSURE SOLUTION THRESHOLD (Mpa)	PALEOBAHIMETRY (m)	OVERBURDEN (m)	FLUID PRESSURE INFLUENCE (%)	REACTIVATION CRITICAL PROBABILITY (%)
Filettino	20	10	1000	10	0
Ienne	20	10	1000	10	0
Pietrasecca	40	30	1000	10	0
Tornimparte 1	20	10	48	30	20
Tornimparte 2	20	10	368	10	0
Fara 4	20	10	320	10	0
Fara 6	20	10	320	10	0

Tab. 5.9

5.7.2 Comparison between models and field data

Two different tests have been performed on the faults tuning the regional stress value and the throw. In Fig. 5.114 are showed the results for the Filettino fault obtained assuming a regional stress of – 20 MPa (upper graph) and -10 MPa (lower graph) respectively. Changing the regional stress value and maintaining the same throw, the TSI and the DF change their strongly values. In particular, a regional stress of -20 MPa produces a DF of 12 MPa and a TSI of 266 MPa. The values are very high and the comparison between the H/S shows that the difference between them exceeds even the error of the equation (RMS 2.0). A stress of -10 MPa produces a TSI value of 90 MPa and a DF of 3.5 MPa, and the difference between the model and the field data does not exceed the error of the equation. Assuming a stress value lower than 10 the failure condition are not reached and the DF value are negative. The model prediction of the damage–zone width is good. The H/S distribution changes with the distance from the fault plane (Appendix 2) and this distribution depends on the depth and on the fault plane plunge.

In Fig. 5.115 are showed the results of the Ienne fault models obtained assuming a regional stress of – 40 MPa (upper graph) and -32 MPa (lower graph) respectively. Changing the regional stress value and maintaining the same throw, the TSI and the DF strongly change. In particular, a regional stress of -40 MPa produces a deformation function of 2 MPa and a TSI of 324 MPa. The values are very high and the comparison between the H/S shows that the difference between them exceeds even the error of the equation (RMS 2). A stress of -32 MPa produces a TSI value of 140 MPa and a DF of 0.4 MPa and the difference between the model and the field data does not exceed the equation error. Assuming a stress value lower than 10 the break condition are not reached and the DF value are negative. Even in this case, the model prediction of the damage–zone width is good.

In Fig. 5.116 are showed the results for Pietrasecca fault. The upper graphs show two tests assuming a regional stress of -35 MPa and -50 MPa respectively, and assuming the same throw. The modeling prediction is always overestimate respect the field data; otherwise, the fault damage-zone width is well predicted. In the lower graph another test was presented, where the throw value was doubled and the regional stress value is -35 (as the first test). The H/S maximum values now is well predicted, otherwise the damage-zone width is now overestimated.

In Fig. 5.117 are showed the Tornimparte 1 faults results. The tests were performed assuming a stress intensity of -30 (Upper graph) and -50 MPa (Lower graph) respectively. In both the cases the resulting TSI values are very high (First Test – TSI = 538 MPa; Second Test – TSI = 800 MPa); otherwise the DF values are very low (First Test – DF = 1.78 MPa; Second Test – DF = 0.7 MPa). In both the tests the model and the field data do not fit very well due to the occurrence of the fluids pressure which reduces the breaking capacity of the rock. Otherwise the damage-zone width prediction is good.

In Fig. 5.118 are showed the Tornimparte 2 fault results. The two tests were performed assuming a regional stress of -37 MPa (Upper graph) and -25 MPa (Lower graph) respectively, maintaining the same throw. Reducing the stress intensity the predicted H/S values do not strongly change and the model data are overestimated respect to the field data. Despite this overestimation, which anyway does not exceed the equation error, the prediction of the damage-zone width is good. In

addition, the higher value of stress intensity does not correspond to high value of DF and TSI (First Test – DF = 1.7 MPa TSI = 1 MPa; Second Test – DF = 0.3 MPa TSI = 0.5 MPa).

In Fig. 5.119 are showed the results of Fara 6 fault. The tests are performed assuming two different regional stress intensity: -25 MPa (upper graph) and -20 MPa (lower graph), respectively. The H/S prediction does not show any evident difference and both the tests show an overestimation of the model data respect to the field data. The values of DF are low (First Test – DF = 2 MPa; Second Test – DF = 0.4 MPa) but the stress intensity is high, so that, in this case as well, the fluids pressure strongly affects the deformation distribution.

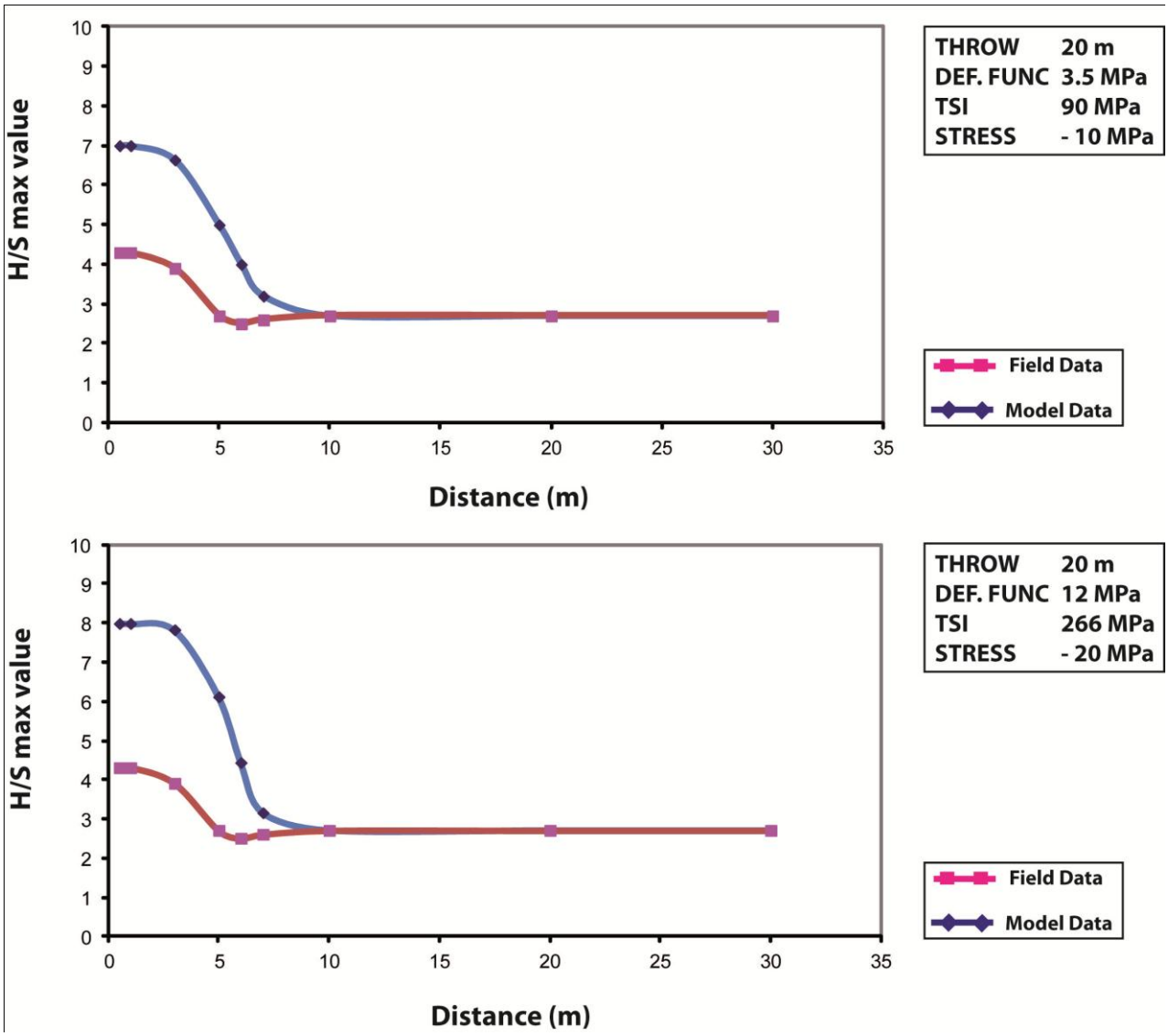

Fig. 5.114 – Comparison between the model and the field data for Filettino fault

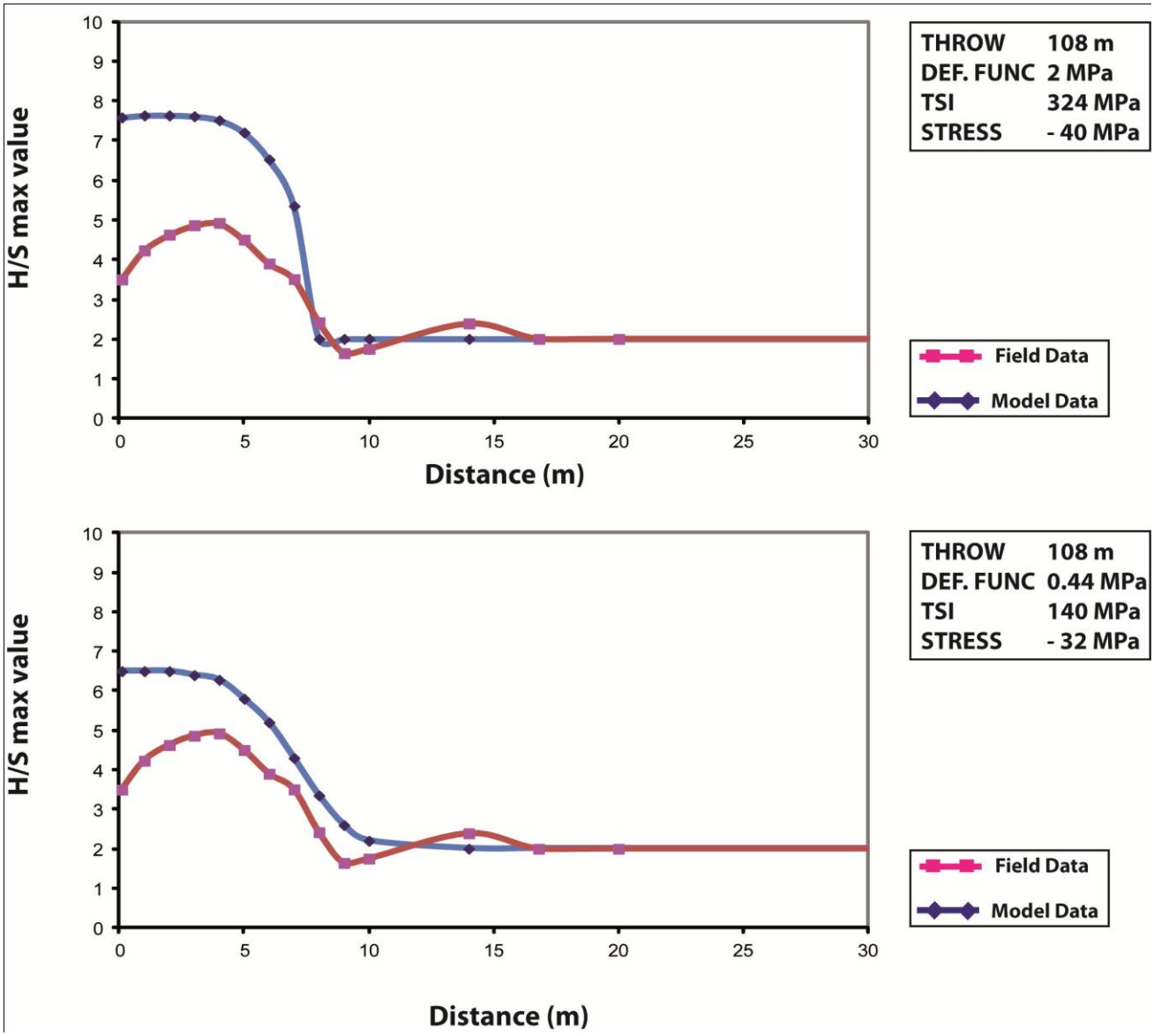

Fig. 5.115 - Comparison between the model and the field data for Ienne fault

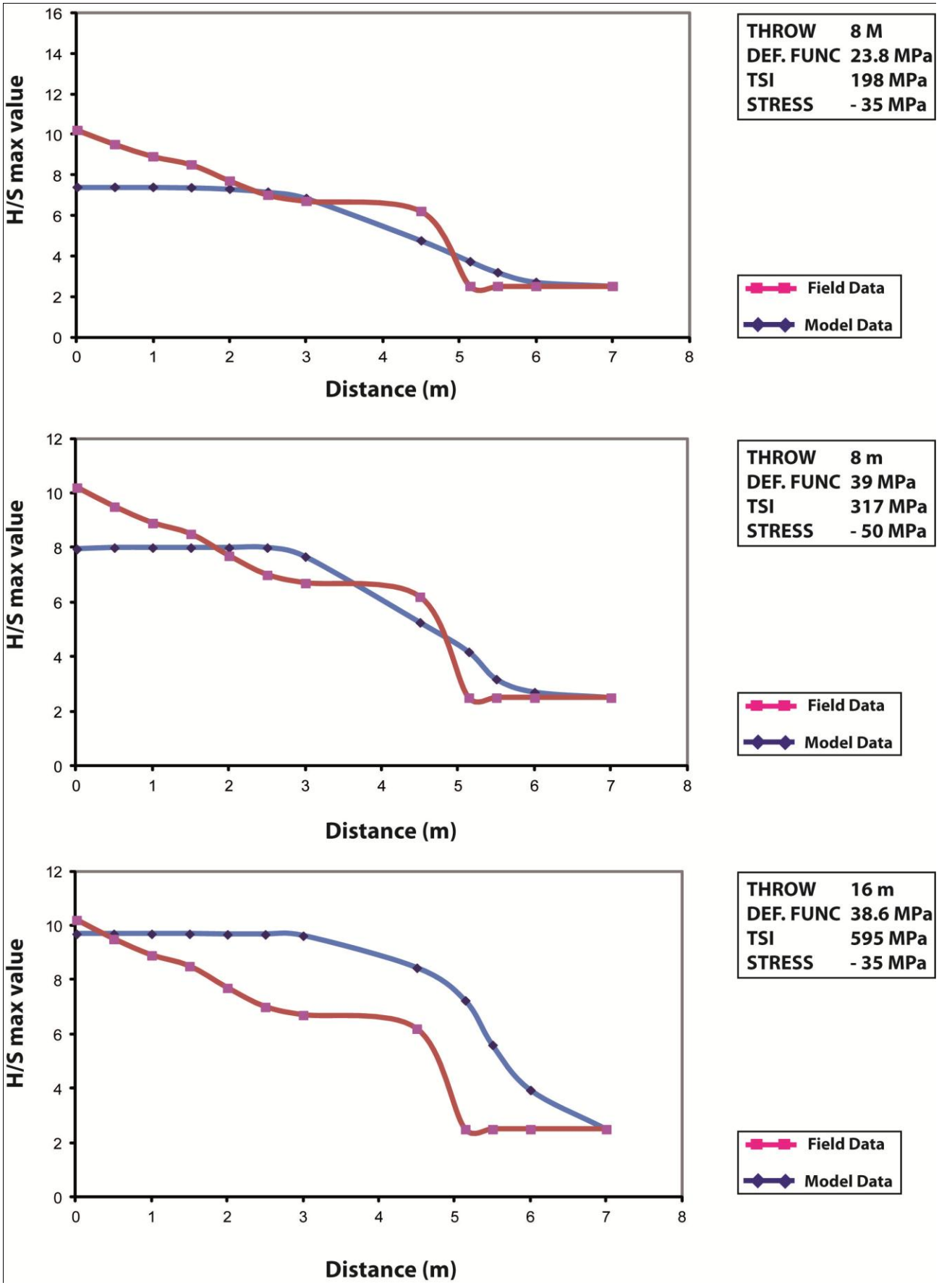
H/S max value
Distance (m)
THROW 8 M
DEF. FUNC 23.8 MPa
TSI 198 MPa
STRESS - 35 MPa
Field Data
Model Data
H/S max value
Distance (m)
THROW 8 m
DEF. FUNC 39 MPa
TSI 317 MPa
STRESS - 50 MPa
Field Data
Model Data
H/S max value
Distance (m)
THROW 16 m
DEF. FUNC 38.6 MPa
TSI 595 MPa
STRESS - 35 MPa
Field Data
Model Data

Fig. 5.116 - Comparison between the model and the field data for Pietrasecca fault

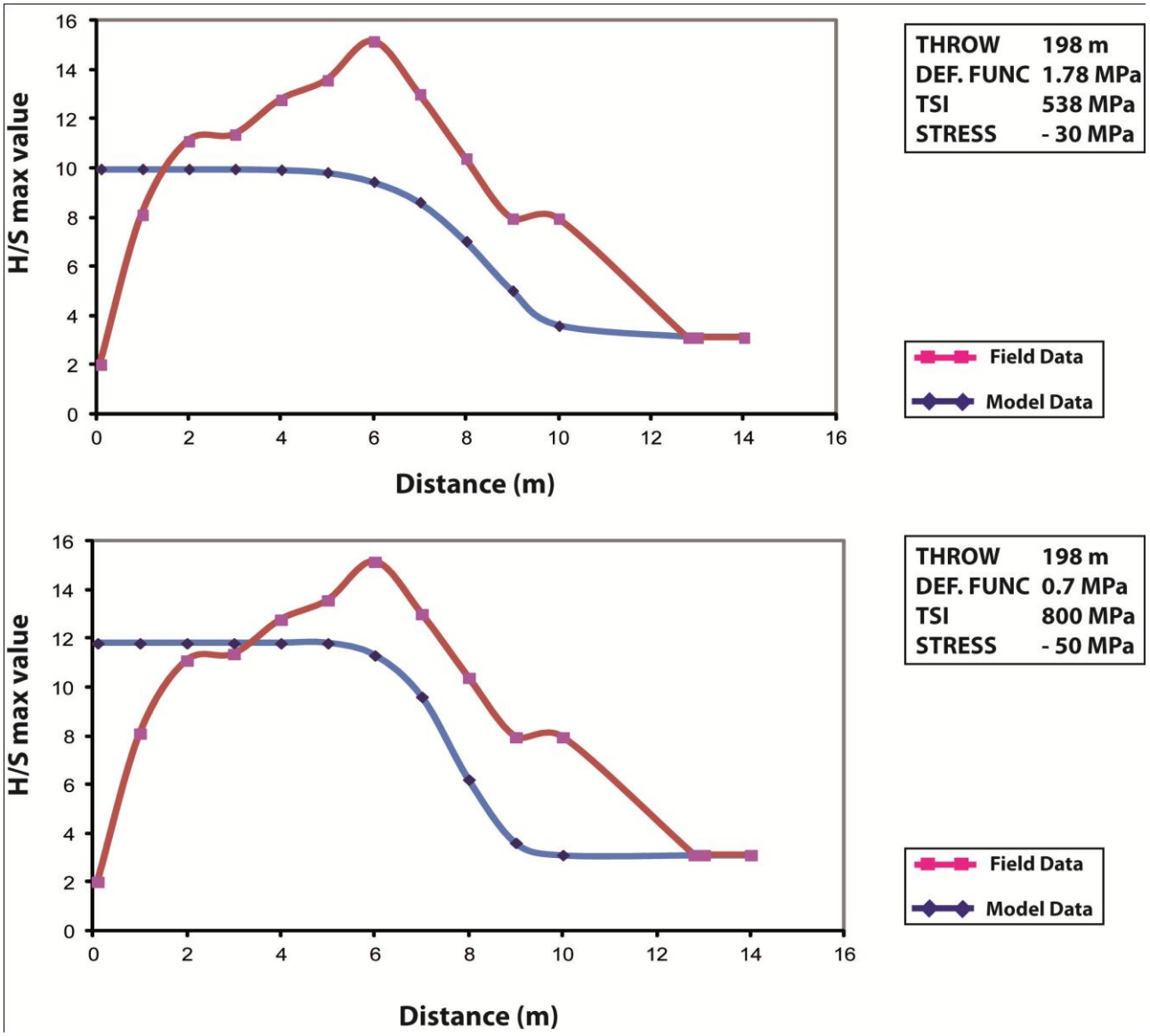

Fig. 5.117 - Comparison between the model and the field data for Tornimparte 1 fault

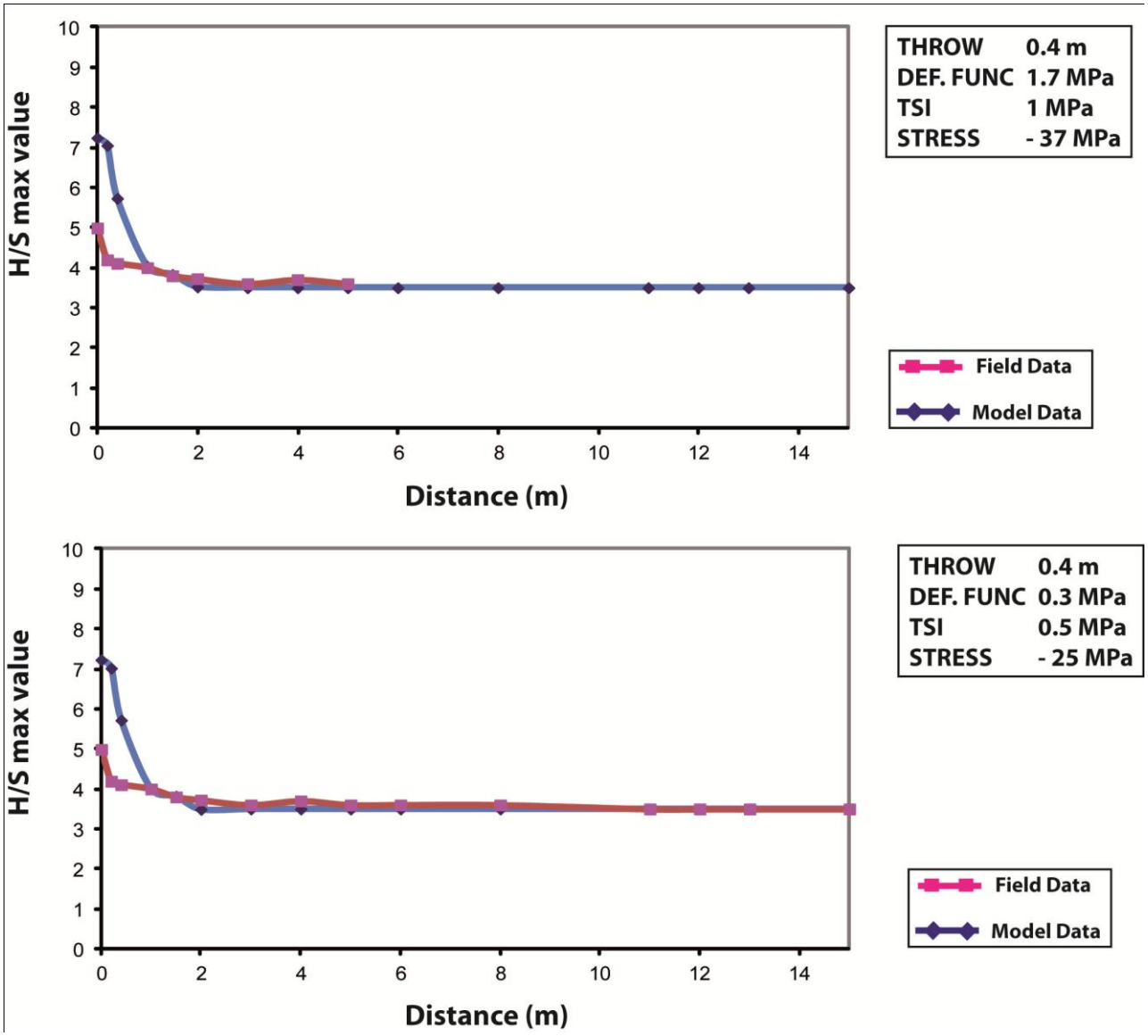

Fig. 5.118 - Comparison between the model and the field data for Tornimparte 2 fault

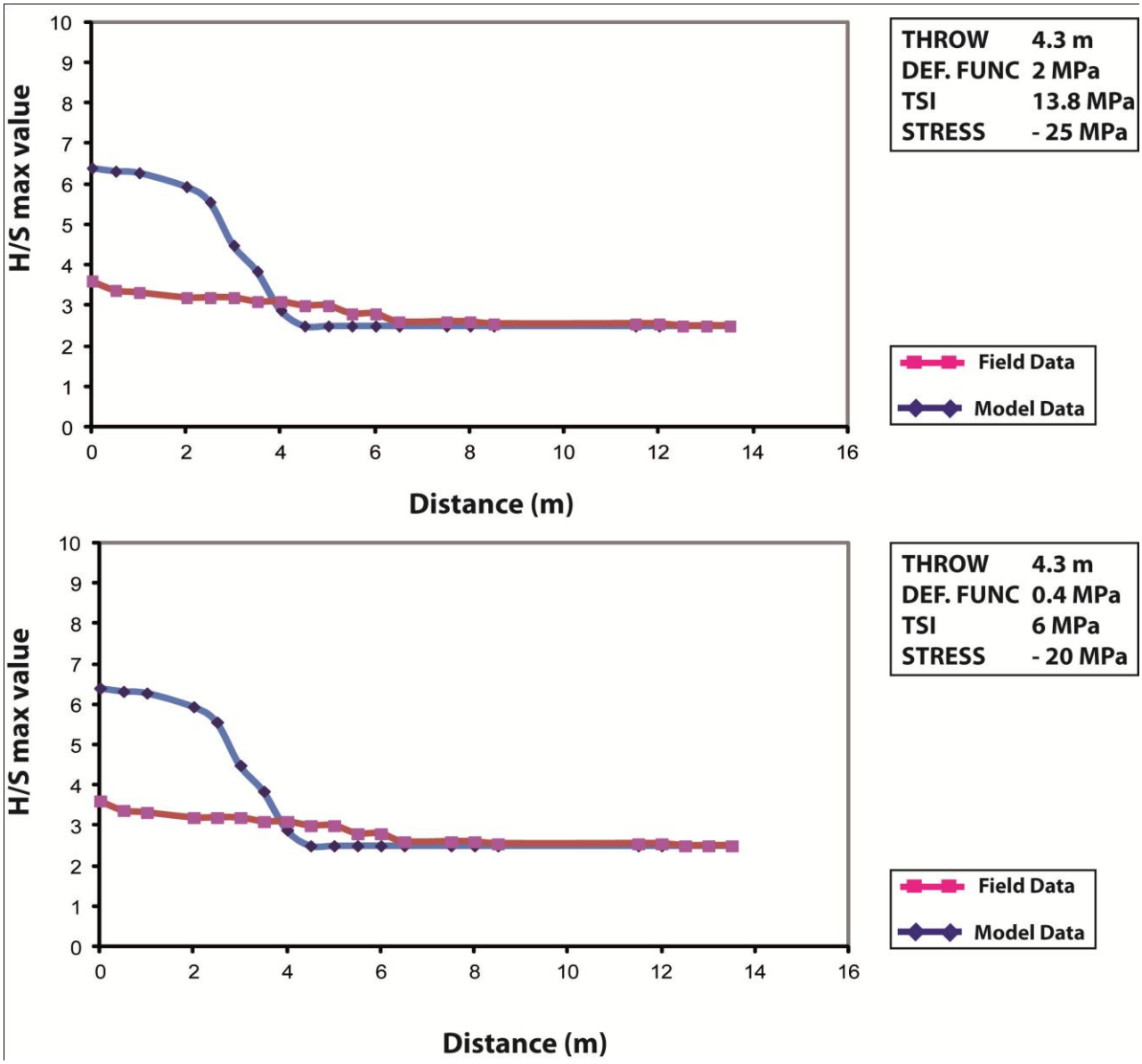

Fig. 5.119 - Comparison between the model and the field data for Fara 6 fault

6 – DISCUSSIONS

6.1 Fracture analysis

Out of the four main types of fracture cleavages, most of the fractures that were found in the fault damage zones can be grouped in two types, the synthetic shear fractures (i.e. the Riedel R Planes) and pressure-solution surfaces, depending on the resulting stress conditions. Less frequently we observe the formation of extensional fractures (i.e. joints) related to negative minimum stress conditions as in the presence of high fluid pressures.

Detailed field analyses of fault-related fractures have been performed. In the current work we define as a fracture all the extensional joints and the pressure-solution surfaces related to the stress accumulation due to the fault development.

6.1.1 Rock lithology and the intensity deformation

The analysed faults are located on three main protoliths, deposited in different sedimentary environments: Group *a)* shallow marine carbonate deposits, represented prevalently by mudstone, oolitic-packstone, wakestone, and dolostone; Group *b)* carbonate ramp deposits, represented by calcareous grainstones; Group *c)* platform-basin transition deposits, represented by carbonate mudstone (Dunham, 1964). In addition, we characterized the Group *d)* dolostone lithologies, interpreted as being the result of the diagenesis.

The carbonate lithologies have an expected matrix porosity between ≈ 1% and ≈ 10 % (Graham et al. 2003), while the dolostone has higher expected porosities ≈ 10% to ≈ 20 %.

The presence of impurities in the protoliths has been quantified by means of the insoluble content analysis. The resulting analysis is summarized in the graph of Fig. 6.1, where the x-axis corresponds to the pristine rock samples and the y-axis corresponds to the fault rock samples. A good linear correlation has been found for the faults belonging to the group *a)*, *b)*, and *c)* (R = 0.7). The samples collected in fault damage-zones are characterized by higher insoluble content than the samples collected in the pristine rocks. The faults belonging to Group *d)*, that are the dolostone protoliths, are not characterized by this linear relation. Meaning that the dolomitization is related to the diagenesis and enhanced by the fluid circulation, it induced pressure-solution process which increases the insoluble content of the fault rocks.

The different lithologies are characterized by different deformation patterns due to their different mechanical behaviour. In particular, by means of the *in situ* analysis of the regional deformation, it has been noticed that Group *a)* lithologies show mainly joints and extensional fractures, while Group *b)*, *c)*, *d)* lithologies show essentially pressure solution cleavages. Furthermore, the intensity of deformation of the protolith depends strongly on the rock type (Fig. 6.2), showing lower H/S values (mean H/S value = 2.6) for the group *a)*, and higher values (mean H/S value = 5.1) for the group *b)* and *c)*.

In addition, the regional H/S depends strongly on the tectonic environment (see Fig. 6.3). In the graph of Fig. 6.3 the relation between the regional tectonic contest and the deformation intensity measured as H/S mean value is analysed. The studied faults are divided in three groups based on

the regional tectonic contest in which each fault is located. The red columns correspond to the faults located in a thrust and fold tectonic contest; the blue columns correspond to the fault located in a strike-slip contest; the green columns are the faults located in a post-orogenic tectonic contest. The data show that the strike-slip tectonic contests are the most deformed showing H/S values ranging between 5 and 2.1. The faults located in a thrust belt tectonic contest and in a post-orogenic extension contest show a lower value of regional H/S, ranging between 3.9 and 2. This different behaviour is less pronounced for the faults, whose patterns and deformation intensity distribution depends strongly on other factors, such as the other characteristics of the mechanical layering (i.e. the bed thickness or the clay interbedding content) and fault characteristics (i.e. the fault kinematic, the throw, the age of deformation, the deformation depth, the time of active stress) which rule strongly the stress distribution and consequently the brittle deformation distribution.

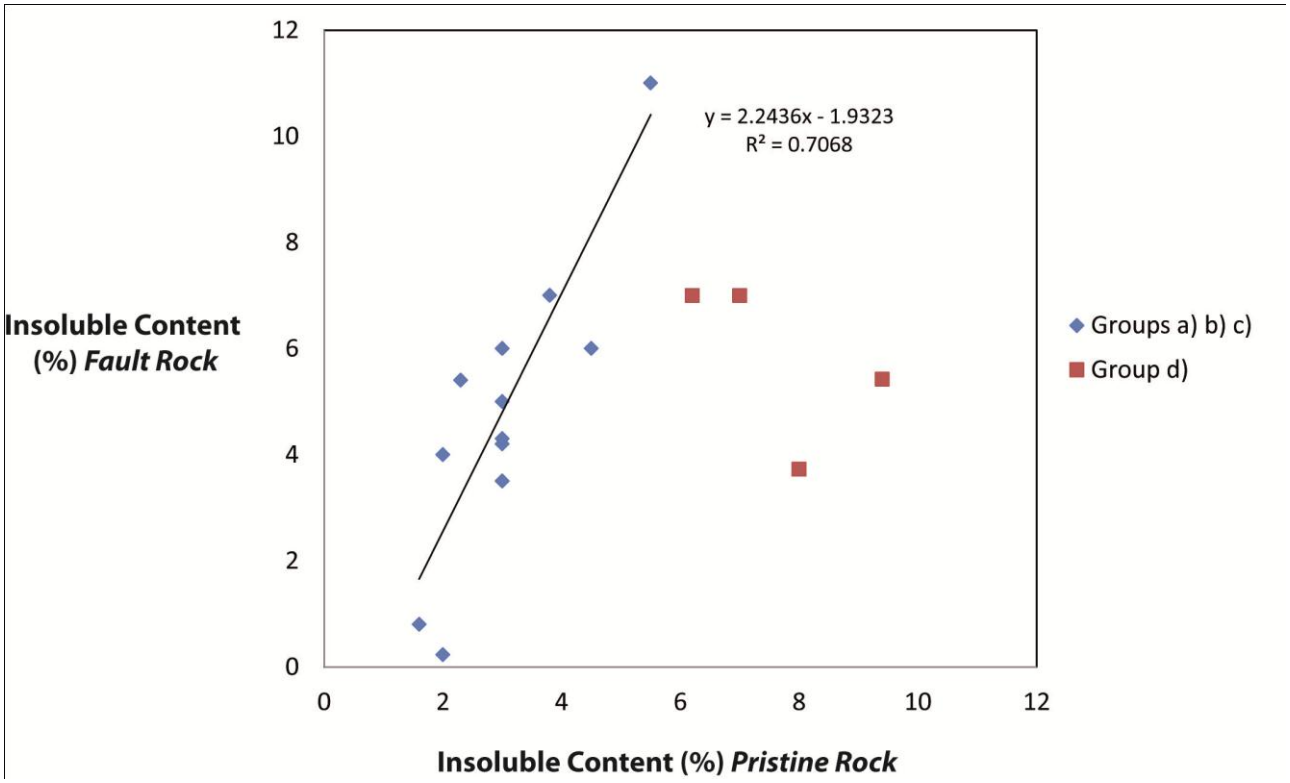

Fig. 6.1 – Pristine rock insoluble content values versus fault rock insoluble content. The blue dots corresponds to the shallow marine carbonate deposits (Group *a*) and the carbonate ramps deposits (Group *b*); the red dots corresponds to the Platform-basin transition deposits (Group *c*) and the dolostone (Group *d*)

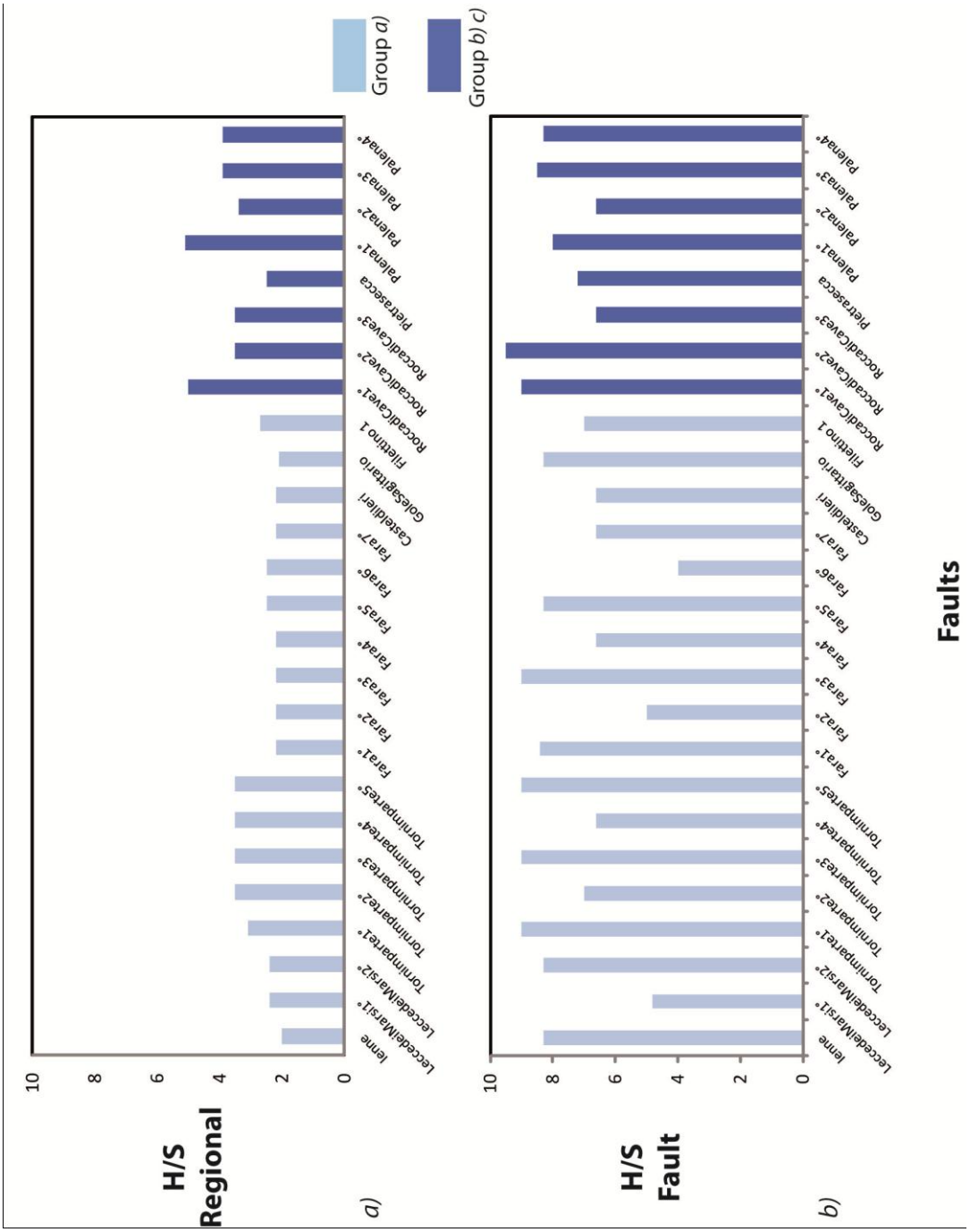

Fig. 6.2– H/S values versus faults; a) Fault values; b) Regional values

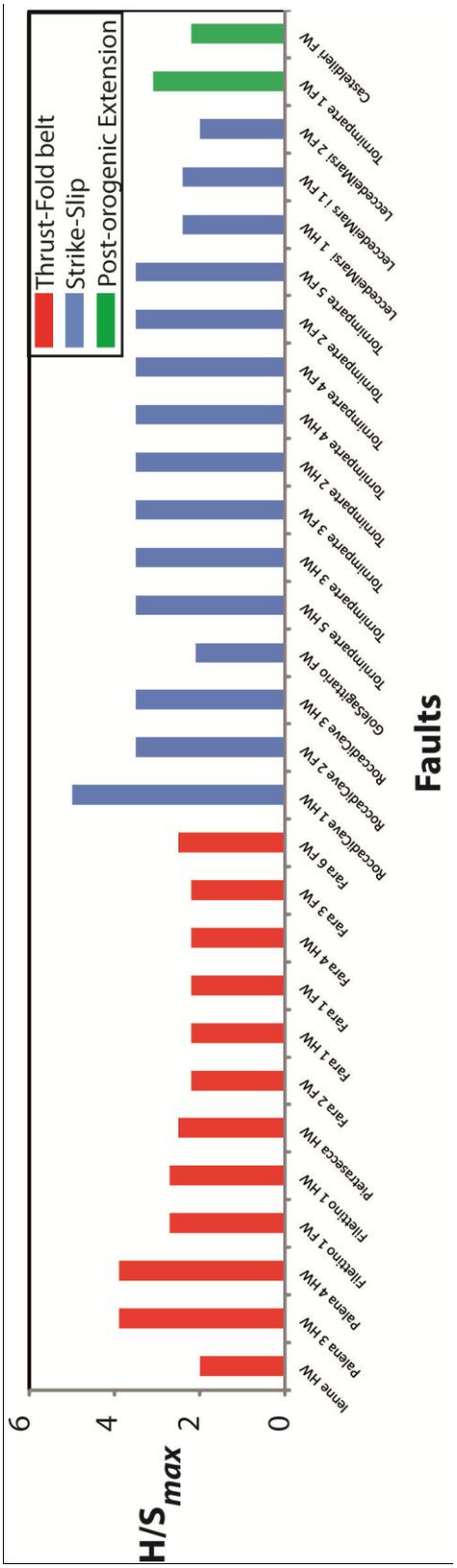

Fig. 6.3 - Regional deformation intensity (H/S) in different tectonic contests. The red columns correspond to the faults located in a fold and thrust contest; the blue columns correspond to the faults located in a strike-slip contest; the green columns correspond to the faults located in a post-orogenic extensional contest

6.1.2 Regional and fault related deformation

To compare the fault intensity of deformation to the regional one the maximum value of H/S ratio has been computed, for both the hangingwall and the footwall of faults. For the faults showing the exponential trend, the maximum H/S value reached on the fault plane was used. For the faults showing the Semi-Gaussian and the Gaussian trend the peak value was used.

The results of the field study prove that the intensity of fault-related deformation (H/S) is always significantly higher than the regional one, ranging 9.5-2.7 and 5-2 respectively, and the lower H/S threshold 2 and the higher one 9.5 has been defined (Fig. 6.4). The deformation intensity of the larger scale faults (seismic scale faults) is not always higher than the deformation of the smaller scale faults (subseismic scale faults), as is the case of the Filettino fault and the Rocca di Cave 2 fault which shows H/S values of ≈ 4 and ≈ 10, respectively (Fig. 6.4). Since the scale of faults is mostly related to the throw, this data suggest that other features affect the development of the deformation, such as the regional deformation imprinting, the time of the stress application, and the fluid circulation.

In addition, high values of fault deformation intensity do not correspond to higher value of regional related deformation intensity. We have concluded that the regional deformation strongly depends on the tectonic environment and it is added to the fault one, but at the same time it does not affect the fault directly.

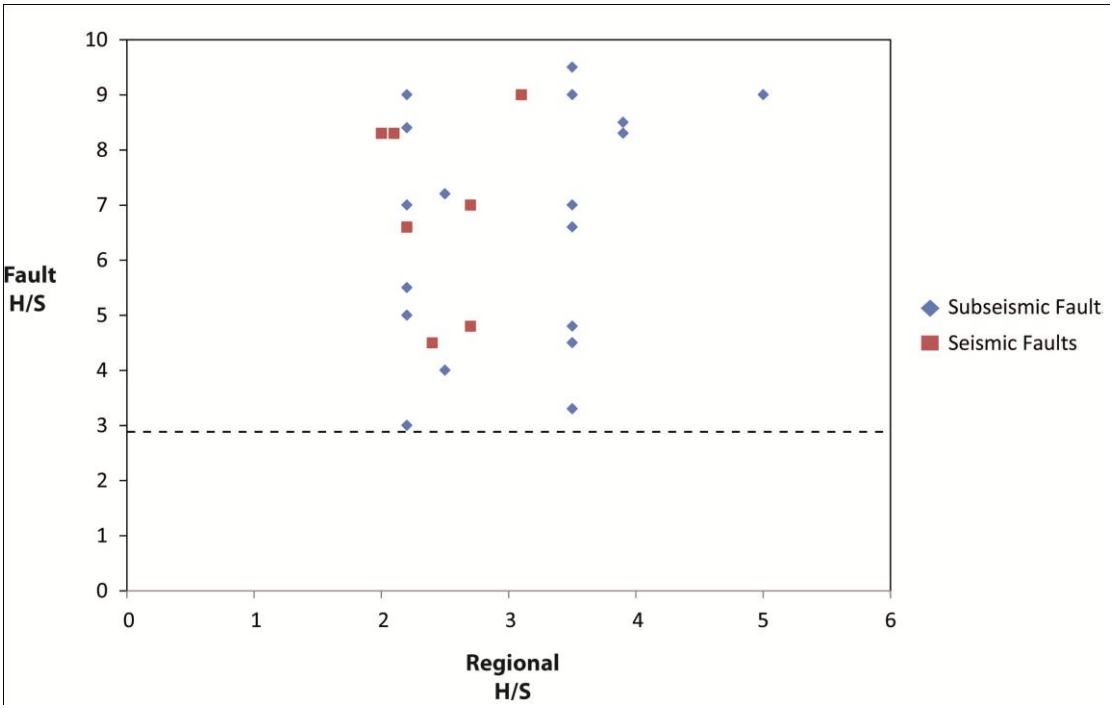

Fig. 6.4 – Fault related deformation versus regional related deformation intensity for the seismic (blue dots) and the subseismic scale faults (red dots). The black dotted line corresponds to the low threshold of the deformation intensity (H/S)

6.1.3 Fault kinematic and the deformation intensity

The fault kinematic is one of the main factors affecting the intensity and the distribution of the fault-related deformation. It was quantified by means of the rotax analyses and the studied faults have been classified in 4 main groups, based on the rotax plunge (Fig. 6.5):

a) Rotax Plunge 0°-10° PURE DIP-SLIP
b) Rotax Plunge 10°-30° DIP-SLIP
c) Rotax Plunge 30°-60° OBLIQUE-SLIP
d) Rotax Plunge > 60° STRIKE-SLIP

As shown in the diagram, the majority of the studied faults show a pure dip-slip movement. The faults showing the highest rotax are the Tornimparte 4 fault, the Fara 3 fault, and the Palena 4 fault, with values of 60°, 80°, and 66° respectively.
The fault kinematics was compared with the intensity of deformation in the graph of Fig. 6.6), where the maximum H/S mean values are plotted versus the rotax plunges. We can observe that below the threshold of 15° there is no relation between the H/S and the rotax plunge value (the blue dots in the graph). Over the threshold of 15° we distinguish two main groups, both having a good linear correlation between the studied variables (R^2 0.9 and R^2 0.7 respectively), and suggesting that the H/S is related to the fault kinematics. This is true mostly for the faults which show a combined dip-strike kinematic, which are probably characterized by higher stress conditions.

FAULT	ROTAX
RoccadiCave 1	38
RoccadiCave 2	50
RoccadiCave 3	36
Filettino	8
Ienne	2
Pietrasecca	2
Tornimparte 1	10
Tornimparte 2	28
Tornimparte 3	15
Tornimparte 4	60
Tornimparte 5	50
LeccedeiMarsi 1	10
LeccedeiMarsi 2	10
GoleSagittario	40
Casteldileri	10
Fara 1	10
Fara 2	45
Fara 3	80
Fara 4	30
Fara 6	30
Palena 3	14
Palena 4	66

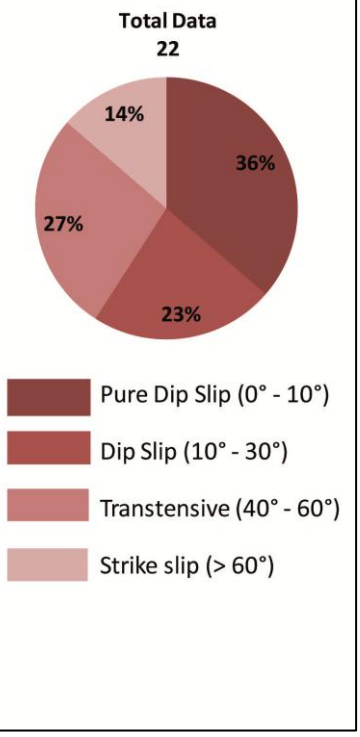

Fig. 6.5 – Fault classification by the fault movement by means of rotax plunge

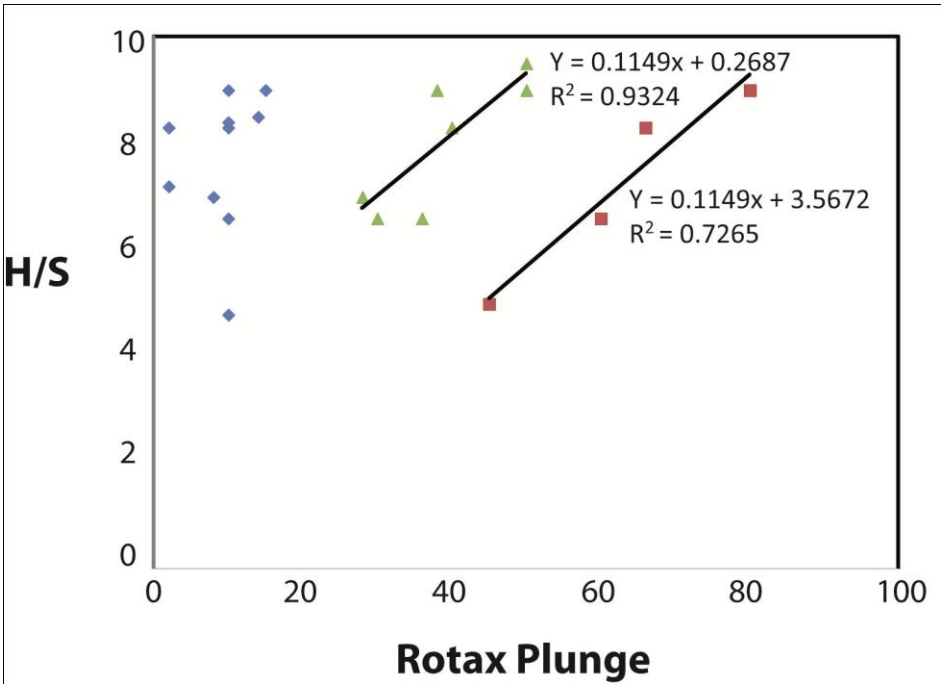

Fig. 6.6 – Intensity of deformation (H/S) versus Rotax Plunge

6.1.4 Fault throws and fault scales

The total throw computation, which takes into account the along strike throw component, was carried out in order to study the relation between the throw and the deformation intensity. The studied faults have been divided in two main groups, based on the fault scale (Fig. 6.7):

1) Seismic scale faults, having the throw higher than 10 m
2) Subseismic scale faults, having the throw higher than 10 m

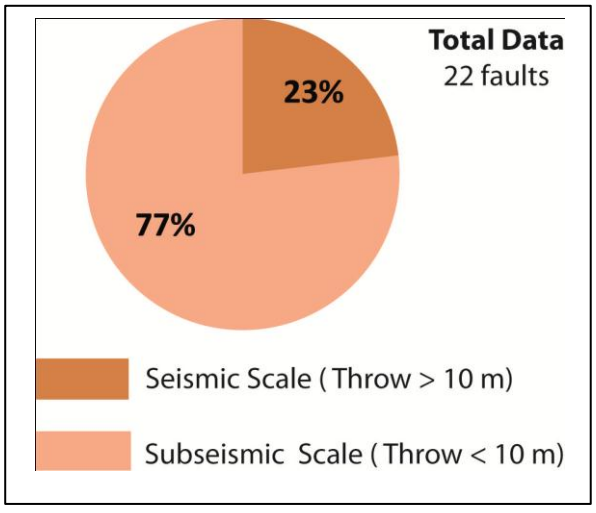

Fig. 6.7 – Fault scale classification by the total throw

6.1.5 Systematic and non-systematic fracture system

Generally, each main systematic fracture (MFC) set shows the development of another set normal to it (SFC) (Fig. 6.8 *a*) and in this work the *in situ* quantification was performed. The relation concerning the H/S of Fig. 6.8 *b* was found. It shows that the intensity of deformation of the MFC is higher than the SFC. This result suggests the temporal evolution of these sets: firstly the MFC, that is more fractured, and secondary the SFC, that is less fractured. This relation could be a predictive tool to estimate the deformation intensity of the associated fracture cleavages and has strong implications in terms of connectivity predictions.

In addition, this data suggests that the fracturing evolution is controlled by the anisotropy of the lithons confirming the evolutionary model proposed by Billi et al. 2003. In fact, when the fracture intensity is high, the fracture-bounded rock lithons have a strongly elongated shape. This shape anisotropy facilitates fracturing perpendicularly to the elongated direction.

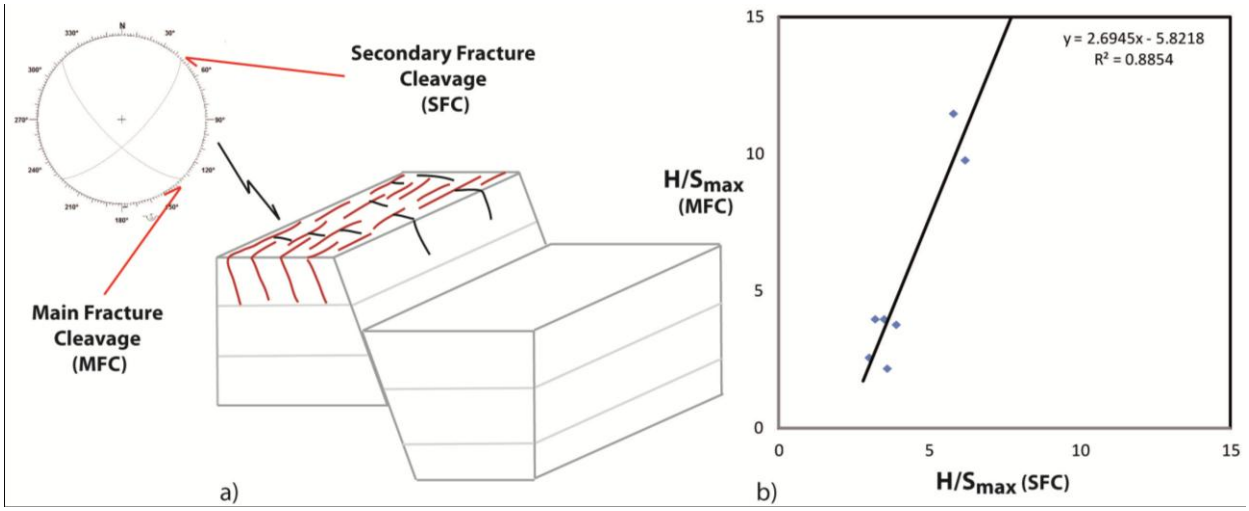

Fig. 6.8 – *a)* Main fracture cleavage and secondary fracture cleavage; *b)* Comparison between the main fracture cleavage (MFC) and secondary fracture cleavage (SFC) deformation intensity (H/S_{max})

In the graph of Fig. 5.90 the H/S mean values of the main fracture cleavage were compared as well as the secondary fracture cleavage related to fault. The two fracture sets are almost perpendicular and their development is almost contemporary.

The data is plotted by a linear trend with R^2 of 0.8. This relation shows that the increase of the main fracture cleavage deformation intensity is higher than the secondary fracture cleavage one. The main fracture cleavages reach higher values of deformation intensity (H/S max = 12) then the secondary fracture cleavage (H/S max = 6).

This relation could be a predictive tool to estimate the deformation intensity of the associated fracture cleavages.

6.1.6 Stratabound and non-stratabound fractures

An important issue concerning the study of fracturing in layered rocks is the role of the mechanical layering constrain in the development of fractures (Gross et al. 2007). The fracture heights of the studied faults range from metres to millimetres and the fractures can be both stratabound and non-stratabound. The faults can be divided into two main groups: one group is composed mostly of subseismic scale faults which show a prevalence of stratabound fractures. The second group is mostly composed of seismic scale faults with some subseismic scale faults characterized by a strike-slip movement. This second group shows both stratabound and non-stratabound fractures. These results suggest that the bedding constrains on the development of fracturing in an early stage of fault evolution (subseismic scale faults) (Fig. 6.9). Increasing the fault size (seismic scale faults) and the related stress intensity, the mechanical layering does not constrain the evolution of fracture and allows the development of non-stratabound fractures.

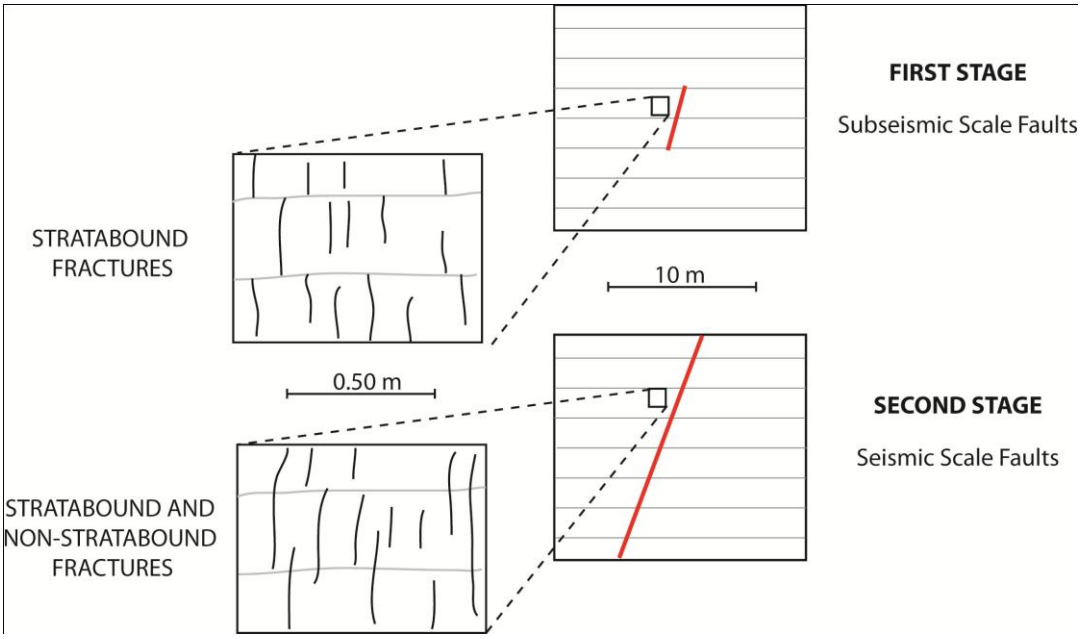

Fig. 6.9 – Evolutionary model of fractures development in layered rocks; a) First stage, b) Second stage

6.1.7 Hangingwall and footwall deformation

The analysis of hangingwall and footwall H/S scan lines suggests that the structural pattern across the fault zone is asymmetric, confirming the results of Mandl 1988, 2000; Knott et al. 1996. In particular, the fault hangingwall show always higher H/S values than the fault footwalls, ranging 8.4-3.5 and 7-2 respectively. We suggest that it is probably relate to two distinct main processes acting contemporarily. The increase of throw by time produces different stress conditions in the fault hangingwall and in the footwall (Fig. 6.10 step 1). In the case of a normal fault, in the fault hangingwall the kinematic stress induced by the fault movement produces a vertical stress tensor oriented as the regional σ_1. This occurrence induces an increase of the stress and, hence the

deformation intensity. Otherwise, in the fault footwall the induced kinematic vertical stress tensor has an opposite orientation in respect to the regional one. It induces a decrease of the stress and, hence a decrease of the deformation intensity. The second process that affects the deformation distribution is the erosion rate. In fact, adding the erosion process (Fig. 6.10) the asymmetry between the hangingwall and the footwall becomes higher.

As the intensity of deformation is different, the spatial analyses of the deformation of the fault hangingwall and the footwall show very similar patterns suggesting the acting of the same deformation mechanism.

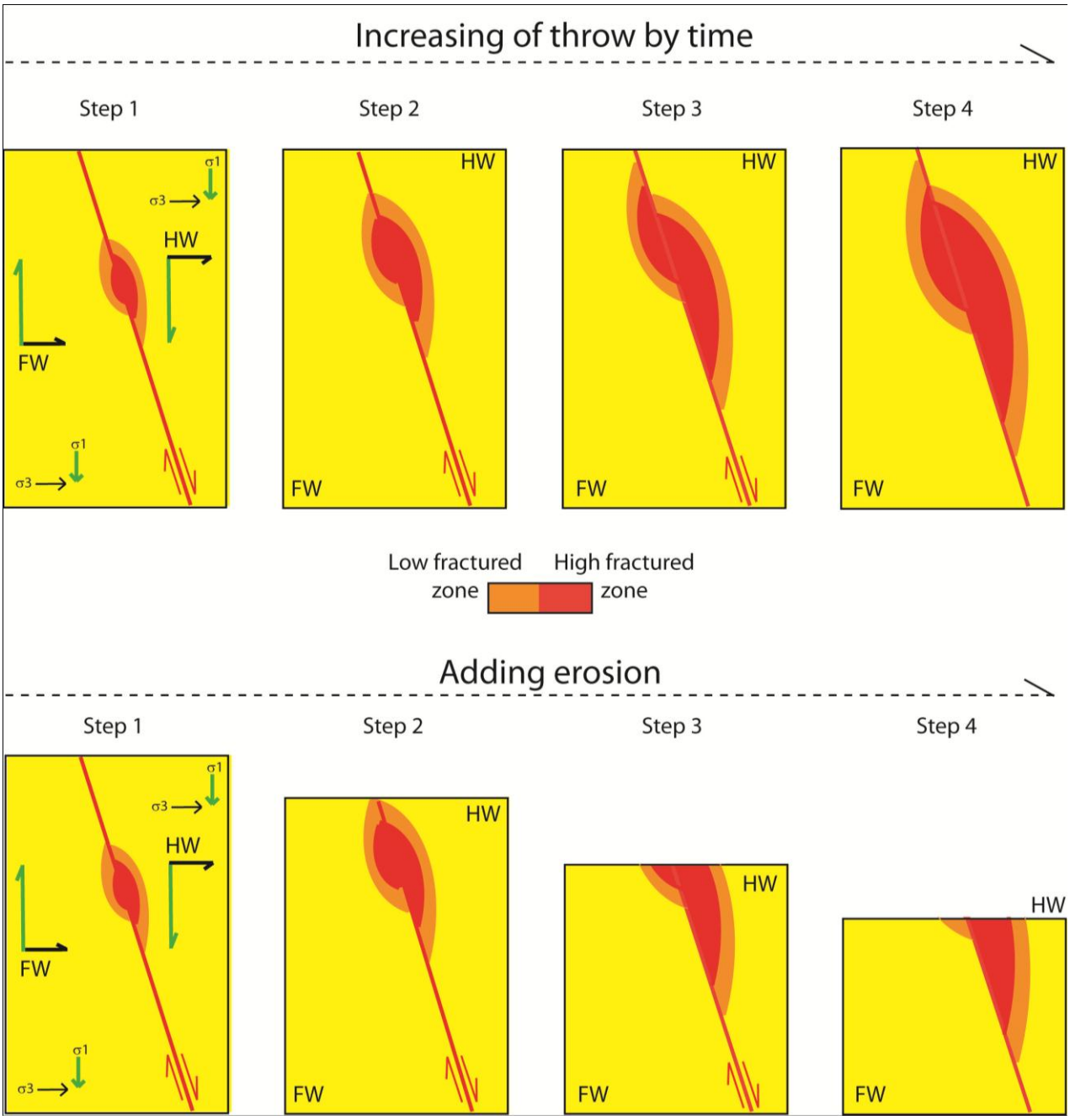

Fig. 6.10 – 2-D Evolutionary model of deformation distribution in the hangingwall and footwall (case of a normal fault)

6.2 The damage-zone width

A new methodology was improved to define the boundaries between the damage zone and the pristine rock although this passage is almost gradational. The methodology was tested on 5 faults which represent a good variability in term of scale and throw. These faults show a decreasing H/S trend of the FRF down to the regional values and at the same time show an increase of the FRF frequency. In particular, the limit between the damage-zone and the pristine rock was fixed at the distance where both the azimuth and the H/S stabilize on the regional values the results show that for the subseismic faults a good relation exists between the computed damage-zone width and the maximum value of fault-related H/S. It suggests that the damage-zone's width increases with the increase of acting stress and this stress is proportional to the intensity of deformation (H/S). On the contrary, the relation is not a good one for the seismic scale faults, suggesting a decreasing in the development of the damage-zone caused by the stress concentration on the fault plane, which causes the development of the fault-core, as described by Storti et al. (2003).

6.2.1 Damage-zone width and throw

In the graph of Fig. 6.11 *a* the data of the damage-zone widths have been compared with the fault throws. A very poor correlation was found, so that the two groups, seismic and subseismic faults, have been analysed separately.

The computed damage-zone widths of the subseismic scale faults have been compared with their fault throws Fig. 6.11 *b*. In the graph two different groups of faults are identified: the first group (damage-zones < 10 m) is characterized by faults in which damage-zone's width increases with throw. These faults follow a power low trend, suggesting that the development of the damage-zone is more intense for lower throw, hence for early faults. When the fault develops the damage-zone development becomes less intense. This occurrence is probably due to the development of fault-core in the inner part of the fault zone. The trend confirms the results pointed out by Micarelli et al. (2006) even though the computed damage-zone widths are significantly underestimated. This may relate to the different methodology used to estimate the damage-zone width. The second group of faults (damage zone > 10 m) shows no correlation between the damage-zone width and the throw.

The presence of these two groups are probably related to different mechanism of fault propagation and, hence of fracturing development. In particular, the second groups is probably composed of a fault developed at the tip of major faults (seismic scale fault) and characterized by higher values of regional deformation and damage-zone width Salvini et al. (1999).

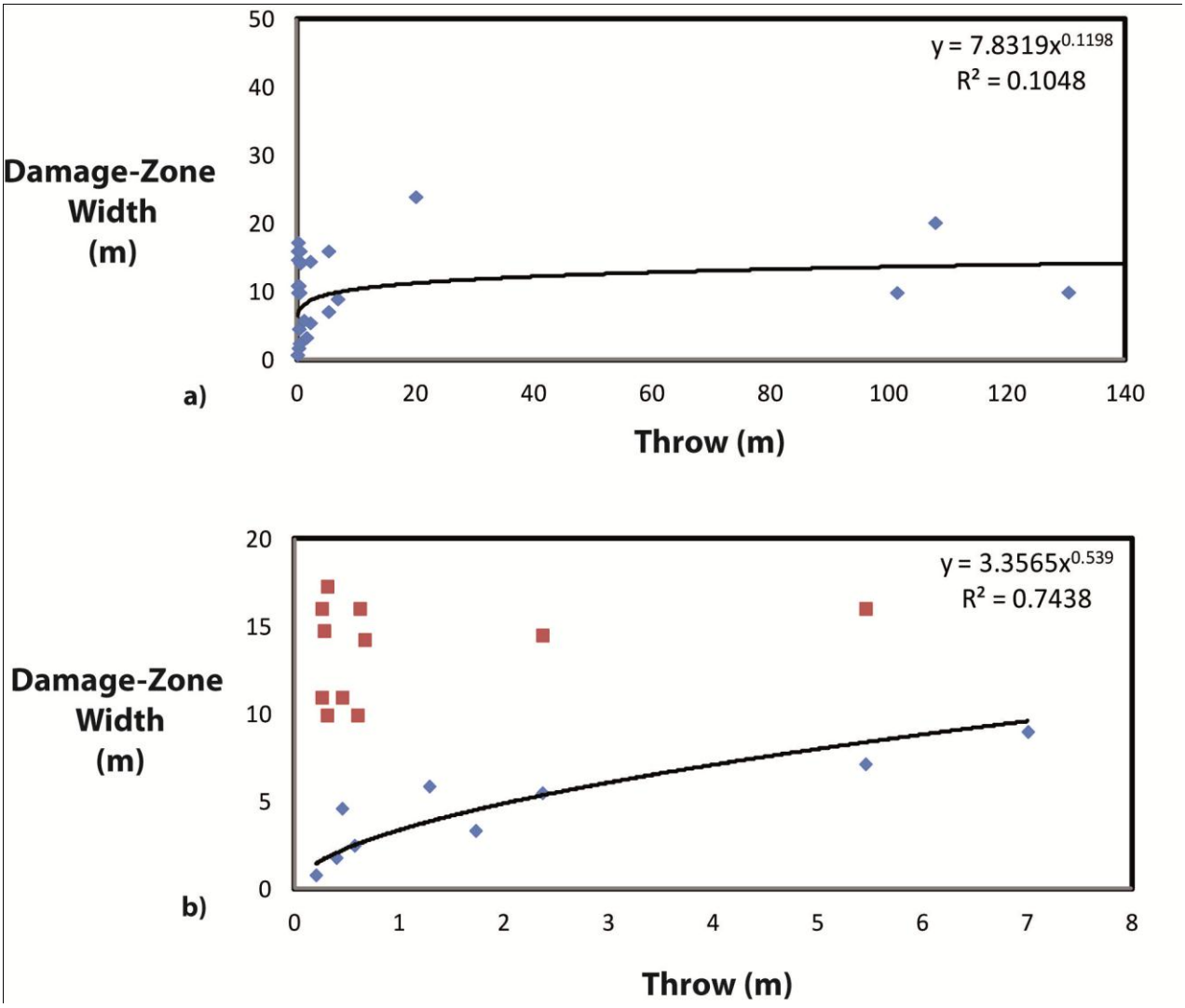

Fig. 6.11 – Damage-zone width versus throw; a) Seismic and subseismic scale faults; b) Subseismic scale faults

6.3 The spatial analysis of deformation

The spatial analysis of fault related deformation (H/S) demonstrates that the majority of the studied faults show a clear variation of the deformation intensity with an increase of distance from the master fault plane. This is true except for the case of the Lecce dei Marsi 1, Palena 4, and Fara 3 faults. This may relate to a primary cause: the three faults show a value of fault-related deformation intensity very similar to the regional one (fault-related H/S max value: 2.7; regional-related H/S max value: 3), so that it is difficult to discriminate among them.

Three main deformation trends through the distance from the fault plane have been detected and characterized, although the presence of secondary shear features causes locally increases of the H/S value (Fig. 6.12), and their presence was removed by a smoothing procedure. The first trend (Fig. 6.12 *a*) is characterized by an exponential decrease of the deformation intensity from the highest value nearby the fault plane to lower values far from the fault plane (Total number of

faults: 7). The second trend (Fig. 6.12 *b*) is characterized by a Semi-Gaussian decrease of the deformation intensity through the distance from the fault plane (Total number of faults: 2). The third deformation trend (Fig. 6.12 *c*) is characterized by a Gaussian trend which shape (height, width and position of the peak) depends on the fault and rock characteristic such as the evolution of the fault-core, the fault throw, the lithology (Total number of faults: 8). Our data demonstrate that the subseismic scale faults can show both the exponential or the semi-Gaussian decrease, while the seismic scale faults show essentially the Gaussian trend. These lower values of deformation on the fault plane are probably due to the occurrence of two processes: the development of the pressure solution, which cause the anastomization of the fractures and the reduction of the H/S; the recementation of the rock due to the fluid circulation in developed fault-cores.

We can observe that the subseismic scale faults show essentially the exponential or a semi-Gaussian decrease, while the seismic scale faults show essentially the peak trend. In addition, the Gaussian fit analyses highlights the occurrence of the "*infilling process*", whose effect increases by approaching the master fault plane. This process consists in the increase of the number of H/S clusters near the fault plane and in their decrease moving away from the fault. It proves that the stress produced by the fault evolution strongly affects the development of fracturing in fault damage-zone. The azimuth spatial analysis of the fault-related fracture demonstrates that the infilling process exists also when the deformation is high. On the other hand, the value of the deformation intensity (H/S) has a maximum threshold (H/S 12, measured in the Castel di Ieri fault) over which the development of pressure-solution cleavage produces a strong increase of the fracturing spacing against the height of the fracture, so that the H/S value remains constant. Two main typologies of fault-cores are recognized on the field: a continuous and cemented one and a non-continuous fault-core. The continuous and cemented fault-core is related to the seismic-scale faults, while the majority of small scale faults (subseismic scale) do not show a fault-core.

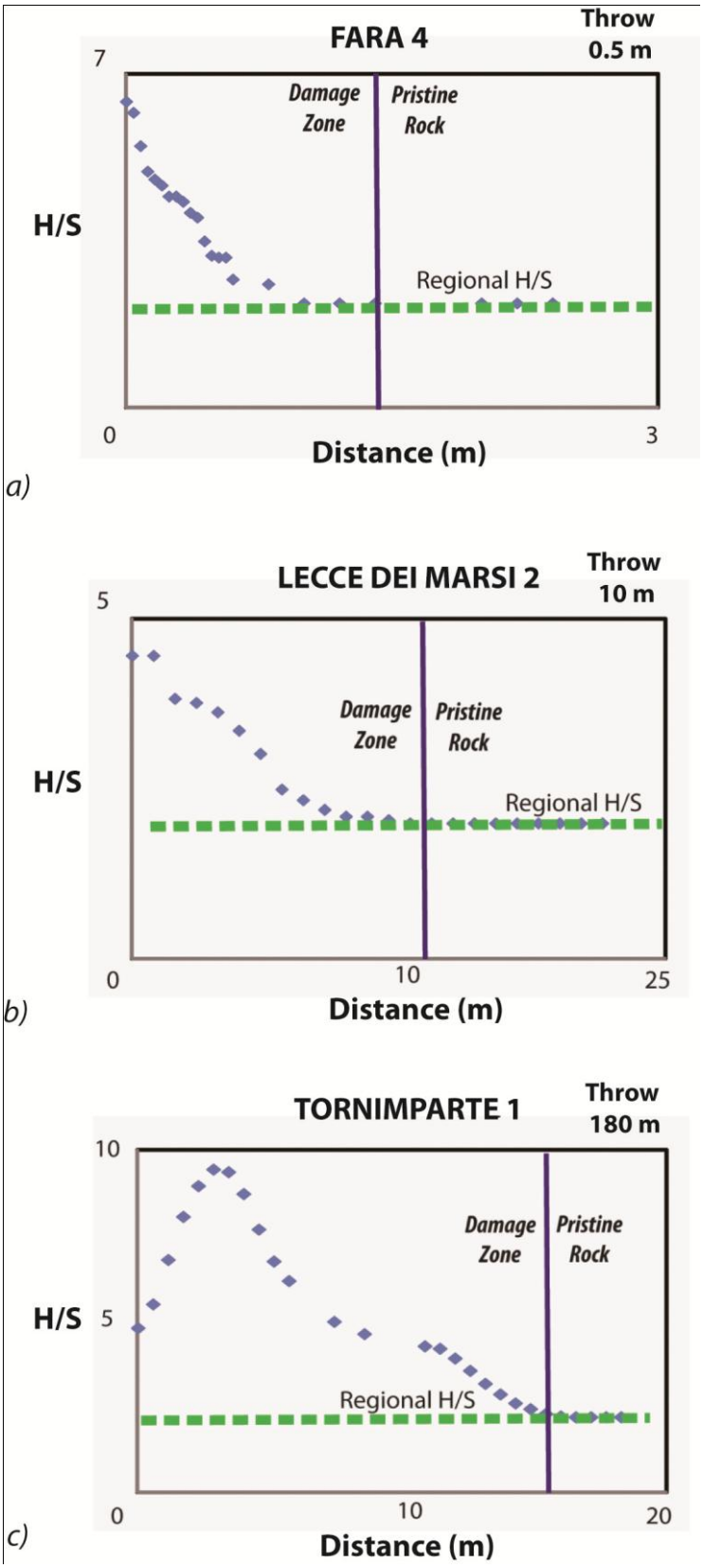

Fig. 6.12 – H/S smoothed data. a) First trend: Exponential; b) Second trend: Semi-Gaussian; c) Third trend: Gaussian

6.4 The analytical modelling: Monte Carlo analysis

Several tests have been performed before finding the best equation able to reproduce the observed trends. The final equation has this implicit form:

$$\mathbf{H/S} = (\textit{Term 1} + \text{Regional H/S}) * \textit{Term 2}$$

Term 1 is:

$$\textit{Term 1} = \mathbf{H} * e\,[-1.383 * (\text{Distance} / \mathbf{W})\hat{}\mathbf{M}]$$

Term 2 is:

$$\textit{Term 2} = \text{Distance} / (\text{Distance} + \mathbf{R})$$

With:
H that is the H/S maximum mean value minus the regional H/S and it controls the height of the equation peak (Fig. 16 Final equation I Type).
W that is the distance from the fault-plane where the H/S became ½. It controls the width of the curve (Fig. 16 Final equation I Type).
R that is the *C-C* Number (Fig. 16 Final equation I Type).
M that is the position of the peak. It governs the shape of the curve and the damage-zones maturity (Fig. 16 Final equation I Type).

The two terms can be related to the main geological process that controls the distribution of the deformation intensity in a fault zone. In particular, *Term 1* is related to the fault kinematic (K) because it increases the H/S value; Term 2 is related to the pressure solution and the cementation process (C-C), because it causes a decrease of the H/S value.
A Monte Carlo simulation has been done on the single faults to verify if the equation was able to fit all the fault trends. To understand which of the geological factors mostly affects the intensity of deformation in fault damage-zones the resulting parameters of the Monte Carlo analysis for the single faults was used. The correlation analysis between the parameters and the geological variables input in the simulation, shows that the throw (Correlation Number: 0.78), and the regional deformation (Number of Correlation: 0.85) are the main geological factors affecting the fracturing distribution in fault zones. Otherwise, the other considered variables have less influence in the fracturing development. This result has been fundamental to link the geological variables to the equation mathematical terms.
Eventually, a Monte-Carlo analysis was performed using the input data from all the studied faults in order to find the final parameters which provides a deformation intensity prediction with an error of +/- 2 H/S, which is the RMS resulting from simulation.

6.5 Fracture predictive modelling

This final equation was implemented in fracturing predictive software and the models of 6 faults have been performed. The results of the tests show that the predicted H/S is overestimated in respect to the field data, and this overestimation is always lower than the equation error (RMS = 2). This is true except for the case of the Pietrasecca fault, which tests, both performed using 8 m of throw, show an underestimation of the predicted H/S. Increasing the throw value to 16 m we can observe an overestimation of 2, similar to the other faults. We can conclude that the Pietrasecca computed throw is probably lower than the real one. This addition of throw is probably due to the presence of a strike-slip fault that includes the Pietrasecca fault in its movement.

The damage-zone widths are well predicted by the model. On the other hand the H/S distribution is well predicted for the faults characterized by the decreasing trend (such as Filettino, Pietrasecca, Tornimparte 2, and Fara 6 faults) but it is less reliable for the faults that show the peak trend, as Ienne and Tornimparte 1 faults.

6.6 Conceptual model of fault damage-zones evolution and the implications in fault permeability

This work points out that the evolution of fracturing in carbonate fault damage-zones is mostly governed by the evolution of the faults in time and space. Fig. 6.13 proposed a conceptual model of the damage-zone evolution for a normal fault, which resumes the main results provided in this work.

The step 1 represents the early stage of fault evolution (subseismic scale faults). At this stage, the damage-zone's width is characterized essentially by stratabound fractures that in turn are responsible of a low vertical connectivity between the layers. The increase of the throw (Step 2) produces the increase of the damage-zone width, the development of non-stratabound fractures, and the development of several fractures sets, which frequencies increases approaching to the fault plane (infilling process). At this stage, the intensity of deformation (H/S) increases and the development of non-stratabound fracture strongly enhance the vertical and connectivity. Increasing throw, the fault-core develops induced by the stress concentration due to grinding and comminution of grains (Step 3). Recementation and pressure solution processes in the damage-zone sector nearer to the fault plane causes the decrease of both the connectivity and permeability, although they hold high values far from the fault plane. The recementation process change substantially the rehology of the rocks and allows a secondary fracturing process (Step 4) which reduces the H/S values nearby the master fault plane. If this process is pervasive the H/S becomes lower than the regional one. In addition, the stress conditions produced by the fault movement cause an asymmetry in the distribution of deformation in the hangingwall and in the footwall, which cause the juxtaposition of zone characterized by different permeability.

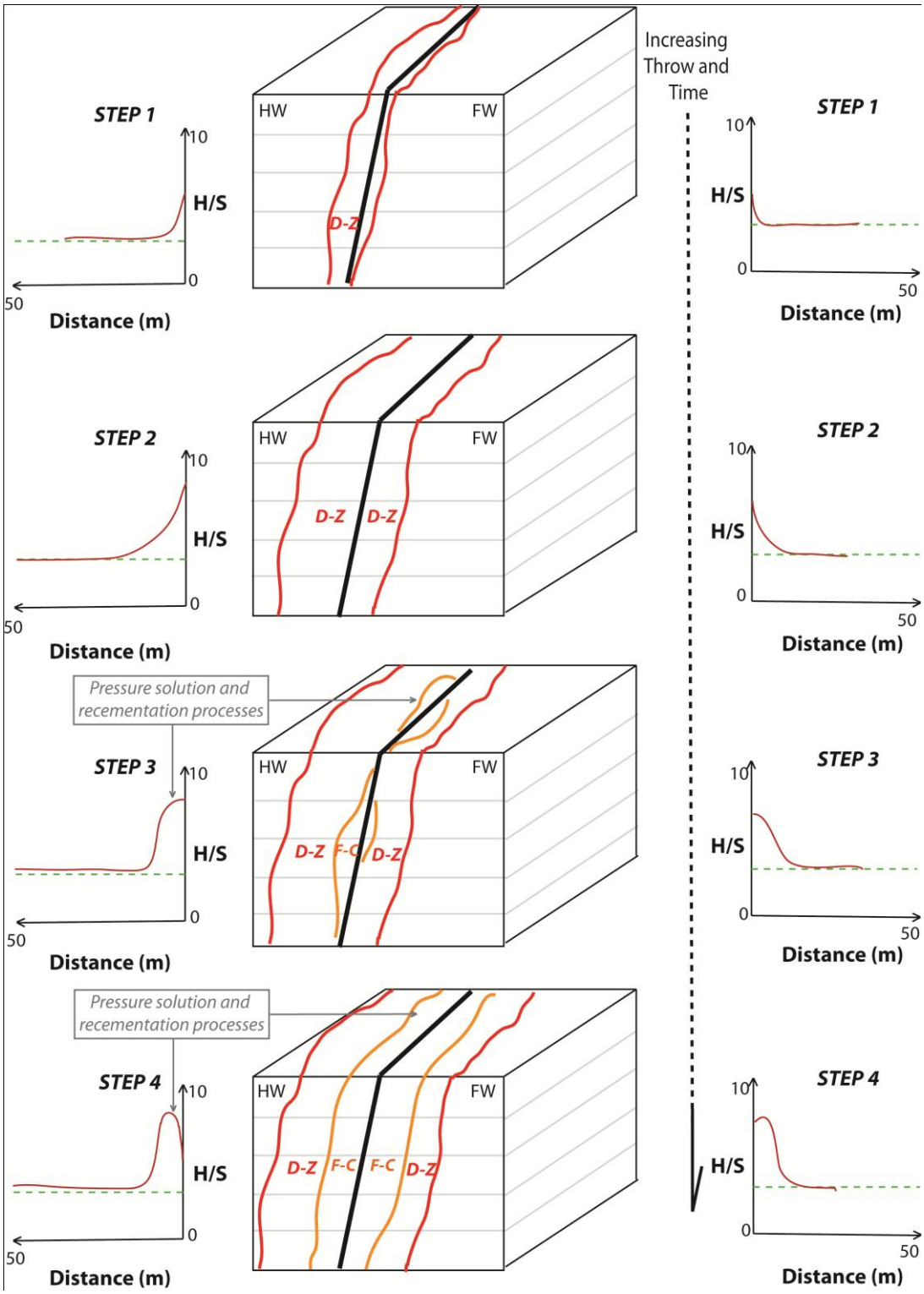

Fig. 6.13 – Conceptual model of the damage-zone evolution in time and space; *D-Z* is the damage-zone; *F-C* is the fault-core

7- MAJOR REMARKS AND CONCLUSIONS

- The tectonic environments and the rock rehologies strongly affect the development, the characteristics the intensity, and of the regional deformation pattern. On the contrary, the fault deformation pattern is controlled by other fault characteristic, such as the throw, the age of the fault, the depth of deformation which affect the stress condition and distribution in fault zones.
- The clay analyses performed on the protolith samples suggest that the clay content depends on the rock type. On the other hand, the clay content analyses performed on the fault damage-zones samples suggest that the clay content is controlled by the evolution of the deformation process, namely the pressure-solution enhanced mostly by the fluid circulation related to the fault movement. The dolomitization, related to the diagenesis and enhanced by the fluid circulation, induced pressure-solution process which increases the insoluble content of the fault rocks.
- The fault-related deformation intensity (H/S) is always significantly higher than the regional one, ranging 9.5-2.7 and 5-2 respectively, so that we can determine the lower threshold of H/S as 2.7 for faults and 2 for regional deformation
- The fault kinematic rules the development of the fault deformation patterns. This is true mostly for the faults that showed double dip-slip and strike-slip kinematics.
- The total throw is computed, which take into account the strike component of the fault movement and the studied faults was classified in two main groups: the seismic scale faults, having throw ranging between 200 and 100 m, and the subsesimic scale faults having throw lower than 10 m.
- The evolution of fault-related fracture sets is controlled by the rock anisotropy and the intensity of deformation of the main fracture cleavage is always higher than their suborded.
- The development of the stratabound and the non stratabound fractures in layered rocks is related to the stress intensity and to the fault scale. In particular, the subseismic scale faults mostly show the abundance of the stratabound fracture. On the other hand, the seismic scale faults show the development of both stratabound and non stratabound fractures.
- The analysis of hangingwall and footwall H/S suggests that the structural pattern across the fault zone is asymmetric. This evidence is related to the different stress conditions in time added to the increase of throw.
- A new methodology was improved to define the boundary between the damage zone and the pristine rock. A good relation exists between the damage-zone width and the intensity of deformation (H/S) for the subseismic scale faults.
- Although, all the studied faults show a damage-zone, not all show a fault-core. In particular, the subseismic scale faults essentially do not show a developed core, and if it

is present it is characterized by isolated lenses. On the other hand, the seismic scale faults show a continuous and often recemented fault-core.

- A power low trend was found between the damage-zone widths and the fault throws, suggesting that the fault damage-zones fracturing process is more intense in the early stage of fault development.
- The fault-related deformation intensity shows a clear variation through the distance from the master fault plane and three main trends have been detected: a) Exponential decrease; b) Semi-Gaussian decrease of the H/S value; c) Gaussian decrease.
- The “infilling process” increases approaching to the fault plane although the H/S value remains constant or decreases.
- The Monte Carlo converging method provides a statistical tool to study the geological factors affecting the fracturing evolution in the fault damage-zone. The results show that the throw affects the deformation distribution mainly in the early stage of fault evolution, confirming the results of Salvini et al. (1999).
- A general equation was found to define quantitatively the distribution of the intensity of deformation in fault damage-zones, whose parameters have a geological meaning and are related to the stress intensity. This equation provides a deformation intensity prediction with an error of + 2 H/S, which is the RMS resulting from simulation.
- The equation was implemented in the fracturing predictive software. The comparison between the models and the field data proves that the resulting models provide a reliable prediction of fracturing distribution in fault damage-zones.

8 – REFERENCES

Ackermann, R. V., R. W. Schlische, 1997. Clustering of small normal faults around larger faults. Geology 25, 1127–1130

Agosta F., Alessandroni M., Antonellini M., Tondi E., Giorgioni M., 2010. From fractures to flow: A field-based quantitative analysis of an outcropping carbonate reservoir. Tectonophysics 490, 197–21

Agosta F., Aydin A., 2006. Architecture and deformation mechanism of a basin-bounding normal fault in Mesozoic platform carbonates, central Italy. Journal of Structural Geology 28, 1445-1467

Ameen, M. S., 1995. Fractography: fracture topography as a tool in fracture mechanics and stress analysis. In M. S. Ameen, Geological Society Special Publication, 92-240

Antonellini M., Aydin A., 1994. Effect of faulting on fluid flow in porous sandstones: petrophysical properties. AAPG Bulletin 78, 355-377

Aydin 2000. Fractures, faults, and hydrocarbon entrapment, migration and flow. Marine and Petroleum Geology 17, 797-814

Bally, A.W., Burbi, L., Cooper, C. and Ghelardoni, R., 1988. Balanced sections and seismic reflection profiles across the central Apeennines. Memorie Società Geologica Italiana, 35, 257-310

Balsamo F., Storti F., Cappanera F., Tosi G., 2011. Sub-seismic sccale fracture pattern and *in situ* permeability data in the chalk atop of the Krempe salt ridge at Lagerdorf (NW Germany): Inference on synfolding stress field evolution and its impact on fracture connectivity. Marine and Petroleum Geology 28, 1315-1332

Bastesen E, Braathen A., 2010. Extensional faults in fine grained carbonates e analysis of fault core lithology and thickness-displacement relationships. Journal of Structural Geology 32, 1609-1628

Bastesen E, Braathen A., Nøttveit H. , Gabrielsen R., Skar T. 2009. Extensional fault cores in micritic carbonate – Case studies from the Gulf of Corinth, Greece. Journal of Structural Geology 31, 403–420

Berg S.S., Skar T., 2005. Controls on damage zone asymmetry of a normal fault zone: outcrop analyses of a segment of the Moab fault, SE Utah. Journal of Structural Geology 27, 1803-1822

Bigi, G., D. Cosentino, M. Parotto, R. Sartori and P. Scandone, 1990. *Structural Model of Italy (1:500000),* sheet n. 4, CNR-PFG

Billi A., Salvini F., Storti F. 2003. The damage zone-fault core transition in carbonate rocks: implications for fault growth, structure and permeability. Journal of Structural Geology 257, 1779–1794

Billi A., Storti F., 2004. Fractal distribution of particle size in carbonate cataclastic rocks from the core of a regional strike–slip fault zone. Tectonophysics 384, 115–128

Billi A., 2005. Grain size distribution and thickness of breccia and gouge zones from thin (<1 m) strike-slip fault cores in limestone. Journal of Structural Geology 27, 1823–1837

Billi A., 2007. On the extent of size range and power law scaling for particles of natural carbonate fault cores. Journal of Structural Geology 29, 1512-1521

Billi A., 2009. Microtectonics of low-P low-T carbonate fault rocks. Journal of Structural Geology 32, 1392-1402

Blenkinsop T., 1991. Cataclasis and processes of particle size reduction. Pure and Applied Geophysics 136, 59–86

Bonnet E., Bour O., Odling N. E., Davy P., Main I., Cowie P., Berkowitz B., 2001. Scaling of fracture systems in geologic media. Reviews of Geophysics 39, 347–383

BP, 2011. Statistical Review of World Energy.

Bruhn R. L., W. T. Parry W. T., Yonkee W. A., Thompson T. 1994. Fracturing and Hydrothermal Alteration in Normal Fault Zones. Pure and Applied Geophysics 142, 609-644

Caine S. J., Evans J., Forster C. B., 1996. Fault zone architecture and permeability structure. Geology 11, 1025-1028

Carta Tettonica d'Italia 1:500000, 1981

Cavinato, G.P., Cosentino, D., Funiciello, R., Parotto, M., Salvini, F. and Tok, M., 1994. Constraints and new problems for a geodynamical model of the Central Italy (CROP II Civitavecchia-Vasto deep seismic line). Boll. Geofis. Teor. Appl., 36

Cello G., Tondi E., Van Dijk J. P., Mattioni L., Micarelli L., Pinti S., 2003. Geometry, kinematics and scaling properties of faults and fractures as tools for modeling geofluid reservoirs: examples from the Apennines, Italy. In: Niewland D.A. New insight into structural interpretation and modeling. Geological Society, London, Special Publications 212, 7-22

Centamore E., Nisio S., 2003. Effects of uplift and tilting in the Central-Northern Apennines (Italy). Quaternary International, 101/102, 93-101

Chester F. M., Logan J. M., 1986. Implications for mechanical properties of brittle faults from observations of the Punchbowl Fault Zone, California, Pure and Applied Geophysics 124, 79–106

Chester F. M., Evans J. P., Biegel R. L., 1993. Internal structure and weakening mechanisms of the San Andreas faults. Journal of Geophysical Research 98, 771-786

Cipollari, P. and Cosentino, D., 1992b. Considerazioni sulla strutturazione della catena dei Monti Aurunci: vincoli stratigrafici. Studi Geologici Camerti, Vol. Spec., 151-156

Cipollari P., Cosentino D., 1995. Miocene unconformities in the Central Apennines: geodynamic significance and sedimentary basin evolution. Tectonophysics 252, 375-389

Doglioni C., 1995. Geological remarks on the relationships between extension and convergent geodynamic settings. Tectonophysics 252, 253-267

Dunham R. J., 1962. Classification of carbonate rocks according to depositional texture in HAM, W. E., Classification of carbonate rocks, AAPG Memoir, 1, 108-121

Durney D. W., Kisch H. J., 1994. A field classification and intensity scale for first-generation cleavages. Journal of Australian Geology & Geophysics 15, 257–295

Eberli G.P., Bernoulli D., Sanders D., Vecsei A., 1993. From aggradation to progradation: the Maiella platform (Abruzzi, Italy). In Simo A. J., Scott R., Masse J. P., eds. Cretaceous Carbonate Platform. AAPG Memoir, 56, 213-232

Endignoux. L., Moretti, I. and Roure, F., 1989. Forward modelling of the southern Apennines. Tectonics, 8: 1095- 1104

Endres T., Lohr H., Trappe H., Samiee R., Thierer P. O, Krawczyk C. M., Tanner D. C., Oncken O., Kukla P. A., 2008. Quantitative fracture prediction from seismic data. Petroleum Geoscience 14, 369-377

Engelder T., 1974. Cataclasis and the generation of fault gouge. Geological Society of American Bulletin 85, 1515–1522

Evans J., Forster C., Goddard J., 1997. Permeability of fault-related rocks and implication for hydraulic structure of fault zones. Journal of Structural Geology 19, 1393-1404

Faccenna C., Davy P., Brun J.P., Funiciello R., Giardini D., Mattei M., Nalpas T., 1996. The dynamics of back-src extension: an experimental approach to the opening of the Tyrrhenian Sea. Geophysical Journal International 126, 781-795

Faccenna C., Jolivet L., Piromallo C, Morelli A., 2003. Subduction and the depth of convection in the Mediterranean mantle. Journal of Geophysical Research 108, 2099

Faulkner, D.R., Mitchell, T.M., Healy, D., Heap, M.J., 2006. Slip on ‘‘weak’’ faults by the rotation of regional stress in the fracture damage zone. Nature 444, 922–925.

Ferrill D. A., Morris A. P., 2003. Dilational normal faults. Journal of Structural Geology 25, 183-196

Fisher Q. J., Harris S. D., McAllister E., Knipe R. J., Bolton A. J. 2001. Hydrocarbon flow across faults by capillary leakage revisited. Marine and Petroleum Geology 18, 251-257

Galadini F., Messina P., Giaccio B., Sposato A., 2003. Early uplift history of the Abruzzi Apennines (central Italy): available geomorphological constraints. Quaternary International, 101/102, 125-135

Gauthier B. D. M., Lake S. D., 1993. Probabilistic modelling of faults below the limit of seismic resolution in Pelican field, North Sea, offshore United Kingdom. AAPG Bulletin 77, 761–777

Ghisetti F., Vezzani L., 1997. Inferring path of deformation and development of arcs in the fold-and-thrust belt of central Apennines, Italy). Tectonics, 16, 523-536

Ghisetti F, Vezzani L, 1999. Depth and modes of Pliocene–Pleistocene crustal extension of the Apennines (Italy). Terra Nova 11, 67–72

Graham B. Antonellini M., Aydin A., 2003, Formation and growth of normal faults in carbonates within a compressive environment. Geology 31, 11-14

Gross M., Eyal Y., 2007. Throughgoing fractures in layered carbonate rocks. Geological Society of American Bulletin 119, 1387-1404

Gross M. R., Fischer M. P., Engelder T., Greenfield R.J., 1995. Factors controlling joint spacing in interbedded sedimentary rocks: integrating numerical models with field observations from the Monterey Formation (U.S.A). In: Ameen, M.S. (Ed.), Fractography: Fracture Topography as a Tool in Fracture Mechanics and Stress Analysis. Geological Society Special Publication 92, 215–233

Gudmundsson, A. 2004. How mechanical layering affects local stresses, unrests, and eruptions of volcanoes. Geophysical Research Letters 31, 1-4

Gudmundsson, A. 2006. How local stresses control magma-chamber ruptures, dyke injections, and eruptions in composite volcanoes. *Earth Science Reviews*, *79,* 1-31

Hadizadeh J. 1994. Interaction of cataclasis and pressure solution in a low-temperature carbonate shear zone Pure and Applied Geophysics 143, 255-280

Jones G., Fisher O. J., Knipe R. J., 1998. Faulting, fault sealing and fluid flow in hydrocarbon reservoirs, Geological Society, Special Publication 147-319

Kim Y. S, Sanderson D. J., 2009. Inferred fluid flow through fault damage zones based on the observation of stalactites in carbonate caves. Journal of Structural Geology 32, 1305–1316

Kim Y. S., Peacock D. C. P., Sanderson D. J., 2004. Fault damage zones. Journal of Structural Geology 26, 503–517

Knipe R. J., 1997. Juxtaposition and seal diagrams to help analyse fault seals in hydrocarbon reservoirs. American Association of Petroleum Geologists Bulletin 81, 187-195

Knott S. D., Beach A., Brockbank P. J., Brown J. L., McCallum J. E., Welbon A. I., 1996. Spatial and mechanical controls on normal fault populations. Journal of Structural Geology 18, 359–372

Larsen B., Grunnaleite I., Gudmundssonc A., 2009. How fracture systems affect permeability development in shallow-water carbonate rocks: An example from the Gargano Peninsula, Italy. Journal of Structural Geology 32, 1212-1230

Long J. C. S., Aydin A., Brow, S. R., Einstein H. H., Hestir K., Hsieh,P. A., Myer L. R., Nolte K. G., Norton D. L., Olsson O. L., Paillet F. L., Smith J. L., Thomson L. , 1996. In Rock fracture and fluid flow: contemporary understanding and applications. Washington, DC: National Academy Press, 551

Malinverno and Ryan, 1986. Extension in the Tyrrhenian sea and shortening in the Apennines as result of arc migration driven by sinking of the lithosphere. Tectonics 5, 227-245

Mandl G., 1988. Mechanics of tectonic faulting. Models and basic concepts. Elsevier, Amsterdam

Mandl G., 2000. Faulting in Brittle Rocks. An Introduction to the Mechanics of Tectonic Faults. Springer, Berlin

Manzocchi T., Walsh J. J., Nell P., Yelding G., 1999. Fault trasmissibility multipliers for flow simulation models. Petroleum Geoscience 5, 53-63

Marchegiani, L., Van Dijk, J.P., Gillespie, P.A., Tondi, E., Cello, G., 2006. Scaling properties of the dimensional and spatial characteristics of fault and fracture systems in the Majella Mountain, central Italy. Geological Society of London. Special Publication 261, 113–131

McGrath A. G., Davison I., 1995. Damage zone geometry around fault tips. Journal of Structural Geology 17, 1011–1024

McLeod A., Dawers N. H., Underhill J. R., 2000. The propagation and linkage of normal faults: insights from Strahspey Brent Statjjord fault array, northen North Sea. Basin Research 12, 263-284

Micarelli L., Moretti I., Daniel J. M., 2003. Structural properties of rift-related normal faults: the case study of the Gulf of Corinth, Greece. Journal of Geodynamics 36, 275–303

Micarelli L., Benedicto A., Wibberley C. A. J., 2006. Structural evolution and permeability of normal fault zones in highly porous carbonate rocks. Journal of Structural Geology 28, 1214–1227

Miccadei E., 1993. Geologia dell'area alto Sagittario- Alto Sangro (Abruzzo, Appennino Centrale). Geologica Romana 29, 463-481

Miccadei E., Parotto M., Piacentini T., 1998. Assetto geologico-strutturale dei Monti della Conca Subequana (Appennino Abruzzese, Italia centrale). Geologica Romana, 34, 31-50

Mimran Y., 1976. Strain determination using a density distribution technique and its application to deformed Upper Cretaceous Dorset Chalks. Tectonophysics 31, 175–192

Mimran Y., 1977. Chalk deformation and large-scale migration of calcium carbonate. Sedimentology 24, 333–360

Moretti I., 1998. The role of faults in hydrocarbon migration. Petroleum Geoscience 4, 81-94

Mosegaard K., Tarantola A., 1995. Monte Carlo sampling of solutions to inverse problems. Journal of Geophysical Research 100

Mutti M., Bernoulli D., Eberli G., Vecsei A., 2008. Depositional geometries and facies associations in an Upper Cretaceous prograding carbonate platform margin (Orfento Supersequence, Maiella, Italy). Journal of Sedimantary Research 66, 749-765

Narr W, Suppe J. 1991. Joint spacing in sedimentary rocks. Journal of Structural Geology 13, 1037-1048

Nelson R.A. (2001). *Geologic analysis of naturally fractured reservoirs* .

Odling N. E., Harris S. D., Vaszi A. Z., Knipe R. J., 2005. Properties of fault damage zones in silicoclastic rocks: a modelling approach. The Geological Society of London, Special Publications 249, 43-59

Ortega O. J., Marrett R. A., Laubach S. E., 2006. A scale-independent approach to fracture intensity and average spacing measurement. AAPG Bulletin 90,193–208

Parotto, M., Praturlon, A., 1975. Geological summary of the Central Apennines. Quad. Ric. Sci. 90, 257–311

Parnell J., Watt G. R., Middleton D., Kelly J, Baron M., 2004. Deformation band control on hydrocarbon migration. Journal of Sedimentary Research 74, 552-560

Patacca, E. and Scandone, P., 1989. Post-Tortonian mountain building in the Apennines. The role of the passive sinking of a relic lithospheric slab. Atti dei Convegni Lincei, 157-176

Patacca E., Sartori R., Scandone P., 1990. Tyrrhenian basin and apenninic arcs: kinematic relations since Late Tortonian times. Memorie Società Geologica Italiana 45, 425-451

Patacca, E., Sartori, R. and Scandone, P., 1992a. Tyrrhenian Basin and Apenninic Arcs: kinematic relations since late Tortonian times. Memorie Società Geologica Italiana 45, 425-451

Pickering G., Bull J. M., Sanderson D. J., 1995. Sampling power-law distributions. Tectonophysics, 248, 1–20

Putnis, A., Mauthe, G., 2001. The effect of pore size on cementation in porous rocks. Geofluids 1, 37–41.

Dunham R. J., 1962. Classification of carbonate rocks according to depositional texture. In: Classification of carbonate rocks. AAPG Memoir 1, 108-121

Rawling G., Goodwin L., Wilson J., 2001. Internal architecture, permeability structure, and hydrologic significance of contrasting fault-zone types. Geology 29, 43-46

Sage, L., Mosconi, A., Moretti, I., Riva, E. and Roure, F., 1991. Cross section balancing in the Central Apennines: an application of LOCACE. AAPG Bullettin, 75: 832-844

Salvini F., Vittori E., 1982 – Analisi strutturale della linea Olevano-Antrodoco-Posta ("Ancona-Anzio" *Auctt*.): metodologia di studio delle deformazioni fragili e presentazione del tratto meridionale. Memorie della Società Geologica Italiana24, 337-355

Salvini F., Billi A., Wise D.U., 1999. Strike-slip fault-propagation cleavage in carbonate rocks: the Mattinata Fault zone. Journal of Structural Geology 21, 1731–1749

Sammis C.G., Biegel R., 1989. Fractals, fault-gouge and friction. Pure and Applied Geophysics 131, 254–271

Sartori, R., 1989. Drillings of ODP Leg 107 in the Tyrrhenian Sea: tentative basin evolution compared to deformations in the surrounding chains. Atti dei Convegni Lincei 80, 139-156

Schlische R. W., Young S. S., Ackermann, Gupta A., 1996. Geometry and scaling relations of population of very small rift-related normal faults. Geology 24, 683-686

Schlumberger Market Analysis 2007

Scholz C. H., Cowie P. A. 1990. Determination of total strain from faulting using slip measurements. Nature 346, 837-839

Scrocca D., Carminati E., Doglioni C., 2006. Arretramento dello slab adriatico e tettonica compressiva attiva nell'Appennino centro-settentrionale. Rendiconti Società Geologica Italiana, 2.

Serva L., Salvini F., 1978. Analisi statistica delle deformazioni meccaniche in alcune strutture dell' Appennino laziale. Bollettino Società Geologica Italiana 95, 1219-1233.

Sibson R., 1977. Fault rocks and fault mechanisms. Journal of the Geological Society, London 133, 191–213

Sibson, R.H., 1996. Structural permeability of fluid-driven fault-fracture meshes. Journal of Structural Geology 18, 1031–1042.

Sibson R., 2000. Fluid involvement in normal faulting. Journal of Geodynamics 29, 469-499

Sibson, R. H., 2003. Thickness of the seismic slip zone. Geological Society American Bullettin 93, 1169–1178.

Stewart I., Hancock P., 1991. Scales of structural heterogeneity within neotectonic normal fault zone in the Aegean region. Journal of Structural Geology 13, 191–204

Storti F., Balsamo F., Salvini F., 2007. Particle shape evolution in natural carbonate granular wear material. Terra Nova 19, 1–9

Storti F., Rossetti F., Laufer L.A., Salvini F., 2006. Consistent kinematic architecture in the damage zones of intraplate strike-slip fault systems in North Victoria Land, Antarctica and implications for fault zone evolution. Journal of Structural Geology 28, 50–63

Storti F., Billi A., Salvini F., 2003. Particle size distributions in natural carbonate fault rocks: insights for non-self-similar cataclasis. Earth and Planetary Science Letters 206, 173-186

Storti F., Salvini F., McClay K**.** 1997. Fault-related folding in sandbox analogue models of thrust wedges Journal of Structural Geology 19, 583-602

Swan A. R. H., Sandilands M., 1995. Introduction to Geological Data Analysis. Blackwell, Oxford

Tarantola A., 2005. Inverse Problem Theory. Society for Industrial and Applied Mathematics

Tavani S., Storti F., Munoz J. A., 2010. Scaling relationships between stratabound pressure solution cleavage spacing and layer thickness in a folded carbonate multiplayer of Northen Apennines (Italy). Journal of Structural Geology 32, 278-287

Tavani S., Storti F., Fernandez O., Munoz J. A., Salvini F., 2006. 3-D deformation pattern analysis and evolution of the Anisclo anticline, southern Pyrenees. Journal of Structural Geology 28, 695-712

Vezzani L., Ghisetti F., 1998. Carta geologica dell'Abruzzo 1:100000

Wibberley C. A. J., Yielding G., Di Toro G., 2008. Recent advances in the understanding of fault zone internal structure: a review. The geological Society of London, Special Publication 299, 5-33

Wise D. U., Funiciello R., Parotto M., Salvini F., 1985. Topographic lineament swarm: clues to their origin from domains analysis of Italy. Geological Society of America Bulletin 96, 952–967

Yielding G., Needham T. Jones H., 1996. Sampling of fault populations using sub-surface data: a review. Journal of Structural Geology 18, 135-146

Yelding G., Freeman B., Needham D. T., 1997. Quantitative seal prediction: a case study from Oseberg Syd. Norwegian Petroleum Society Special 7, 107-124

Yielding G., Bretan P., Freeman B., 2010. Fault seal calibration: a brief review. The geological Society of London, Special Publication 347, 243-255

9 - APPENDICES

Appendix 1 – Monte Carlo results

ROCCA DI CAVE 1 FAULT

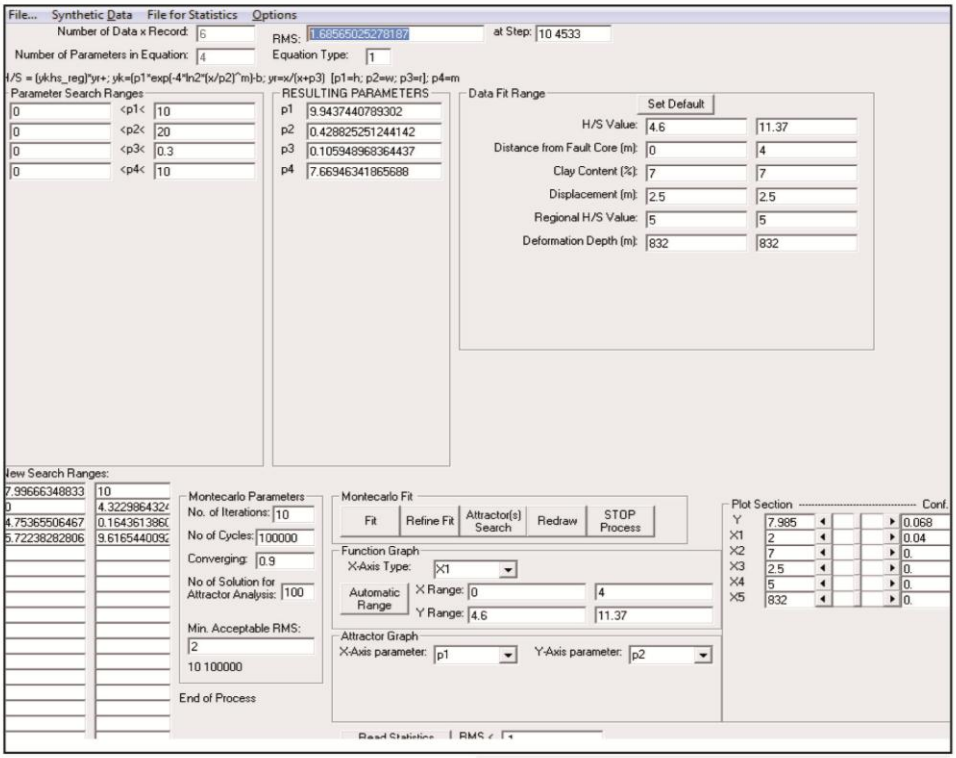

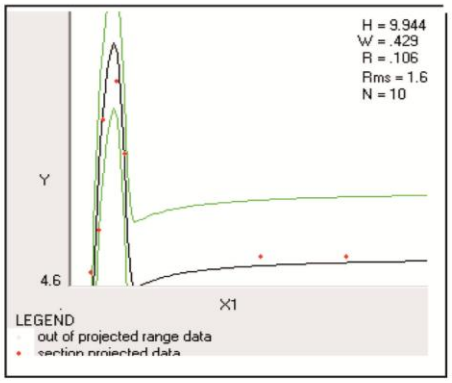

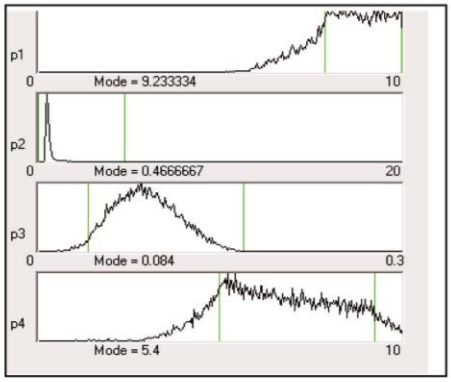

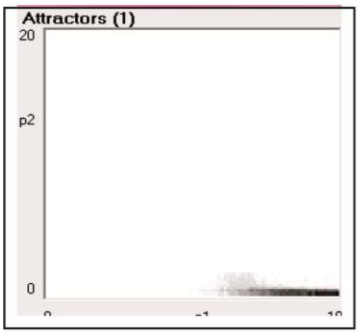

ROCCA DI CAVE 2 FAULT

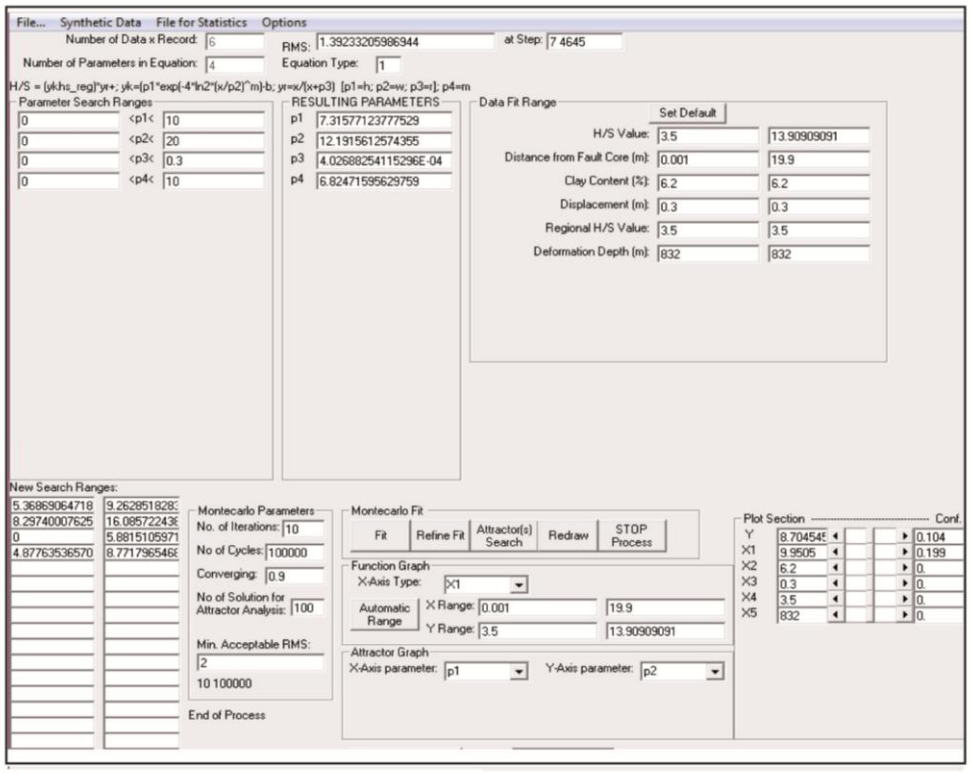

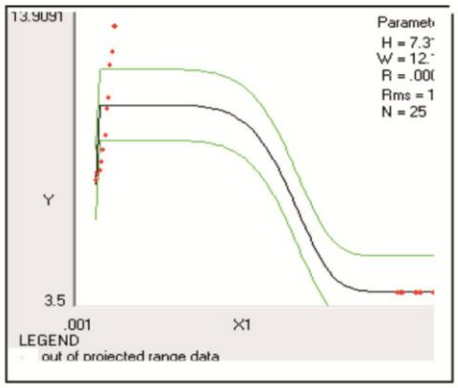

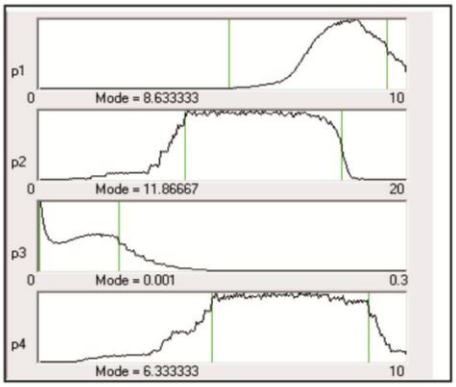

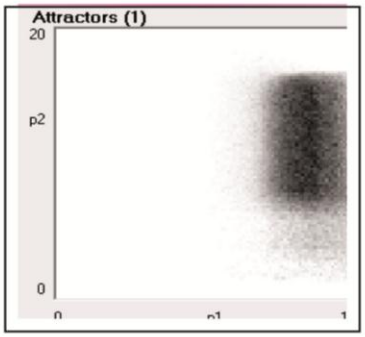

ROCCA DI CAVE 3 FAULT

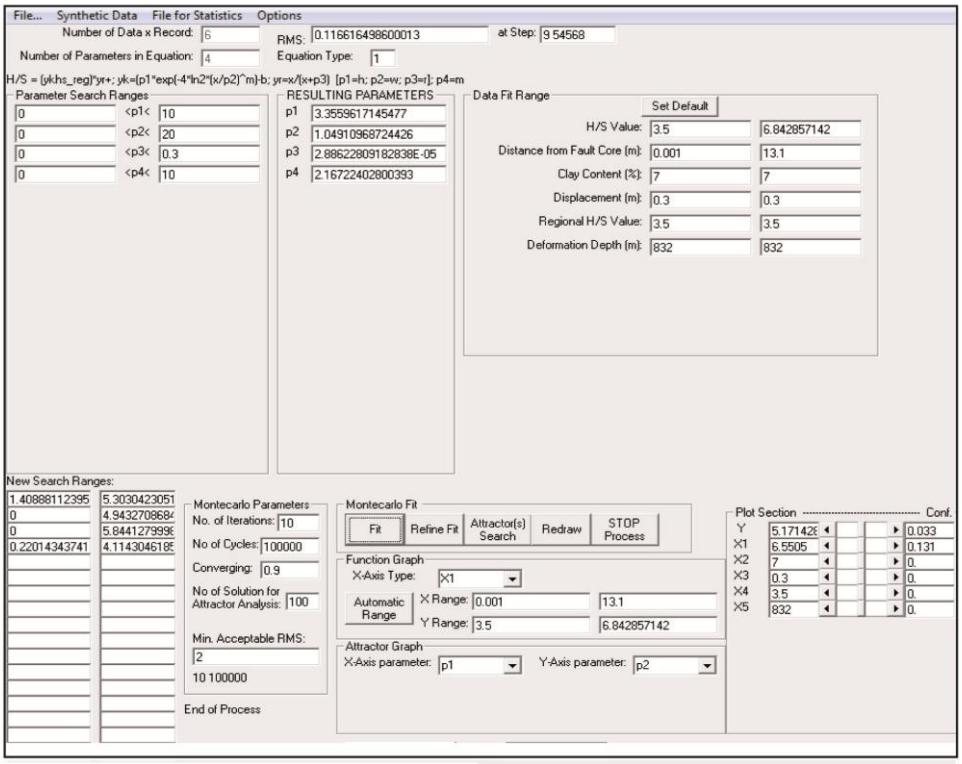

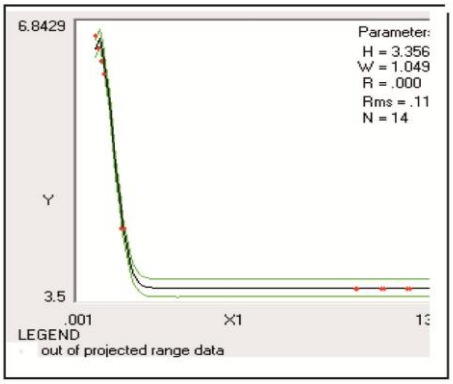

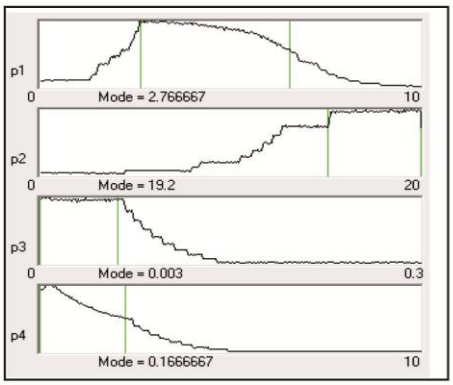

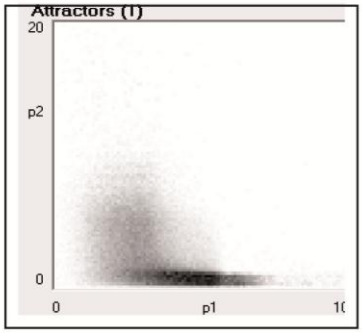

FILETTINO FAULT

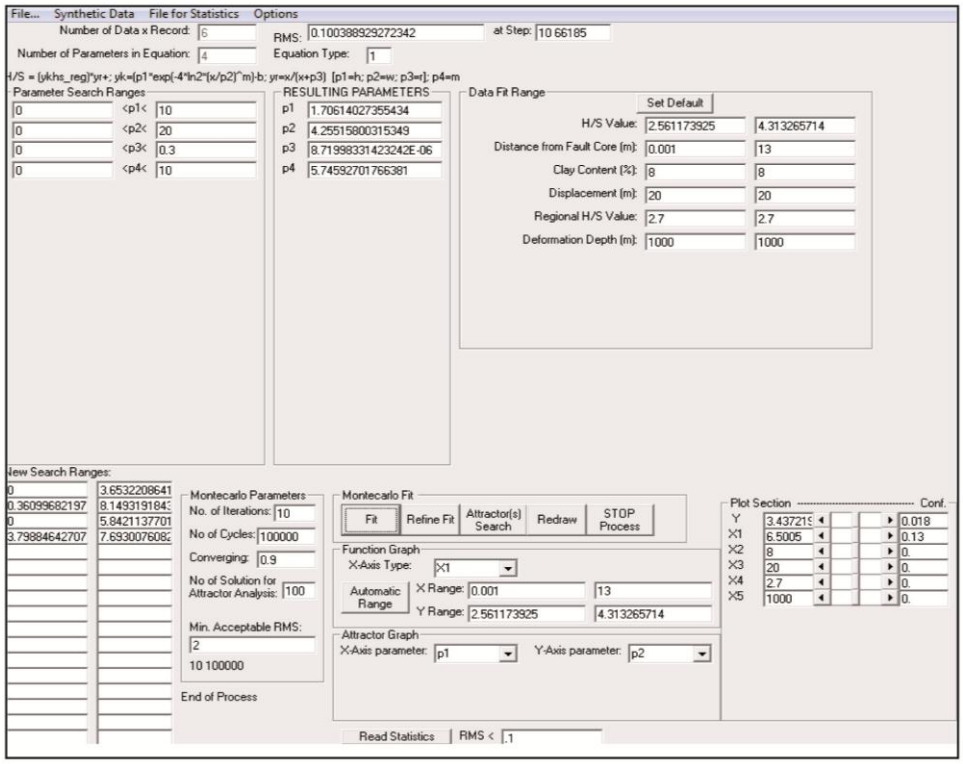

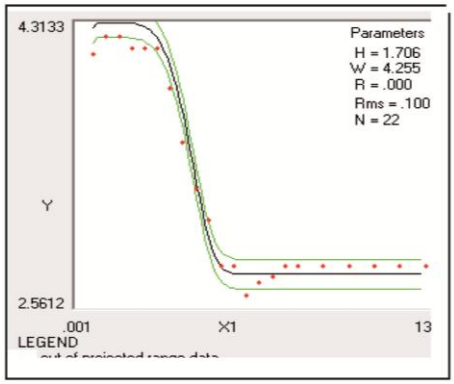

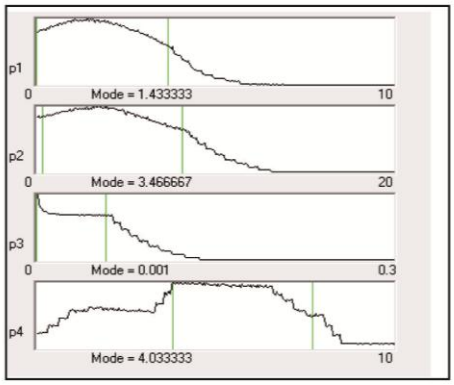

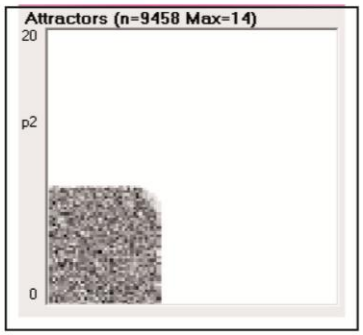

IENNE FAULT

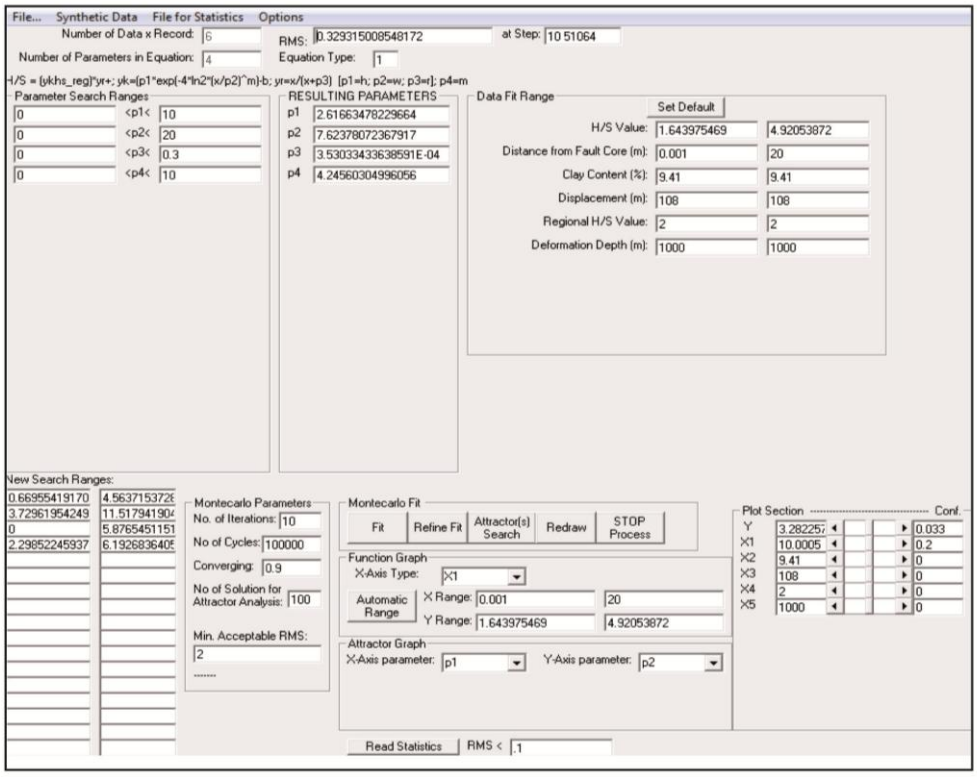
File... Synthetic Data File for Statistics Options
Number of Data x Record: 6
RMS: 0.329315008548172
at Step: 10 51064
Number of Parameters in Equation: 4
Equation Type: 1
H/S = (ykhs_reg)*yr+; yk=(p1*exp(-4*ln2*(x/p2)^m)-b; yr=x/(x+p3) [p1=h; p2=w; p3=r]; p4=m
Parameter Search Ranges
RESULTING PARAMETERS
p1 2.61663478229664
p2 7.62378072367917
p3 3.53033433638591E-04
p4 4.24560304996056
Data Fit Range
Set Default
H/S Value: 1.643975469 4.92053872
Distance from Fault Core (m): 0.001 20
Clay Content (%): 9.41 9.41
Displacement (m): 108 108
Regional H/S Value: 2 2
Deformation Depth (m): 1000 1000
New Search Ranges:
Montecarlo Parameters
No. of Iterations: 10
No of Cycles: 100000
Converging: 0.9
No of Solution for Attractor Analysis: 100
Min. Acceptable RMS: 2
Montecarlo Fit
Fit
Refine Fit
Attractor(s) Search
Redraw
STOP Process
Function Graph
X-Axis Type: X1
Automatic Range
X Range: 0.001 20
Y Range: 1.643975469 4.92053872
Attractor Graph
X-Axis parameter: p1
Y-Axis parameter: p2
Plot Section
Conf.
Y 3.282257 0.033
X1 10.0005 0.2
X2 9.41 0
X3 108 0
X4 2 0
X5 1000 0
Read Statistics
RMS < .1

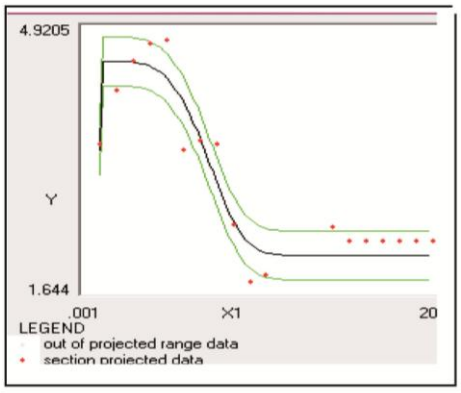
4.9205
Y
1.644
.001
X1
20
LEGEND
out of projected range data
section projected data

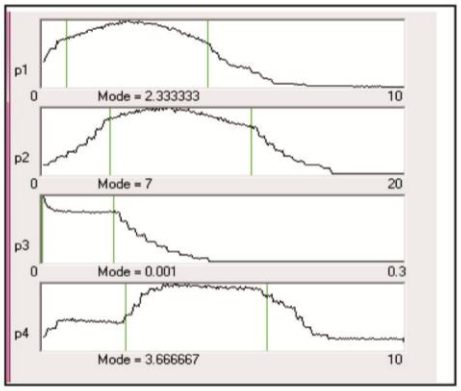
p1
0
Mode = 2.333333
10
p2
0
Mode = 7
20
p3
0
Mode = 0.001
0.3
p4
Mode = 3.666667
10

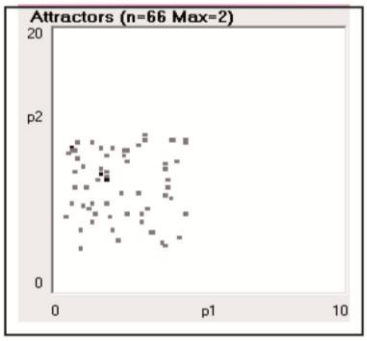
Attractors (n=66 Max=2)
20
p2
0
0
p1
10

PIETRASECCA FAULT

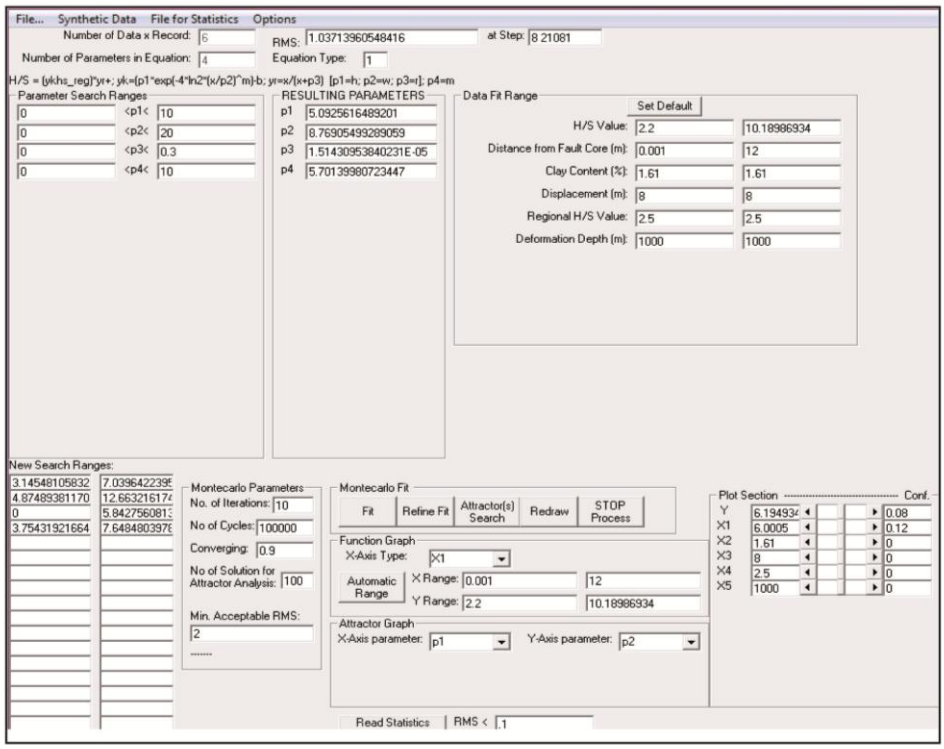

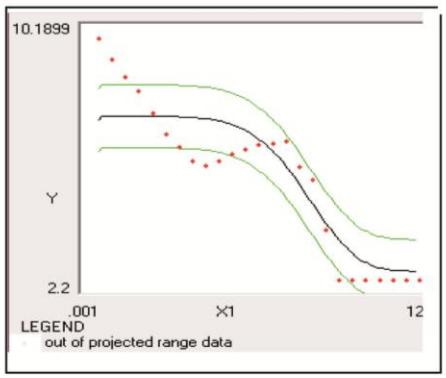

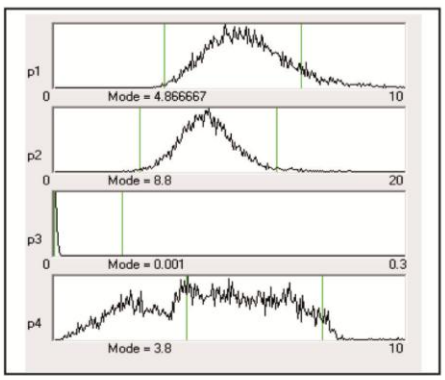

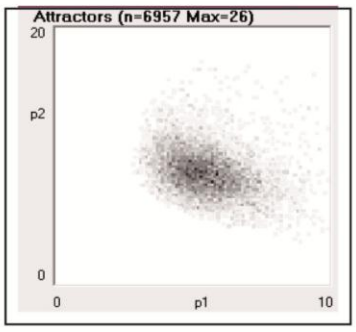

TORNIMPARTE 1 FAULT

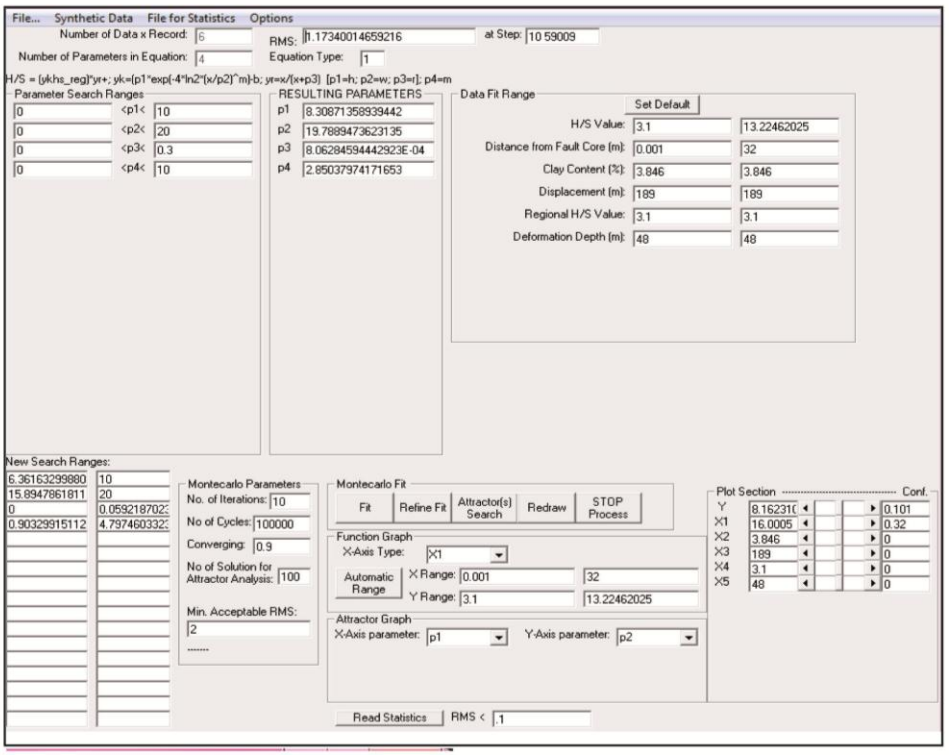

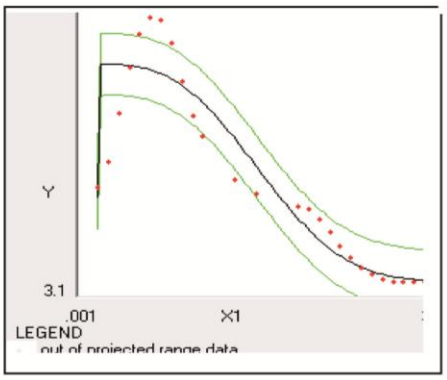

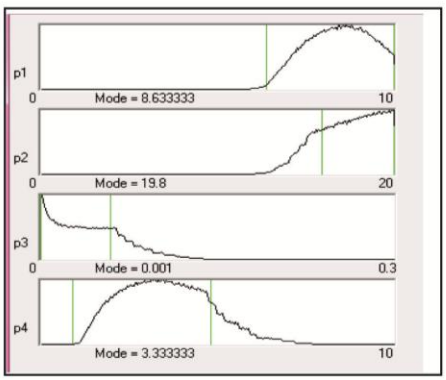

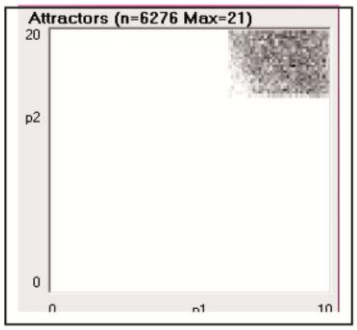

TORNIMPARTE 2 FAULT

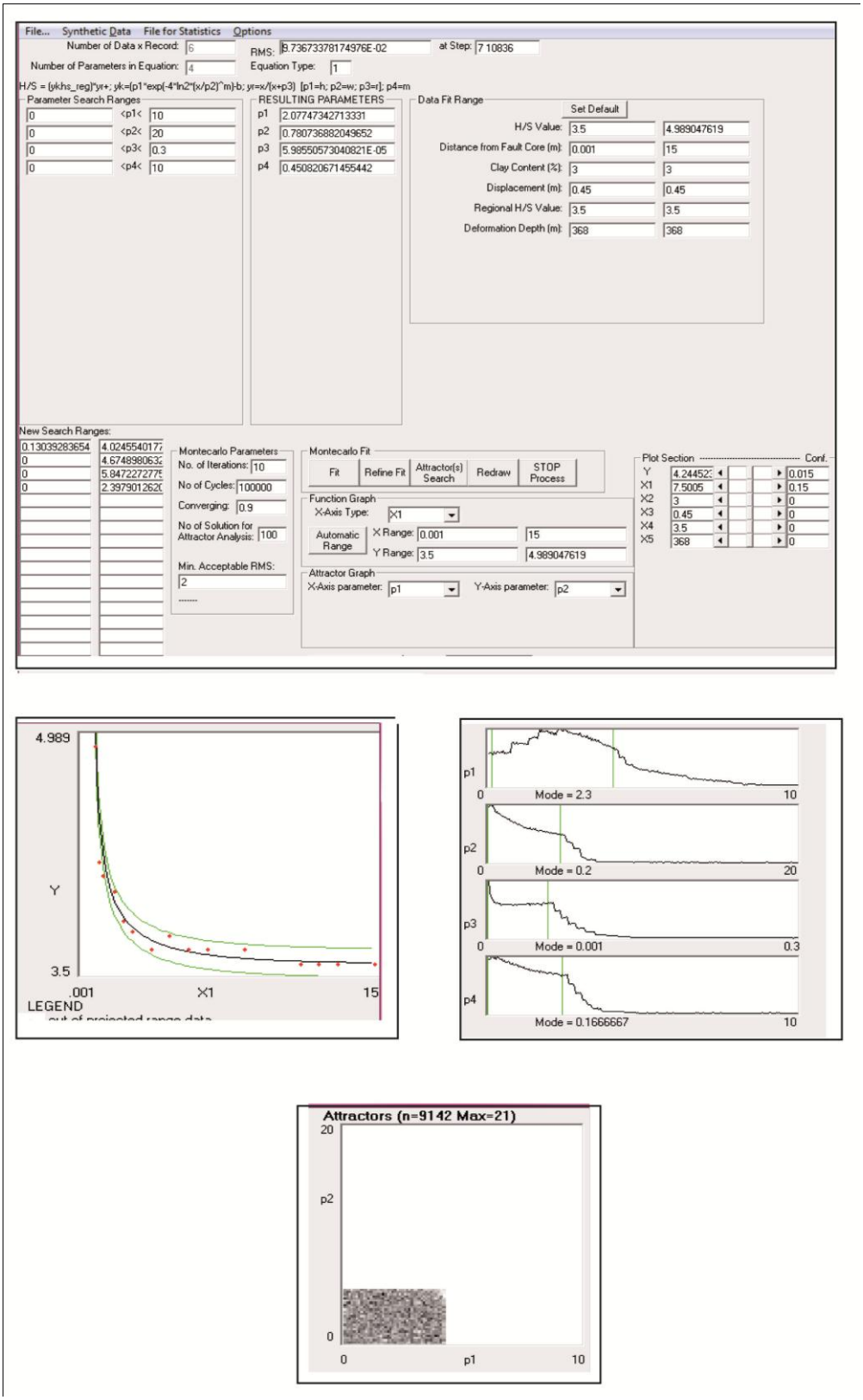

TORNIMPARTE 3 FAULT

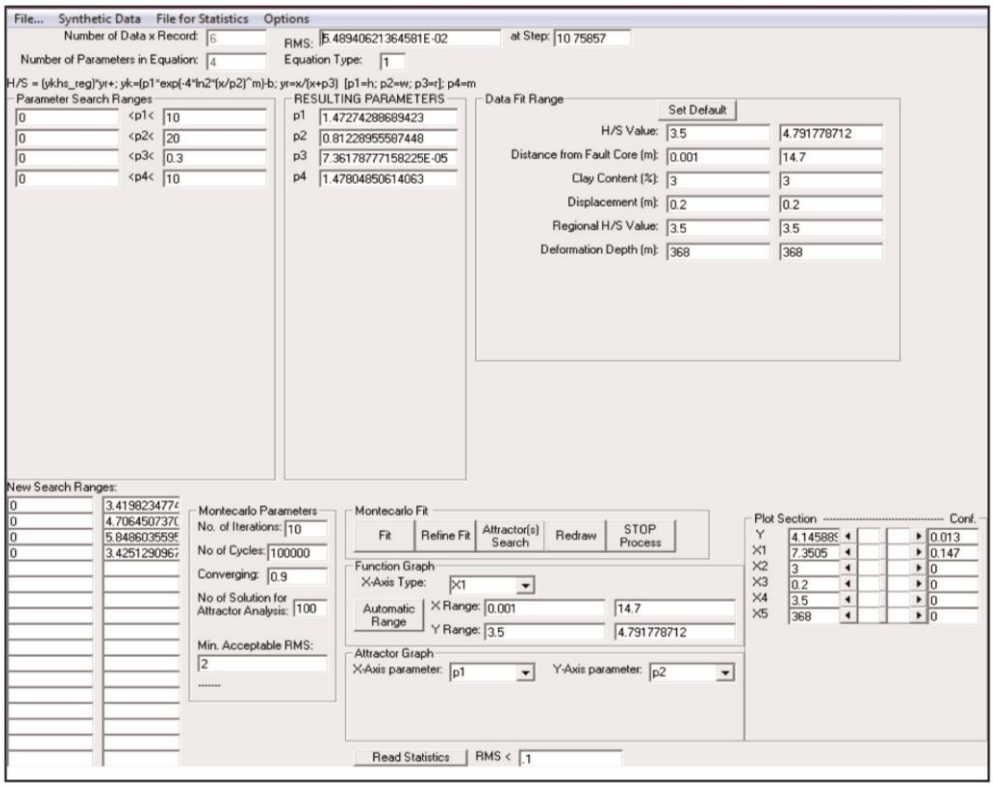

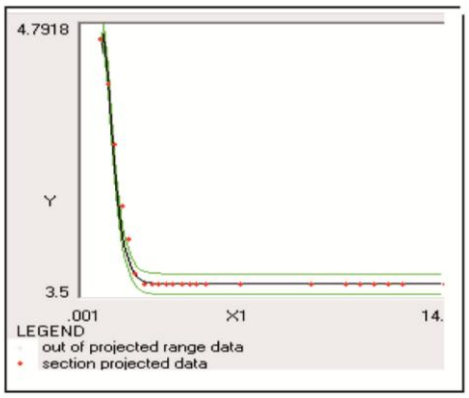

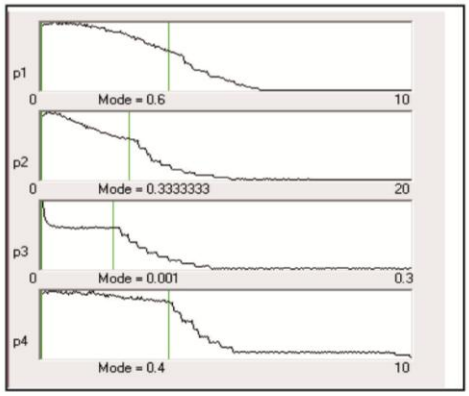

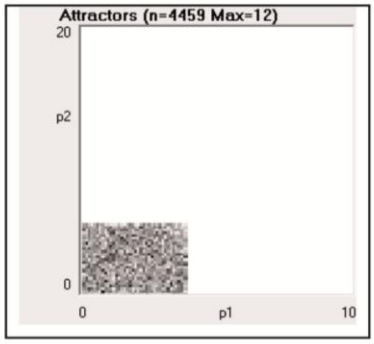

TORNIMPARTE 5 FAULT

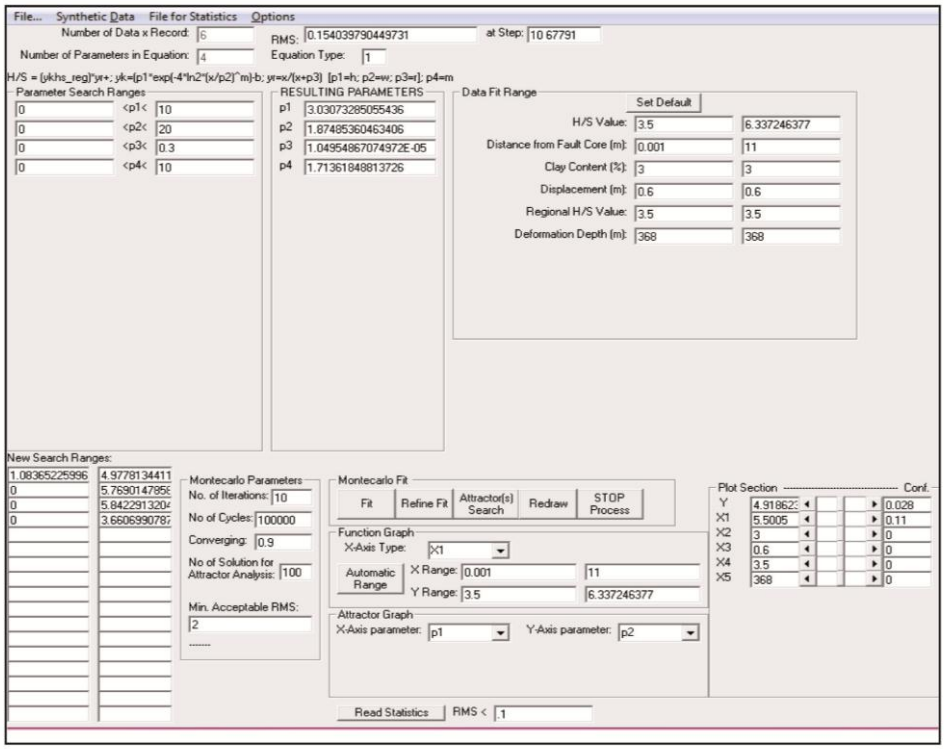

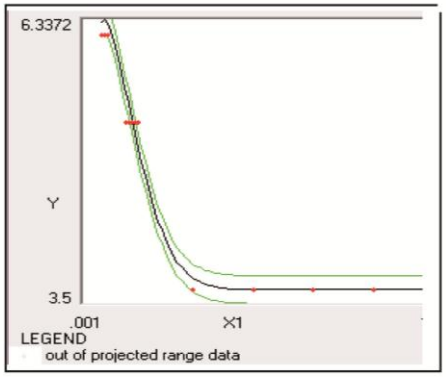

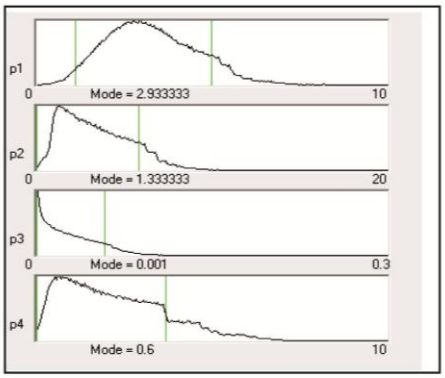

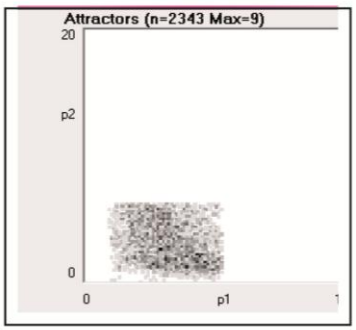

LECCE DEI MARSI 2 FAULT

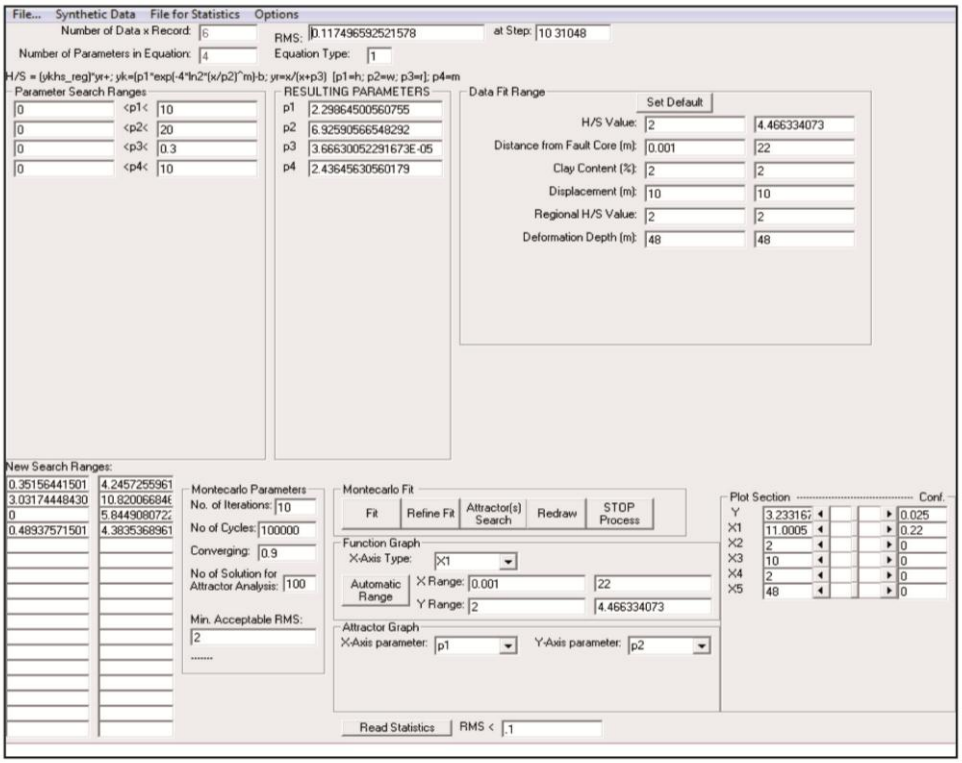

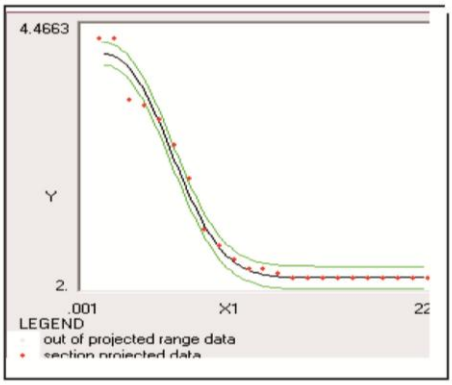

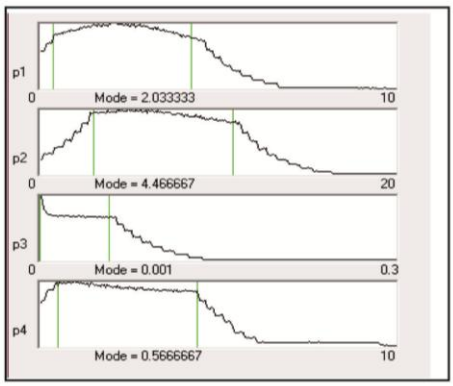

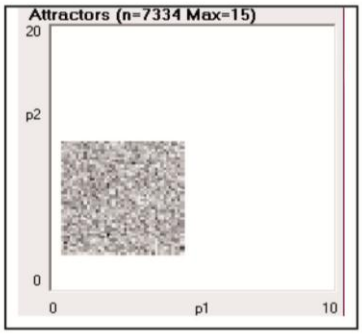

GOLE DEL SAGITTARIO FAULT

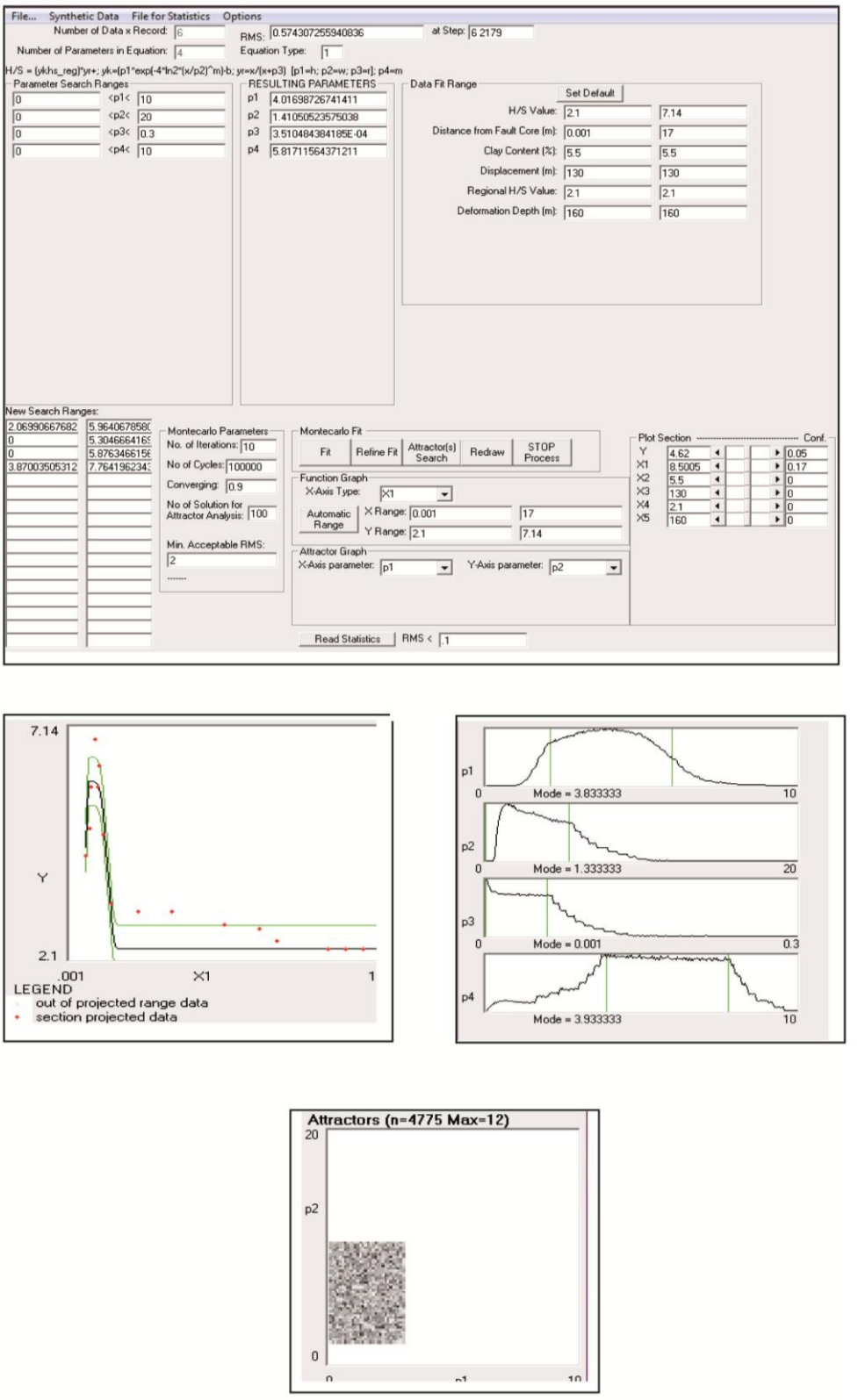

CASTEL DI IERI FAULT

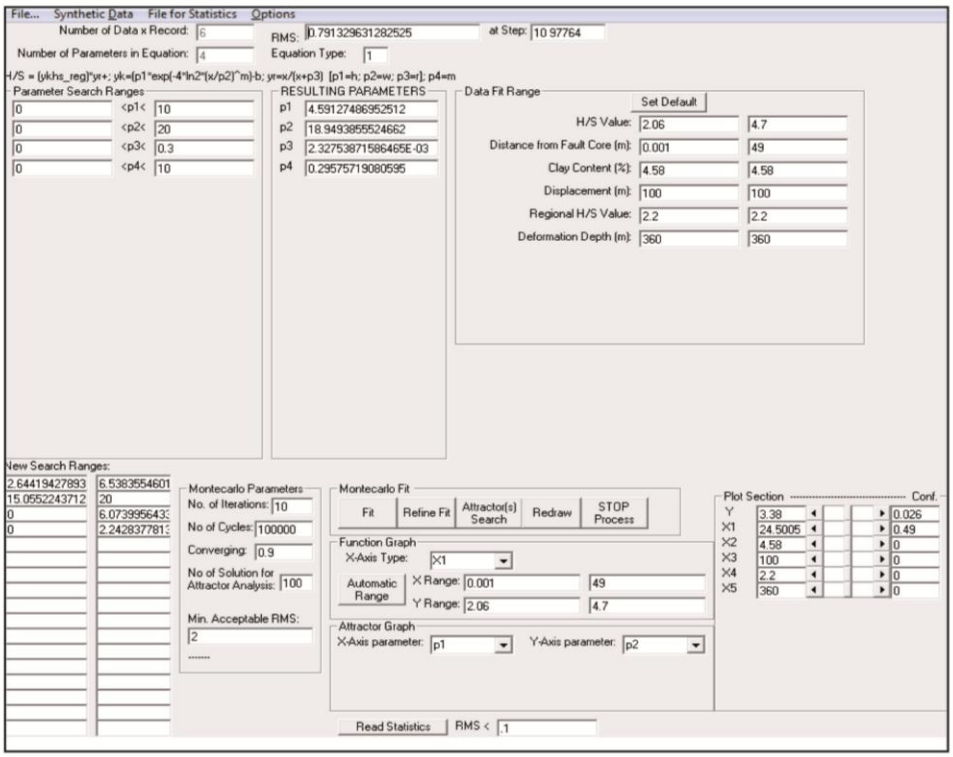

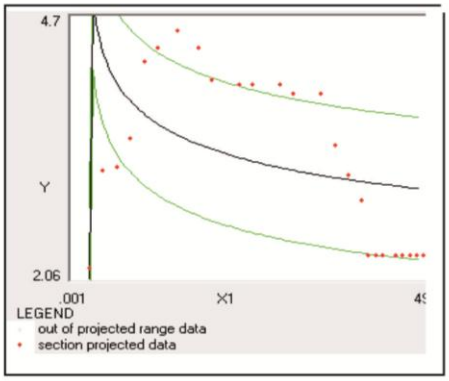

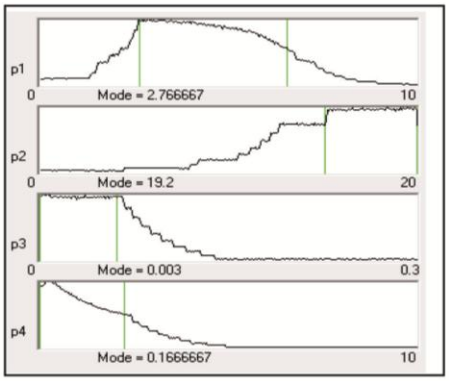

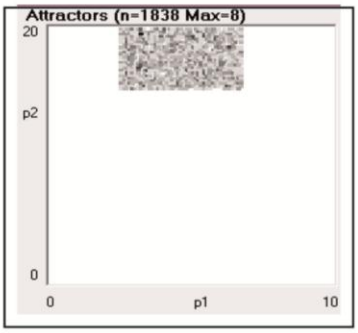

FARA 1 FAULT

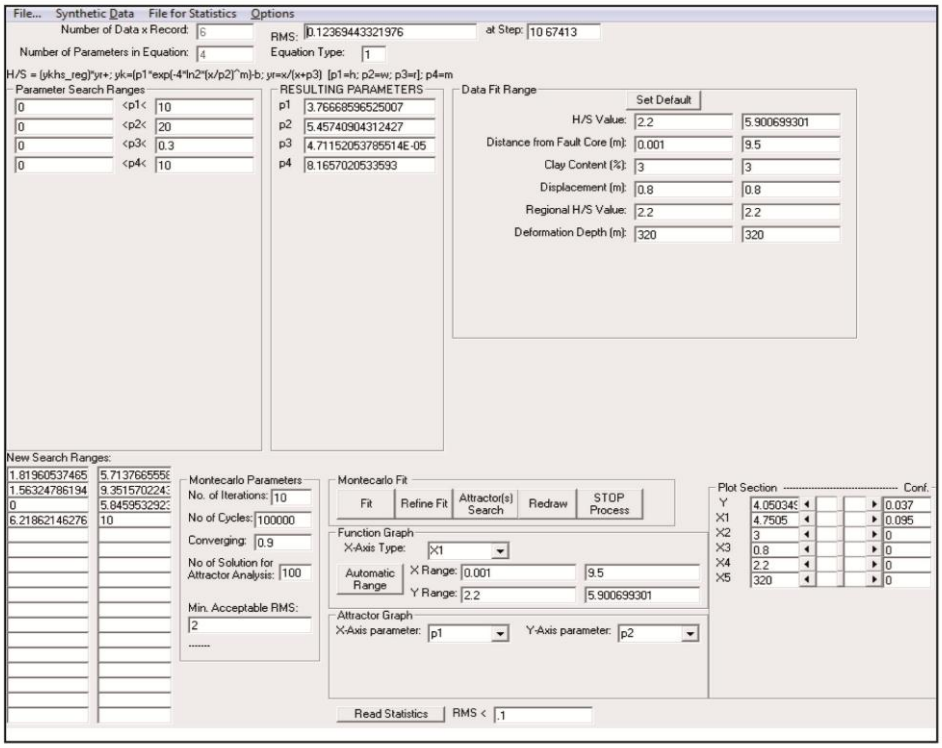
File... Synthetic Data File for Statistics Options
Number of Data x Record: 6
RMS: 0.12369443321976
at Step: 10 67413
Number of Parameters in Equation: 4
Equation Type: 1
H/S = (ykhs_reg)*yr+; yk=(p1*exp(-4*ln2*(x/p2)^m)+b; yr=x/(x+p3) [p1=h; p2=w; p3=r]; p4=m
Parameter Search Ranges
RESULTING PARAMETERS
p1 3.76668596525007
p2 5.45740904312427
p3 4.711520537855 14E-05
p4 8.1657020533593
Data Fit Range
Set Default
H/S Value: 2.2 5.900699301
Distance from Fault Core (m): 0.001 9.5
Clay Content (%): 3 3
Displacement (m): 0.8 0.8
Regional H/S Value: 2.2 2.2
Deformation Depth (m): 320 320
New Search Ranges:
Montecarlo Parameters
No. of Iterations: 10
No of Cycles: 100000
Converging: 0.9
No of Solution for Attractor Analysis: 100
Min. Acceptable RMS: 2
Montecarlo Fit
Fit
Refine Fit
Attractor(s) Search
Redraw
STOP Process
Function Graph
X-Axis Type: X1
Automatic Range
X Range: 0.001 9.5
Y Range: 2.2 5.900699301
Attractor Graph
X-Axis parameter: p1
Y-Axis parameter: p2
Plot Section
Conf.
Y 4.050345 0.037
X1 4.7505 0.095
X2 3 0
X3 0.8 0
X4 2.2 0
X5 320 0
Read Statistics
RMS < .1

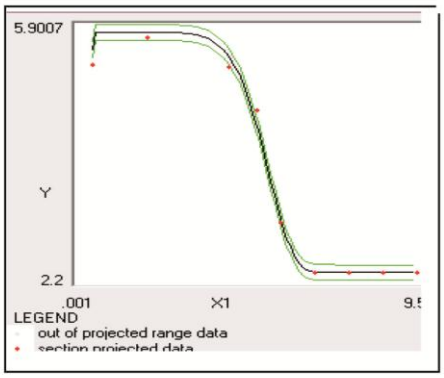
5.9007
Y
2.2
.001
X1
9.5
LEGEND
out of projected range data

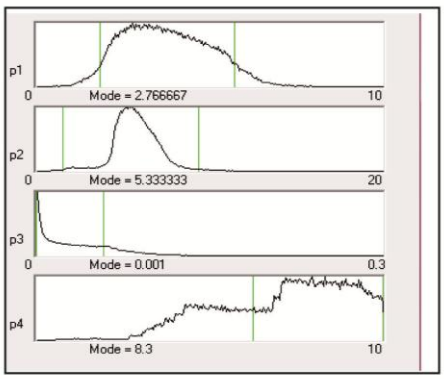
p1
0
Mode = 2.766667
10
p2
0
Mode = 5.333333
20
p3
0
Mode = 0.001
0.3
p4
Mode = 8.3
10

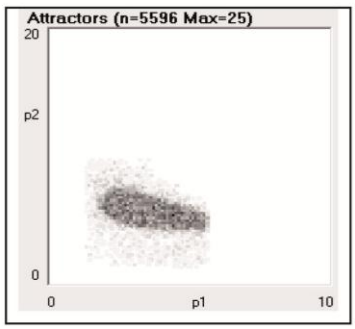
Attractors (n=5596 Max=25)
20
p2
0
0
p1
10

FARA 2 FAULT

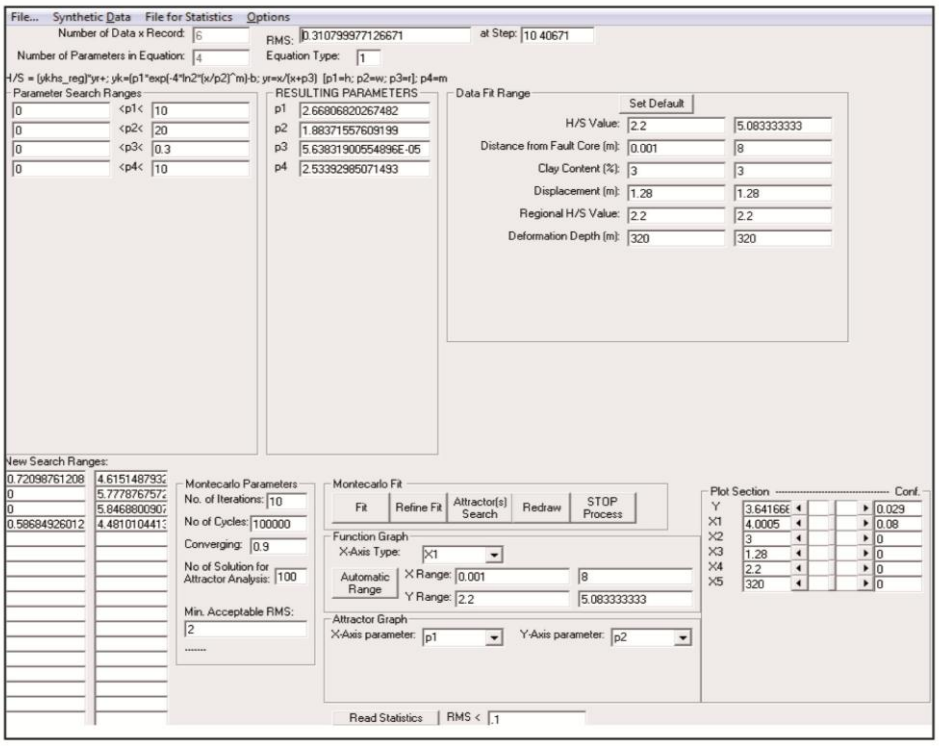
File... Synthetic Data File for Statistics Options
Number of Data x Record: 6
RMS: 0.310799977126671
at Step: 10 40671
Number of Parameters in Equation: 4
Equation Type: 1
H/S = (yk:hs_reg)*yr+; yk:=(p1*exp(-4*ln2*((x/p2)^m)+b; yr=x/(x+p3) [p1=h; p2=w; p3=t]; p4=m
Parameter Search Ranges
RESULTING PARAMETERS
p1 2.66806820267482
p2 1.88371557609199
p3 5.63831900554896E-05
p4 2.53392985071493
Data Fit Range
Set Default
H/S Value: 2.2 5.083333333
Distance from Fault Core (m): 0.001 8
Clay Content (%): 3 3
Displacement (m): 1.28 1.28
Regional H/S Value: 2.2 2.2
Deformation Depth (m): 320 320
New Search Ranges:
Montecarlo Parameters
No. of Iterations: 10
No of Cycles: 100000
Converging: 0.9
No of Solution for Attractor Analysis: 100
Min. Acceptable RMS: 2
Montecarlo Fit
Fit
Refine Fit
Attractor(s) Search
Redraw
STOP Process
Function Graph
X-Axis Type: X1
Automatic Range
X Range: 0.001 8
Y Range: 2.2 5.083333333
Attractor Graph
X-Axis parameter: p1
Y-Axis parameter: p2
Plot Section
Conf.
Y 3.64166
X1 4.0005 0.08
X2 3 0
X3 1.28 0
X4 2.2 0
X5 320 0
Read Statistics
RMS < .1

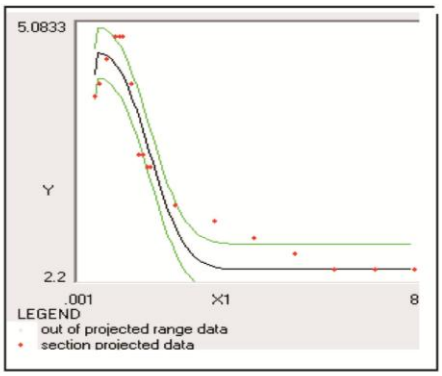
5.0833
Y
2.2
.001
X1
8
LEGEND
out of projected range data
section projected data

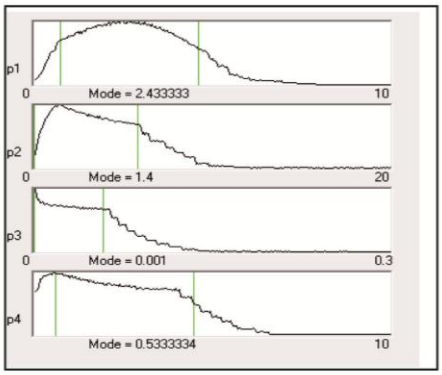
p1
0
Mode = 2.433333
10
p2
0
Mode = 1.4
20
p3
0
Mode = 0.001
0.3
p4
Mode = 0.5333334
10

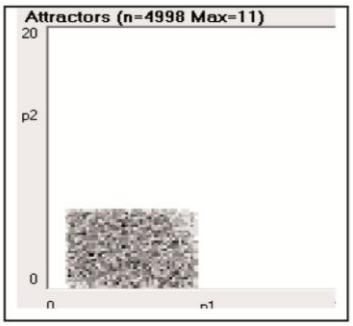
Attractors (n=4998 Max=11)
20
p2
0
0
p1

FARA 4 FAULT

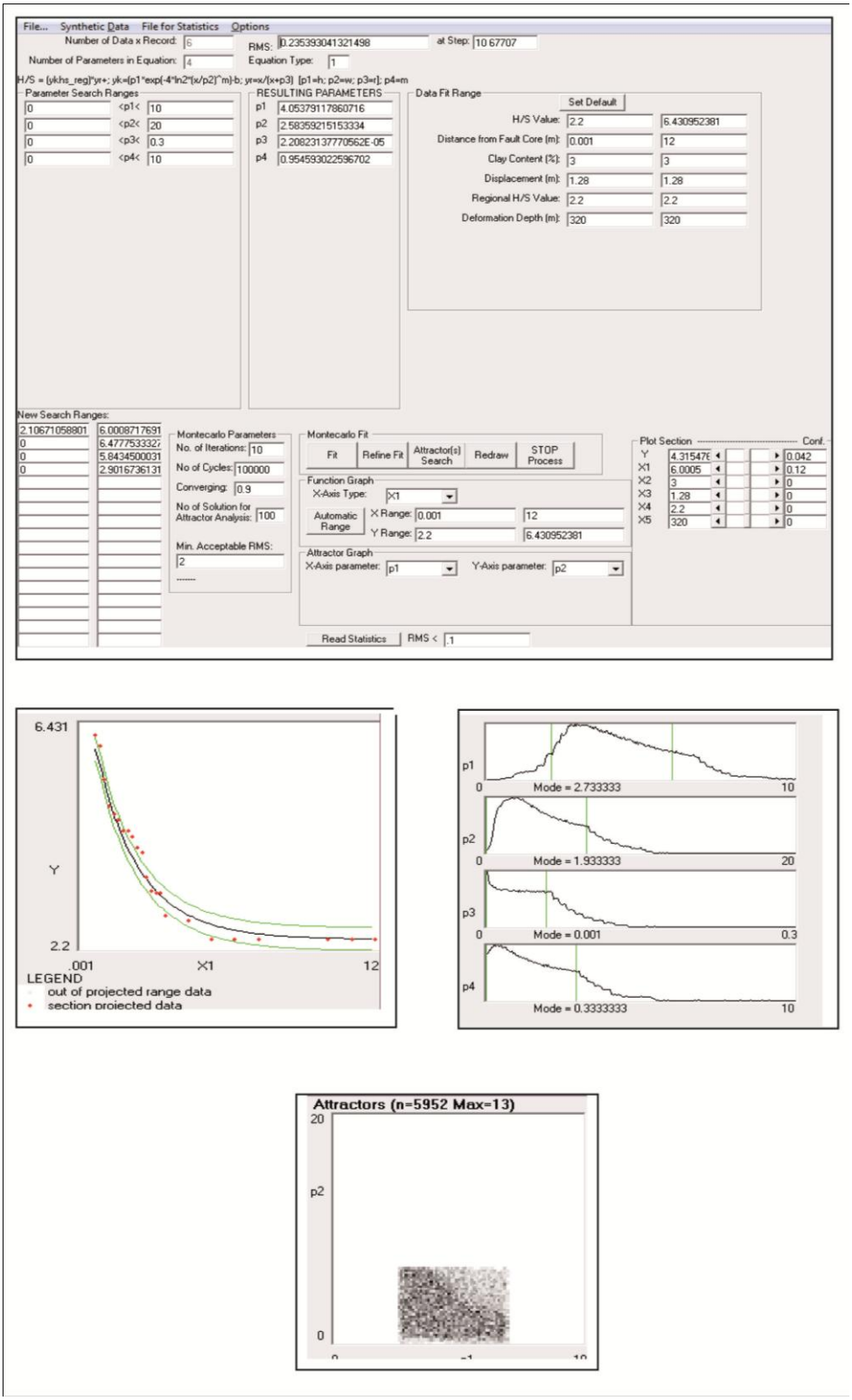
File... Synthetic Data File for Statistics Options
Number of Data x Record: 6
RMS: 0.235393041321498
at Step: 10 67707
Number of Parameters in Equation: 4
Equation Type: 1
H/S = (ykhs_reg)*yr+; yk=(p1*exp(-4*ln2*(x/p2)^m)+b; yr=x/(x+p3) [p1=h; p2=w; p3=r]; p4=m
Parameter Search Ranges
RESULTING PARAMETERS
p1 4.05379117860716
p2 2.58359215153334
p3 2.20823137770562E-05
p4 0.954593022596702
Data Fit Range
Set Default
H/S Value: 2.2 6.430952381
Distance from Fault Core (m): 0.001 12
Clay Content (%): 3 3
Displacement (m): 1.28 1.28
Regional H/S Value: 2.2 2.2
Deformation Depth (m): 320 320
New Search Ranges:
Montecarlo Parameters
No. of Iterations: 10
No of Cycles: 100000
Converging: 0.9
No of Solution for Attractor Analysis: 100
Min. Acceptable RMS: 2
Montecarlo Fit
Fit
Refine Fit
Attractor(s) Search
Redraw
STOP Process
Function Graph
X-Axis Type: X1
Automatic Range
X Range: 0.001 12
Y Range: 2.2 6.430952381
Attractor Graph
X-Axis parameter: p1
Y-Axis parameter: p2
Plot Section
Conf.
Read Statistics
RMS < .1

6.431
Y
2.2
.001
X1
12
LEGEND
out of projected range data
section projected data

p1
0
Mode = 2.733333
10
p2
0
Mode = 1.933333
20
p3
0
Mode = 0.001
0.3
p4
Mode = 0.3333333
10

Attractors (n=5952 Max=13)
20
p2
0

FARA 6 FAULT

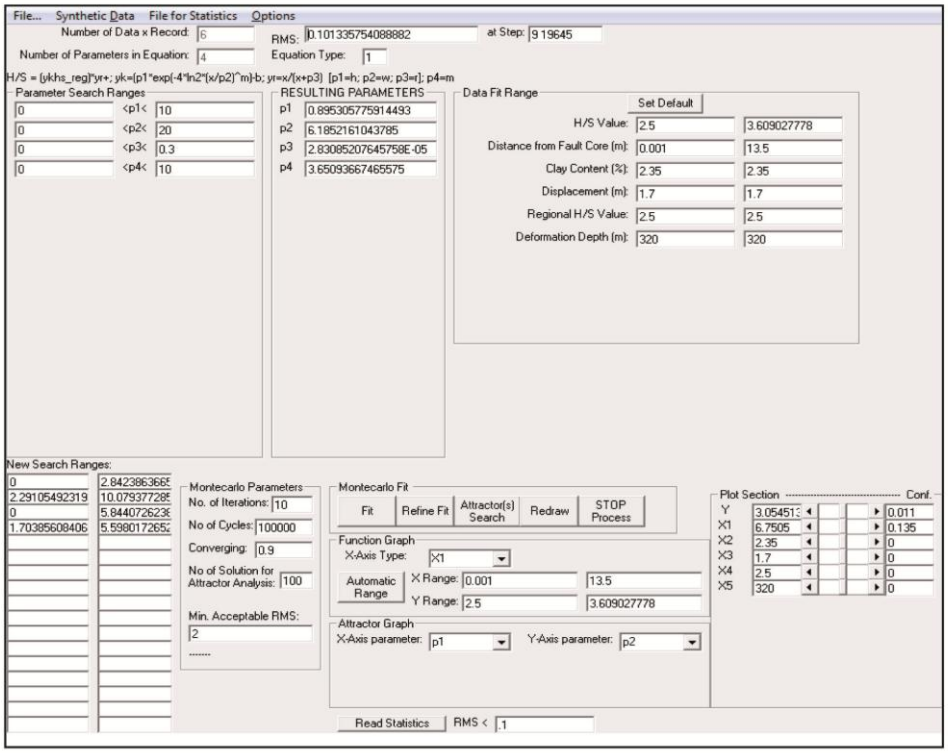
File... Synthetic Data File for Statistics Options
Number of Data x Record: 6
RMS: 0.101335754088882
at Step: 9 19645
Number of Parameters in Equation: 4
Equation Type: 1
H/S = (ykhs_reg)*yr+; yk=(p1*exp(-4*ln2*(x/p2)^m)+b; yr=x/(x+p3) [p1=h; p2=w; p3=r]; p4=m
Parameter Search Ranges
RESULTING PARAMETERS
p1 0.895305775914493
p2 6.1852161043785
p3 2.83085207645758E-05
p4 3.65093667465575
Data Fit Range
Set Default
H/S Value: 2.5 3.609027778
Distance from Fault Core (m): 0.001 13.5
Clay Content (%): 2.35 2.35
Displacement (m): 1.7 1.7
Regional H/S Value: 2.5 2.5
Deformation Depth (m): 320 320
New Search Ranges:
Montecarlo Parameters
No. of Iterations: 10
No of Cycles: 100000
Converging: 0.9
No of Solution for Attractor Analysis: 100
Min. Acceptable RMS: 2
Montecarlo Fit
Fit
Refine Fit
Attractor(s) Search
Redraw
STOP Process
Function Graph
X-Axis Type: X1
Automatic Range
X Range: 0.001 13.5
Y Range: 2.5 3.609027778
Attractor Graph
X-Axis parameter: p1
Y-Axis parameter: p2
Plot Section
Conf.
Y 3.054513 0.011
X1 6.7505 0.135
X2 2.35 0
X3 1.7 0
X4 2.5 0
X5 320 0
Read Statistics
RMS < .1

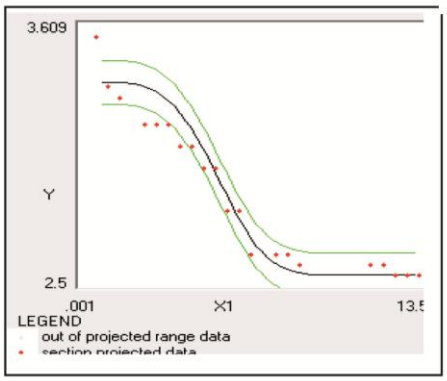
3.609
Y
2.5
.001
X1
13.5
LEGEND
out of projected range data

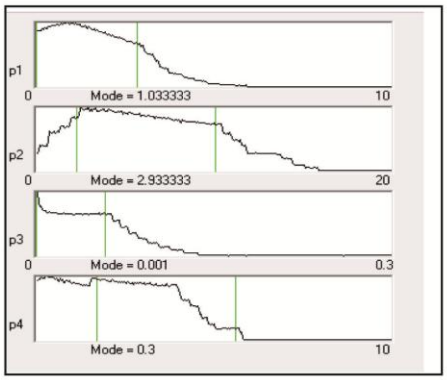
p1
0
Mode = 1.033333
10
p2
0
Mode = 2.933333
20
p3
0
Mode = 0.001
0.3
p4
Mode = 0.3
10

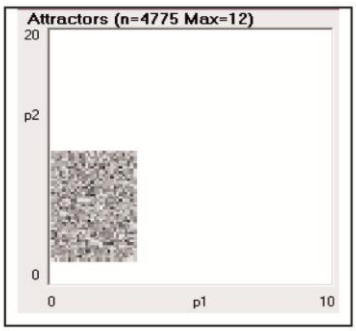
Attractors (n=4775 Max=12)
20
p2
0
0
p1
10

Appendix 2 – Fracture predictive modelling results

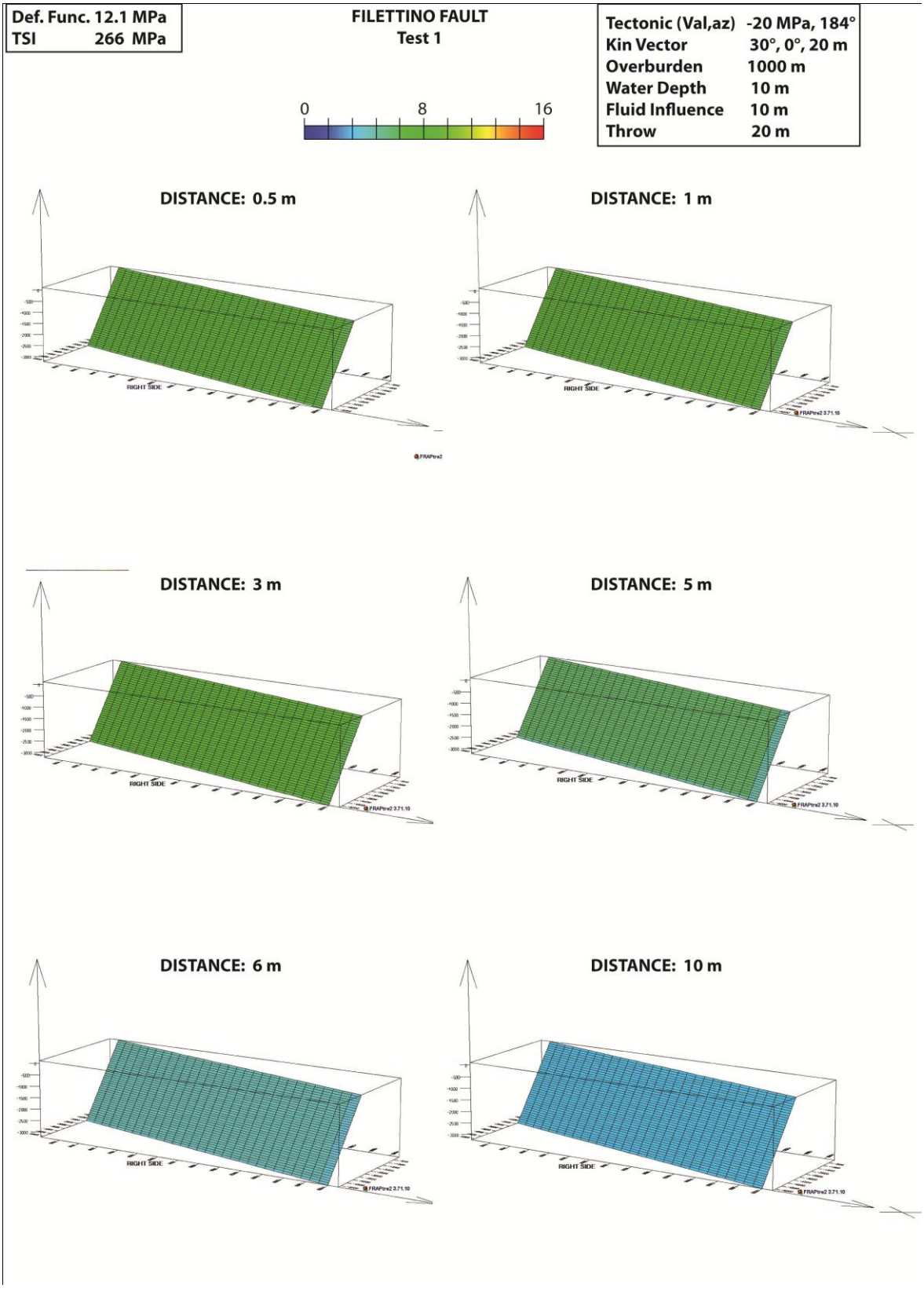

Def. Func.	3.5 MPa
TSI	90 MPa

FILETTINO FAULT
Test 2

Tectonic (Val,az)	-10 MPa, 184°
Kin Vector	30°, 0°, 20 m
Overburden	1000 m
Water Depth	10 m
Fluid Influence	10 m
Throw	20 m

DISTANCE: 0.5 m

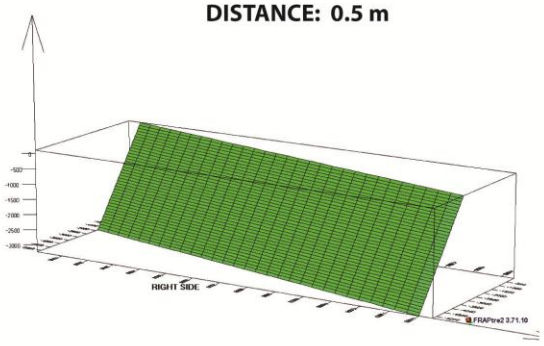

DISTANCE: 1 m

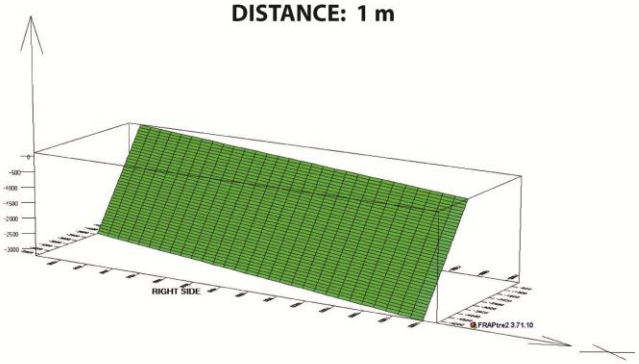

DISTANCE: 3 m

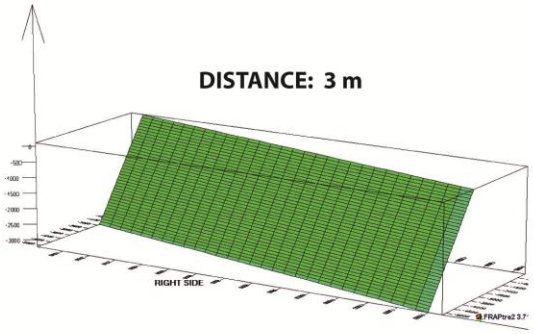

DISTANCE: 5 m

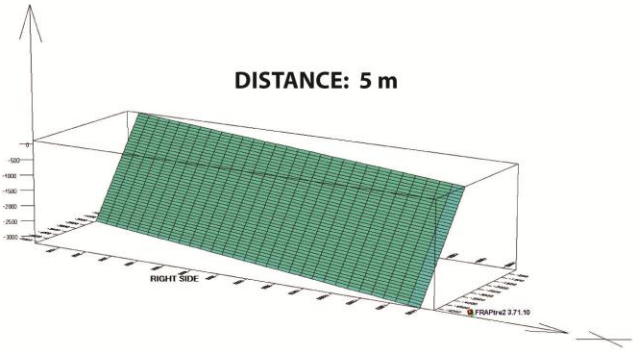

DISTANCE: 6 m

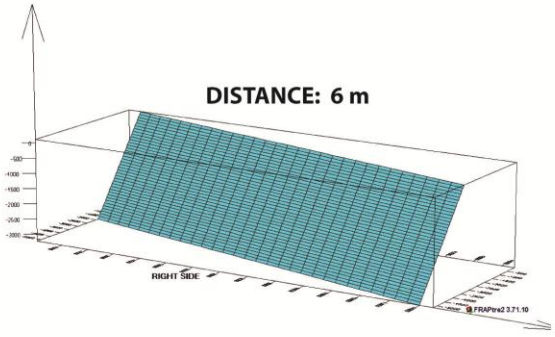

DISTANCE: 10 m

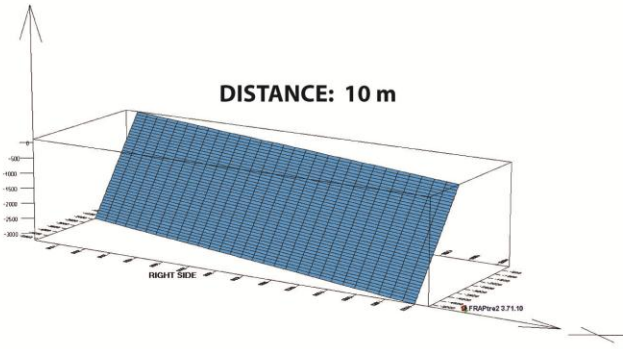

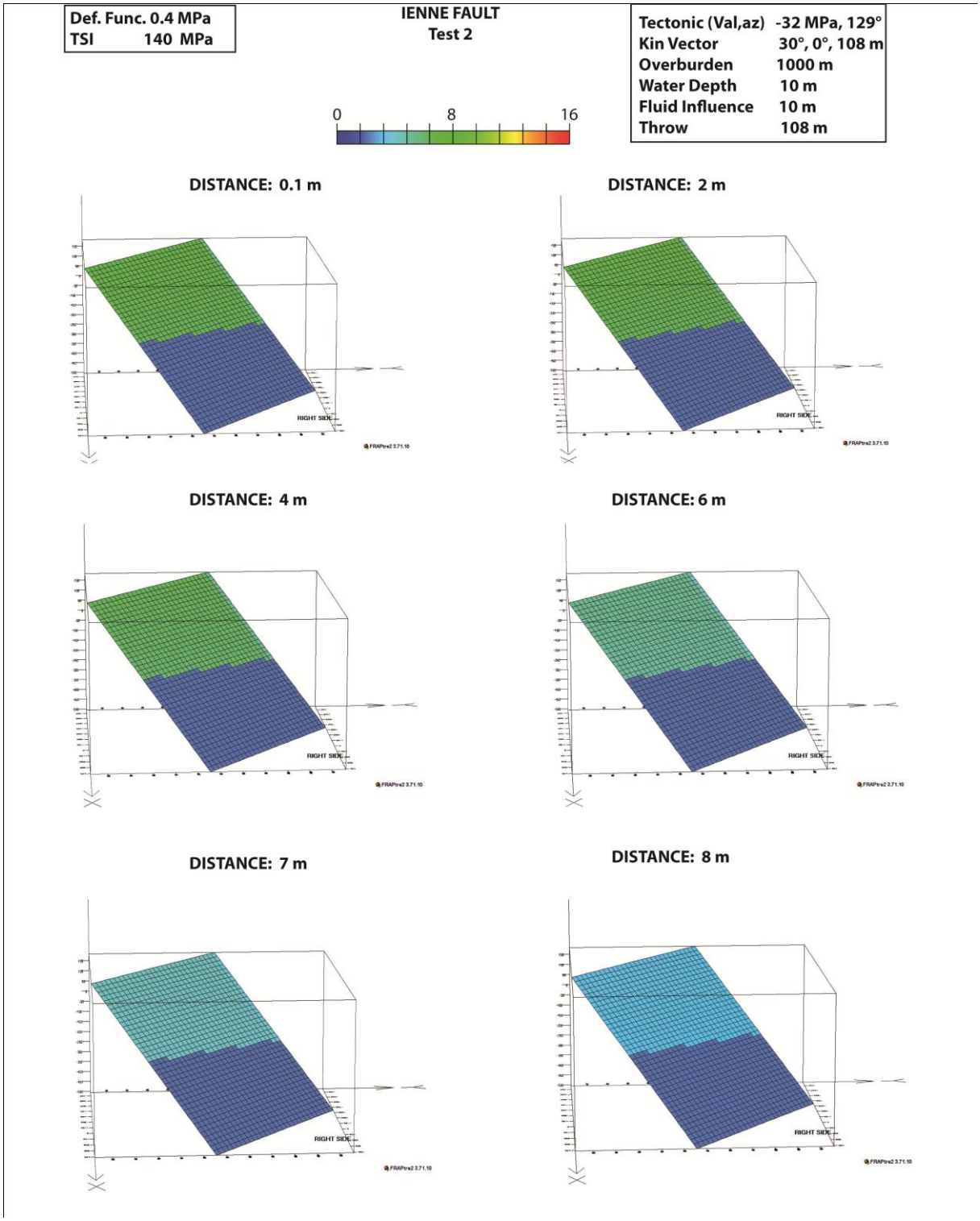
Def. Func. 0.4 MPa
TSI 140 MPa
IENNE FAULT
Test 2
0
8
16
Tectonic (Val,az) -32 MPa, 129°
Kin Vector 30°, 0°, 108 m
Overburden 1000 m
Water Depth 10 m
Fluid Influence 10 m
Throw 108 m
DISTANCE: 0.1 m
DISTANCE: 2 m
DISTANCE: 4 m
DISTANCE: 6 m
DISTANCE: 7 m
DISTANCE: 8 m
RIGHT SIDE

(continued from previous page)

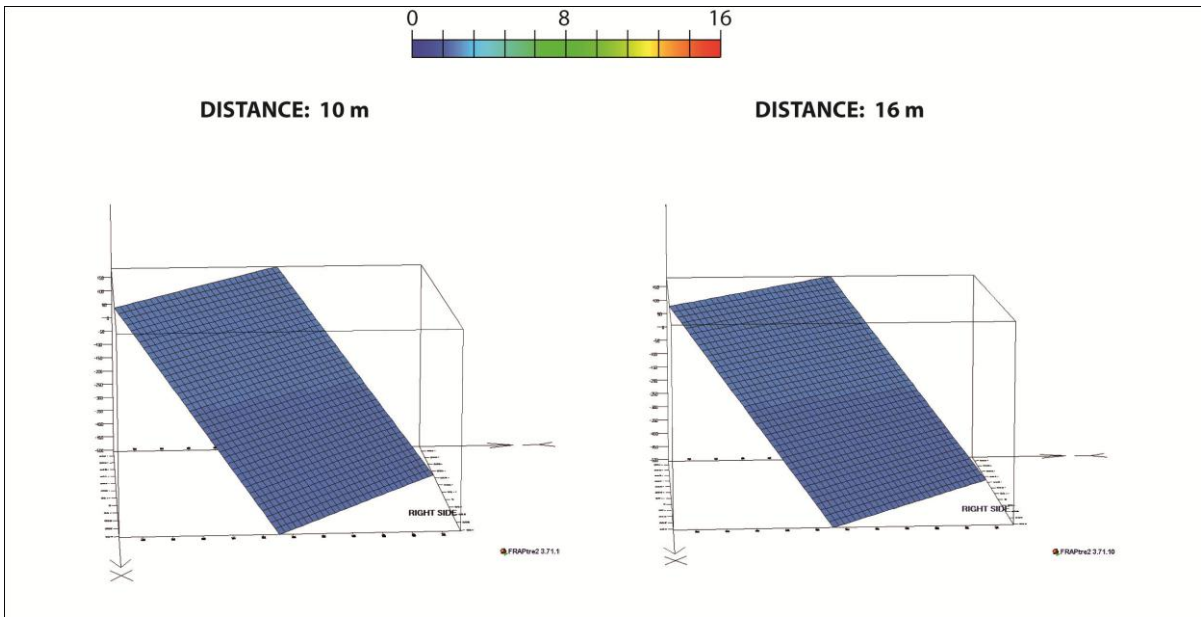

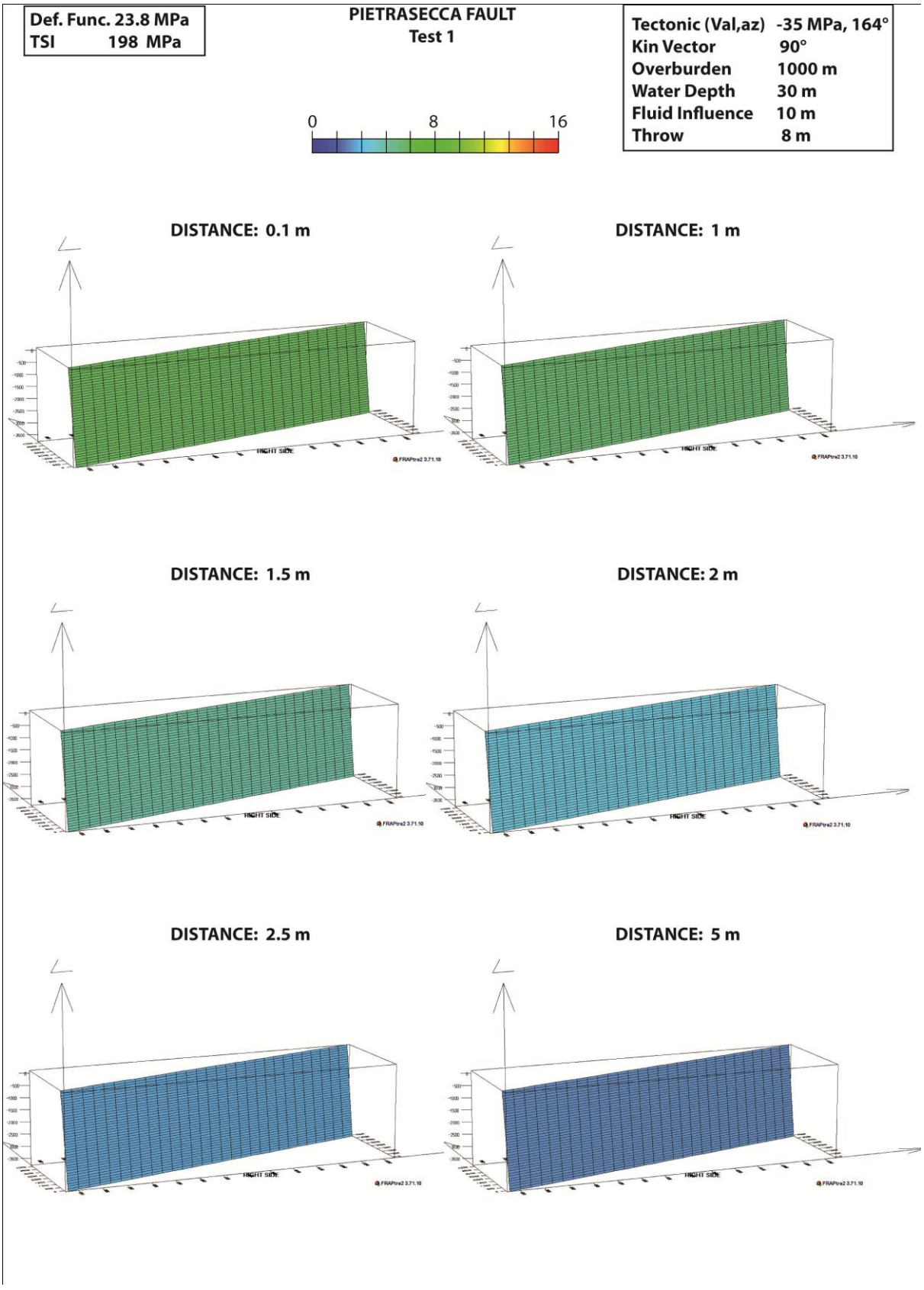
Def. Func. 23.8 MPa
TSI 198 MPa
PIETRASECCA FAULT
Test 1
0
8
16
Tectonic (Val,az) -35 MPa, 164°
Kin Vector 90°
Overburden 1000 m
Water Depth 30 m
Fluid Influence 10 m
Throw 8 m
DISTANCE: 0.1 m
DISTANCE: 1 m
DISTANCE: 1.5 m
DISTANCE: 2 m
DISTANCE: 2.5 m
DISTANCE: 5 m

(continued from previous page)

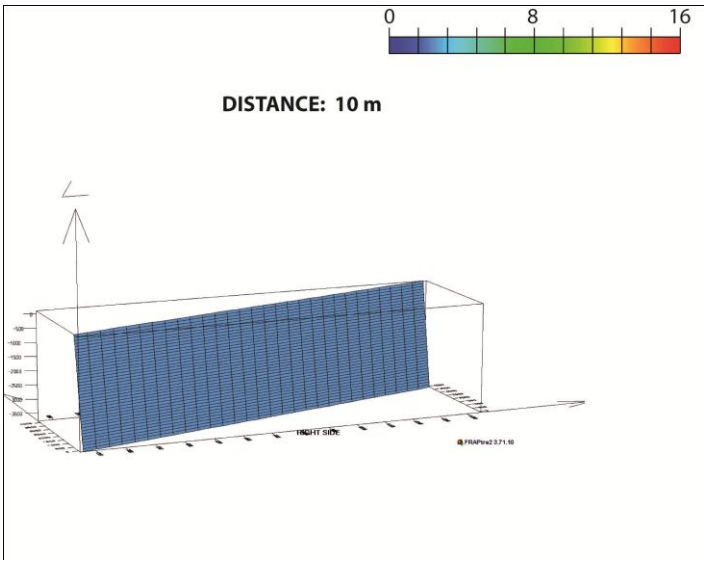

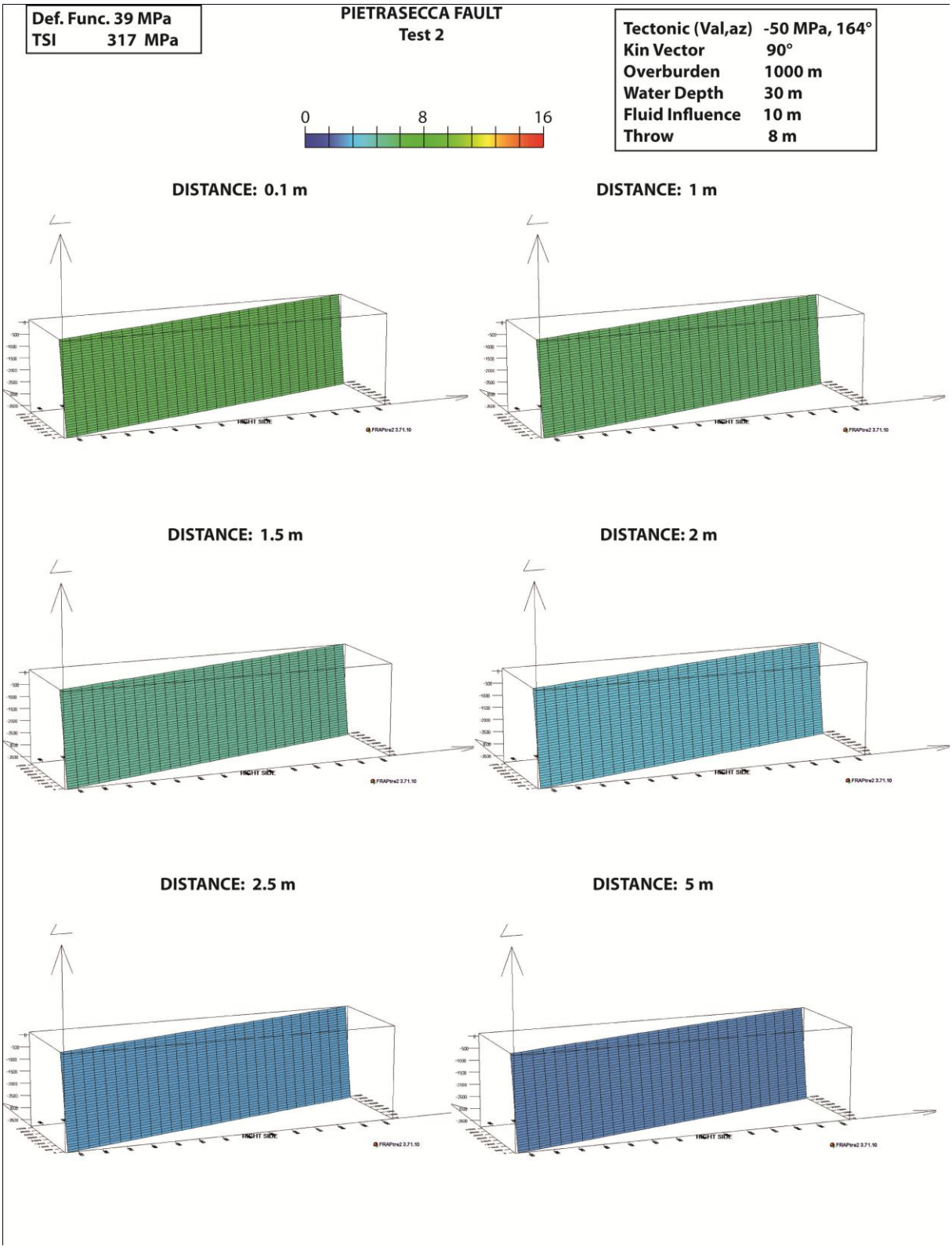
Def. Func. 39 MPa
TSI 317 MPa
PIETRASECCA FAULT
Test 2
0
8
16
Tectonic (Val,az) -50 MPa, 164°
Kin Vector 90°
Overburden 1000 m
Water Depth 30 m
Fluid Influence 10 m
Throw 8 m
DISTANCE: 0.1 m
DISTANCE: 1 m
DISTANCE: 1.5 m
DISTANCE: 2 m
DISTANCE: 2.5 m
DISTANCE: 5 m

(continued from previous page)

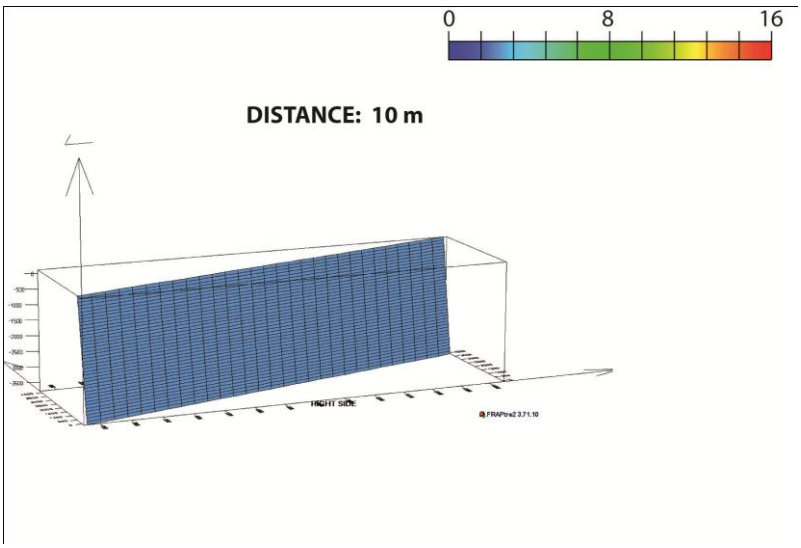

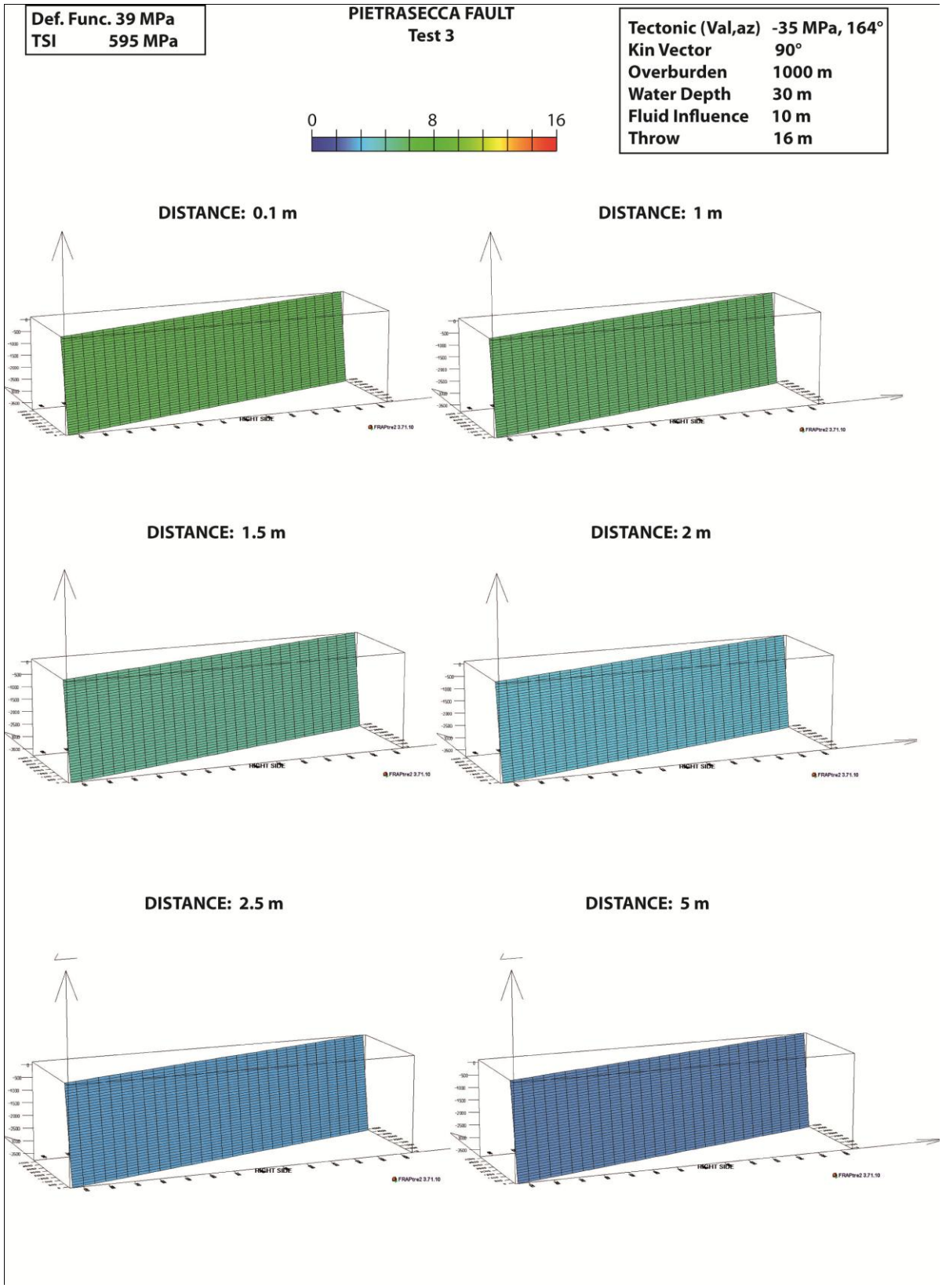
Def. Func. 39 MPa
TSI 595 MPa
PIETRASECCA FAULT
Test 3
0
8
16
Tectonic (Val,az) -35 MPa, 164°
Kin Vector 90°
Overburden 1000 m
Water Depth 30 m
Fluid Influence 10 m
Throw 16 m
DISTANCE: 0.1 m
DISTANCE: 1 m
DISTANCE: 1.5 m
DISTANCE: 2 m
DISTANCE: 2.5 m
DISTANCE: 5 m

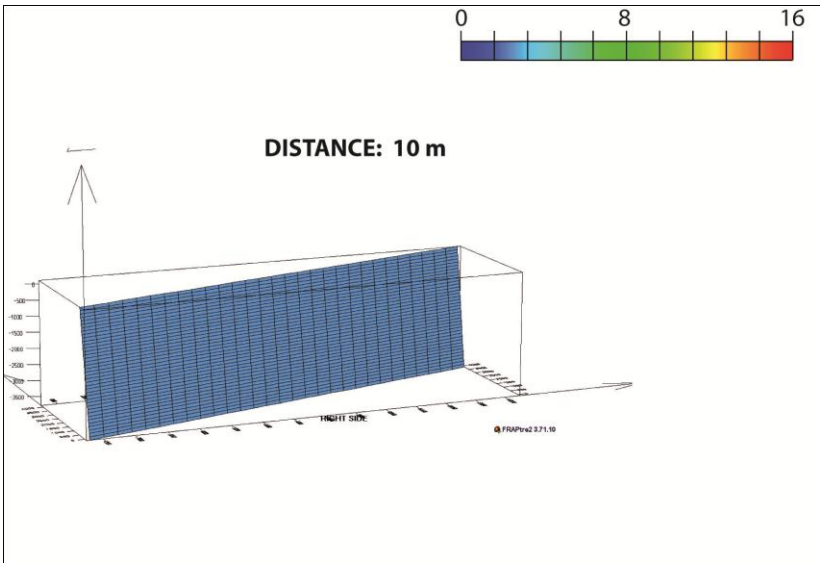
0
8
16
DISTANCE: 10 m

Def. Func. 1.8MPa	
TSI	535 MPa

TORNIMPARTE 1 FAULT
Test 1

Tectonic (Val,az)	-30 MPa, 310°
Kin Vector	30°
Overburden	48 m
Water Depth	10 m
Fluid Influence	10 m
Throw	198 m

DISTANCE: 0.1 m

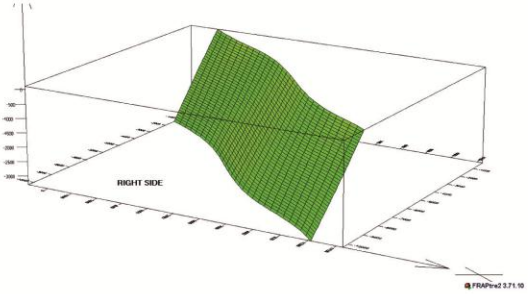

DISTANCE: 3 m

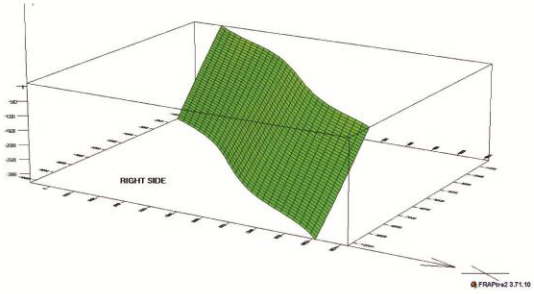

DISTANCE: 6 m

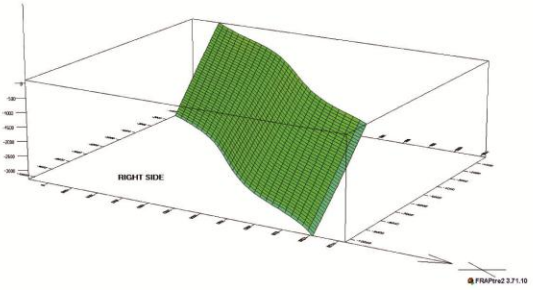

DISTANCE: 9 m

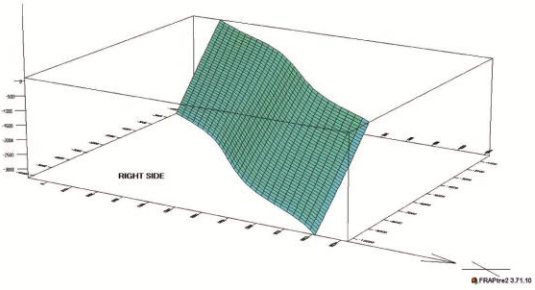

DISTANCE: 10 m

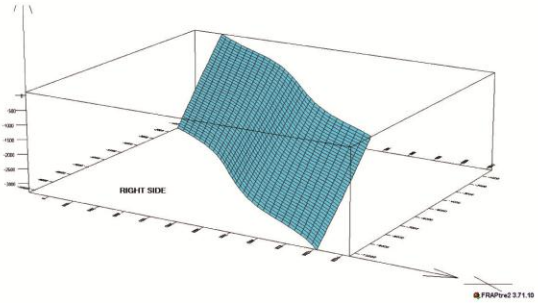

DISTANCE: 15 m

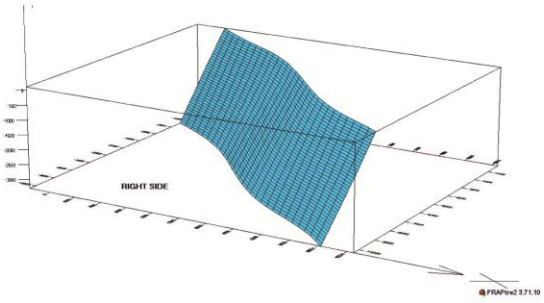

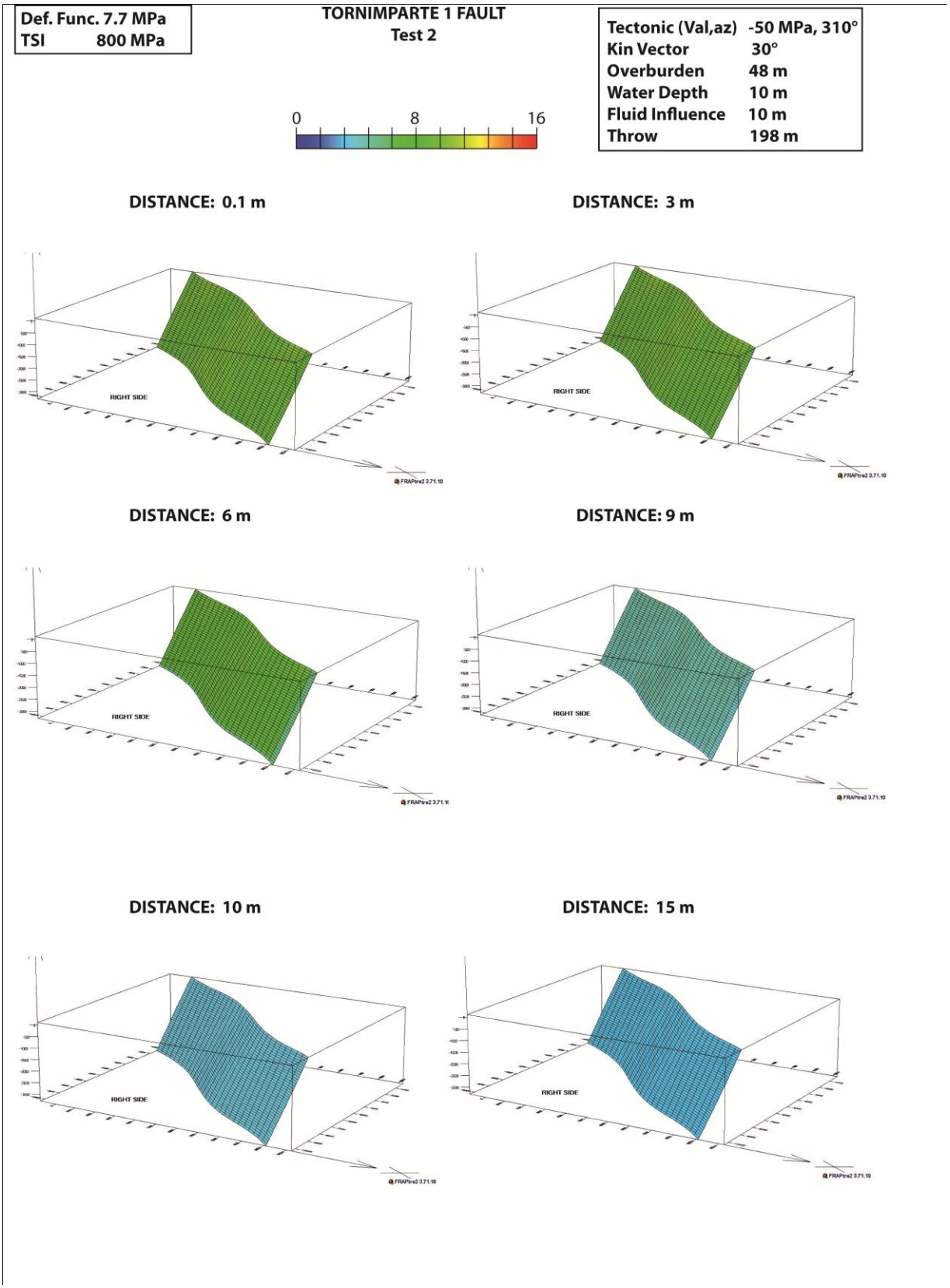
Def. Func. 7.7 MPa
TSI 800 MPa
TORNIMPARTE 1 FAULT
Test 2
0
8
16
Tectonic (Val,az) -50 MPa, 310°
Kin Vector 30°
Overburden 48 m
Water Depth 10 m
Fluid Influence 10 m
Throw 198 m
DISTANCE: 0.1 m
DISTANCE: 3 m
DISTANCE: 6 m
DISTANCE: 9 m
DISTANCE: 10 m
DISTANCE: 15 m
RIGHT SIDE

Def. Func. 1.8 MPa
TSI 1 MPa

TORNIMPARTE 2 FAULT
Test 1

Tectonic (Val,az)	-37 MPa, 184°
Kin Vector	30°
Overburden	368 m
Water Depth	10 m
Fluid Influence	10 m
Throw	0.4 m

DISTANCE: 0.1 m

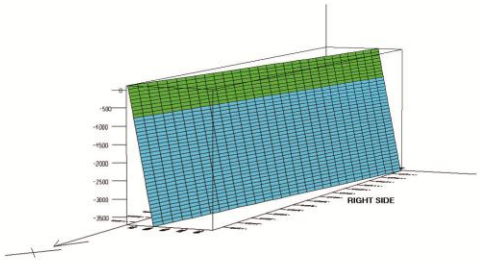

DISTANCE: 0.4 m

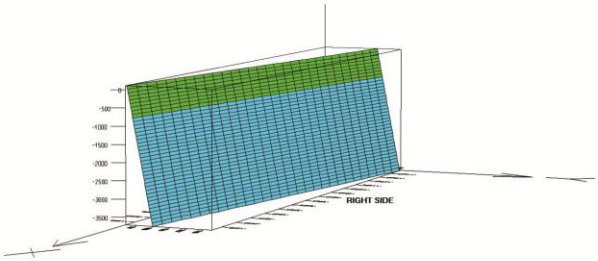

DISTANCE: 1.5 m

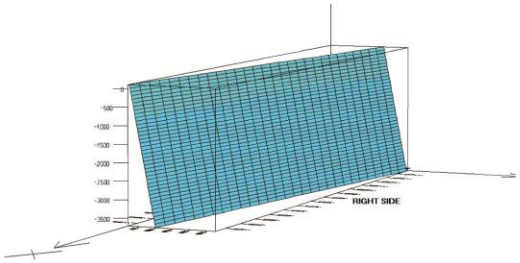

DISTANCE: 2 m

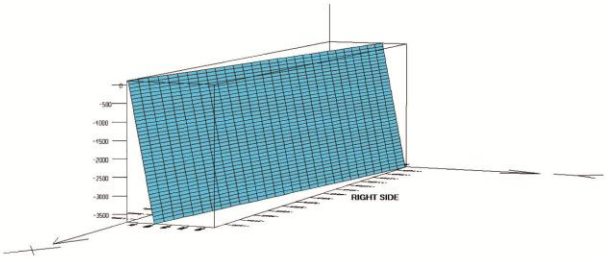

DISTANCE: 5 m

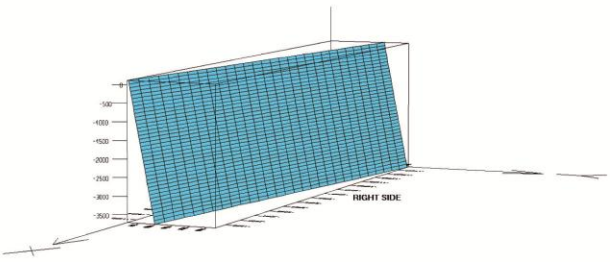

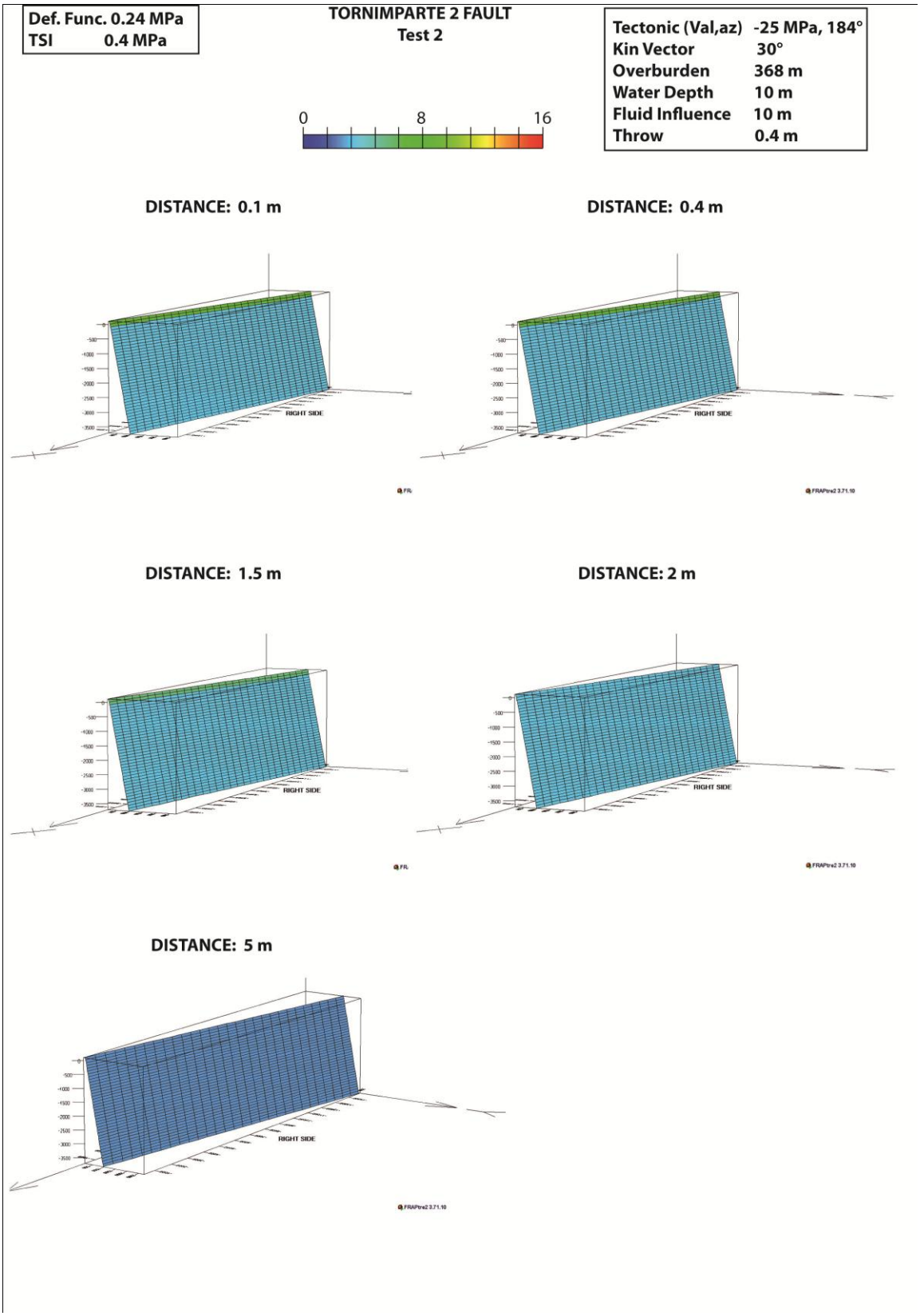
Def. Func. 0.24 MPa
TSI 0.4 MPa
TORNIMPARTE 2 FAULT
Test 2
0
8
16
Tectonic (Val,az) -25 MPa, 184°
Kin Vector 30°
Overburden 368 m
Water Depth 10 m
Fluid Influence 10 m
Throw 0.4 m
DISTANCE: 0.1 m
DISTANCE: 0.4 m
DISTANCE: 1.5 m
DISTANCE: 2 m
DISTANCE: 5 m
RIGHT SIDE

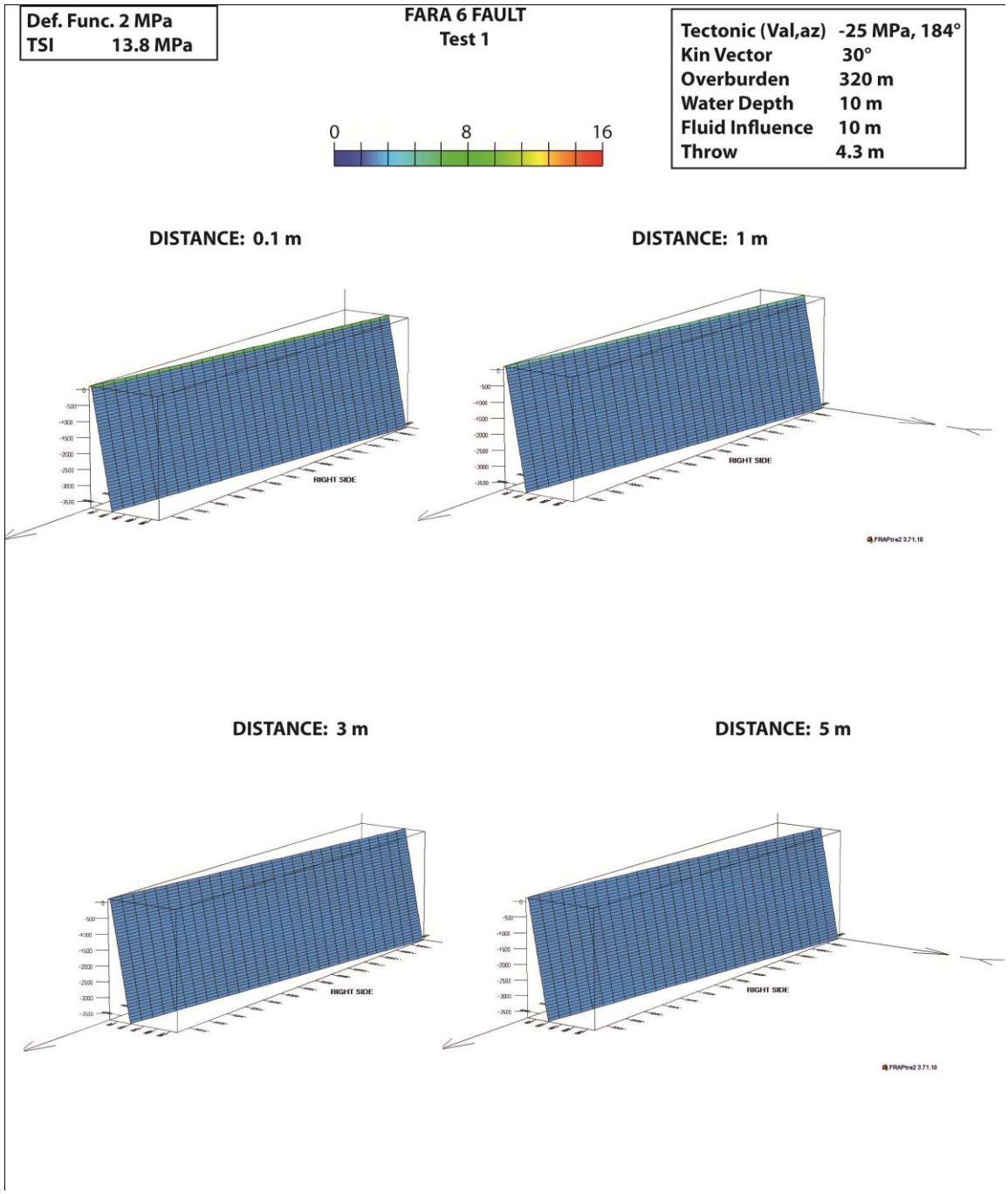
Def. Func. 2 MPa
TSI 13.8 MPa
FARA 6 FAULT
Test 1
0
8
16
Tectonic (Val,az) -25 MPa, 184°
Kin Vector 30°
Overburden 320 m
Water Depth 10 m
Fluid Influence 10 m
Throw 4.3 m
DISTANCE: 0.1 m
DISTANCE: 1 m
RIGHT SIDE
RIGHT SIDE
DISTANCE: 3 m
DISTANCE: 5 m
RIGHT SIDE
RIGHT SIDE

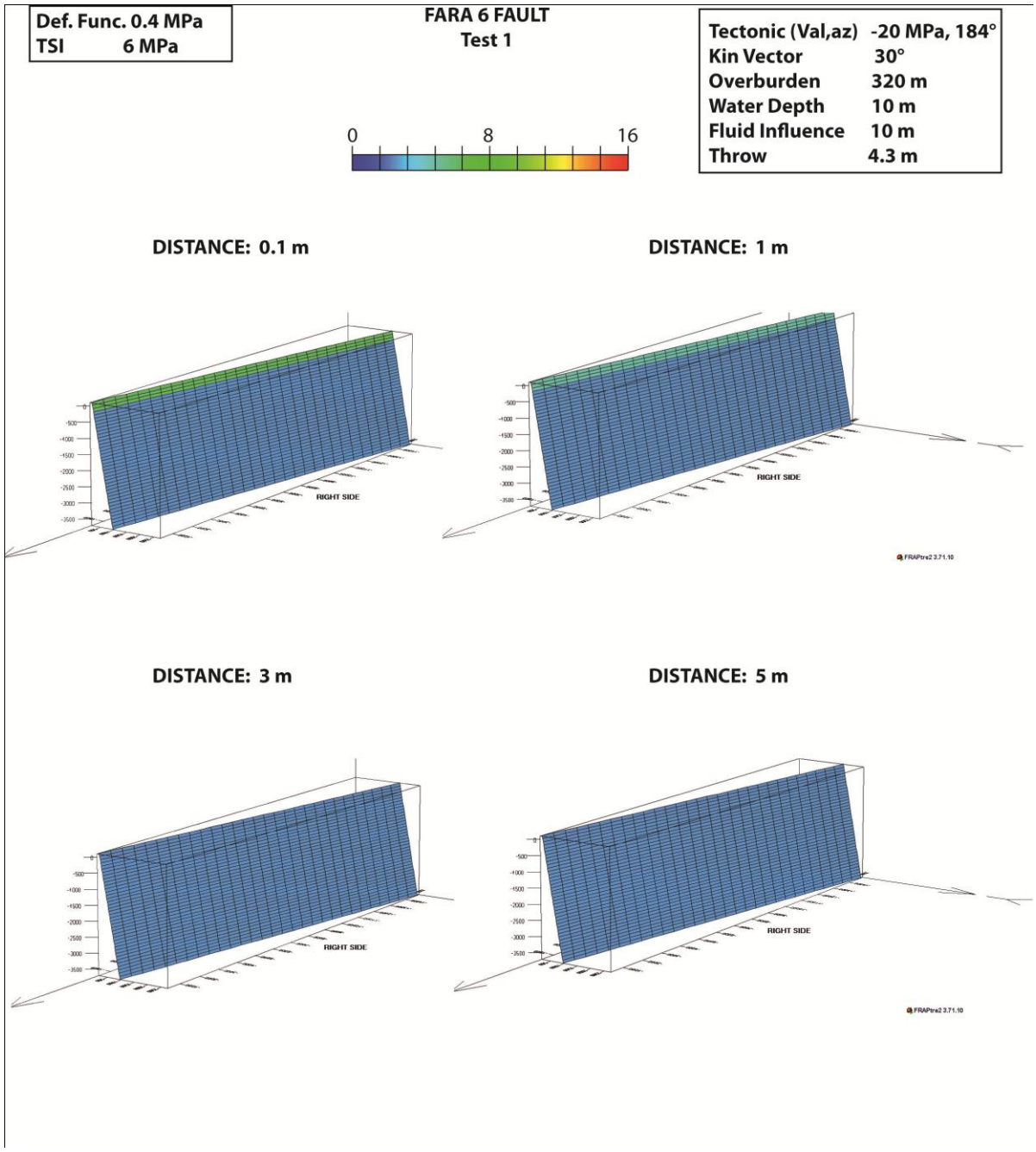
Def. Func. 0.4 MPa
TSI 6 MPa
FARA 6 FAULT
Test 1
0
8
16
Tectonic (Val,az) -20 MPa, 184°
Kin Vector 30°
Overburden 320 m
Water Depth 10 m
Fluid Influence 10 m
Throw 4.3 m
DISTANCE: 0.1 m
DISTANCE: 1 m
DISTANCE: 3 m
DISTANCE: 5 m
RIGHT SIDE
FRAPtre2 3.71.10